

Alma Mater Studiorum – Università di Bologna

DOTTORATO DI RICERCA IN

**Ingegneria Energetica, Nucleare e del
Controllo Ambientale**

Ciclo XXIV

Settore Concorsuale: 09/C2 – Fisica Tecnica

Settore Scientifico-disciplinare: ING-IND/10 – Fisica Tecnica Industriale

**CFD Modeling of Two-Phase Boiling
Flows in the Slug Flow Regime with an
Interface Capturing Technique**

Presentata da: MIRCO MAGNINI

Coordinatore Dottorato:

Prof. Antonio Barletta

Relatori:

Dr. Beatrice Pulvirenti

Prof. John R. Thome

Esame finale anno 2012

Acknowledgments

The first and biggest acknowledgment is for my supervisor Dr. Beatrice Pulvirenti, who gave me the opportunity to begin this doctoral course. La Bea has been my supervisor since my graduation thesis and I am grateful for her constant guidance, the fruitful discussions we have had and her friendship.

I will be always thankful to Professor John Richard Thome, who gave me the opportunity to spend six months as a visiting PhD student at the Laboratory of Heat and Mass Transfer of the École Polytechnique Fédérale de Lausanne, Switzerland. I am honored by his acceptance to become the co-tutor of this thesis.

I would like to express my gratitude to Professor Iztok Zun from the Faculty of Mechanical Engineering of the University of Ljubljana, Slovenia, who accepted to come as an external member for the PhD exam Committee. I am grateful to Dr. Rémi Revellin from the Centre de Thermique de Lyon of the University of Lyon, France, and to Professor Catherine Colin from the Institut de Mécanique des Fluides de Toulouse of the University of Toulouse, France, who accepted to review this thesis. Their detailed and useful comments highlighted some lacks on this work and allowed to achieve a more complete manuscript.

A special thanks to Dr. Vittoria Rezzonico, coordinator of the HPC center and Dr. Anne Possoz of DIT, EPFL, which gave me the chance to resort strongly to parallel computations, a fundamental resource to achieve the results discussed with this thesis.

Last but not least, I thank my family for their constant support and my girlfriend Monica, at my side since several years and fundamental to wash away the numerics from the mind at the end of the day.

Abstract

Microscale flow boiling is currently the most promising cooling technology when high heat fluxes have to be dissipated. The slug flow regime occupies a large area in the microscale two-phase flow pattern map, thus the understanding of the thermal and hydrodynamic features of the flow plays a fundamental role in the design of microevaporators. The current experimental techniques are still inadequate to capture the small scales involved in the flow, while the recent advances in the multiphase CFD techniques provide innovative tools to investigate the two-phase flow. However, the scientific literature concerning with numerical modeling of flow boiling patterns is still poor, such that several aspects of the flow are not clarified yet.

The objective of this thesis was to improve the commercial CFD software Ansys Fluent to obtain a tool able to perform accurate simulations of flow boiling in the slug flow regime. The achievement of a reliable numerical framework allows a better understanding of the bubble and flow dynamics induced by the evaporation and makes possible the prediction of the wall heat transfer trends.

In order to save computational time, the flow is modeled with an axisymmetrical formulation. Vapor and liquid phases are treated as incompressible and in laminar flow. By means of a single fluid approach, the flow equations are written as for a single phase flow, but discontinuities at the interface and interfacial effects need to be accounted for and discretized properly. Ansys Fluent provides a Volume Of Fluid technique to advect the interface and to map the discontinuous fluid properties throughout the flow domain. The interfacial effects are dominant in the boiling slug flow and the accuracy of their estimation is fundamental for the reliability of the solver. Self-implemented functions, developed *ad-hoc*, are introduced within the numerical code to compute the surface tension force and the rates of mass and energy exchange at the interface related to the evaporation. Several validation benchmarks

assess the better performances of the improved software.

Various adiabatic configurations are simulated in order to test the capability of the numerical framework in modeling actual flows and the comparison with experimental results is very positive. The study of the dynamics of evaporating bubbles begins with a grid convergence analysis and a discussion on the effect of different boundary conditions, in order to clarify some numerical aspects on the modeling of the flow. The simulation of a single evaporating bubble underlines the dominant effect on the global heat transfer rate of the local transient heat convection in the liquid after the bubble transit. The simulation of multiple evaporating bubbles flowing in sequence shows that their mutual influence can strongly enhance the heat transfer coefficient, up to twice the single phase flow value.

Keywords: flow boiling, microchannel, slug flow, evaporation model, interface reconstruction algorithm, volume of fluid.

Sommario

L'ebollizione in microcanali è attualmente la tecnologia di raffreddamento più promettente per lo smaltimento di alti flussi termici. Siccome il regime di slug flow occupa una porzione piuttosto ampia della mappa dei modelli di flusso bifase in microcanali, la comprensione delle caratteristiche termofluidodinamiche del moto svolge un ruolo fondamentale nella progettazione di microevaporatori. Le correnti tecniche sperimentali sono ancora inadeguate a compiere misure su scale così piccole, mentre i passi in avanti compiuti recentemente dalle tecniche CFD multifase forniscono degli strumenti innovativi per analizzare i flussi bifase. Ciononostante, la letteratura scientifica riguardante la modellazione numerica di flussi in ebollizione è ancora scarsa e diversi aspetti fisici non sono stati ancora chiarificati.

Questa tesi si è posta l'obiettivo di migliorare il codice commerciale CFD Ansys Fluent, per ottenere un solutore in grado di compiere simulazioni accurate di flussi in ebollizione nel regime di slug flow. Un codice numerico affidabile permette una miglior comprensione della dinamica della bolla causata dall'evaporazione e rende possibile la stima dello scambio termico alla parete.

Per limitare il costo computazionale delle simulazioni, il flusso fisico è modellato con una formulazione assialsimmetrica. Le fasi liquido e vapore sono incomprimibili ed in moto laminare. Attraverso un approccio di tipo single fluid, le equazioni che governano il moto sono scritte come per un flusso a fase singola, tuttavia discontinuità ed effetti di interfaccia vanno introdotti e discretizzati in maniera propria. Fluent dispone di una tecnica di tipo Volume of Fluid per l'avvezione dell'interfaccia e per mappare le discontinue proprietà del fluido su tutto il dominio. Nello slug flow gli effetti di interfaccia sono dominanti, di conseguenza l'accuratezza con cui essi sono calcolati è fondamentale per la veridicità del solutore. A tale scopo, sono state introdotte nel codice numerico delle funzioni esterne, sviluppate appositamente per

il calcolo della tensione superficiale e dello scambio di massa ed energia all'interfaccia come conseguenza dell'evaporazione. Le migliori prestazioni del codice modificato rispetto a quello originale sono dimostrate attraverso numerosi casi test.

Per provare la validità del nuovo codice numerico nella riproduzione di reali configurazioni di flusso, sono stati simulati diversi flussi adiabatici ed il confronto con i risultati sperimentali è molto positivo. Lo studio della dinamica delle bolle durante l'evaporazione comincia con una analisi della convergenza di griglia e una discussione sugli effetti di diverse condizioni al contorno, allo scopo di capire alcuni aspetti numerici sulla modellazione del flusso. La simulazione dell'evaporazione di una bolla singola evidenzia che la convezione transitoria nel liquido, successivamente al passaggio della bolla, ha un effetto dominante sul coefficiente di scambio termico globale. La simulazione di bolle multiple che evaporano in sequenza mostra che la loro influenza reciproca migliora notevolmente il coefficiente di scambio, fino a due volte rispetto ad un flusso a fase singola.

Contents

Acknowledgments	iii
Abstract	v
Sommario	vii
Contents	ix
List of Tables	xiii
List of Figures	xv
Nomenclature	xxi
Introduction	xxvii
1 Mathematical formulation of two-phase flows	1
1.1 Formulation without surface tracking	2
1.2 Formulation with surface tracking	4
1.2.1 Two-fluid formulation	5
1.2.2 Single fluid formulation	8
1.3 The Front Tracking algorithm	11
1.4 The Level-Set method	13
1.5 The Volume Of Fluid method	15
1.6 Hybrid methods	19
1.7 Surface tension force modeling	20

2	Elongated bubbles flow: a review	25
2.1	Vertical circular channels	26
2.1.1	Experiments and analytical models	27
2.1.2	Numerical simulations	30
2.2	Horizontal circular channels	33
2.2.1	Experiments and analytical models	34
2.2.2	Numerical simulations	49
2.3	Concluding remarks: open issues on flow boiling in microscale	56
3	Modeling of interfacial effects	57
3.1	The interface reconstruction algorithm	58
3.1.1	The Height Function algorithm	62
3.2	The evaporation model	69
3.2.1	The interface temperature condition	69
3.2.2	The numerical model	74
4	Ansys Fluent solver and the implementation of the UDF	79
4.1	The flow equation set	80
4.2	Fluent discretization procedure	81
4.2.1	Temporal discretization	82
4.2.2	Spatial discretization	83
4.2.3	Reconstruction of the cell centered gradients	84
4.2.4	The final algebraic equation	86
4.3	Discretization of the volume fraction equation	87
4.4	Pressure-velocity coupling: the PISO algorithm	92
4.4.1	Interpolation of cell-centered pressures on cell faces	95
4.5	The energy equation	96
4.6	The additional scalar equation for the evaporation rate	96
4.7	Boundary conditions	97
4.8	User-Defined Functions	99
4.8.1	Initialization of the volume fraction field	101
4.8.2	Implementation of the surface tension force	101
4.8.3	Implementation of the evaporation model	102
4.9	Fluent solution procedure	103

4.10	Concluding remarks: flow solver set-up	107
5	Validation of the numerical framework	109
5.1	Reproduction of a circular interface	109
5.2	Simulation of an inviscid static droplet	112
5.3	Isothermal bubble rising in stagnant liquid	117
5.3.1	Two-dimensional inviscid rising bubble	117
5.3.2	Axisymmetrical bubble rising in viscous liquid	119
5.4	Vapor bubble growing in superheated liquid	123
5.4.1	Discrete domain and initial conditions	124
5.4.2	Initial thermal boundary layer placement	125
5.4.3	Working fluids properties	126
5.4.4	Setting of diffusion parameter	127
5.4.5	Results	128
5.5	Concluding remarks	131
6	Results on elongated bubbles motion in adiabatic condition	133
6.1	Taylor bubbles rising in vertical circular channels	133
6.1.1	Simulation sensitivity analysis	134
6.1.2	Comparison with PIV analysis	137
6.1.3	Numerical simulations of Taylor bubbles: results	140
6.2	Elongated bubbles in horizontal circular channels	144
6.3	Concluding remarks: limits of the computations	153
7	Results on elongated bubbles motion with evaporation	155
7.1	Grid convergence analysis	156
7.2	Flow boundary conditions	165
7.3	Flow and temperature field	172
7.3.1	Comparison of bubble nose position with a theoretical model	185
7.4	Heat transfer with multiple bubbles	188
7.4.1	Simulation conditions	188
7.4.2	Bubbles dynamics	190
7.4.3	Heat transfer performance	193
	Conclusions	205

A Numerically induced capillary waves in the simulation of multiphase flows	211
A.1 Stability analysis of a static droplet	212
A.2 Numerical origin of the capillary wave	215
A.3 Numerical simulations of the static droplet	216
A.3.1 Oscillation time period	217
A.3.2 Droplet profile evolution	218
A.3.3 Velocity fields	220
Bibliography	221
List of Scientific Publications	235
Curriculum Vitae	237

List of Tables

3.1	Relative magnitude of microscale effects on the interface temperature deviation from the saturation condition.	72
4.1	Comparison of the Green-Gauss cell based and node based schemes for the reconstruction of cell centered gradients.	86
4.2	Comparison of the Fluent body-force-weighted and PRESTO formulations to compute face-centered pressures.	95
5.1	Comparison of experimental and numerical terminal shape and Reynolds number for gas bubbles rising in stagnant viscous liquids.	120
5.2	Properties of the working fluids chosen for the simulation of a vapor bubble growing in superheated liquid.	126
6.1	Parameters varied in the rising Taylor bubble sensitivity analysis. . .	135
6.2	Comparison of numerical results with experimental correlations for flow within horizontal channels.	148
7.1	Properties of R113 liquid and vapor at saturation conditions for $T_{sat} = 50^{\circ}\text{C}$	157
7.2	Properties of R245fa liquid and vapor at saturation conditions for $T_{sat} = 31^{\circ}\text{C}$	189
7.3	Heat transfer coefficients at the axial locations under analysis.	196
7.4	Comparison of the heat transfer performance obtained with the simulation with the values predicted by correlations.	199
A.1	Summary of the parameters varied in the numerical simulations. . .	217
A.2	Comparison of analytical and numerical periods of the oscillations. .	219

List of Figures

1.1	Example of computational grids for BFM and ALE method.	7
1.2	Example of moving front and fixed grid for the Front Tracking method.	11
1.3	Example of the level-set field across an interface.	13
1.4	Example of the volume fraction field across an interface.	16
1.5	Different VOF-based interface reconstruction methods.	18
1.6	Spurious velocity field across a circular interface.	22
2.1	White and Beardmore [1] flow pattern map for Taylor bubbles rising in stagnant liquid.	28
2.2	Revellin <i>et al.</i> [2] elongated bubble images for R134a at 30 °C within a 2 mm, 0.8 mm and 0.5 mm diameter channel.	34
2.3	Han and Shikazono transition map [3] for the influence of gravitational effects on the slug flow within horizontal microchannels.	35
2.4	Han and Shikazono [3] experimental measured liquid film thickness for slug flow within horizontal microchannels.	39
2.5	Microchannel slug flow snapshot for R245fa, horizontal 0.5 mm circular channel, $G = 517 \text{ kg/m}^2\text{s}$, $x = 0.047$, $T_{sat} = 34.4 \text{ °C}$	40
2.6	Flow pattern map of Triplett <i>et al.</i> [4] for air-water flow in a 1.1 mm horizontal circular channel.	41
2.7	Comparison of the predicted bubble velocity with respect to the liquid mean velocity, for various models.	44
2.8	Scheme of the bubble-liquid slug unit in the Thome <i>et al.</i> three-zones model [5].	46
2.9	Walsh <i>et al.</i> [6] experimental local Nusselt number for slug flow in the thermal entrance zone of a horizontal microchannel.	47

3.1	Example of the volume fraction field across a circular arc and Height Function approximated interface.	61
3.2	Sketch of the continuous height function.	62
3.3	Examples of Height Function algorithm steps	68
3.4	Scaling effect on the contribution of different physical effects on the interfacial superheating.	73
3.5	Steps of Hardt and Wondra evaporation model [7] for the derivation of the mass source term.	77
4.1	Example of a computational control volume.	83
4.2	Geometrical reconstruction of the volume fraction equation convective term by an Eulerian split advection technique.	90
4.3	Fluent pressure-based segregated solution procedure for VOF-treated two-phase flows.	105
5.1	HF and Youngs computed norm vector error norm convergence rate in the reproduction of a circular interface.	111
5.2	HF and Youngs computed curvature error norm convergence rate in the reproduction of a circular interface.	111
5.3	Velocity error norm in the simulation of an inviscid static droplet for HF and Youngs methods.	114
5.4	Velocity field arising in the simulation of an inviscid static droplet when computing the interface curvature by the HF algorithm.	114
5.5	Interface pressure jump error norm in the simulation of an inviscid static droplet for HF and Youngs methods.	115
5.6	Pressure profiles across a droplet in the simulation of an inviscid static droplet for HF and Youngs algorithms.	116
5.7	Terminal bubble shapes for the simulations of an inviscid rising bubble in stagnant liquid.	118
5.8	Velocity vectors around a gas bubble rising in viscous stagnant liquid at low and high Morton numbers.	122
5.9	Initial condition for the simulation of a vapor bubble growing in superheated liquid.	124

5.10	Initial dimensionless temperature profile at the bubble interface on the liquid side.	125
5.11	Numerical smoothing of the evaporation rate at the interface.	127
5.12	Temperature and vapor volume fraction profiles across the interface at different time instants.	128
5.13	Velocity vectors and bubble interface positions for water bubble simulation at various time instants.	129
5.14	Vapor bubble radius over time for analytical and numerical solutions.	130
6.1	Bubble initial configuration for the simulation of Taylor bubbles rising in vertical channels.	134
6.2	Sensitivity analysis results	137
6.3	Liquid flow field around a Taylor bubble rising in stagnant liquid.	138
6.4	Velocity profiles of the liquid above a rising Taylor bubble	139
6.5	Velocity profiles of the liquid within the liquid film and below a rising Taylor bubble.	140
6.6	Terminal shape of the Taylor bubbles for the numerical simulations.	142
6.7	Location of the rising Taylor bubbles simulation runs within the White and Beardmore [1] flow pattern map.	143
6.8	Bubble terminal shapes for flow within horizontal channels.	146
6.9	Static pressure profiles along the channel axis for flow within horizontal channels.	147
6.10	Pressure field and velocity vectors across the bubble for $Ca= 0.0125$ and $Re= 625$	150
6.11	Profiles of the dimensionless axial velocity of the liquid along the radial direction at various axial locations in the wake and in the liquid film for $Ca= 0.0125$ and $Re= 625$	151
6.12	Streamlines of the defect flow field in the wake and the film region for $Ca= 0.0125$ and $Re= 625$	152
7.1	Initial configuration for the simulations involved in the grid convergence analysis.	158
7.2	Initial wall temperature and heat transfer coefficient.	158
7.3	Velocity of the bubble nose.	159

7.4	Bubble profiles at $t = 5.5$ ms.	159
7.5	Bubble volume growth rate.	160
7.6	Bubble evolution at various time instants.	161
7.7	Heat transfer coefficients at $t = 7.5, 8.5, 9.5$ ms.	163
7.8	Heat transfer coefficients at $t = 10.5, 11.5, 12.5$ ms.	164
7.9	Bubble evolution during evaporation, from $t = 4.5$ ms to 12.5 ms at time intervals of 1 ms.	166
7.10	Bubble volume growth rate and velocity of rear, nose and center of gravity.	167
7.11	Bubble profiles at various time instants obtained with different bound- ary conditions.	169
7.12	Bubble evolution during evaporation, from $t = 4.5$ ms to 14.5 ms at time intervals of 1 ms, $q = 20$ kW/m ²	171
7.13	Velocity of the bubble rear and nose, $q = 20$ kW/m ²	172
7.14	Average liquid axial and radial velocity and contours of the velocity field.	174
7.15	Wall temperature, heat transfer coefficient and temperature contours in the wake.	175
7.16	Wall temperature, heat transfer coefficient and temperature contours in the region occupied by the bubble.	176
7.17	Local enhancement on the heat transfer induced by the two-phase flow.	177
7.18	Temperature and axial velocity profiles at $z/D = 10, 11, 12.4$	178
7.19	Temperature and axial velocity profiles at $z/D = 12.65, 12.83, 13.5$	179
7.20	Temperature and axial velocity profiles at $z/D = 14, 14.5, 19$	180
7.21	Fluid flow, temperature field and heat transfer in the wavy region of the film.	182
7.22	Comparison of the local bulk heat transfer coefficient with the heat conduction based heat transfer coefficient.	183
7.23	Comparison of bubble nose position and volume with Consolini and Thome model [8].	186
7.24	Heat flux absorbed by the bubble evaporation.	187
7.25	Evolution of two bubbles flowing in sequence during evaporation.	191
7.26	Leading and trailing bubbles position and velocity during evaporation.	192

7.27	Profiles of the bubble before and at the end of the heated region. . .	193
7.28	Heat transfer coefficient at various axial locations.	195
7.29	Time-averaged heat transfer coefficient.	197
7.30	Comparison of the simulation heat transfer coefficient with the model.	202
A.1	Initial non-dimensional droplet radius distribution.	215
A.2	Numerical dimensionless velocity norm with respect to the non-dimensional time.	218
A.3	Non-dimensional droplet radius evolution in time.	220

Nomenclature

Roman Letters

A_f	area of the computational cell face	[m ²]
$Bo = \frac{\rho g D}{\sigma}$	Bond number	[-]
b	generic fluid property	
$Ca = \frac{\mu U}{\sigma}$	Capillary number	[-]
$Co = \left(\frac{\sigma}{g(\rho_l - \rho_g) D^2} \right)^{1/2}$	Confinement number	[-]
$Co = \frac{\Delta t}{V / \sum_f^{N_f} \mathbf{u}_f \cdot \mathbf{n}_f A_f}$	Courant number	[-]
c_p	constant pressure specific heat	[m ² s ⁻² K ⁻¹]
D	diameter	[m]
	diffusion constant	[m ²]
E	interfacial energy transfer	[kg m ⁻¹ s ⁻³]
	mass average energy	[m ² s ⁻²]
$Eo = \frac{\rho g D^2}{\sigma}$	Eötvös number	[-]
e	specific internal energy	[m ² s ⁻²]
$Fr = \frac{U}{\sqrt{gD}}$	Froude number	[-]
G	mass flux	[kg m ⁻² s ⁻¹]
\mathbf{g}	gravity vector	[m s ⁻²]
H	level-set smoothed Heaviside function	[-]
	height function	[m]
h	heat transfer coefficient	[kg s ⁻³ K ⁻¹]
	grid spacing	[m]
	specific enthalpy	[m ² s ⁻²]

h_{lv}	latent heat of vaporization	$[\text{m}^2 \text{s}^{-2}]$
I	indicator function	$[-]$
\mathbf{I}	identity tensor	$[-]$
L	length	$[\text{m}]$
L_s	liquid slug length	$[\text{m}]$
M	molecular weight	$[\text{kg mol}^{-1}]$
\mathbf{M}	interfacial momentum transfer vector	$[\text{kg m}^{-2} \text{s}^{-2}]$
$\text{Mo} = \frac{g\mu^4}{\rho\sigma^3}$	Morton number	$[-]$
m	bubble relative drift velocity	$[-]$
\dot{m}	interphase mass flux	$[\text{kg m}^{-2} \text{s}^{-1}]$
N, N_l, N_v	normalization factors	$[-]$
$\text{Nu} = \frac{hD}{\lambda}$	Nusselt number	$[-]$
$N_f = \frac{\rho g^{1/2} D^{3/2}}{\mu}$	inverse viscosity number	$[-]$
\mathbf{n}	interface unit norm vector	$[-]$
$\text{Pe} = \frac{\rho c_p U D}{\lambda}$	Peclet number	$[-]$
$\text{Pr} = \frac{\mu c_p}{\lambda}$	Prandtl number	$[-]$
p	pressure	$[\text{kg m}^{-1} \text{s}^{-2}]$
q	heat flux	$[\text{kg s}^{-3}]$
\dot{q}	interphase heat flux	$[\text{kg s}^{-3}]$
R	radius	$[\text{m}]$
	universal gas constant	$[\text{kg m}^2 \text{s}^{-2} \text{mol}^{-1} \text{K}^{-1}]$
$\text{Re} = \frac{\rho U D}{\mu}$	Reynolds number	$[-]$
r	radial coordinate	$[\text{m}]$
S_E	energy source term	$[\text{kg m}^{-1} \text{s}^{-3}]$
S_m	momentum source term	$[\text{kg m}^{-2} \text{s}^{-2}]$
S_α	volume fraction source term	$[\text{kg m}^{-3} \text{s}^{-1}]$
S_ρ	mass source term	$[\text{kg m}^{-3} \text{s}^{-1}]$
S_φ	evaporation rate equation source term	$[\text{kg m}^{-3} \text{s}^{-1}]$
T	temperature	$[\text{K}]$
t	time	$[\text{s}]$
\mathbf{t}	interface unit tangent vector	$[-]$
U	velocity	$[\text{m s}^{-1}]$

\mathbf{u}	velocity vector	$[\text{m s}^{-1}]$
V	volume	$[\text{m}^3]$
\mathbf{V}	interface velocity vector	$[\text{m s}^{-1}]$
$We = \frac{\rho U^2 D}{\sigma}$	Weber number	$[-]$
x	x coordinate	$[\text{m}]$
	mass fraction	$[-]$
\mathbf{x}	position vector	$[\text{m}]$
y	y coordinate	$[\text{m}]$
z	axial coordinate	$[\text{m}]$
z_h	axial coordinate relative to the entrance in the heated region	$[\text{m}]$

Greek Letters

α	volume fraction	$[-]$
β	gas phase volumetric flow rate	$[-]$
	Scriven model growth constant	$[-]$
Γ	interfacial mass transfer	$[\text{kg m}^{-3} \text{s}^{-1}]$
γ	thermal diffusivity	$[\text{m}^2 \text{s}^{-1}]$
$\Delta x, \Delta y$	horizontal and vertical grid spacing	$[\text{m}]$
δ	Dirac delta-function	
	liquid film thickness	$[\text{m}]$
δ_T	thickness of the thermal boundary layer	$[\text{m}]$
ϵ	void fraction	$[-]$
κ	interface curvature	$[\text{m}^{-1}]$
λ	thermal conductivity	$[\text{kg m s}^{-3} \text{K}^{-1}]$
μ	dynamic viscosity	$[\text{kg m}^{-1} \text{s}^{-1}]$
ρ	density	$[\text{kg m}^{-3}]$
σ	surface tension coefficient	$[\text{kg s}^{-2}]$
	accommodation coefficient	$[-]$

$\boldsymbol{\tau}$	shear stress tensor	$[\text{kg m}^{-1} \text{s}^{-2}]$
ϕ	level-set function	$[\text{m}]$
	kinetic mobility	$[\text{kg m}^{-2} \text{s}^{-1} \text{K}^{-1}]$
	generic flow variable	
φ, φ_0	smeared and original evaporation rate	$[\text{kg m}^{-3} \text{s}^{-1}]$

Subscripts

b	bubble, bulk
c	cell-centroid-centered value
ex	exact value
f	cell-face-centered value
G	center of gravity
g	gas
if	relative to the interface
l	liquid
N	bubble nose
n	node-centered value
R	bubble rear
ref	reference conditions
s	superficial
sat	saturation conditions
sp	single phase
tp	two-phase
v	vapor
w	wall
∞	relative to system ambient conditions

Acronyms

ALE	Arbitrary Lagrangian Eulerian
BFM	Boundary Fitted Method
CD	Centered finite Difference
CFD	Computational Fluid Dynamics
CLSVOF	Coupled Level-Set and Volume Of Fluid
CSF	Continuum Surface Force Method
CSS	Continuum Surface Stress Method
ENO	Essentially Non-Oscillatory
FT	Front Tracking
GSM	Ghost Fluid Method
HF	Height Function
LS	Level-Set
LVIRA	Least-squares Volume of fluid Interface Reconstruction Algorithm
MAC	Marker and Cell
MPI	Message Passing Interface
MUSCL	Monotonic Upstream-centered Scheme for Conservation Laws
PDA	Photocromic Dye Activation
PISO	Pressure Implicit Splitting of Operators
PIV	Particle Image Velocimetry
PLIC	Piecewise Linear Interface Calculation
PRESTO	PRessure STaggering Option
PROST	Parabolic Reconstruction Of Surface Tension
RPI	Renssealer Polytechnic Institute
SIMPLE	Semi Implicit Method for Pressure-Linked Equations
SIMPLEC	SIMPLE Consistent
SLIC	Single Line Interface Calculation
SOU	Second Order Upwind
UDF	User Defined Function
VOF	Volume Of Fluid
WENO	Weighted Essentially Non-Oscillatory

Introduction

Microscale flow boiling as the most promising cooling technology for high heat density devices

The number of transistors that can be placed inexpensively on an integrated circuit is growing as an exponential function of the time, as stated by the Moore's law. The necessity to cool down such electronic devices, whose power density is increasing, requires cooling processes more and more efficient.

The Uptime Institute estimates that within the 2014 the heat load per product footprint of data centers is going to exceed 10 W/cm^2 . Currently, the most widely used cooling technology for microprocessors within data centers is refrigerated air cooling. The heat power generated in the chip by Joule's effect is conducted across a thermal interface material in contact with the silicon chip die itself and then across a heat spreader cooling element, where finally it is transferred to refrigerated air by convection [9].

Nowadays, the electronic cooling technology is facing the challenge of removing more than 300 W/cm^2 from the electronic chip. The poor global efficiency together with the waste of energy related to the whole refrigerating system, is making the refrigerated air technology inadequate to face the increasing heat fluxes to be dissipated. One promising solution is the application of two-phase cooling directly on the chip through microchannels evaporators. The main advantages of two-phase flow boiling heat transfer compared to other cooling methods are [10]: lower mass flow rate of the coolant, lower pressure drop, lower temperature gradients due to saturated flow conditions, heat transfer coefficient increasing with heat flux. Among the drawbacks, the microscale flow and heat transfer trends are not yet fully clarified and the macroscale models does not apply reliably.

The cooling of data centers, laser-diodes, microchemical reactors, portable computer chips, aerospace avionics components, automotive and domestic air conditioning, are some of the industrial applications which the microscale two-phase cooling technology is now penetrating.

The importance of the slug flow regime in the microscale

The slug flow (also known as segmented flow, Taylor flow, elongated bubbles flow, etc.) is one of the most important flow patterns in the microscale, as it occupies a large area on the flow map [4]. Due to the recirculating flow within the liquid slugs, such flow pattern enhances heat and mass transfer from the liquid to the wall. The large interfacial area promotes liquid-vapor mass transfer, the presence of the bubbles separating the liquid slugs reduces axial liquid mixing. The evaporation of the liquid film surrounding the bubble increases strongly the local heat transfer coefficient [5].

Hence, the remarkable heat transfer performance achievable by such flow makes it recommended to all those applications involving the cooling of high heat load densities.

In spite of its great potential, the understanding of the local mechanisms enhancing mass, momentum and energy transfer is far from being complete. The reason is that the current experimental techniques aimed to characterize the flow and the temperature field, successful in the macroscale, are still inadequate to capture the dynamics of the small scales involved.

On the other hand, the multiphase computational fluid dynamics evolved greatly in the recent years. Numerical techniques more and more accurate to simulate interfacial flows appeared in the scientific literature, providing a reliable tool to investigate the local features of the slug flow. Therefore, several experimental findings on microscale two-phase flow have been anticipated by the numerics.

The multiphase CFD approach

The most advanced multiphase CFD techniques are able to perform a direct numerical simulation of the interface. Interfacial effects, such as surface tension or evaporation/condensation, are introduced in the flow equations through appropriate

models involving the local interface topology, without resorting to empiricism.

Since the birth of such advanced techniques, several research groups have been developing and proposing in-house numerical frameworks, aimed to simulate specific two-phase flow configurations. Simultaneously, various commercial general purpose CFD solvers have been appearing in the market, with specific multiphase tools. One of the commercial CFD solvers most widely used for industrial applications is Ansys Fluent [11], mainly because of the several multiphysics packages provided and the robustness of the algorithms implemented.

Ansys Fluent is widely employed as well by several academic research groups as a tool associated with the scientific research. The basic numerical algorithms implemented are fairly accurate, thus the researcher who desires to investigate a specific physical flow, whose models are absent or limited within the solver, can focus only on the implementation and validation of additional user-defined subroutines.

However, keep in mind that since dealing with a commercial software, a preliminary stage of validation of the numerical framework with analytical solutions or experimental results is necessary before employing the software as a research tool.

The microscale two-phase flow phenomena recently studied with a multiphase CFD approach are numerous: effect of the acting forces on the shape and velocity of the bubble, pressure drop generated by the bubbly flow, flow dynamics within the liquid slugs, bubble formation at orifices, gas-liquid behavior at T-junctions, role of the gas-liquid-wall contact angle, heat transfer at the wall without phase change, dynamics of the evaporating bubble and influence of the operating conditions. Although several numerical studies are appearing dealing with adiabatic and diabatic microscale slug flow without phase change, only few studies concern with evaporating bubbles and the related heat transfer performance. The local flow dynamics responsible of the enhancement of the wall heat transfer, as detected in experiments, has not been investigated yet. The mutual influence of multiple bubbles flowing in sequence in a slug flow is not known. A quantitative comparison of the heat transfer coefficient measured in experiments with the results of numerical simulations still lacks.

The objective of this thesis is to tackle the mentioned open issues.

CFD modeling of two-phase boiling flows in the slug flow regime with an interface capturing technique

The main objective of this thesis is to study through the CFD approach the thermal and hydrodynamic characteristics of the slug flow in microchannels in flow boiling conditions, by means of the following steps: assessment of appropriate physical and numerical models to reproduce the physical phenomena involved; optimal set-up of the numerical solver to replicate actual experimental conditions; validation of the numerical framework by comparison with analytical solutions and experimental results for numerous multiphase flow configurations; analysis of the flow and temperature fields generated by the dynamics of the single evaporating bubble and multiple bubbles flowing in sequence. In order to save computational time, the boiling flows are modeled through an axisymmetrical formulation.

The writing and subsequent validation of a new in-house CFD code with this aim would have required a time longer than the duration of the doctoral course. The modification of a pre-existing in-house solver would have taken time to learn the code and to adequately improve programming skills. In order to focus mainly on the physical aspects of the flow, it was decided to work with the commercial CFD solver Ansys Fluent versions 6.3 and 12, whose single phase package and interface advection scheme, based on interface capturing, have already been validated by the scientific community.

Great attention was paid to the analysis and implementation of models to estimate the interfacial effects that drive the flow. The computation of an accurate local interface curvature is fundamental for the correct estimation of the surface tension force. The poorly accurate Fluent original model for interface curvature calculation has been replaced by an Height Function algorithm which is currently one of the most accurate schemes. An evaporation model computing the rates of mass and energy exchange at the interface proportional to the local interface superheating has been introduced in the numerical solver.

Both the models are implemented as user defined subroutines written in *C* code and they are capable of parallel computing. The resort to parallel computing, up to 128 parallel processors, allowed to complete the highest computational demanding simulation performed for this thesis in three weeks, while serial computing would

have taken years to end.

The accuracy and the efficiency of the models implemented allowed to obtain numerical results in good agreement with experiments for the flow configurations simulated. Besides academic research purpose, the entire numerical framework offers a reliable engineering tool for industrial applications dealing with two-phase flows.

This thesis is organized as follows:

- Chapter 1: mathematical formulation of two-phase flow and review of the CFD techniques aimed to multiphase modeling;
- Chapter 2: review of experimental and numerical studies on Taylor flow in vertical channels and slug flow in microchannels;
- Chapter 3: physical basis and numerical discretization of the models implemented to evaluate interfacial effects;
- Chapter 4: details of the Ansys Fluent solution algorithms and procedure, development of the User Defined Functions;
- Chapter 5: validation of the numerical framework with typical benchmarks;
- Chapter 6: results on the adiabatic simulation of Taylor bubbles rising in stagnant liquid within vertical channels and elongated bubbles flowing in horizontal microchannels;
- Chapter 7: results on the simulation of evaporating single and multiple elongated bubbles flowing within horizontal microchannels;
- Conclusions;
- Appendix: capillary waves appearing in the simulation of multiphase flows as additional effect of the numerical discretization of the surface tension force.

This three years doctoral project was developed at the Department of Energy, Nuclear and Environmental Control Engineering of the University of Bologna, Italy, under the supervision of Dr. Beatrice Pulvirenti. Part of the work was conducted during a six months visiting period at the Laboratory of Heat and Mass Transfer of the Swiss Federal Institute of Technology (EPFL), under the supervision of Prof. John R. Thome.

Chapter 1

Mathematical formulation of two-phase flows

The definition of “multiphase flow” includes an enormous field of physical phenomena, each of these ruled by specific natural laws. As well, the scale of the flow being studied is of main importance to understand which effects have to be considered for an easy, but reliable, modeling.

Even though the attention is limited to two-phase liquid-gas flows, the vastness of the phenomena, the scaling effects and the differences among the possible interactions are so wide that a unique mathematical formulation of the problem is not practical nor achievable. As a consequence, an all-able numerical solver for multiphase flows does not exist.

Hence, when facing with the modeling of a multiphase flow, the first step consists in the choice about which specific aspects to focus on, in order to derive a thorough mathematical description.

Considering liquid-gas flows within confined domains, two different approaches arise on the basis of the importance of the surface tension effects at the interface.

Two-phase flows driven by interfacial effects require the knowledge of the interface topology to quantify accurately the inter-phase transfer mechanisms. An example could be the modeling of slug flows. For such flows, a mathematical description based on the surface tracking is fundamental.

Two-phase flows whose interface effects can be accounted for without the need to know the interface geometry require a different formulation. An example of such

flow is the modeling of an entire channel in which nucleate boiling occurs, in which the size of the bubbles is much smaller than the channel's diameter.

Since this thesis deals with surface tension driven evaporating flows, the surface tracking formulations are described more in detail in the Section 1.2.

In the following, it will always be referred to a liquid-vapor evaporating two-phase flow in a confined domain, for Newtonian incompressible fluids and constant surface tension.

1.1 Formulation without surface tracking

When one of the two phases is very dilute and it fills only a small part of the flow domain (roughly below 10%), the dilute phase is considered as the dispersed phase, within the continuous one. The effect of the volume fraction occupied by the dispersed phase on the modeling of the continuous phase is negligible, as well as the particle-particle interactions. The best formulation for such flows is the *Discrete Phase Model*: the Eulerian single phase flow equations are solved for the continuous phase, while the discrete particles characterizing the dispersed phase are tracked in a Lagrangian way. Models are necessary in order to quantify the phases interactions.

When the volume fraction of the dispersed phase is higher and the tracking of the single particles would be computationally too expensive, an Eulerian-Eulerian approach is better. Two sets of ensemble-averaged conservation equations are written for both phases and solved throughout the domain. The phases are mathematically treated as *interpenetrating continua*, filling up the entire domain. Averaged conservation equations are formulated for each phase on the basis of the phase volume fraction. Such a formulation is known in the literature as the *two-fluid formulation*. Actually, more than two sets of equations can be written to study additional fields (multifield models), with the individual fields representing topologically different flow structures within a given phase, see for instance Podowski and Podowski [12].

The original two-fluid formulation is ascribable to the work of Ishii [13], who derived the following governing equations for the mass, momentum and energy balances for the k -th phase:

$$\frac{\partial(\alpha_k \rho_k)}{\partial t} + \nabla \cdot (\alpha_k \rho_k \mathbf{u}_k) = \Gamma_k \quad (1.1)$$

$$\frac{\partial(\alpha_k \rho_k \mathbf{u}_k)}{\partial t} + \nabla \cdot (\alpha_k \rho_k \mathbf{u}_k \mathbf{u}_k) = -\alpha_k \nabla p_k + \nabla \cdot (\alpha_k \boldsymbol{\tau}_k) + \alpha_k \rho_k \mathbf{g} + \mathbf{M}_k \quad (1.2)$$

$$\begin{aligned} \frac{\partial(\alpha_k \rho_k e_k)}{\partial t} + \nabla \cdot (\alpha_k \rho_k \mathbf{u}_k e_k) = & -\nabla \cdot (\alpha_k \mathbf{q}_k) + \nabla \cdot [\alpha_k (-p_k \mathbf{I} + \boldsymbol{\tau}_k) \cdot \mathbf{u}_k] + \\ & + \alpha_k \rho_k \mathbf{g} \cdot \mathbf{u}_k + E_k \end{aligned} \quad (1.3)$$

where α_k , ρ_k , p_k , \mathbf{u}_k , $\boldsymbol{\tau}_k$, e_k , \mathbf{q}_k are respectively the volume fraction, density, pressure, velocity, shear stress tensor, specific internal energy, local heat flux of the phase k . \mathbf{g} is the gravity vector. \mathbf{I} is the identity tensor. Γ_k , \mathbf{M}_k , E_k are the net interfacial transfer per unit volume of mass, momentum and energy for the phase k . The shear stress tensor for a Newtonian fluid is expressed as follows:

$$\boldsymbol{\tau}_k = \mu_k^e \left[\nabla \mathbf{u}_k + (\nabla \mathbf{u}_k)^T \right] \quad (1.4)$$

where μ_k^e is the k -th phase effective viscosity.

Appropriate closure laws are necessary to model turbulence, interfacial transfers and thermal boundary conditions for the near-wall heat transfer.

When the liquid is the continuous phase, turbulence within the liquid is normally modeled using the $k - \epsilon$ model, modified to include the effect of bubble-induced turbulence. The dispersed gas phase is assumed to be laminar.

Interphase mass and energy transfer occurs at the gas-liquid interface near the heated wall as a consequence of an evaporating heat flux, and in the bulk liquid as a consequence of gas evaporation or condensation due to superheated or subcooled liquid. These effects are quantified by mechanistic models such as the Ranz-Marshall correlation [14] for the interface mass transfer, and the RPI model by Kurul and Podowski [15] for the wall evaporating heat flux. The mentioned models involve empirical relationships to compute the frequency of the bubble detachment from the wall, the mean bubble departure and bulk diameter, the number of wall nucleation sites and other physical entities.

Interphase momentum transfer for bubbly flows involves drag, lift, virtual mass, turbulent dispersion and lubrication forces. Mechanistic models for their computation are set-up by tuning some coefficients, on the basis of a previous validation with experimental data.

For what concerns the near wall treatment of the heat transfer, the common approach is to partition the wall heat flux into three components: a single phase

heat flux (outside the influence area of the bubbles) $q_{1\Phi}$, an evaporation heat flux (generating the bubbles) q_e and a quenching heat flux q_Q . These three components are modeled as functions of the local difference between the wall temperature and the temperature of the liquid adjacent to the wall. Starting from the constant heat flux q_w boundary condition at the wall, the wall temperature is obtained by solving the equation:

$$q_w = q_{1\Phi} + q_e + q_Q \quad (1.5)$$

The key issue for the accurate modeling of multiphase flows by the use of the two-fluid formulation is not only the correct formulation of the mentioned closure laws, but also the reliability of the empirical relationships employed, typically validated for a narrow range of operating conditions. The recent advances within the two-fluid formulation regard more precise closure laws, based on correlations optimized for specific operating conditions, see for instance Tu and Yeoh [16], Podowski and Podowski [12], Končar *et al.* [17] and Chen *et al.* [18].

In order to avoid resorting to empiricism to predict interfacial flows accurately, it is necessary to switch to a surface tracking technique, with all the advantages and the limitations that are going to be described in the next Section.

1.2 Formulation with surface tracking

The approach based on the surface tracking formulation is also known as *Direct Numerical Simulation* of interface motion (not of turbulence), because no closure laws for interfacial effects are needed.

The direct tracking of the interface demands for an additional computational effort which, depending on the method used, can be considerable. Moreover, the computational grid necessary to solve the interface is finer than the one needed to discretize the ensemble-averaged equations.

For this reason, the surface tracking formulation is far from being applied to study the same flow configurations allowed by the former formulation. In spite of this limitation, it provides an insight on the local fluid-dynamics effects occurring near an interface that, currently, neither experimental techniques can give.

The surface tracking formulation is based on two general assumptions [19]. A

sharp interface, with zero thickness, is assumed. Actually, the interface has a finite thickness, which represents a transition region for the fluids properties. But for length scales for which the continuum hypothesis is valid, the assumption of sharp interface is correct. The second principle, following from the first one, is that the intermolecular forces determining the interface dynamics can be modeled in the continuum scale as capillary effects, quantified by the surface tension, concentrated on the sharp interface.

The surface tracking formulations can be split into two families, depending on the identification or description of the interface: through a mathematical relation $f(\mathbf{x}, t) = 0$ which explicitly locates the surface points on the spatial-temporal domain; by a marker or indicator function $I(\mathbf{x}, t)$, defined in the whole domain, whose values implicitly locate the interface. The former leads to the *two-fluid formulation* of the problem (analogous to the discussed two-fluid formulation without surface tracking, but without the interpenetrating continua assumption), with two sets of flow equations solved in each subdomain occupied by the individual phase, coupled at the interface with appropriate jump conditions. The latter leads to the *single fluid formulation*, with a single set of flow equations solved throughout the domain, and variable fluid properties and interfacial effects included as source terms in the equations.

Since this thesis deals with a single fluid formulation, this is treated more extensively in the Subsection 1.2.2, while in the following Subsection the two-fluid formulation is briefly introduced.

1.2.1 Two-fluid formulation

By the two-fluid formulation, the flow domain is divided into subdomains filled with the individual phases. Each subdomain is a single-phase domain, for which the single-phase Navier-Stokes equations hold:

$$\frac{\partial \rho}{\partial t} + \nabla \cdot (\rho \mathbf{u}) = 0 \quad (1.6)$$

$$\frac{\partial(\rho \mathbf{u})}{\partial t} + \nabla \cdot (\rho \mathbf{u} \mathbf{u}) = -\nabla p + \nabla \cdot \boldsymbol{\tau} + \rho \mathbf{g} + \mathbf{f} \quad (1.7)$$

$$\frac{\partial(\rho c_p T)}{\partial t} + \nabla \cdot (\rho c_p \mathbf{u} T) = -\nabla \cdot \mathbf{q} + \boldsymbol{\tau} : \nabla \mathbf{u} \quad (1.8)$$

where all the fluid properties and flow variables refer to the phase filling the considered subdomain. f is a generic body force. c_p is the constant pressure specific heat. The shear stress tensor $\boldsymbol{\tau}$ for a Newtonian fluid can be expressed as follows:

$$\boldsymbol{\tau} = \mu \left[\nabla \mathbf{u} + (\nabla \mathbf{u})^T \right] \quad (1.9)$$

and the heat flux \mathbf{q} can be expressed by means of the Fourier law:

$$\mathbf{q} = -\lambda \nabla T \quad (1.10)$$

with λ being the thermal conductivity.

Each set of equations is coupled with the sets belonging to the adjacent subdomains by interfacial jump equations, which serve as boundary conditions for the solution of the flow problem. Appropriate interfacial jump conditions were firstly derived by Ishii [13]. Juric and Tryggvason [20] modified them according to the assumptions of thin and massless interface, constant surface tension and negligible energy contribution of interphase stretching. They proposed the following jump conditions respectively for the mass, normal and tangential stresses and thermal energy for an interface separating the fluids 1 and 2:

$$\dot{m} = \rho_1(\mathbf{u}_1 - \mathbf{V}) \cdot \mathbf{n} = \rho_2(\mathbf{u}_2 - \mathbf{V}) \cdot \mathbf{n} \quad (1.11)$$

$$p_2 - p_1 = -\dot{m} \left(\frac{1}{\rho_2} - \frac{1}{\rho_1} \right) + (\boldsymbol{\tau}_2 \cdot \mathbf{n}) \cdot \mathbf{n} - (\boldsymbol{\tau}_1 \cdot \mathbf{n}) \cdot \mathbf{n} + \sigma \kappa \quad (1.12)$$

$$(\boldsymbol{\tau}_2 \cdot \mathbf{n}) \cdot \mathbf{t} = (\boldsymbol{\tau}_1 \cdot \mathbf{n}) \cdot \mathbf{t} \quad (1.13)$$

$$\begin{aligned} (\mathbf{q}_1 - \mathbf{q}_2) \cdot \mathbf{n} = & -\dot{m} [h_{1,2} + (c_{p,2} - c_{p,1})(T_{if} - T_{sat})] - \frac{\dot{m}^3}{2} \left(\frac{1}{\rho_2^2} - \frac{1}{\rho_1^2} \right) + \\ & + \dot{m} \left[\frac{(\boldsymbol{\tau}_2 \cdot \mathbf{n}) \cdot \mathbf{n}}{\rho_2} - \frac{(\boldsymbol{\tau}_1 \cdot \mathbf{n}) \cdot \mathbf{n}}{\rho_1} \right] \end{aligned} \quad (1.14)$$

where V is the interface velocity, \mathbf{n} and \mathbf{t} are the interface unit normal and tangential vectors, \dot{m} is the interphase mass flux, $h_{1,2}$ is the specific enthalpy jump related to the phase change, T_{if} is the interface temperature and T_{sat} is the equilibrium saturation temperature corresponding to the reference ambient system pressure. The surface tension force is expressed as $\mathbf{f}_\sigma = \sigma \kappa \mathbf{n}$ where σ is the surface tension coefficient and κ the interface curvature.

Equation (1.11) states that without phase change the normal velocity is continuous at the interface. Generally, a no-slip condition is postulated at the interface,

such that also the tangential velocity is continuous.

An additional boundary condition to set the interface temperature T_{if} is necessary to complete the formulation.

The two-fluid formulation is suitable for those multiphase numerical methods employing moving grids to fit the interface with the computational mesh: full Lagrangian methods, in which all the grid points are moved according to the computed flow field; boundary fitted methods (BFM) [21], in which the mesh is built in such a way that it is always orthogonal to the interface, see Fig. 1.1(a); arbitrary Lagrangian-Eulerian algorithms (ALE), in which only the computational mesh close to the interface is moved with the flow field to fit the interface as shown in Fig. 1.1(b), see for instance Hirt *et al.* [22], Li *et al.* [23] and Ganesan and Tobiska [24].

The main advantages of the numerical methods based on the two-fluid formulation is that the interfacial effects can be accurately placed where they actually act, the interface topology (normal vector and curvature) can be precisely computed through

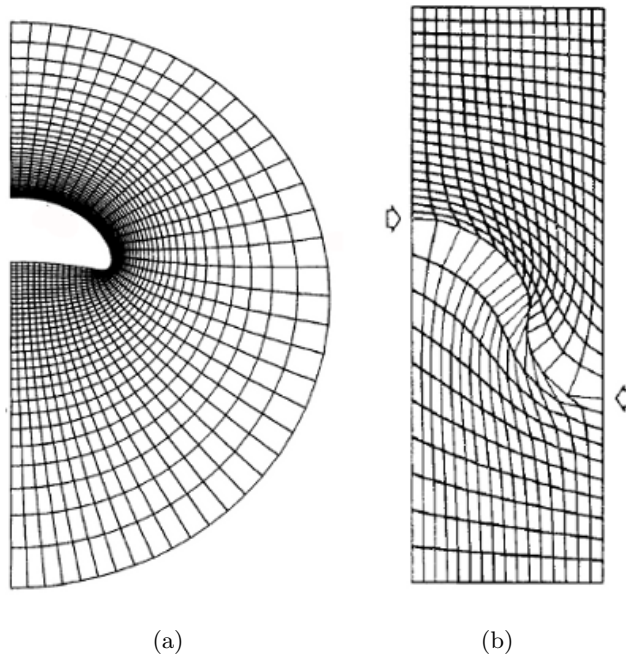


Figure 1.1: Examples of computational grids for a BFM from [21] in (a) and ALE method from [22] in (b). The arrows in (b) locate the Lagrangian interface.

geometrical considerations and the mass is well preserved. On the other hand, the numerical solution of flow equations with jump boundary conditions require methods very different from the single-phase flow ones; the numerical management of the deforming interface is tough, the most when break-up or coalescence occur; highly deforming interfaces can affect the accurateness of the methods.

1.2.2 Single fluid formulation

Through the single fluid formulation a single set of flow equations is written and solved throughout the whole flow domain. The flow domain is considered filled with a fluid whose properties change abruptly at the phases boundary. The interfacial effects are included in the flow equations as source terms concentrated at the interface, thus modeled by δ functions. Thus, the jump conditions (1.11)–(1.14) in the single fluid formulation are replaced by δ functions and the only boundary conditions needed are those related to the domain boundary.

The transport equations take the following form:

$$\frac{\partial \rho}{\partial t} + \nabla \cdot (\rho \mathbf{u}) = \dot{m} \delta_S(\mathbf{x}) = \int_{\Gamma(t)} \dot{m} \delta(\mathbf{x} - \mathbf{x}_S) ds \quad (1.15)$$

$$\frac{\partial(\rho \mathbf{u})}{\partial t} + \nabla \cdot (\rho \mathbf{u} \mathbf{u}) = -\nabla p + \nabla \cdot \boldsymbol{\tau} + \rho \mathbf{g} + \int_{\Gamma(t)} \sigma \kappa \mathbf{n} \delta(\mathbf{x} - \mathbf{x}_S) ds \quad (1.16)$$

$$\frac{\partial(\rho c_p T)}{\partial t} + \nabla \cdot (\rho c_p \mathbf{u} T) = -\nabla \cdot \mathbf{q} + \boldsymbol{\tau} : \nabla \mathbf{u} - \int_{\Gamma(t)} \dot{q} \delta(\mathbf{x} - \mathbf{x}_S) ds \quad (1.17)$$

where $\Gamma(t)$ represents the phases interface and \dot{q} is the interphase heat flux. $\delta(\mathbf{x} - \mathbf{x}_S)$ is a multidimensional delta function which is non-zero only where $\mathbf{x}_S = \mathbf{x}$, with $\mathbf{x}_S = \mathbf{x}(s, t)$ being a parametrization of $\Gamma(t)$ [20].

An additional model is necessary to express the interfacial effects related to phase change, identified by \dot{m} and \dot{q} , by means of a proper condition for the interface temperature.

Since the flow equations (1.15)–(1.17) are formally the same as the single-phase flow ones (see Eqs. (1.6)–(1.8)) except for additional source terms, and they are subject to the same boundary conditions, similar solution methods can be employed. However, additional arrangements are necessary:

- definition of a marker function $I(\mathbf{x}, t)$ in order to identify each fluid and then to compute the fluid properties;

- a method to update the marker function as the interface evolves;
- modeling of the interfacial effects expressed by the delta function and approximation of the delta function on the computational grid;
- reconstruction of the interface geometry in terms of normal vector and curvature in order to compute the surface tension effects.

Typically, the marker function is a function whose value is 1 in a chosen primary phase and 0 in a secondary phase. It is defined by the use of the delta function as follows:

$$I(\mathbf{x}, t) = \int_{\Omega(t)} \delta(\mathbf{x} - \mathbf{x}_S) dV \quad (1.18)$$

where $\Omega(t)$ is a control volume. The gradient of the marker function, which is non-zero only if $\Omega(t)$ includes part of the interface $\Gamma(t)$, identifies the interface normal vector:

$$\nabla I = \int_{\Gamma(t)} \mathbf{n} \delta(\mathbf{x} - \mathbf{x}_S) ds = \mathbf{n} \delta_S(\mathbf{x}) \quad (1.19)$$

Through such definition of the indicator function, each generic fluid material property b can be expressed as:

$$b(\mathbf{x}, t) = b_2 + (b_1 - b_2)I(\mathbf{x}, t) \quad (1.20)$$

with b_1 and b_2 being the specific properties of the fluids. By the definition (1.18) of the marker function, the fluid properties vary abruptly across the interface, leading to numerical instabilities in the solution of the flow equations, especially when dealing with high density and viscosity ratios. Then, a common approach is to employ a smoothed version of the marker function.

The single fluid formulation is practical for the modeling of two-phase flows on fixed grids. Nowadays, most of the numerical algorithms based on this formulation derive from the original Marker And Cell (MAC) method developed in 1965 by Harlow and Welch [25, 26], see McKee *et al.* [27] for a review. Currently, most of the multiphase CFD codes with surface tracking are based on the single fluid formulation rather than a two-fluid one, because it avoids the management of a moving

grid, thus dealing more automatically with high interface deformations, break-up or coalescence. However, the implicit treatment of break-up and coalescence has to be intended as a “numerical” treatment, which does not lead necessarily to a physical meaningful representation of it.

The method used to advect the indicator function splits the numerical schemes based on the single fluid formulation into two categories:

- *interface tracking* methods: the interface is represented by marker points, connected together to form a moving front, advected in a Lagrangian way by the flow field computed on the background fixed grid. Thus, the interface is advected explicitly by moving the marker points and every time step the indicator function is reconstructed by knowing their positions.
- *interface capturing* methods: the interface topology is implicit in the indicator function field, which is advected by solving a conservation equation. The conservation equation for the marker function can be derived substituting the Eq. (1.20) written for the phase density in the mass conservation equation (1.15), leading to the following pure mass and marker function conservation equations [28], respectively:

$$\nabla \cdot \mathbf{u} = 0 \tag{1.21}$$

$$\frac{\partial I}{\partial t} + \mathbf{u} \cdot \nabla I = (\mathbf{u} - \mathbf{V}) \cdot \nabla I \tag{1.22}$$

Depending on how the marker function is advected, each method has its own way to approximate the delta function and to compute the interface geometry. Three among the most known approaches are discussed in the following sections. The *Front Tracking* (FT) algorithm, which is an interface tracking scheme, and the *Level-Set* (LS) algorithm, which is an interface capturing scheme, are briefly introduced. The *Volume Of Fluid* (VOF) algorithm, which is an interface capturing method, is described more extensively as it is the algorithm implemented in the CFD solver Ansys Fluent version 12 and before, used in this thesis.

1.3 The Front Tracking algorithm

Among the several versions of the Front Tracking algorithm for multiphase fluid-dynamics, the most famous is the one developed by Unverdi and Tryggvason [30]. In their implementation, the governing flow equations are solved in the background fixed grid. The interface, or front grid, is used to advect the marker points and to compute the interfacial source terms. The Figure 1.2 reports a sketch of the grids configuration.

The way chosen by the authors to transfer information from the fixed grid to the front grid and *vice versa* is based on a smoothing transition approach. The interface becomes a transition region between the fluids, where the two grids interact. By this method, only the fixed grid points included in the transition region influence the dynamics of the front, while the interfacial effects computed on the front grid are transferred only in the fixed grid point included in the transition region. Moreover, across the transition region the fluid properties vary smoothly from side to side.

The smoothing operation is done by appropriate approximation on the fixed grid of the delta function appearing in the source terms of Eqs. (1.15)–(1.17).

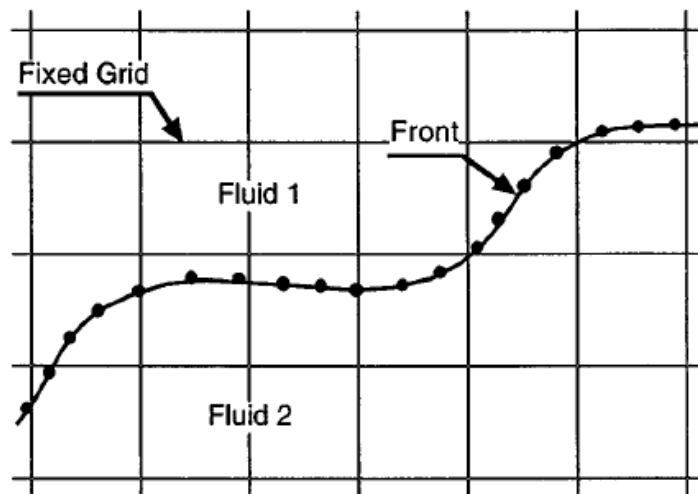


Figure 1.2: Example of a front grid separating the primary from the secondary fluid on a background fixed grid, from [29].

The interface is advected in a Lagrangian way by integrating the following:

$$\frac{d\mathbf{x}_S}{dt} \cdot \mathbf{n} = \mathbf{V}_S \cdot \mathbf{n} \quad (1.23)$$

where x_S identifies the points of the front. V_S is the local front velocity, it is interpolated from the velocities $u_{i,j,k}$ computed on the fixed grid points, considering only the points \mathbf{x} included in the transition region by using weight functions $w_{i,j,k,S} = w(\mathbf{x} - \mathbf{x}_S)$:

$$\mathbf{V}_S = \sum_{i,j,k} w_{i,j,k,S} \mathbf{u}_{i,j,k} \quad (1.24)$$

As the interface topology is updated, the marker function $I(\mathbf{x}, t)$ have to be reconstructed on the fixed grid to compute the fluid properties by the Eq. (1.20). The smoothed transition approach by Juric and Tryggvason [20] obtains the marker function field by integrating its gradient on the fixed grid, solving the following Poisson equation:

$$\nabla \cdot \nabla I = \nabla^2 I = \nabla \cdot \int_{\Gamma(t)} \mathbf{n} \delta(\mathbf{x} - \mathbf{x}_S) ds \quad (1.25)$$

The integral appearing at the RHS, as well as the source terms in Eqs. (1.15)–(1.17), are solved in the fixed grid by the discrete version of the smoothed delta function, based on the same weight functions $w_{i,j,k,S}$. By calling Φ the generic interface effect to be transferred on the fixed grid, the integrals are discretized as follows:

$$\Phi_{i,j,k} = \sum_S \Phi_S w_{i,j,k,S} \frac{A_S}{V_{i,j,k}} \quad (1.26)$$

where A_S is the area of the front element S and $V_{i,j,k}$ the volume of the i, j, k grid element. The thickness of the transition region Δ is chosen through the definition of the weight functions by asking that $w_{i,j,k,S} \neq 0$ only if $(\mathbf{x} - \mathbf{x}_S) < \Delta/2$. Juric and Tryggvason chose the Peskin and McQueen weight functions [31], for which $\Delta = 4$ grid cells.

A consequent benefit of computing interfacial effects on the front grid, is the precise computation of interfacial normal vector and curvature, leading to the accurate evaluation of surface tension effects. Since the interface is described by the marker points, whose position is known, its topology can be computed by geometrical considerations.

The main advantages of the Front Tracking methods is the explicit advection of the interface and the capability to evaluate interfacial effect right at the interface, where they actually act. The representation of the interface with marker points makes it independent of the fixed grid size. However, the direct advection of the marker points does not guarantee the conservation of the mass, therefore accurate interpolation and advection schemes are necessary. Moreover, the moving interface grid demands particular care when break-up or coalescence occur, to overcome connectivity and remeshing problems.

1.4 The Level-Set method

In the Level-Set approach [32] the marker function is a smooth function $\phi(\mathbf{x}, t)$, defined as the signed minimum distance of \mathbf{x} from the interface. The phases interface

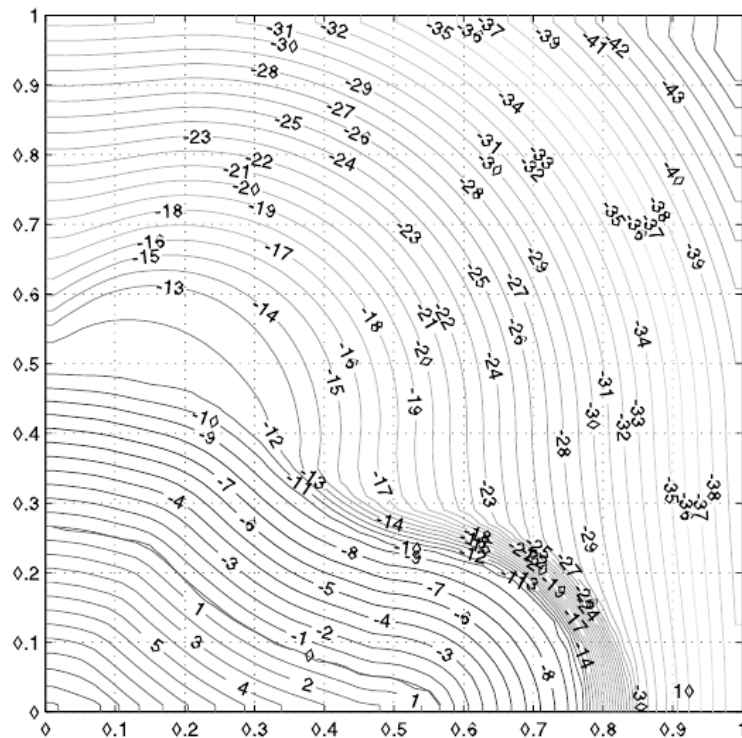


Figure 1.3: Iso-level curves from a level-set formulation [28]. The zero value iso-level curve locates the phases interface.

is identified as the zero level set $\phi(\mathbf{x}, t) = 0$, while positive values correspond to one phase and negative values to the other. See Figure 1.3 as example.

The level-set function can be used to compute the interface unit normal vector and curvature:

$$\mathbf{n} = \frac{\nabla\phi}{|\nabla\phi|} \quad \text{and} \quad \kappa = -\nabla \cdot \mathbf{n} = -\nabla \cdot \frac{\nabla\phi}{|\nabla\phi|} \quad (1.27)$$

The level-set function is initialized by imposing $|\nabla\phi| = 1$, such that it represents a signed distance from the interface. Since the interface $\phi(\mathbf{x}, t) = 0$ moves with the fluid flow, it is advected by solving the transport equation following from the Eq. (1.22) [28]:

$$\frac{\partial\phi}{\partial t} + \mathbf{u} \cdot \nabla\phi = \frac{\dot{m}}{\rho} |\nabla\phi| \quad (1.28)$$

The discretization of the convective term in the Eq. (1.28) requires the use of high order schemes, such as ENO or WENO [33], to avoid unphysical oscillations of the interface.

The computation of the fluid properties by use of the Eq. (1.20) needs for the definition of a Heaviside function. A smoothed Heaviside function $H(\phi)$ is constructed on the level-set function field, to obtain a smeared distribution of the fluid properties across the interface [34]:

$$H(\phi) = \begin{cases} 0 & \text{if } \phi < -\epsilon \\ (\phi + \epsilon)/(2\epsilon) + \sin(\pi\phi/\epsilon)/(2\pi) & \text{if } |\phi| < \epsilon \\ 1 & \text{if } \phi > \epsilon \end{cases} \quad (1.29)$$

where ϵ defines the thickness of the transition region represented by the smeared interface, as seen previously for the Front Tracking method. The interface thickness is $2\epsilon/|\nabla\phi|$, then 2ϵ when the level-set function is initialized (such that $|\nabla\phi| = 1$).

However, as the time-integration of Eq. (1.28) begins, even though the zero level set $\phi = 0$ always captures the phases interface, the level-set function ceases to be a distance function away from the interface. As a consequence, $|\nabla\phi| = 1$ is not guaranteed anymore and a smearing or a stretching of the transition region could occur, leading to loose or gain of mass.

Sussman *et al.* [32] overcame this problem by a reinitialization procedure. After a certain amount of simulation time steps the level-set function is reinitialized

around the zero level-set curve, in order to ensure the condition $|\nabla\phi| = 1$. This is accomplished by solving the following partial differential equation:

$$\frac{\partial\phi}{\partial\tau} + S(\phi_0)(|\nabla\phi| - 1) = 0 \quad (1.30)$$

together with the initial condition:

$$\phi(\mathbf{x}, \tau = 0) = \phi_0(\mathbf{x}) \quad (1.31)$$

where ϕ_0 is the un-initialized field and $S(\phi_0)$ a sign function [32]. Equation (1.30) is integrated in the pseudo-time τ until a steady state is reached, thus guaranteeing the condition $|\nabla\phi| = 1$ for the new field ϕ .

As for the Front Tracking algorithm, the interfacial effects are non-zero only within the transition region identified by the not null values of a smoothed delta function, which can be generated taking the gradient of the Heaviside function:

$$\delta(\phi) = \frac{dH}{d\phi} \quad (1.32)$$

The large use of the Level-Set algorithm in the multiphase CFD community is related to its simplicity, because only one additional equation is required with respect to the single phase case. Moreover, the interface normal vector and curvature can be accurately computed by derivatives of the smooth level-set function, thus giving a good surface tension force representation. Unfortunately, an important drawback of the method is the not preservation of mass that the reinitialization procedure can not overcome at all. This problem arises especially when the interface is poorly solved by the grid, as for highly curved interfaces or thin fluid layers.

1.5 The Volume Of Fluid method

With the Volume Of Fluid method [35], the chosen marker function is the step function defined by Eq. (1.18). The phases interface can be located as the curve for which $\nabla I \neq 0$. The fluid material properties can be directly computed as reported in Eq. (1.20).

The advection of the marker function, thus of the interface, is obtained by the solution of a transport equation derived from Eq. (1.22):

$$\frac{\partial I}{\partial t} + \mathbf{u} \cdot \nabla I = \frac{\dot{m}}{\rho} \delta_S(\mathbf{x}) \quad (1.33)$$

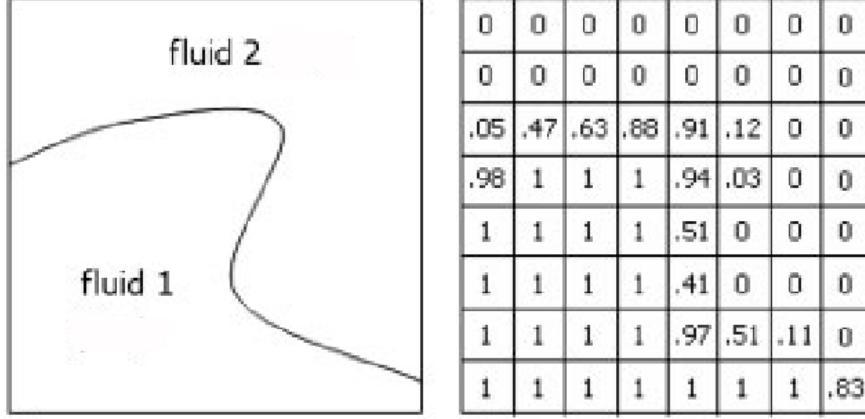


Figure 1.4: Example of the volume fraction field (right) across an interface (left), from [36].

The discrete version of the marker function is its spatial integration within the computational cell volume and it is called volume fraction α :

$$\alpha = \frac{1}{\Omega} \int_{\Omega} I(\mathbf{x}) d\Omega \quad (1.34)$$

with Ω being the volume of the computational cell. The so-defined volume fraction represents the ratio of the cell volume occupied by the reference phase, and it is 1 if the cell is filled with the reference phase, 0 if empty and $0 < \alpha < 1$ for an interfacial cell. See as instance Fig. 1.4. By knowing the volume fraction value of the cell, the generic fluid property b can be computed:

$$b = b_2 + (b_1 - b_2)\alpha \quad (1.35)$$

Interface unit normal vector and curvature can be computed as follows:

$$\mathbf{n} = \frac{\nabla\alpha}{|\nabla\alpha|} \quad \text{and} \quad \kappa = -\nabla \cdot \mathbf{n} = -\nabla \cdot \frac{\nabla\alpha}{|\nabla\alpha|} \quad (1.36)$$

As for the previous numerical schemes, a smoothed delta function is used to identify a transition region across which the fluid properties vary smoothly and where the interfacial effects are concentrated. Using the relation (1.19) for the discrete volume fraction gradient together with the Eq. (1.36) for the interface norm vector, a discrete delta function can be expressed as:

$$\delta(\alpha) = |\nabla\alpha| \quad (1.37)$$

The conservation equation to solve in order to update the volume fraction field follows from the spatial integration of the Eq. (1.33) within the computational cell. Employing the definition of the volume fraction (1.34) and the divergence theorem it follows:

$$\frac{\partial \alpha}{\partial t} + \frac{1}{\Omega} \int_S I(\mathbf{x}) \mathbf{u} \cdot \mathbf{n} dS = \frac{\dot{m}}{\rho} |\nabla \alpha| \quad (1.38)$$

where S is the surface bounding the cell. Note that only the volume fraction equation for the reference phase is solved, while the volume fraction of the secondary phase is simply evaluated as $1 - \alpha$.

The second term at the LHS is the convective term and it quantifies the volume fraction fluxes across the cell faces. In the interpolation of the volume fraction values from cells to faces centroids, the standard derivation schemes lead to undesired numerical effects because the volume fraction field is not continuous across the interface. Low-order schemes diffuse too much the interface while high order schemes maintain a sharp interface, but they cause oscillations. A widely spread solution to this problem is to compute geometrically the volume fraction fluxes across the cell faces for interface and near interface cells, as originally proposed by Noh and Woodward [37]. This procedure consists in an interface reconstruction step, in which a linear piecewise approximation of the interface within the cell is built. It follows an advection step for the Eq. (1.38), where the fluxes are computed in a geometrical way by advecting the interface along a direction normal to itself.

In the original *Simple Line Interface Calculation* (SLIC) algorithm by Noh and Woodward [37], the Eq. (1.38) is solved by a split advection along the two (or three) spatial directions. For the advection in the horizontal direction the interface is approximated by a vertical line, *vice versa* in the other direction. The full part of the cell is identified by means of the cell volume fraction gradient.

Later, Hirt and Nichols [35] modified slightly this method, imposing a unique orientation of the interface line to advect the volume fraction in the different directions. The orientation of the interface line, in two dimensions horizontal or vertical, was chosen according to the volume fraction gradient, representing the interface norm vector.

Youngs [38] developed the *Piecewise Linear Interface Calculation* (PLIC) algorithm, in which the straight interface line within each interface cell can be arbitrarily oriented with respect to the coordinate axis. The choice of the orientation is based

on the volume fraction gradient. The VOF algorithm implemented in Ansys Fluent 12 and earlier versions is based on the PLIC reconstruction, which numerical algorithm is discussed in the Section 4.3.

The figure 1.5 shows the different reconstructions of the same interface topology for the aforementioned methods.

The advantage of the VOF method is its relative simplicity, since as for the Level-Set only one additional transport equation is necessary with respect to the single phase case. However, the discretization of the convective term within the volume fraction equation needs for not conventional algorithms to avoid smearing or oscillation of the interface. The positive consequence following from the use of such algorithms is that mass conservation close to machine accuracy can be achieved.

On the other hand, the interface curvature computed by Eq. (1.36) is poorly accurate, due to the inadequacy of conventional derivation schemes when dealing with not continuous functions. Ansys Fluent computes the interface norm vector and curvature through the Eq. (1.36), therefore it lacks of accuracy in the reconstruction of the interface topology, thus in the estimation of the surface tension force. Since the correct evaluation of the surface tension effects plays a fundamental role in the simulation of interfacial flows, an additional algorithm to compute a precise curvature is suggested. The recent literature is rich of such curvature calculation algorithms. In

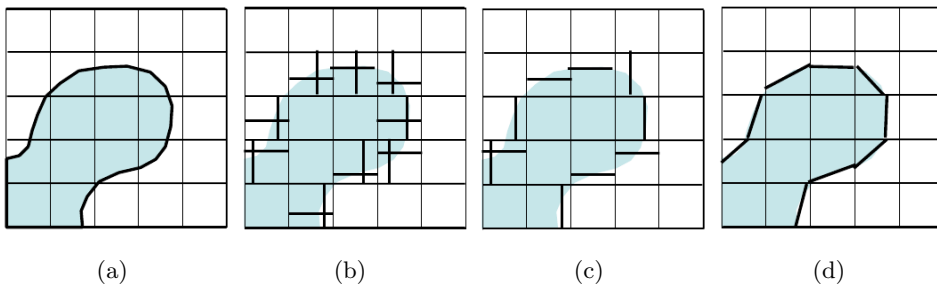


Figure 1.5: Different VOF reconstructions of the actual interface sketched in (a): (b) SLIC reconstruction [37], the interface is oriented horizontally or vertically depending on the advection direction; (c) Hirt and Nichols reconstruction [35], with a single horizontal or vertical orientation; (d) PLIC reconstruction [38], with an arbitrarily oriented interface. Figure taken from [19].

the Section 3.1 a brief related overview is presented, followed by a detailed discussion of the method chosen and implemented through external functions to improve the CFD solver employed.

1.6 Hybrid methods

The borders between the described algorithms, as well as between the single and two-fluid formulation, are not to be intended as rigid boundaries. Every method has peculiar advantages, as well as drawbacks, which can be overcome by merging different techniques. As a matter of fact, several hybrid methods based on the coupling of the described formulations appeared in the recent computational multiphase literature.

As instance, in order to overcome the LS limitation regarding the not preservation of mass, and the VOF limitation regarding the poor accuracy on surface tension effect computation, Sussman and Puckett [39] developed a *Coupled Level-Set and Volume Of Fluid* (CLSVOF) algorithm. Within their formulation, both the level-set and the volume fraction equations are solved simultaneously. The fluid material properties are updated according to the level-set field, as well as the terms appearing in the surface tension force. A PLIC advection of the interface is performed by approximating the interface as a linear segment orthogonal to the norm vector computed by means of the level-set function $\mathbf{n} = \nabla\phi/|\nabla\phi|$. In order to preserve the mass, the reinitialization of the level-set function is not obtained solving the Eq. (1.30) but reconstructing an exact signed distance function from the volume fraction updated field.

Nichita [40] implemented the CLSVOF algorithm within the CFD software Ansys Fluent, by coupling User-Defined LS subroutines to the Fluent's default VOF scheme.

Aulisa *et al.* [41] coupled a Front Tracking algorithm with a Volume Of Fluid scheme, to overcome the mass preservation troubles of the FT and the inaccuracy of the PLIC algorithm within the VOF. At each time step, for every interface cell, the polygon representing the reference phase within the cell, obtained by connecting the interface marker points, is advected by the fluid flow by advecting its vertices in a Lagrangian fashion. The updated polygon is used to compute the fluxes of

the volume fraction across the interface cell faces, thus solving the Eq. (1.38) by a geometrical reconstruction of the convective term more precise than the PLIC one. Subsequently, the old marker points are reset and new marker points are generated within each interface cell. This is done by imposing that the area of the polygon representing the reference phase is the same as the one given by the volume fraction, thus enforcing mass conservation. Accurate surface tension effects can be computed reconstructing the interface topology by the marker points locations.

In order to complete this list of hybrid single fluid formulation based algorithms, a merging of FT and LS schemes is mentioned. Enright *et al.* [42] developed a so-called *Particle Level-Set method* in which marker particles identifying the interface are used to reinitialize the level-set function when the poorly solved interface would lead to the failure of the mass conservation.

1.7 Surface tension force modeling

From a macroscopic point of view, the surface tension force is a surface force acting on the phases interface.

For a constant surface tension coefficient, this surface force in the two-fluid formulation can be imposed as a boundary jump condition at the interface, expressed as $\mathbf{f}_{\sigma,s}(\mathbf{x}_S) = \sigma\kappa(\mathbf{x}_S)\mathbf{n}(\mathbf{x}_S)$, see Eq. (1.12).

The single fluid formulation with a fixed grid technique makes more convenient to introduce the surface tension as a body force within the momentum equation, thus considering the capillary force as a volume force, as seen in Eq. (1.16). In order to have a surface tension force concentrated at a finite thickness interface, it is formulated as $\mathbf{f}_{\sigma,v}(\mathbf{x}) = \sigma\kappa(\mathbf{x})\mathbf{n}(\mathbf{x})\delta_S(\mathbf{x})$.

The most employed method to model the surface tension force as a volume force is the *Continuum Surface Force* (CSF) proposed by Brackbill *et al.* [43] in the 1991. By this method, the surface tension force is interpreted as a continuous effect acting across a finite thickness interface, identified by the marker function proper of the algorithm used to track the interface:

$$\mathbf{f}_{\sigma,v}(\mathbf{x}) = \frac{\rho(\mathbf{x})}{\langle \rho \rangle} \sigma\kappa(\mathbf{x}) \frac{\nabla \tilde{I}(\mathbf{x})}{[I]} \quad (1.39)$$

where \tilde{I} is a smoothed version of the indicator function proper of the method and

$[I]$ is the jump in the function across the interface. The density correction term $\rho / \langle \rho \rangle$ with $\langle \rho \rangle = (\rho_1 + \rho_2)/2$, does not affect the total magnitude of the force applied, but weights the force more toward regions of higher density.

In the VOF formulation \tilde{I} is the volume fraction α and $[\alpha] = 1$. Thus the volume force is located on the finite transition region where $\nabla\alpha \neq 0$, leading to a smooth variation of the pressure field (if $\kappa \neq 0$) across the interface. It is pointed out that the CSF formulation requires the computation of the local interface curvature κ .

Alternative well-known formulations are: the *Continuum Surface Stress* (CSS) proposed by Lafaurie *et al.* [44], which avoid resorting to the interface curvature; the *Ghost Fluid Method* (GFM) developed by Liu *et al.* [45], which applies the surface tension force to a narrower region than CSF, leading to a more realistic jump in the pressure field across the interface.

The implementation of the capillary force by the CSF model is known to be a tough issue, for the computation of the related terms (as example κ) and for its discretization in the numerical grid. Inaccuracies lead to the so-called “spurious velocities”, or “parasitic currents”, unphysical velocity fields appearing across the interface, see Fig. 1.6 for an example. These numerical artefacts occur as interfacial vortices which may lead to a not natural deformation of the interface, up to its break-up, with the consequent failure of the simulation. The presence of spurious vortices could strongly affect the reliability of the numerical results, leading to a misunderstanding of the physical phenomenon being simulated. As instance, the numerically enhanced momentum transport enhances locally the heat transport, thus leading to higher heat exchanges in presence of a heated wall.

Harvie *et al.* [46] analyzed the magnitude of the spurious velocities in order to find a correlation with the simulation conditions and they found that the magnitude does not necessarily decrease by refining the mesh grid.

To understand the origin of the spurious currents let write the single fluid formulation of the momentum equation (1.16) for an incompressible, inviscid two-phase flow, without gravity, and interface advected by the VOF method:

$$\rho \frac{D\mathbf{u}}{Dt} = -\nabla p + \sigma \kappa \nabla \alpha \quad (1.40)$$

where D/Dt represents the material derivative. The density correction term is omit-

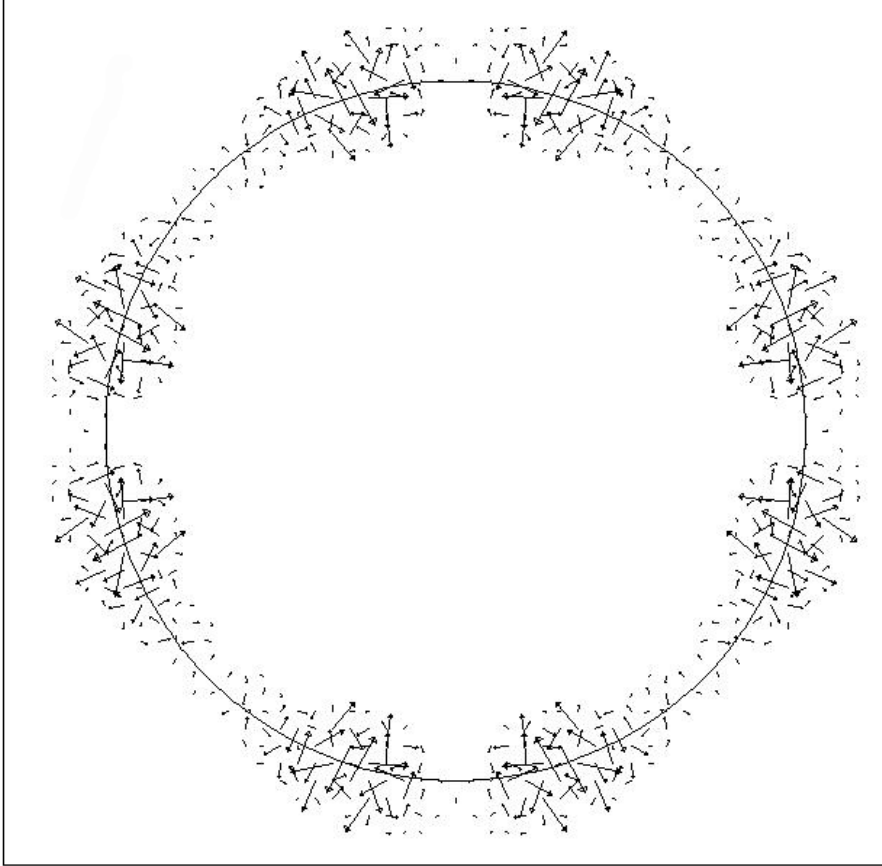


Figure 1.6: Example of the spurious velocity field across a circular interface, with interface advected by a VOF method and curvature computed differencing the volume fractions by Eq. (1.36).

ted for simplicity. If the pressure gradient and the capillary force are perfectly balanced across the interface, both the sides of the equation are zero and none velocity field arises. Then, the appearance of the parasitic currents at the interface is due to the unbalance of pressure and capillary terms within the momentum equation. As observed firstly by Renardy and Renardy [47] and later by Francois *et al.* [48], the following conditions must hold in order to achieve such balance, thus minimizing the parasitic currents:

- the pressure and volume fraction gradients have to be evaluated at the same grid location and discretized with the same derivation scheme. Francois *et al.*

[48] and Popinet [49] developed a so-called balanced-force algorithm to solve the momentum equation following this guideline.

- the numerically computed interface curvature can not be perfect, but it needs to be as much accurate as possible. This is the reason of the growing literature regarding VOF-based algorithms for a better estimation of the interface curvature.

The most spread test case to assess if these conditions are adequately respected, is the analysis of the magnitude of the unphysical flows arising in the simulation of a two-phase flow involving a circular droplet in absence of external forces, as it will be done in the validation Section 5.2.

Chapter 2

Elongated bubbles flow: a review

The elongated bubbles regime appears in two-phase flow when the gas phase velocity is reasonably high with respect to the liquid, but not so high as to switch to annular flow. This flow pattern is called slug-flow due to the liquid slugs between the bullet-shape gas bubbles, the latter also referred to as Taylor bubbles.

It is known that the hydrodynamics of Taylor flow allows a good heat and mass transfer between bubbles, liquid plugs and the wall. Then, the capability of numerical codes to accurately predict these flow configurations is of great interest, especially in the area of microfluidics, in which this flow pattern is very common.

Typical features of Taylor bubbles are a spherical nose shape, whose sharpness depends on the importance of the inertial forces over the capillary forces. The bubble tail is flat for low viscosity liquids, due to the recirculation vortices acting on the rear of the bubble. When the viscous forces are noticeable, the bubble's rear is spherical oblate and the flow pattern on the wake might not show any vortex.

The bubble traps a thin liquid film between it and the channel wall. The dynamics of the film varies depending on the channel orientation, due to the effect of gravitational forces. For upward rising bubbles in stagnant liquid, the film becomes thinner from the top of the bubble to the bottom, due to the acceleration of the trapped downward falling liquid. If the wall shear stress balances the gravitational forces, the film becomes stable and its thickness remains constant downward along

the bubble, with a value proportional to the viscous forces.

For bubbles moving within a horizontal channel, pushed by a liquid flow, the film thickness decreases from the nose to the rear of the bubble, where it may become almost stagnant. When the gravitational forces are negligible the film thickness for circular channels is constant all around the bubble. Gravity tends to move the bubble upward, thus thinning the film above the bubble. Depending on the bubble length and on the operating conditions, the film may become thinner up to a constant thickness, decrease monotonically also up to the wall dryout or show some waves in the proximity of the bubble's rear.

The review presented in this Chapter focuses on those elongated bubbles flows which can be approximated, thus modeled, by an axisymmetrical geometry. This situation is typical in the following configurations:

- circular vertical channels, where the gravity force acts along the channel's axis. The adiabatic upward rise of bubbles will be considered.
- circular horizontal channels, with negligible gravitational effects. This assumption is valid when capillary forces dominate over buoyancy, characteristic of the field of applications of microscale two-phase flows. Adiabatic, diabatic and evaporating flows will be considered.

The intention, at the basis of the following review, is not to provide a list of all the experimental and numerical literature regarding the elongated bubble flow, which would be an endless effort. Instead, the idea is to cite and to describe briefly those works that we consider as milestones for the Taylor flow understanding, as well as those numerical studies which have been fundamental in the realization of this thesis.

2.1 Vertical circular channels

The beginning of the research on elongated bubbles rising in vertical channels can be date to 1943, with the analytical and experimental study of Dumitrescu [50]. For years, simplified analytical models and visualization techniques constituted the tool for the analysis of the flow. At the end of the '80s the Particle Image Velocimetry allowed the characterization of the liquid flow field around the bubble. Reliable

numerical techniques for the CFD simulation of such flows appeared at the beginning of the '90s.

In the following subsections, the major analytical and experimental studies on Taylor bubbles are treated separately from numerical ones.

2.1.1 Experiments and analytical models

From a general point of view, buoyancy, viscous, inertial and interfacial forces act on the rising bubble and determine the terminal shape and velocity. The adjective “terminal” is necessary in order to identify the steady rising of the bubble, at the end of a transient stage during which the bubble deforms and accelerates. The early research on elongated bubbles rising within circular channels in stagnant liquid was based on the non-dimensional analysis to identify representative dimensionless groups able to describe which forces are dominant in the flow.

In his pioneer work, Dumitrescu [50] applied the potential flow theory to describe the profile of an air bubble rising in stagnant water, coming to the conclusion, validated by experimental evidence, that the terminal bubble velocity can be predicted as $U_b = 0.346(gD)^{1/2}$, with D being the channel diameter.

Later, Bretherton [51] theoretical analysis, confirmed by experiments, concluded that if $\Delta\rho gD^2/\sigma < 3.37$, where $\Delta\rho$ is the difference among the fluids densities, the bubble does not rise at all.

White and Beardmore [1] identified the following non-dimensional groups to predict the terminal velocity of single Taylor bubbles rising in stagnant liquid:

$$\text{Eo} = \frac{\rho_l g D^2}{\sigma}, \quad \text{Mo} = \frac{g \mu_l^4}{\rho_l \sigma^3}, \quad \text{Fr} = \frac{U_b}{\sqrt{gD}}, \quad \frac{\rho_l}{\rho_g}, \quad \frac{\mu_l}{\mu_g}, \quad \frac{L_b}{D}$$

where the subscripts l and g refer, respectively, to specific liquid and gas properties. Eötvös number (Eo) quantifies the importance of buoyancy to interfacial forces, Morton number (Mo) is the fluid property group, Froude number (Fr) compares inertial to gravitational forces. Density and viscosity ratios are ignored for typical liquid to gas properties ratios, bubble length L_b to channel diameter D ratio is unimportant [1]. The authors performed a wide series of experiments in the range

$Eo = [3, 400]$ and $Mo = [10^{-12}, 10^3]$, and they summarized the results for the terminal velocity of the bubble in the map reported in Fig. 2.1.

According to the Fig. 2.1, the following regimes can be identified:

- $Eo < 4$, the bubble does not rise at all, thus gravitational effects are negligible. Bretherton found this limit to be $Eo = 3.37$ [51].
- $Eo > 70$, capillary effects are negligible.
- $Fr < 0.05$, inertial effects are negligible.
- $Mo < 10^{-8}$, viscosity effects are negligible.

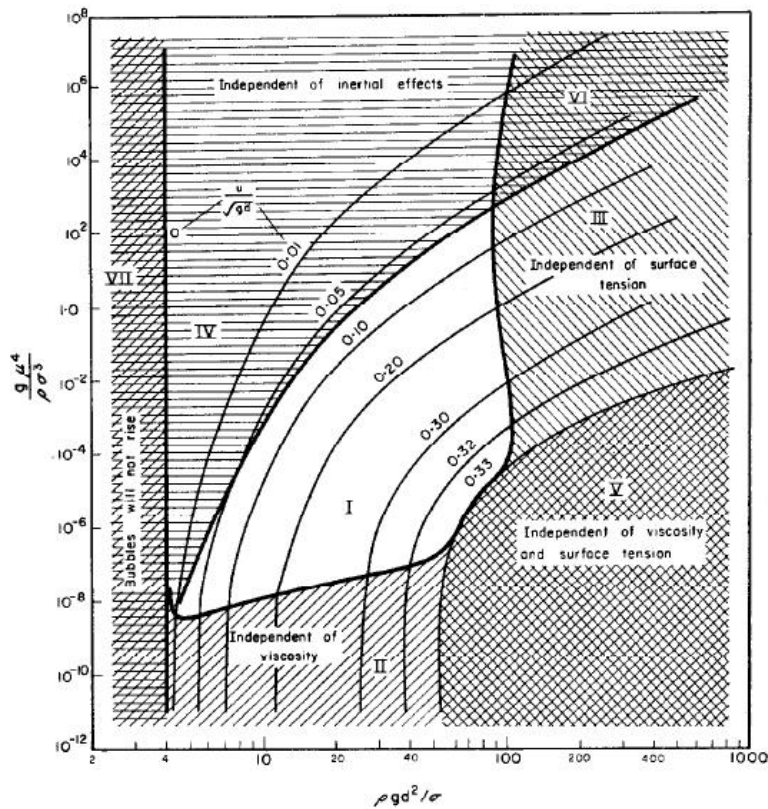


Figure 2.1: White and Beardmore [1] flow pattern map for Taylor bubbles rising in stagnant liquid.

Brown [52] applied lubrication theory to solve the Navier-Stokes equations within the falling liquid film surrounding a Taylor bubble rising in a vertical cylindrical channel. The theoretical solution for the velocity field within the stable film led to the following expression for the stable film thickness δ :

$$\delta = \left(\frac{3\mu_l U_b}{2\rho_l g} (R - \delta) \right)^{1/3} \quad (2.1)$$

with R being the channel's radius. A stable film means that gravitational and shear stress forces balance, such that the film becomes flat.

Nicklin *et al.* [53] analyzed bubbles rising within a vertical circular channel with a cocurrent liquid flow. They pointed out that the bubble velocity is a superimposition of two components, the bubble drift due to buoyancy and the transport of the mean flow:

$$U_b = U_{b,0} + C U_l \quad (2.2)$$

where $U_{b,0}$ is the velocity that the bubble would move at in a stagnant liquid and U_l is the mean velocity of the liquid flow. C is a dimensionless coefficient which can be interpreted as the ratio of the maximum to the mean liquid velocity, thus $C = 1.2$ for turbulent flows and $C = 2$ for laminar flows.

Campos and Guede de Carvalho [54] performed an experimental campaign of air bubbles rising in a stagnant water/glycol mixture, using powders to analyze the wake flow. They identified the limit for axisymmetrical wakes as the condition $N_f < 500$, with $N_f = (\text{Eo}^3/\text{Mo})^{1/4}$ being the inverse viscosity number. Moreover, the authors estimated theoretically the minimum length of the bubble to reach a constant film thickness. Applying lubrication theory and the Bernoulli theorem along the free surface streamline from the top of the bubble to the stable film, they proved that the film becomes stable and the flow is independent of bubble length when:

$$L_b > L_{b,min} = \frac{[\rho_l g \delta^2 / (2\mu_l) + U_b]^2}{2g} \quad (2.3)$$

confirming their theory by experiments.

The first detailed velocity field measurements around a Taylor bubble was made by DeJesus *et al.* [55]. They used Photocromic Dye Activation (PDA) to obtain liquid velocity vectors for the region above the bubble nose, in the liquid film and in the wake. The test case was an air bubble rising within a $D = 25.4$ mm channel filled with stagnant kerosene, with $Eo = 194$ and $Mo = 2.9 \cdot 10^{-9}$. For such conditions, a turbulent wake occurred. They confirmed the Dumitrescu hypothesis of a boundary-layer development shape for the falling film, which can be considered as one-dimensional and inviscid along the bubble.

Bugg and Saad [56] used Particle Image Velocimetry (PIV) to detect the liquid flow field for a flow characterized by $Eo = 100$ and $Mo = 0.015$, thus laminar. They sketched the bubble shape by hand directly from the PIV image and used the data obtained to validate a numerical code.

Nogueira *et al.* [57] coupled the PIV technique with a Pulsed Shadow Technique in order to detect directly the bubble profile. They performed a wide experimental campaign for both stagnant and co-current liquid flows spanning a large viscosity ratio range.

2.1.2 Numerical simulations

Numerical simulations on rising Taylor bubbles attempted initially to predict the terminal shape and velocity of the bubble, since these data were the only available from experiments. Then, the more advanced experimental techniques such as PDA and PIV, which characterize the liquid flow field around the bubble, provided data to validate the advancing numerical techniques. Subsequently, proved the reliability of the numerical frameworks, the simulations have been used not only in addition, but also as a substitution for the practical activity.

The velocities involved in the Taylor flow simulations are typically low enough to allow the use of an incompressible and laminar flow model. The channel sizes are big enough for a no-slip condition at the wall to be true. Unless otherwise specified, the use of such assumptions is implied in this subsection.

Early numerical works on Taylor bubbles solved the Navier-Stokes equations around the bubble by assuming *a priori* its shape. Modern simulations appeared in 1991 with the work of Mao and Duckler [58], which modeled the axisymmetric rising of a single bubble, treating the interface as a free surface with zero shear stress. The bubble shape was obtained as part of the solution, imposing that the normal stress at the interface satisfied the condition of constant pressure within the bubble. The comparison of the numerical terminal velocity with the White and Beardmore map for some cases within the viscosity- and surface tension-free regime were satisfactory.

Tomiyaama *et al.* [59] were the first to employ a surface tracking scheme, the VOF model, to simulate two-dimensional rising bubbles. They studied successfully the bubble terminal shapes for a variety of conditions as well as the effect of an imposed shear field on the bubble trajectory.

Kawaji *et al.* [60], in the 1997, were the first to have the chance to validate the numerical liquid flow field around the bubble, thanks to the experimental PDA results of DeJesus *et al.* [55]. Using an axisymmetrical uniform grid with a VOF-based numerical framework and a reference frame moving with the bubble to reduce the computational domain, they studied the effect of the bubble length on the flow. They found that none of the lengths set had any influence in the terminal velocity of the bubble, which remained the same for all the simulation runs. However, all the lengths chosen by the authors respected the condition (2.3), hence their result is not surprising. Moreover, they studied the effect of the bubble wake flow on a trailing Taylor bubble. The consequence is the radial displacement of the trailing bubble into a zone of reduced drag force, thus causing an acceleration which may lead to the coalescence of the bubbles.

Bugg *et al.* [61] implemented a VOF axisymmetrical framework to simulate rising bubbles under several different conditions. They spanned the various regimes reported in the White and Beardmore map [1], showing in which way the flow deforms the bubble shape according to the dominant forces.

They performed one grid independence test and found that a uniform mesh grid with 25 cells in the radial direction are enough to guarantee grid convergence. The

film thickness of this test case was around $1/4$ of the channel's radius, thus 6-7 cells discretized the liquid film. However, the same grid was able to lead to good results also for thinner films, with only 2 computational cells inside the film. A channel length of $8D$ was enough to allow the rise to reach the steady state. Two different initial shapes for the bubble were tested and it was observed that the initial condition only influences the transient stage of the rising.

More recently, Ndinisa *et al.* [62] tested, by a rising bubble simulation, three different numerical schemes to treat the interface with the commercial CFD solver CFX [63]: a two-fluid formulation based algorithm without surface tracking, a VOF method without geometrical reconstruction of the fluxes and a mixture of the two. The comparison was made through the PIV experimental results by Bugg and Saad [56].

The uniform grid mesh employed discretized the liquid film with around 10 computational cells. The bubble was initialized as a cylinder. The most correct terminal velocity was obtained by the VOF method, but the best results in the whole flow field were obtained by the hybrid scheme, since the VOF experienced a serious smearing of the interface on the wake. This is a typical effect deriving by the use of conventional schemes to discretize the convective term within the volume fraction equation, rather than implementing geometrical reconstruction algorithms.

Taha and Cui [64] used the commercial solver Fluent [11] and a VOF three-dimensional model to simulate rising bubbles both in stagnant and cocurrent flowing liquid. They compared successfully with experimental terminal velocities for laminar but also turbulent flows, by use of a RNG $k - \epsilon$ turbulence model. They studied the disturbances and the asymmetries generated by the turbulent wake, which may lead to the detachment of small portion of the bubble.

A uniform computational grid with 52 cells in the radial direction was used for all the axisymmetrical simulation runs. No information are available for what concerns the minimum number of grid cells discretizing the liquid film in their cases. The bubble was initialized as a slug. They set a non-stationary reference frame, moving with the predicted velocity of the bubble.

Chen *et al.* [65] employed a LS axisymmetrical framework to model the transient formation of Taylor bubbles in a vertical nozzle/tube co-flow arrangement. They analyzed the effect of gas and liquid superficial velocities and of the gas-liquid interface contact angle with the orifice on the bubble formation, detachment and subsequent length.

The grid employed was very coarse for the film thickness obtained, since in the thinnest case less than one cell was included within the film.

It is worth to mention the work of Hayashi *et al.* [66], who employed a VOF axisymmetrical formulation to simulate the rising of Taylor drops, not bubbles. They gave detailed information concerning the set-up of the simulation as well as the initial conditions. However, as for the cited Taha and Cui [64] paper, it is not possible to derive the minimum number of cells within the film.

2.2 Horizontal circular channels

The flow of elongated bubbles in horizontal capillary tubes begun to be studied in order to provide an index for the velocity of the liquid flow. Fairbrother and Stubbs [67] in the 1935 published a pioneering work about the prediction of the liquid mean velocity based on the velocity of a drifted bubble.

For years, theoretical models based on experimental results for the single bubble were proposed and the assumption of negligible gravitational effects was considered valid for channel's diameters below 3 mm.

Since the 90's, the flow of multiple bubbles in horizontal capillary tubes has been analyzed as *slug flow* regime in the context of the microfluidics. As the unimportance of the gravitational effects is a recognized criterion to identify the macro to microscale threshold, the validity of this assumption has been deeply explored.

In spite of over ten years of experiments on microscale slug flow, the current techniques, valid in the macroscale, are still inadequate to capture the local thermal-fluid dynamics generated by the bubbles, due to the small scales involved. Experimental techniques to characterize the flow field, such as the PIV technique, have not been developed yet for the microscale multiphase flow. Instead, the numerics, widely employed in the recent years to simulate such flow, provided a lot of information on the

local flow field, thus preceding subsequent experimental evidences.

In the following subsections, the current criteria for the macro to microscale transition are discussed, together with the single bubble models and the microfluidics findings. Next, those we consider the main recent numerical studies are introduced.

2.2.1 Experiments and analytical models

Macro- to microscale transition

Until the beginning of the 90's, the assumption of negligible gravitational effects on the motion of elongated bubbles in capillary tubes was considered valid for channels diameters below 3 mm. This assumption was verified by direct observation of the film thickness above and below the bubble, and it could be true for standard gravity acceleration and atmospheric pressure, for the fluids most employed at the time.

However, within the context of the microfluidics, refrigerant fluids at high pressures and microgravity conditions began to be adopted, and transition criteria based only on channel's diameters were found to be not anymore reliable. The Figure 2.2 shows an example of the bubble confinement effect occurring by decreasing the channel's diameter for R134a with typical operating conditions. Furthermore, the same channel's diameter could be considered both macro and microscale depending on the operating pressure and gravity.

As well, the macro to microscale transition began to be more and more evident, because the macroscale methods for the multiphase flow were unable to predict microscale trends. Among the transition criteria, the unimportance of gravitational effects was recognized to play a fundamental role.

Kew and Cornwell [68] in 1997 proposed a criterion based on the balance of capil-

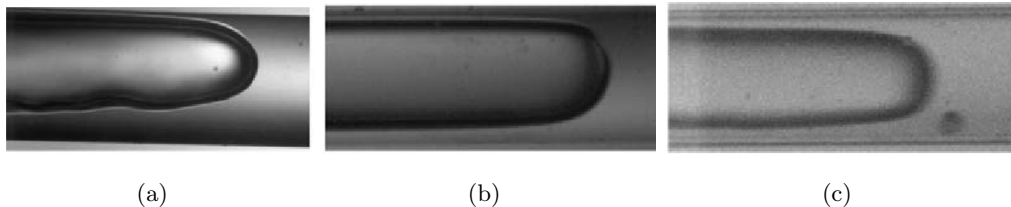


Figure 2.2: Revellin *et al.* [2] elongated bubble images for R134a at 30 °C within a 2 mm, 0.8 mm and 0.5 mm diameter channel.

lary and gravitational forces, quantified in the following definition of the Confinement number Co :

$$Co = \left(\frac{\sigma}{g(\rho_l - \rho_g)D^2} \right)^{1/2} \quad (2.4)$$

and they suggested the transition to occur at $Co = 0.5$.

Han and Shikazono [3] performed a large experimental campaign comparing the film thicknesses below and at the side of the bubble, by direct measurement of the film thickness by a Laser focus displacement meter. On the basis of their results with water, ethanol and FC-40 as working fluids, they identified the transition as a function of the Capillary number and Bond number defined in the following, as can be observed by the data plot reported in Fig. 2.3.

$$Ca = \frac{\mu_l U_b}{\sigma}, \quad Bo = \frac{\rho_l g D^2}{\sigma} \quad (2.5)$$

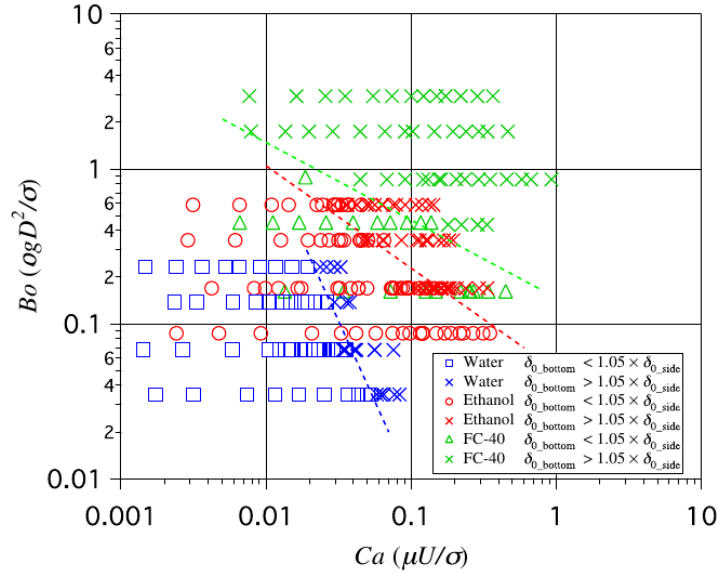


Figure 2.3: Han and Shikazono transition map from [3]. The cross marks correspond to cases in which the bottom liquid film thickness is 5% larger than that at the tube side while the squares identify a side film thickness within 5% of the bottom one. The dash lines locate the transition based on this criterion.

The most recent transition criterion was published by Ong and Thome [69] in the 2011. They measured top and bottom film thicknesses by capturing the interface by image processing of high speed videos, suggesting that the gravity forces are fully suppressed by the surface tension when $Co \geq 1$.

Experiments and theory on the single bubble dynamics

Fairbrother and Stubbs [67] early experiments on a single elongated bubble flow in a capillary tube, showed the relative drift velocity m of the bubble to be a function of the dimensionless group $\mu_l U_b / \sigma$ only, later named Capillary number:

$$m = \frac{U_b - U_l}{U_b} = Ca^{1/2} \quad (2.6)$$

valid for $Ca < 0.015$. They computed m indirectly, by pushing an air bubble within a capillary tube initially full of liquid and weighting the amount of liquid expelled from the tube. By knowing the initial weight of the liquid stored, the relative drift velocity of the bubble could be derived as:

$$m = 1 - \frac{w}{w_0} = \frac{\delta}{R} \left(1 - \frac{\delta}{R} \right) \quad (2.7)$$

with w and w_0 being the weight per unit length respectively of the fluid expelled and of the fluid initially stored. The procedure, correct only for axisymmetrical flows, led also to the film thickness δ as shown at the most RHS of Eq. (2.7). The bubble velocity, necessary for the correlation (2.6), was obtained by dividing the distance covered by the bubble's nose by the time, measured with a stop-watch. Note that Eqs. (2.6) and (2.7) can be merged to derive a correlation for the liquid film thickness.

Later, in the 1960 Taylor [70] repeated Fairbrother and Stubbs experiment, extending it to Capillary number up to 2, by using very viscous fluids. He employed strong syrup-water mixtures, glycerine and a lubricating oil. By coupling each fluid with the relative tube diameter, the smallest Confinement number of his campaign was 0.75, thus rather close to Ong and Thome [69] criterion for negligible gravitational effects.

Taylor did not provide any fit to its data, but he showed graphically that Eq. (2.6) is reliable up to $Ca < 0.09$, while for higher Capillary numbers the relative drift

velocity tends to the asymptotic value $m = 0.56$.

At the same time, Bretherton [51] developed a theoretical model of the flow to predict the relative drift velocity and the pressure drop across the bubble. His model was based on the assumption of negligible gravity, thus axisymmetric flow, and low bubble velocity, thus small Capillary number. The limitation on the Capillary number is equivalent to consider negligible inertial effects.

By these approximations, the bubble nose was assumed to be spherical with curvature $2/R$ and the Navier-Stokes equation within the liquid film was solved applying the lubrication theory. The analysis led to the following expressions for the relative bubble drift velocity m and pressure drop Δp :

$$m \simeq 1.29(3\text{Ca})^{2/3}, \quad \Delta p \simeq 7.16\left(\frac{\sigma}{D}\right)(3\text{Ca})^{2/3} \quad (2.8)$$

Bretherton conducted also an experimental work to assess the reliability of Eq. (2.8) to predict m . He performed experiments on a tube of 1 mm of diameter, with benzene and aniline as working fluids and air bubbles. The Confinement number for such conditions are $\text{Co} = 1.81$ for benzene and $\text{Co} = 2.03$ for aniline, thus well within the condition suggested by Ong and Thome [69] for axisymmetric flow. Bretherton's comparison with experiments assessed that Eq. (2.8) well predicts m for $\text{Ca} < 0.003$. Thus, Eq. (2.8) together with Eq. (2.7) and the assumption that $\delta/D \ll 1$ leads to the widely used correlation for the film thickness:

$$\frac{\delta}{D} \simeq 0.67\text{Ca}^{2/3} \quad (2.9)$$

More recently (2000), Aussillous and Qu  r   [71] performed an experimental campaign to study single elongated bubbles in small tubes at high Capillary number, such as Taylor's case. Differently from Taylor, they employed low viscosity fluids and obtained high Capillary numbers by means of high speed moving bubbles. Bubble velocities and liquid film thicknesses were deduced from video recordings. All the conditions tested led to Confinement numbers over unity.

The authors found that, depending on the fluid, by increasing the Capillary number there is a deviation in the film thickness from the Taylor law, with the film

thicker than the predicted value. They suggested it to happen because of the not anymore negligible inertial effects, which tend to sharpen the bubble's nose.

They split the film dynamics into two regimes. In the visco-capillary regime, the bubble velocity is low and the inertial effects are negligible. In this regime, the film dynamics is well captured by the analysis of Bretherton and Taylor, unified in the following law:

$$\frac{\delta}{D} \sim \frac{\text{Ca}^{2/3}}{1 + \text{Ca}^{2/3}} \quad (2.10)$$

But, over a threshold for the Capillary number, the flow enters in the visco-inertial regime. The inertia tends to thicken the liquid film in such a way that the assumption $\delta/D \ll 1$ is not anymore valid. They introduced the Weber number to represent the inertial effects:

$$\text{We} = \frac{\rho_l U_b^2 D}{\sigma} \quad (2.11)$$

By a scaling analysis in which the Weber number accounts for the inertial effects in the film dynamics, Aussillous and Quéré derived the following relation for the film thickness:

$$\frac{\delta}{D} \sim \frac{\text{Ca}^{2/3}}{1 + \text{Ca}^{2/3} - \text{We}} \quad (2.12)$$

Kreutzer *et al.* [72] in the 2005 used numerical simulations to explore the effect of the inertia in the flow of a single bubble, in terms of film thickness, bubble shape and pressure drops. As previously reported by Aussillous and Quéré [71], Kreutzer *et al.* found the film thickness to increase with the bubble velocity, see the results plotted in Fig. 2.4. In addition, they observed that the bubble nose is sharpened and the bubble rear is flattened by the inertial effects.

Kreutzer *et al.* fitted the numerical pressure drop data by a modified version of the Bretherton's Eq. (2.8) to account for the inertial term, leading to the following expression:

$$\Delta p = 1.08 \left(\frac{\sigma}{D} \right) (3\text{Ca})^{2/3} \text{Re}^{1/3} \quad (2.13)$$

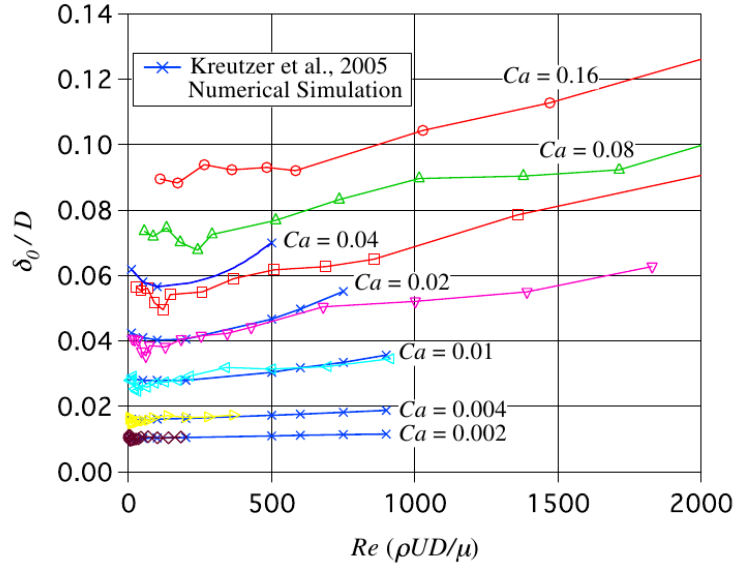


Figure 2.4: Liquid film thickness to channel's diameter ratio as a function of the Reynolds number, for different Capillary numbers. The figure is taken from [3] and reports the numerical results of Kreutzer *et al.* [72] as crosses and blue lines, compared with the experimental results of Han and Shikazono [3].

where the Capillary and Reynolds number ($Re = \rho U D / \mu$) were computed using the sum of gas and liquid superficial velocity instead of the bubble velocity. Each single phase superficial velocity is the average velocity that the phase would move at if it flow alone in the channel with its volumetric flow rate. Kreutzer and coworkers tested the Eq. (2.13) by comparison with experiments performed in a vertical channel. The dependence of the pressure drops on the Reynolds and Capillary numbers were well predicted, but a good agreement with experimental data was obtained raising the coefficient 1.08 to 2.6. The authors justified the deviation as effect of the impurities present in the fluid in actual experiments, generating surface tension gradients resulting in Marangoni effect, which raises the pressure drops.

Han and Shikazono [3] in the 2009 carried out a large database of experimental results on liquid film thicknesses for elongated bubbles in horizontal circular capillary tubes. The film thickness above, below and at the sides of the bubble, was measured by a Laser focus displacement meter.

In agreement with the mentioned previous works, they observed the inertia effect on the film thickness to be weak at low Capillary numbers, but to increase at higher Ca. The Fig. 2.4 shows that for $Ca < 0.002$ the film thickness is independent of Re, for $0.002 < Ca < 0.01$ it increases monotonically with Re, for $Ca > 0.01$ the dependence becomes more complex.

In order to fit their database of film thicknesses, they modified the scaling analysis proposed by Aussillous and Quéré [71], to account for the effects of the inertia on the bubble nose curvature. When the gravitational effects were not negligible, the thickness at the bubble sides was considered as reference value. Their expression for the liquid film thickness, in the following it is reported the one for $Re < 2000$, is currently the most updated available in the literature:

$$\delta/D = \frac{0.67Ca^{2/3}}{1 + 3.13Ca^{2/3} + 0.504Ca^{0.672}Re^{0.589} - 0.352We^{0.629}} \quad (2.14)$$

where the dimensionless groups have to be computed using the velocity of the bubble.

Slug flow in microchannels

The several years of research applied to the macroscale two-phase flow have led to the definition of detailed flow pattern maps and reliable heat transfer and pressure drop correlations. When dealing with microscale two-phase flows, the methods and the correlations developed for the macroscale does not work anymore. Thus, the first aim of the multiphase microfluidics has been to modify or reformulate maps and correlations, according to the different physical effects arising in the microscale.

The motion of elongated bubbles in microchannels, also known as slug flow, is a flow regime that has been deeply examined within the microfluidics. An example of such flow is reported in the Fig. 2.5. The reason of the importance of the elongated

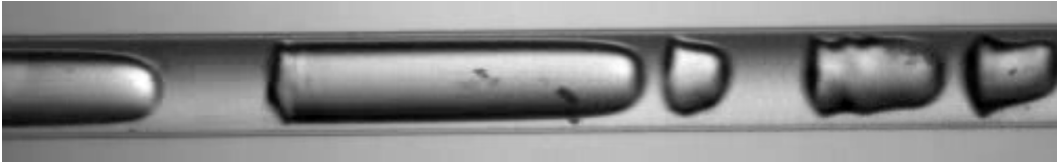


Figure 2.5: Microchannel slug flow snapshot from [73] for R245fa, horizontal 0.5 mm circular channel, $G = 517 \text{ kg/m}^2\text{s}$, $x = 0.047$, $T_{sat} = 34.4 \text{ }^\circ\text{C}$.

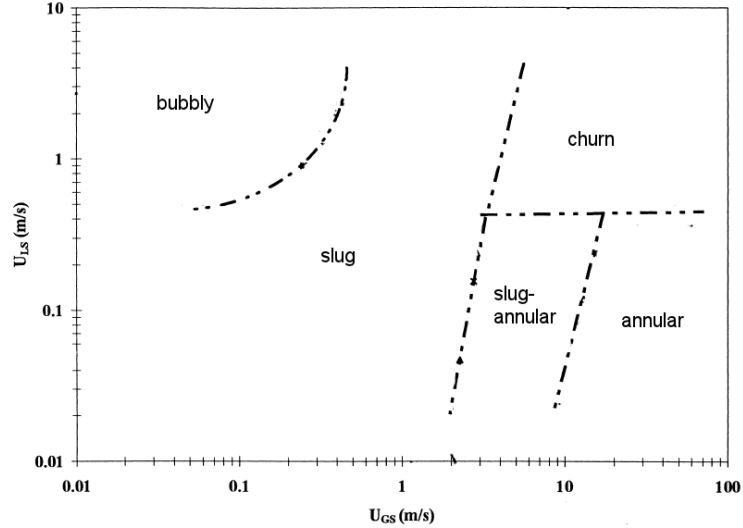


Figure 2.6: Flow pattern map of Triplett *et al.* [4] for air-water flow in a 1.1 mm horizontal circular channel. Liquid and gas superficial velocities are used to identify the regimes.

bubbles flow for engineering applications can be figured out through Fig 2.6. Figure 2.6 reports Triplett *et al.* [4] experimental flow pattern map for an air-water mixture flowing within a 1.1 mm horizontal circular channel. The transition lines were obtained by direct visualization of the flow. The map shows that the slug flow region is the widest one, thus highlighting the importance of the slug flow in microchannels.

Several flow pattern maps were proposed after Triplett *et al.* work, for different channel sizes, fluids and operating conditions. Transition lines were always traced according to the flow visualization and some empirical models appeared in the literature to predict the regime transitions. However, there was a noticeable disagreement among the maps proposed by the different experimental works. The discrepancy came from to the difficulty to obtain good high-speed images used to identify by visualization the regimes, but also from the arbitrary definition of the flow patterns themselves. Thus, the capture of a transition line was subjective to who was processing the images.

The development of objective techniques to characterize each flow pattern has been of great importance. Revellin and Thome [2] achieved this goal by employing an optical technique to detect the bubbles within the channel. By this method, several information such as bubble length, velocity and frequency could be obtained, leading to a clearer distinction among the different regimes. The original idea of Revellin and Thome [74] has been to create a diabatic and dynamic flow pattern map, by a vapor quality-mass flux plot. Diabatic means that in the experiments the gas bubbles were vapor bubbles created by evaporation, thus heating the channel. Dynamics means that the flow pattern transition lines were extrapolated by mechanistic models, which involved the physics of the flow. The models are able to predict the transition lines among the regimes, according to the operating conditions and the fluid properties as well. For what concerns the slug flow, an isolated bubble and a coalescing bubble regime were detected.

When dealing with single elongated bubble simulations, there is not a unique way to define the vapor quality x of the flow. The problem comes from the absence of leading and trailing bubbles which confine the liquid slugs ahead and behind of the bubble. Therefore, a reference length identifying the distance between the bubbles, necessary to estimate the vapor mass flow rate, is missing and it can only be defined arbitrarily. However, by knowing the mass flux G (as the mean velocity of the liquid inflow multiplied by the liquid density), the range of variation for the vapor quality may be determined by the use of the Revellin and Thome models for the transition. The transition between the isolated bubble IB and the coalescing bubble CB regimes is located as:

$$x_{IB/CB} = 0.763 \left(\frac{q\rho_g\sigma}{\mu_l h_{lv} G^2} \right)^{0.41} \quad (2.15)$$

where h_{lv} is the latent heat of vaporization and q the constant wall heat flux. The transition between the coalescing bubble and annular regime A is identified as:

$$x_{CB/A} = 0.00014 \left(\frac{GD}{\mu_l} \right)^{1.47} \left(\frac{G^2 D}{\sigma \rho_l} \right)^{-1.23} \quad (2.16)$$

These expressions can be used to estimate the range $[0, (x_{IB/CB} \text{ or } x_{CB/A})]$ within which the vapor quality may fall.

Let it consider now the bubble velocity. The bubble velocity is linked to the void fraction ϵ as $\epsilon = U_{sg}/U_b$, where U_{sg} is the gas superficial velocity that can

be obtained as $U_{sg} = Gx/\rho_g$. The void fraction can be predicted as a function of the volumetric flow rate $\beta = U_{sg}/U_s$, where U_s is the flow superficial velocity. The $\epsilon - \beta$ relationship depends on the model used, thus different models lead to different bubble velocity:

$$\text{homogeneous model:} \quad \epsilon = \beta \quad \Rightarrow \quad U_b = U_s \quad (2.17)$$

$$\text{Armand-Treschev correlation} \quad \epsilon = 0.833\beta \quad \Rightarrow \quad U_b = \frac{U_s}{0.833} \quad (2.18)$$

where it is referred to [75] for details about the Armand-Treschev correlation. When dealing with a single bubble flow, the identification of a proper superficial velocity is quite arbitrary, since a unique vapor quality can not be defined. Considering a single bubble simulation, the superficial velocity can be meant as the average velocity of the liquid inflow U_l , which can be substituted to U_s into the Eqs. (2.17) and (2.18).

Another relation for the prediction of the bubble velocity, by knowing the liquid velocity, can be derived through Eq. (2.7) by writing the relative bubble drift velocity as shown in (2.6):

$$U_b = \frac{U_l}{1 - 4\frac{\delta}{D}(1 - \frac{\delta}{D})} \quad (2.19)$$

where the relative film thickness can be computed by one of the correlations discussed previously. The Figure 2.7 shows a comparison of Eqs. (2.17), (2.18) and the Eq. (2.19) with Han and Shikazono [3] correlation (2.14) for the film thickness, to compute the bubble velocity. It is remarkable that the Armand and Treschev correlation (2.18) and Eq. (2.19) overlap when $U_l < 0.6$ m/s. For higher liquid velocity the Eq. (2.19), involving the film thickness, predicts a bubble faster than Eq. (2.18) one, because as the liquid film thickens the drag is reduced and the bubble moves faster.

Agostini *et al.* [76] proposed a model to predict the velocity of evaporating bubbles in microchannels as a function of the bubble length. The model suggested that the bubble velocity increases monotonically with the bubble length, up to an asymptote. This trend can explain the mechanism that leads to bubble coalescence, with longer bubbles that, traveling faster, reach and merge with shorter bubbles. However, Agostini *et al.* model requires the knowledge of the vapor quality, thus it is difficult to be applied to the single bubble flow case.

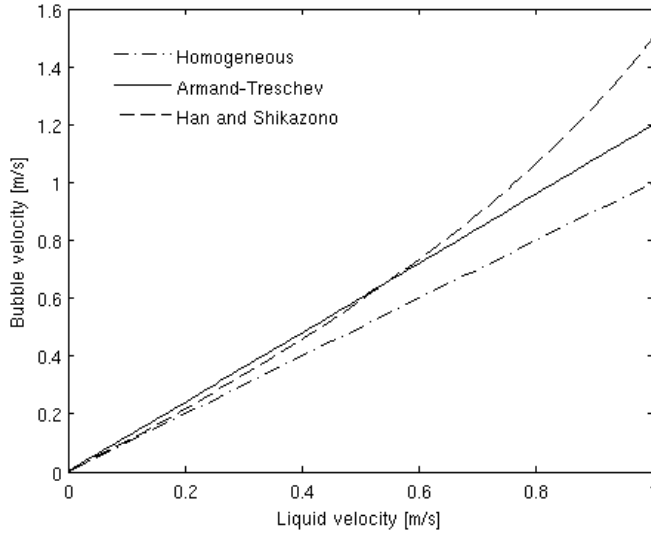


Figure 2.7: Comparison of the bubble velocity with respect to the liquid mean velocity predicted by the homogeneous model (2.17), the Armand-Treschev correlation [75] (2.18), and the (2.19) together with Han and Shikazono correlation (2.14) for the film thickness. The operating fluid is R134a at 31 °C and the channel diameter is 0.5 mm.

The experimental studies on boiling heat transfer in microchannels showed conflicting trends in determining the dependence of the heat transfer coefficient on vapor quality, heat flux and mass flux. As a general evidence, a strong dependence of the heat transfer coefficient on the heat flux and a weak dependence on the vapor quality and mass flux was observed.

Many authors concluded that, since in the macroscale the mentioned dependence is typical of the nucleate boiling, also in the microscale the nucleate boiling is the principal heat transfer mechanism.

However, as it can be observed by Fig. 2.6, the bubbly flow occupies only a small region of the flow pattern map. For vapor qualities over 0.05, only the slug flow and then the annular flow occur, without bubble entrainment in the liquid film. Thus, it is hard to believe that nucleate boiling can dominate the flow, without seeing the typical small bubbles generated by such mechanism.

Instead, Thome *et al.* [77] suggested that the thin film evaporation in the liquid

film is the dominant mechanism for the heat transfer. They showed that a phenomenological boiling heat transfer model for the elongated bubble regime, based on the thin film evaporation, can explain the trends observed for the heat transfer coefficient. The validation of the model by comparison of the predicted heat transfer coefficients with a large experimental slug flow database proved this interpretation.

Thome *et al.* three-zones model [5, 78] splits the single elongated bubble-liquid slug unit into three zones: the liquid slug, the elongated bubble and the vapor slug, see Fig. 2.8(a) for reference. The wall heat transfer coefficients for the liquid and vapor slugs are derived from single-phase correlations. The liquid film is assumed to be stagnant for film thicknesses below 1/100 of the channel diameter, thus the local heat transfer coefficient is computed by one-dimensional heat conduction across the film.

According to their approach, a time-averaged wall heat transfer coefficient at a given location z can be computed as:

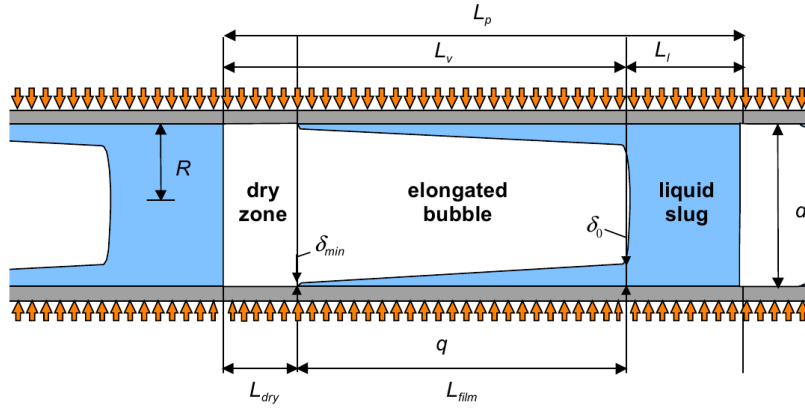
$$h(z) = \frac{t_l}{\tau} h_l(z) + \frac{t_f}{\tau} h_f(z) + \frac{t_v}{\tau} h_v(z) \quad (2.20)$$

where τ is the period of the bubble cycle, t_l/τ , t_f/τ and t_v/τ are respectively the fraction of the period occupied by the liquid slug, the film and the vapor slug. The Figure 2.8(b) shows that as the bubble is passing at the given location, the heat transfer coefficient increases because of the thinning of the liquid film, reaching a maximum and subsequently dropping when dryout occurs.

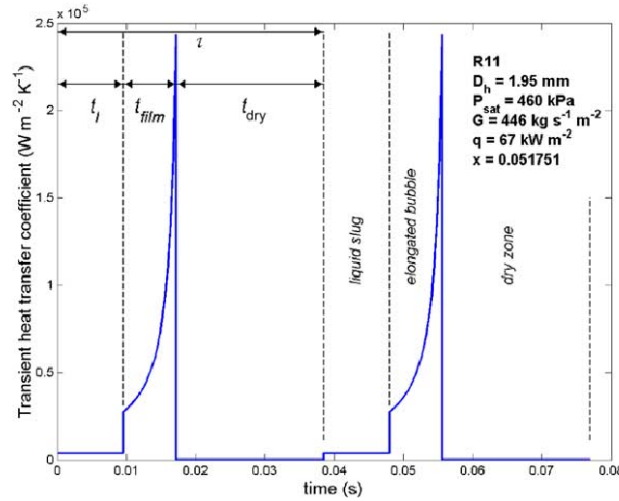
The three-zones model has been widely validated with experimental data for the prediction of time averaged heat transfer coefficients. However, its basic principle of splitting the bubble cycle in two (without dryout) or three stages and computing the heat transfer in the film zone by heat conduction, can be useful to obtain a theoretical profile of the heat transfer coefficient to compare with simulation results.

Thome *et al.* three-zones model applies well at the isolated bubble regime. On the basis of the thin film evaporation Consolini and Thome [8] developed a boiling heat transfer model for the coalescing bubble regime. By application of the mass and energy balance to a control volume bounded by the channel wall, the entrance in the heated zone and a boundary moving with the nose of the generic bubble, the authors derived the following time law governing the motion of the bubble nose:

$$z_N(t) = \frac{G}{\rho_l} \frac{\rho_v h_{lv} D}{4q} \left[\exp\left(\frac{4q}{\rho_v h_{lv} D} t\right) - 1 \right] \quad (2.21)$$



(a)



(b)

Figure 2.8: Thome *et al.* three-zones model [5, 78]: (a) scheme of the bubble-liquid slug unit, (b) transient local heat transfer coefficient at a given axial location during two bubble cycles. Figures from [5].

where z_N is the bubble nose axial location when considered $z = 0$ as the location of the entrance in the heated zone. The nose of the bubble is considered to enter in the heated region at $t = 0$. It is referred to [8] for the model assumptions.

In a recent publication, Walsh *et al.* [6] showed their results on the local Nusselt number at the wall of a microchannel heated by a constant heat flux, for an air/water

slug flow. They used infrared thermography to measure the local temperature of the wall T_w , thus deriving the local Nusselt number as:

$$\text{Nu}(x) = \frac{qD}{\lambda_l(T_w(x) - T_b)} \quad (2.22)$$

where T_b is the bulk temperature of the flow. Walsh and his coworkers observed that the most effective parameter governing the heat transfer is the liquid slug length L_s to channel diameter ratio. The Figure 2.9 reports the time-averaged Nusselt number along the dimensionless position $x^* = x/(D \text{Pe})$ (Peclet number $\text{Pe} = \text{Re} \cdot \text{Pr}$) downstream of the heated section entrance, for different L_s/D ratios. Due to the high thermal diffusivity of the gas phase, only the liquid slugs contribute to the wall cooling. Therefore, in order to reduce the data appropriately, the measured Nusselt number is normalized by the percentage contact area of the liquid phase. This percentage contact area is defined as $1 - \epsilon$, where the void fraction ϵ is considered equal to the volumetric flow rate, according to the homogeneous model. The Figure 2.9 plots also the Nusselt number as predicted by the correlation (2.23) proposed by

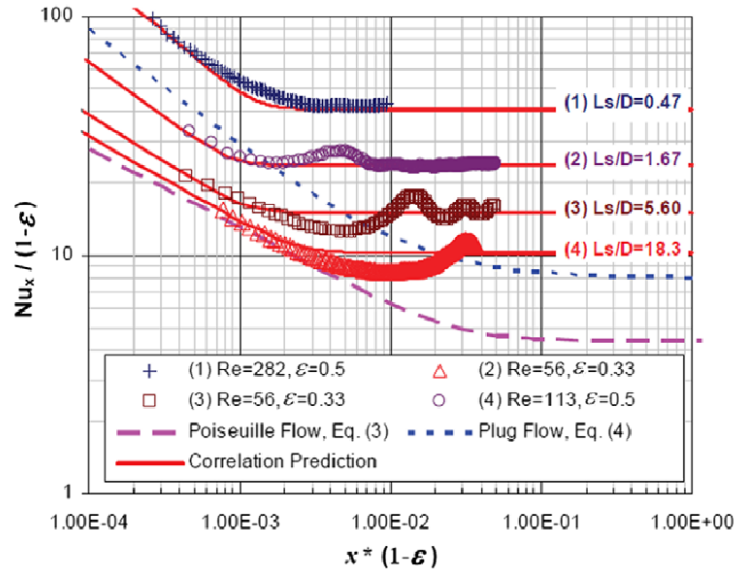


Figure 2.9: Walsh *et al.* [6] local Nusselt number with respect to the dimensionless position $x^* = x/(D \text{Pe})$ downstream of the heated section entrance, for different L_s/D ratios. The Nusselt number and the dimensionless position are normalized by $1 - \epsilon$.

the authors.

The Figure 2.9 shows that the Nusselt number in the entrance region is bounded below by the profile of the single phase developing Poiseuille flow and above by the profile of the single phase developing plug flow, meaning a flow with $Pr=0$. The oscillations in the Nusselt number were ascribed to the internal circulation occurring within the moving liquid slugs. As a consequence of this circulation, fresh liquid from the centerline of the channel is moved toward the wall at the slug leading edge and *vice versa* at the trailing edge. The characteristic length of such flow is the length of the circulation path $2L_s + D$ which also reflects the period of the oscillations on Nu . The Figure 2.9 shows that the length of the thermal entrance region is shorter than the single phase case and it shortens as L_s/D decreases. Walsh *et al.* correlated their database of fully developed Nusselt number on the basis of the single phase value:

$$Nu = (1 - \epsilon) \left[4.36 + 25 \left(\frac{L_s}{D} \right)^{-1/2} \right] \quad (2.23)$$

Subsequently, Howard *et al.* [79] suggested a correction to Walsh *et al.* data reduction to better predict the Nusselt number for fluids other than air/water and to account for a wider range of Capillary numbers. They suggested to compute the void fraction, used to normalize the data, through the following modification of the homogeneous model:

$$\epsilon = \frac{D^2}{(2\delta - D)^2} \beta \quad (2.24)$$

For what concerns the pressure drops within microchannels, most of the models available in the literature are modifications of empirical correlations originally developed for the macroscale. Revellin and Thome [80] performed an experimental campaign of pressure drops measurements for R134a and R245fa within 0.5 mm and 0.8 mm channels and showed that none of 13 models and correlations chosen in the literature were able to predict their data with a good agreement.

As well, a reliable phenomenological model for the prediction of pressure drops, as the three-zones model is for boiling heat transfer, is still missing.

2.2.2 Numerical simulations

Despite the absence of experimental techniques for quantitative measurements of the velocity field in the microscale, necessary to validate the numerical simulations, several two-phase flow phenomena have been studied through the numerics: bubble dynamics, velocity and induced pressure drop; bubble formation at orifices and subsequent dynamics; gas-liquid interface behavior at a T-junction; transient heat transfer at the wall due to the bubble passage; mass, momentum and energy transfer induced by the evaporation.

In the following paragraphs, those we consider the main recent numerical studies are split into adiabatic, diabatic without phase change and diabatic with phase change.

Unless otherwise specified, an incompressible and laminar flow and a no-slip condition at the wall are assumed. Furthermore, it is implied that when the model is axisymmetric, gravitational effects are not accounted for.

Adiabatic studies

Kreutzer *et al.* [72] numerical study on the effect of inertia in the flow of elongated bubbles has already been introduced in the previous subsection. Their numerical framework solved the Navier-Stokes equations only for the liquid phase in an axisymmetrical domain, treating the gas-liquid interface as a free-surface. A reference frame moving with the bubble velocity was employed and the simulations were run until a steady state was achieved. A fully developed laminar flow profile was imposed at both the inlet and outlet boundaries, thus enforcing mass conservation.

Several cases were performed by varying the Capillary and Reynolds numbers, in order to study the effect of the inertia on bubble shape, liquid film thickness and pressure drop. For what concerns their results, it is referred to what already reported in the previous subsection, together with Fig. 2.4 for the film thickness and Eq. (2.13) for the pressure drops.

Qian and Lawal [81] analyzed the bubble formation and subsequent gas and liquid slugs length when gas and liquid are separately fed by a T-junction. The simulations were performed by means of the commercial CFD solver Fluent, tracking the inter-

face by a VOF method. A two-dimensional domain was considered since they did not observe substantial differences on the slugs lengths when using a three-dimensional geometry. Gravity effects were found to be negligible for their operating conditions, for which the minimum Confinement number is 0.9. A velocity inlet and an outflow boundary conditions were applied to the channel inlet and outlet, see the Section 4.7 for an introduction on boundary conditions. The liquid film was not solved by the computational grid, but a zero contact angle with the wall was set in order to have rounded bubble meniscii at the wall when numerical dryout occurs.

Qian and Lawal performed a large campaign of simulations to analyze the effect of the gas and liquid inlet velocities, the inlet geometrical configuration and the fluid properties on the mean length of the gas and liquid slugs. A non-dimensional analysis was developed to derive some correlations for the prediction of the mentioned lengths. They observed that the velocity of the bubbles was always very close to the superficial velocity of the flow, in agreement with the homogeneous model Eq. (2.17).

Kumar *et al.* [82] performed a numerical study similar to Qian and Lawal one, but in U-bends. The commercial solver Fluent with VOF interface capturing scheme was used. The flow dynamics was captured by a three-dimensional model, in which gravity was considered. Velocity inlet and outflow boundary conditions were imposed. The liquid film was not solved by the grid.

The effect of the inlet geometry, as well as channel diameter, bend curvature, fluid properties and wall contact angle on the bubble length was analyzed. Among their results, it is mentioned that the bubble velocity is very close to the superficial flow velocity, as reported for the previous study.

Gupta *et al.* [83] published an excellent review of the recent experimental and numerical works on microchannel elongated bubbles flow. Their aim was to highlight and then clarify through simulations the role of the liquid film and the wall contact angle in the CFD modeling of the slug flow. Their study was carried out through the solver Fluent with VOF interface capturing and an axisymmetrical geometry. A velocity inlet and a constant pressure conditions were applied at the channel inlet and outlet.

The authors performed a detailed grid convergence study and found out that 5

computational cells discretizing the liquid film are necessary to gain convergence in the bubble dynamics. Moreover, uniform cells are recommended to discretize the interface for a better surface tension force estimation.

Gas and liquid phases were introduced in the channel as coflowing streams, thus generating a multiple bubble flow. With $Ca=0.006$ and $Re=280$ as dimensionless numbers, they observed small waves on the interface profile at the rear of the bubble. The film thickness in the flat region was in good accordance with Fairbrother and Stubbs Eq. (2.7), Bretherton Eq. (2.9) and Aussillous and Qu  r   Eq. (2.10). The bubbles velocity was 11% lower than the one predicted by the Armand and Treschev correlation (2.18), but we found it to be in perfect agreement with the Eq. (2.19) when using Han and Shikazono correlation (2.14) and replacing the liquid velocity in (2.19) with the flow superficial one. The pressure drop measured in the simulation was 25% below the value predicted by Kreutzer *et al.* Eq. (2.13).

Diabatic studies without phase change

Fukagata *et al.* [84] analyzed the thermal-fluid dynamics of the slug flow by the simulation of a single bubble-liquid slug unit. The flow was modeled through an axisymmetrical geometry and the Level-Set algorithm was used to track the interface. They imposed a periodic boundary condition for velocity and temperature and a constant heat flux at the wall. A gas bubble was patched in the liquid domain at the beginning of the simulation and a fixed pressure difference generated the flow.

Two separated mechanisms are observed to enhance the heat transfer performance in terms of Nusselt number. The bubble transit forces a recirculating flow within the liquid slugs, thus refreshing the liquid layer near the wall. The high thermal diffusivity of the gas raises the bulk mean temperature in the film region, decreasing the wall-bulk temperature difference and then maximizing the Nusselt number, up to 5 times the single phase one. The local Nusselt number was defined through the wall-bulk temperature difference. The global Nusselt number, averaged over the bubble-slug unit, depends on the flow pattern and it is about 2 times the single phase value for the elongated bubbles regime.

Lakehal *et al.* [85] performed a similar study by the use of the commercial software TransAT [86]. In this case the gas and the liquid phases were injected as

coflow streams. A constant temperature was set at the wall. The domain length was 40 diameters, which was proved to be enough to reach a thermal fully developed condition.

The radial temperature profiles showed that the bubble passage erases part of the thermal boundary layer at the wall, generating temperature gradients at the wall higher than single phase case ones. Furthermore, the high heat diffusion within the gas phase raises the mean bulk temperature thus leading to high heat transfer coefficients. A strong recirculation pattern was observed in the slugs between the bubbles, thus providing fresh liquid at the wall. The local wall Nusselt number shows a periodical profile from a heated length of 15 – 20 diameters, identifying a thermally developed situation. Note that the single phase flow would have taken 70 diameters to develop. The maximum peak in the Nusselt number is 9 times higher with respect to the single phase and it is located at each bubble rear, where there is the minimum film thickness. The Nusselt number averaged on the last 20 diameters of the channel length is 4 times the single phase value for the elongated bubbles flow pattern. According to their numerical database, they suggested the following correlation:

$$\text{Nu} = 3.67 + 0.022\text{Re}_b^{0.8}\text{Pr}_l^{0.4} \quad (2.25)$$

where $\text{Re}_b = \rho_l U_b D / \mu_l$.

Gupta *et al.* [87] employed the commercial software TransAT, based on the LS method, and Fluent, based on the VOF method, to simulate the slug flow formed by a gas-liquid coflow inlet. Both constant temperature and heat flux conditions at the wall were studied. As for the aforementioned works, the mechanism leading to a heat transfer higher than single phase one was noticed to be twofold. The recirculation pattern in the liquid slugs increases the wall heat exchange. The high thermal diffusivity of the gas increases the wall Nusselt number in the film region up to 20 times the single phase value. The average Nusselt number obtained for the second and third bubble-slug unit at a heated length of about 15 diameters, is 3 times the single phase value. Gupta *et al.* also studied the length of the channel and the number of bubbles necessary to obtain a fully-developed Taylor flow and found them to be a function of the Reynolds and Péclet numbers of the flow. According to this condition, they repeated the simulation for a 40 diameters length channel

and found the average Nusselt number for the fifth unit cell to be 2.5 times the single phase value. The authors found the best fit to their numerical data to be the following modified version of the Walsh *et al.* [6] Eq. (2.23):

$$\text{Nu} = (1 - \epsilon) \left[4.36 + 19.2 \left(\frac{L_s}{D} \right)^{-1/2} \right] \quad (2.26)$$

He *et al.* [88] simulated a bubble-liquid slug unit by the use of periodic boundary conditions for the velocity and temperature fields. Their grid convergence analysis suggested that a uniform mesh with 6 cells discretizing the liquid film is enough to obtain converged fields of velocity and temperature. He *et al.* observed that at low Reynolds numbers the recirculating flow within the liquid slugs has a lower effect in enhancing the wall heat transfer than the heat diffusion within the gas. At high Reynolds numbers, the convection is more effective and the wall temperature fluctuations vanishes, as for the presence of a high thermal resistance across an adherent liquid film on the wall. They reported that the Nusselt number averaged within the bubble-slug unit depends on the flow pattern. For the elongated bubbles regime it is 2.5 times higher than the single phase value.

Mehdizadeh *et al.* [89] employed the commercial software Fluent with the VOF method to study the slug flow, also accounting for the axial conduction in the heated wall. They found the axial conduction to cause a time-shifting in the inner and outer wall temperature profiles. The wall stores a significant amount of heat during the bubble passage and release it while the liquid slug is passing. Thus, the local heat transfer is maximum in the liquid slug and reaches a minimum in the liquid film close to the bubble rear, where the axial velocity is very low. However, the liquid film region contributes to the wall heat exchange with the 25% of the overall heat transfer. The wall storage and release capability explains the wide Nusselt number oscillations that they observed, which ranges from 3 to 100. The average Nusselt number for the flow is about 6 times the single phase value. The length of the computational domain was 20 diameters and it was found to be sufficient to achieve a fully developed regime.

Diabatic studies with phase change

Mukherjee and Kandlikar [90] simulated the evaporation of a water vapor bubble within a square microchannel, by use of a LS method to track the interface. A small spherical vapor bubble was patched at the upstream of the channel in the centerline, and a fixed velocity for a superheated liquid inlet was imposed. A constant temperature higher than the saturation one was set at the heated wall. A constant contact angle was imposed in case the interface touch the walls. Gravity effects were found to be negligible.

According to their results, the vapor bubble grows spherically until it approaches the channel's walls, subsequently it stretches and generates a thin liquid film, eventually forming some dry patches. The bubble growth rate is linear with respect to time at the spherical stage of the growth, then it becomes exponential. The liquid velocity downstream the bubble is 40 times higher than the inlet value, due to the evaporation that pushes liquid out of the channel. It was found that, by increasing the superheating of the liquid inflow, the bubble growth rate increases and the dry patches disappear because there is not time for the liquid film to evaporate. By increasing the liquid inlet velocity, the bubble growth rate decreases because the thermal boundary layer gets thinner while the liquid film gets thicker, thus decreasing the interface area exposed to the superheated region.

In the 2009 Mukherjee [91] repeated the same simulations, but patching an initial spherical vapor bubble at one channel's wall. The aim was to study the effects of different advancing and receding contact angles on the bubble growth rate and wall heat exchange.

He found that smaller contact angles favour the elongated growing of the bubble, thus leaving a liquid film between the interface and the walls. The heat exchange at the wall is considerably enhanced in the film region, thus higher bubble growth rates were obtained for smaller contact angles. This dynamics suggested to the author that the thin film evaporation is the preeminent heat transfer mechanism in such flow.

In the 2011 Mukherjee *et al.* [92] performed a parametric study to assess the influence of wall superheat, Reynolds number, surface tension and contact angles on

bubble growth rate and wall heat transfer. They figured out that an increase of the wall superheat favours the bubble nose to move downstream to the channel, allowing a longer liquid film to exist thus increasing the wall heat transfer. The Reynolds number has a little effect on the flow, because the velocities associated to the evaporation phenomena are very high compared to the liquid inflow. The mentioned trends for the heat transfer are in line with those observed by several experimental researchers on microchannels, but such trends are justified in the paper by means of a film evaporation mechanism.

The effect of the surface tension is negligible. The effect of the contact angle is the same reported in the previous Mukherjee work [91].

Suh *et al.* [93] studied the bubble dynamics and the associated flow and heat transfer in parallel microchannels, in order to investigate the conditions leading to reversed flows. The Level-Set algorithm was used to track the interface and it was extended to treat the immersed solid surface separating the channels. Two square channels with shared inlet and outlet manifolds were simulated. A fixed mass flow rate was imposed at the inlet section. A constant wall temperature was set at the bottom wall while the top wall was set as adiabatic. A constant contact angle was fixed in case of three-phase contact lines. The simulated bubbles were patched with a spherical shape upstream the channels in the centerline.

Three different configurations were modeled: two bubbles (one for each channel) created simultaneously; only one bubble created; two bubbles created with a time lag. In the first case, the two bubbles grows identically and move downstream to the channel. In the second case, the bubble grows also upstream, generating a liquid backflow in the inlet manifold. The backflow leads to a different distribution of the heat load in the two channels and the performances of the channel where evaporation occurs are worse than the case without backflow. The third case shows an intermediate situation. The flow reversal is seen to be boosted by higher wall superheat and by smaller contact angles.

2.3 Concluding remarks: open issues on flow boiling in microscale

The published literature about numerical and experimental studies on two-phase flow in microchannels allowed to clarify several aspects of the flow. The role of the forces acting on the bubble on determining bubble shape, pressure drop and steady velocity has been deeply investigated. Gravitational effects are negligible when $Co > 1$, thus allowing the axisymmetrical formulation of the flow problem adopted in the CFD method employed in this work. Accurate and comprehensive flow pattern maps allow to identify the two-phase flow regime by knowing only few variables which describe the flow. Thome *et al.* three-zones model [5] provides a reliable tool to estimate the time-averaged heat transfer coefficient under flow boiling conditions.

Although numerical simulations are currently the only technique which allows to investigate the local features of evaporating flows, only few studies deal with such flow configuration. Physical aspects such as the local thermal-fluid dynamics induced by the evaporating bubble, local estimation of heat transfer performances, the mutual effect of multiple evaporating bubbles and quantitative comparisons with experimental results are still open issues, which we intend to explore by means of CFD simulations.

Chapter 3

Modeling of interfacial effects

The equations governing the two-phase flow when the Volume Of Fluid method is used to capture the interface are the continuity Eq. (1.21), the volume fraction Eq. (1.38), the momentum Eq. (1.16) and the energy Eq. (1.17).

The volume fraction, momentum and energy equations include as source terms the interfacial effects related to surface tension and phase change. The surface tension force, expressed by the CSF method [43], involves the calculation of the local interface curvature κ , see Eq. (1.39). The phase change requires the calculation of the local rates of mass \dot{m} and energy \dot{q} exchanges due to the evaporation.

It is clear that the interface curvature and the rates of mass and energy exchange at the interface require *ad hoc* models for their formulation and discretization on a computational grid. It is referred to *interface reconstruction algorithm* as those algorithms aimed to reconstruct an approximation of the interface topology and to the subsequent estimation of the local interfacial norm vector and curvature. *Evaporation models* are those models which, on the basis of a chosen interface temperature condition, estimate the mass and energy exchanges due to phase change.

The algorithms that we have implemented in the numerical code used in this thesis are the Height Function algorithm for the curvature computation [94] and an evaporation model based on the physical concept of interfacial resistance to the heat transfer [95], introduced in the solver as proposed by Hardt and Wondra [7].

In the following sections, these algorithms are separately treated. For each of

them, the regarding literature is briefly reviewed, then the physical and mathematical basis are discussed and finally the numerical algorithm is reported.

3.1 The interface reconstruction algorithm

An interface reconstruction algorithm has the task to compute the local interface norm vector and curvature as accurate as possible. Furthermore, the features expected from an interface reconstruction algorithm are convergence as the computational grid is refined, precision also when the interface is poorly solved by the grid, independence of the grid topology, simplicity of implementation.

According to our experience, an algorithm satisfying all the mentioned requirements does not exist, in general it can be said that accurate and easy-to-implement algorithms are possible only limiting their range of application to particular grid topologies.

The VOF based interface reconstruction algorithms estimate the local interface unit norm vector and curvature from the volume fraction field. The local interface topology can be estimated once that an approximation of the interface is built within each interfacial cell ($0 < \alpha < 1$). By calling \mathbf{m} the vector tangent at the interface for the generic interfacial cell, the local unit norm vector \mathbf{n} is orthogonal to \mathbf{m} and the local curvature can be estimated as $\kappa = -\nabla \cdot \mathbf{n}$. The way to build this approximation of the interface is the peculiarity of each interface reconstruction algorithm.

The first algorithm with this aim was the PLIC algorithm by Youngs [38] (1984), which is the only scheme available in the CFD software Ansys Fluent version 12 and before. The interface within each interfacial cell is approximated as a piecewise linear segment (see Fig. 1.5(d)) with orientation $(\nabla\alpha)^{-1}$ and position adjusted to match the cell volume fraction. The local interface unit norm vector and curvature are computed as reported in the Eq. (1.36). As discussed in the Section 1.5, this method is poorly accurate and the computed curvature does not converge either refining the computational mesh, as it is proved in Section 5.1.

Puckett [96] proposed the *Least-squares Volume-of-fluid Interface Reconstruction Algorithm* (LVIRA), through which the volume fractions of a 3×3 block of cells are considered to compute a linear approximation of the interface in the center cell of the block. The interface norm vector is the one leading to a linear interface unique for the block that minimizes the difference between the volume fraction defined area of the block and the area of the polygon defined by the interface and the block sides. An initial guess for the norm vector is obtained computing the interface orientation by the finite differences of the interface heights on the side columns of the block. The interface heights in the side columns are obtained by summing the volume fractions columnwise. Once the unit norm vector is known, the curvature is computed as $\kappa = -\nabla \cdot \mathbf{n}$.

Williams [97] proposed to compute the interface topology as Youngs did, but using a smoothed version of the volume fraction field obtained by the convolution with a smoothing kernel of finite size across the interface. When this convolution technique is used to estimate the curvature of a circular interface, the computed curvature converges with the first order with respect to the mesh refinement.

Cummins *et al.* [94] reconstructed a distance function from the interface on the basis of the volume fraction field. This distance function is analogous to the level-set function, it varies smoothly across the interface and the interface topology can be estimated by differencing its values with conventional derivation schemes. The curvature convergence order in the reconstruction of a circle is first order.

Renardy and Renardy developed a *Parabolic Reconstruction Of Surface Tension* (PROST) algorithm [47], approximating the interface as a piecewise parabolic curve within a 3×3 block centered on each interface cell. The coefficients of the parabola are obtained by a fit done by a least-squares algorithm, as for the LVIRA method. The interface curvature is estimated through the coefficients of the parabola.

Helmsen *et al.* [98] suggested a method to approximate the interface similar to the technique used by Puckett [96] to find the initial guess for the LVIRA method. However, a 7×3 block is considered instead of a 3×3 one and its orientation is

chosen according to a preliminary estimation of the norm vector in the central cell. By the local integration of the volume fraction field proper of the LVIRA method, a local discrete field of the height of the interface within the block is obtained, such that the interface segment orientation within the central cell can be computed by finite-differences. This method is called *Height Function* (HF) and, currently, it is the best compromise among accuracy and simplicity, even though its use is restricted to orthogonal grids. The computed curvature converges with the second order of the mesh grid size. The Height Function is the algorithm that we chose and implemented in the numerical solver and it is thoroughly treated in the Subsection 3.1.1.

In the following paragraph, the Youngs algorithm [38] as implemented in the Fluent software is introduced, since it is the default algorithm present in Fluent for curvature computation and it came useful as a benchmark for our HF implementation.

The Youngs algorithm

The interface unit norm vector components are evaluated as derivatives of the volume fraction field:

$$\mathbf{n} = (n_x, n_y) = \frac{1}{|\nabla\alpha|} \left(\frac{\partial\alpha}{\partial x}, \frac{\partial\alpha}{\partial y} \right) \quad (3.1)$$

where the norm of the volume fraction gradient is:

$$|\nabla\alpha| = \left[\left(\frac{\partial\alpha}{\partial x} \right)^2 + \left(\frac{\partial\alpha}{\partial y} \right)^2 \right]^{1/2} \quad (3.2)$$

The derivatives along the horizontal and vertical directions are discretized at the cell center by means of a finite-differences scheme in a 3×3 block. The derivative in the centroid of the center cell (i, j) is computed as average of the derivatives centered on the cell faces. The derivative on each face is computed as average of the derivatives evaluated at the face nodes. The derivative at each node is computed through the volume fraction values of the cells surrounding the node.

This technique allows a smoother derivative of the volume fraction across the interface than a standard 5 cells stencil. The final scheme becomes:

$$\left(\frac{\partial\alpha}{\partial x} \right)_{i,j} = \frac{\alpha_{i-1,j+1} + 2\alpha_{i,j+1} + \alpha_{i+1,j+1} - \alpha_{i-1,j-1} - 2\alpha_{i,j-1} - \alpha_{i+1,j-1}}{2\Delta x} \quad (3.3)$$

$$\left(\frac{\partial \alpha}{\partial y}\right)_{i,j} = \frac{\alpha_{i-1,j-1} + 2\alpha_{i-1,j} + \alpha_{i-1,j+1} - \alpha_{i+1,j-1} - 2\alpha_{i+1,j} - \alpha_{i+1,j+1}}{2\Delta y} \quad (3.4)$$

where Δx and Δy are the grid spacings. See the Figure 3.1 for the indexes reference.

The interface curvature can be computed as the divergence of the norm vector or through the following extended expression proposed by Brackbill *et al.* [43]:

$$\kappa = \frac{1}{|\mathbf{n}|} \left[\left(\frac{\mathbf{n}}{|\mathbf{n}|} \cdot \nabla \right) |\mathbf{n}| - (\nabla \cdot \mathbf{n}) \right] \quad (3.5)$$

It is referred to [43] for the discretization of the terms appearing in (3.5).

The Figure 3.1 reports the volume fraction field across an interface represented by a circular arc. The exact value of the curvature is the inverse of the arc radius, $\kappa = 200$. The curvature computed by the Eq. (3.5) in the central cell of the block is $\kappa_{i,j} = 348$, the 74% higher than the real value.

Even though the Youngs-based Fluent default interface curvature calculation in our implementation is replaced by the HF algorithm, the volume fraction gradient $\nabla \alpha$ and its norm $|\nabla \alpha|$, when required by the solution algorithm, are discretized by use of the Eqs. (3.3) and (3.4).

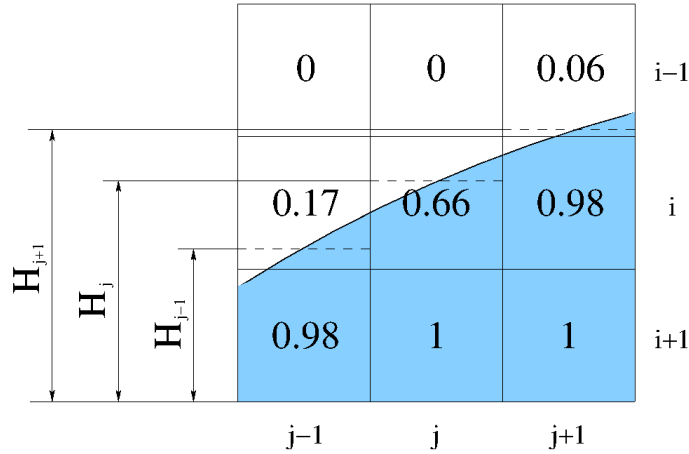


Figure 3.1: Example of the volume fraction field across a circular arc of radius 5 mm. The curvature of the arc is 200 m^{-1} . The computational grid is uniform, with spacing 0.5 mm. The dash segments represent the approximation of the interface by the Height Function algorithm.

3.1.1 The Height Function algorithm

The basic principle of the Height Function algorithm consists in the local integration of the volume fraction field to obtain a smooth scalar field, which represents the height of the interface with respect to a reference axis. The interface norm vector and curvature can be computed by derivatives of this scalar field using conventional finite-differences schemes.

The continuous height function

Let $y = f(x)$ be the mathematical function identifying the interface line in a Cartesian (x, y) reference frame, as shown in the Fig. 3.2. The continuous height function $H(x; h)$ is the height of the interface line $f(x)$, averaged within a local stencil of width h and centered on x :

$$H(x; h) = \frac{1}{h} \int_{x-h/2}^{x+h/2} f(t) dt \quad (3.6)$$

The interface unit norm vector and curvature can be represented by geometrical considerations as:

$$\mathbf{n} = \frac{1}{[1 + (H_x)^2]^{1/2}} (H_x, 1) \quad (3.7)$$

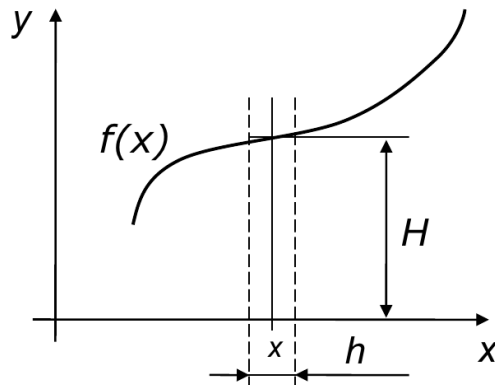


Figure 3.2: Sketch of the continuous height function.

$$\kappa = -\nabla \cdot \mathbf{n} = -\frac{H_{xx}}{[1 + (H_x)^2]^{3/2}} \quad (3.8)$$

where H_x and H_{xx} denotes first and second order derivatives with respect x .

Here, the height function is evaluated as integral over the x -axis, that is the natural choice when $df(x)/dx < 1$. However, when $df(x)/dx > 1$, the inverse function $x = f^{-1}(y)$ can be considered and the interface geometry is computed through derivatives of the width of $f^{-1}(y)$ with respect to the y - axis.

The function $y = f(x)$ may easily become not biunivocal when representing an interface. In this case, local heights or widths can be computed over a translated (x', y') reference frame, which makes $y' = f'(x')$ locally biunivocal. Thus, local heights or widths values are defined, but since the interface geometry is computed through derivatives of heights or widths, the result is correct.

It is remarked the local feature of the height function. The orientation and the position of the axis used as reference for the evaluation of heights or widths at the generic x location is not important. It may vary at every location x , but the best choice at each x is the one that leads to the most accurate computation of the interface topology.

The Equations (3.7) and (3.8) refer to a two-dimensional geometry. For axisymmetrical domains with revolution around the x -axis:

$$\mathbf{n} = \frac{1}{[1 + (H_x)^2]^{1/2}}(H_x, 1) \quad (3.9)$$

$$\kappa = -\frac{H_{xx}}{[1 + (H_x)^2]^{3/2}} - \left(\frac{H_{xx}}{|H_{xx}|} \right) \frac{1}{f(x)[1 + (H_x)^2]^{1/2}} \quad (3.10)$$

For three-dimensional domains:

$$\mathbf{n} = \frac{1}{[1 + (H_x)^2 + (H_y)^2]^{1/2}}(H_x, H_y, 1) \quad (3.11)$$

$$\kappa = -\frac{H_{xx}[1 + (H_y)^2] + H_{yy}[1 + (H_x)^2]}{[1 + (H_x)^2 + (H_y)^2]^{3/2}} \quad (3.12)$$

The discrete height function

In the discrete case, the discrete Height Function can be defined for each interfacial cell ($0 < \alpha < 1$). Let consider the interface cell (i, j) of the Fig. 3.1. The h width

stencil is the grid spacing. The reference axis for the local computation of heights or widths can be arbitrarily chosen among the lines of an orthogonal computational grid. By approximating the interface line as a horizontal piecewise segment if heights are being computed, otherwise vertical (in Fig. 3.1 heights are computed and the interface segments are depicted with dash lines), the local height H_j of the interface for the (i, j) cell is computed by the discrete version of the integral (3.6):

$$H_j = \frac{1}{\Delta x} \sum_{t=-t_{low}}^{t_{up}} \alpha_{i-t,j} \Delta y \Delta x \quad (3.13)$$

where t_{low} is the number of cells separating the (i, j) cell from the reference axis and t_{up} the number of cells separating (i, j) from the top of the block of cells considered. The columnwise sum of the volume fractions identifies the discrete height of the interface. In the Fig. 3.1, $t_{low} = t_{up} = 1$ and $H_j = 1.66\Delta y$. As well, the heights in the side columns can be computed by keeping the same reference axis, leading to $H_{j-1} = 1.15\Delta y$ and $H_{j+1} = 2.04\Delta y$.

By this local discrete field of the interface heights, first and second order derivatives in j can be evaluated through central finite-differences schemes, which are second order accurate with respect to the grid spacing:

$$H_{x:j} = \frac{H_{j+1} - H_{j-1}}{2\Delta x}, \quad H_{xx:j} = \frac{H_{j+1} + H_{j-1} - 2H_j}{(\Delta x)^2} \quad (3.14)$$

The computation of the curvature for the (i, j) cell of the Fig. 3.1 by use of the Eq. (3.8) leads to $\kappa_{i,j} = 200.9$, which is only 0.45% higher than the analytical value.

Generally speaking, the computation of the interface topology with the HF method involves the columnwise or row-wise sum of the volume fractions within a local block of cells whose extension is defined arbitrarily for each interface cell.

The algorithm implemented

For the example depicted in the Fig. 3.1, the HF algorithm is very simple and, once defined the direction of the integration, the expression (3.13) is sufficient to compute heights leading to a very accurate curvature. However, the interface topology when simulating two-phase flows may be much more complicated. For each interfacial cell, the HF algorithm has to be able to choose the best extension of the block of cells to consider for the computation, as well as to give a consistent calculation when more

than one interface cut the block. Moreover, the axisymmetrical case requires the computation of the interface elevation with respect to the revolution axis (see Eq. (3.10)).

The algorithm that we have implemented is a merge of the Malik *et al.* [36] and Hernandez *et al.* [99] versions, with the addition of a routine for the axisymmetrical curvature. The algorithm is written for a two-dimensional or axisymmetrical geometry, with constant grid spacings Δx and Δy .

The following steps describe the procedure to evaluate the curvature in a (i, j) interface cell. Note that, according to the CSF model, the surface tension force computed through the Eq. (1.39) acts in every cell whose volume fraction gradient is different from zero, even if the cell is not cut by the interface ($\alpha = 0, 1$) such that a curvature can not be defined. However, the introduction of a specific routine allows the algorithm to apply well for such cells as well. See Fig 3.3 for indexes reference.

1. Choice between heights and widths. An approximation of the interface is built by considering the volume fractions of a 3×3 block of cells surrounding the (i, j) cell. If the interface forms an angle below 45° with the horizontal direction, an horizontal interface is assumed and a block of cells extended on the vertical direction is considered to compute heights. Otherwise, widths are computed within an horizontally extended block of cells. To accomplish this, the following condition is checked:

$$\left| \sum_{r=-1}^{r=1} (\alpha_{i-1, j+r} - \alpha_{i+1, j+r}) \right| > \left| \sum_{r=-1}^{r=1} (\alpha_{i+r, j+1} - \alpha_{i+r, j-1}) \right|$$

true \rightarrow horizontal interface, vertical stencil.

false \rightarrow vertical interface, horizontal stencil.

The following algorithm will always refer to a vertical oriented stencil.

2. Choice of the stencil extension. The stencil extension has to be sufficient to capture the meaningful volume fraction variations. The stencil is always at least 3 cells width, in order to perform second order accurate derivatives. The number of rows t_{up} over the $i - th$ row is increased till the following two

conditions are being satisfied:

$$\text{sign}(n_y) \cdot \sum_{r=-1}^{r=1} (\alpha_{i-t_{up},j+r} - \alpha_{i-t_{up}+1,j+r}) > 0,$$

$$0 < \sum_{r=-1}^{r=1} \alpha_{i-t_{up},j+r} < 3$$

The preliminary norm vector components (n_x, n_y) are computed by the Youngs formulation given by Eqs. (3.3) and (3.4). A maximum of 3 rows is set. The number of rows t_{low} is chosen by a similar procedure. Figure 3.3(a) reports a sketch of the procedure step.

3. Correction of the local volume fraction field in order to have a monotonic variation along the height direction. This improvement is needed to prevent errors when more than one interface cut the stencil. The volume fractions of the cells located above the $i - th$ row are adjusted if the following condition is satisfied:

$$\text{sign}(n_y) \cdot (\alpha_{i-t,j+r} - \alpha_{i-t+1,j+r}) < 0, \quad t = 1, \dots, t_{up}, \quad r = -1, 0, 1$$

The volume fractions of the cells below the $i - th$ row are adjusted if the following condition is satisfied:

$$\text{sign}(n_y) \cdot (\alpha_{i-t,j+r} - \alpha_{i-t-1,j+r}) > 0, \quad t = -t_{low}, \dots, -1, \quad r = -1, 0, 1$$

For both cases the adjustment is:

$$\alpha_{i-t,j+r}^* = \frac{1}{2} \left(1 + \text{sign}(t) \cdot \text{sign}(n_y) \right)$$

Figure 3.3(b) reports a sketch of the procedure step. At the end of the whole procedure for the (i, j) cell the adjusted volume fractions are reset to their original values.

4. Evaluation of the discrete height function field H in the stencil:

$$H_{j+r} = \sum_{t=-t_{low}}^{t_{up}} \alpha_{i-t,j+r} \cdot \Delta y, \quad r = -1, 0, 1$$

5. Calculation of the offset $_{i,j}$. The height function in the central column H_j could not fall inside the considered cell, this is the case of the cell $(i-1, j)$ in the Fig. 3.3(a). This may happen when the interface cuts the considered cell just a little or not at all. Offset is the number of cells vertically far from (i, j) to the cell where H_j falls. It is evaluated as follows:

$$\text{offset}_{i,j} = \begin{cases} t_{up} - \text{floor}\left(\frac{H_j}{\Delta y}\right) & \text{if } \text{sign}(n_y) > 0 \\ \text{floor}\left(\frac{H_j}{\Delta y}\right) - t_{low} & \text{if } \text{sign}(n_y) < 0 \end{cases}$$

where $\text{floor}()$ stands for the largest previous integer of the number between parenthesis. If $\text{offset}_{i,j} \neq 0$ the curvature of the (i, j) cell is taken equal to the neighbor cell pointed by the offset:

$$\kappa_{i,j} = \kappa_{i-\text{offset},j}$$

Otherwise it is calculated as shown in the next steps.

6. Only for an axisymmetrical geometry, the elevation of the interface with respect to the revolution axis has to be computed ($f(x)$ in Eq. (3.10)). An approximation of the interface line within the cell is built estimating its orientation as inverse of the volume fraction gradient and positioning the segment by means of the Cube Chopping algorithm reported in [100]. The two intersections of the interface segment with the cell sides are computed and then the elevation of the midpoint of the segment is evaluated through geometrical relationships.
7. First and second order derivatives of the local height function field are computed by the schemes reported in Eqs. (3.14) and the curvature is computed according to the two-dimensional (3.8) or axisymmetrical (3.10) expression.

Discussion

The listed procedure allows the evaluation of interface norm vectors which converge with the first order of the mesh element size and second order converging curvatures,

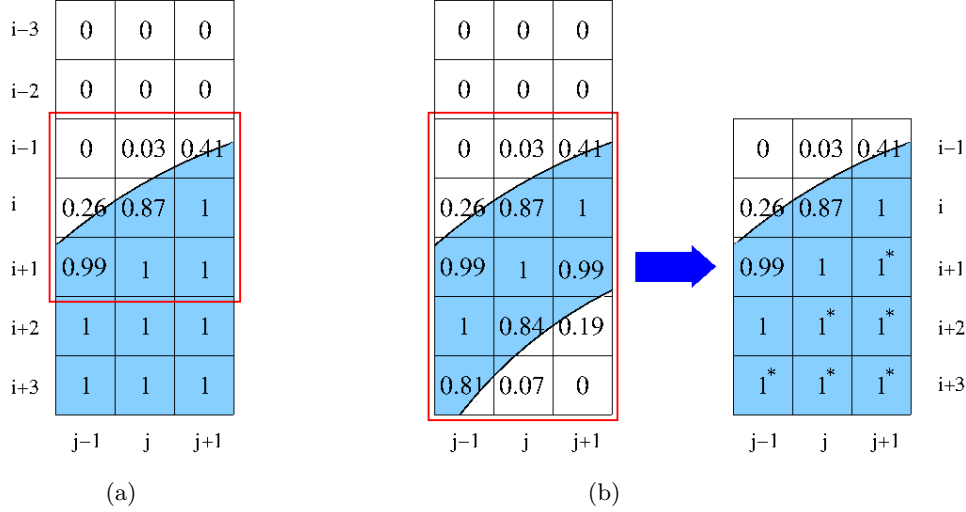


Figure 3.3: Examples of HF algorithm steps. (a) Step 2: the stencil extension for the (i, j) cell calculation is chosen to be 1 row above the i -th ($t_{up} = 1$) and 1 under the i -th row ($t_{low} = 1$), the considered stencil has red colored boundaries. (b) Step 3: within the stencil chosen at step 2, colored in red, the volume fractions of the marked cells are corrected to cancel the presence of a second interface within the stencil. Note that in (a) and (b) the algorithm leads to the same height function values within the stencil, thus to the same curvature for the (i, j) cell, as it actually is. According to the step 5, the curvature in the cell $(i - 1, j)$ is not computed because the cell is marked with an $offset \neq 0$. The curvature of the cell $(i - 1, j)$ will be set equal to the cell below, where the height function of the central column actually falls.

as will be proved in the validation Section 5.1. The algorithm can be easily parallelized providing enough boundary cells to each computing node, since through the MPI protocol each node stores only a partition of the entire computational domain.

The computed curvature refers to the cell centroid curvature. Face-centered curvatures can be obtained by interpolation of cell-centered values [48, 101], but the approach used in the numerical code to solve the momentum equation involves only cell-centered values of the curvature.

The application of the HF algorithm is limited to orthogonal grids due to the heights or widths computation. The version implemented is restricted to constant

grid spacings, Francois and Swartz [102] extended it to not constant grid spacings. The HF algorithm becomes inadequate when the interface local radius is of the order of the grid spacing, Bornia *et al.* [103] showed that with appropriate modifications this limit can be crossed. The HF algorithm is as much accurate as the interface is more aligned with the background grid, while it gets worse for 45° oriented interfaces. Lopez *et al.* [104] proposed a procedure based on the smoothing of the derivatives of H to improve the calculation in the mentioned case.

3.2 The evaporation model

The task of the evaporation model is to compute accurate local mass and energy source terms at the interface as effect of the evaporation, depending on the local temperature field.

The foundation of the evaporation model is the interfacial condition assigned to the temperature. A custom approach is to assume thermodynamic equilibrium at the interface. However, such approximation could be untrue in microscale boiling flows, as a consequence a physical relationship accounting for the relevant additional microscale effects at the interface needs to be applied.

Furthermore, the chosen physical model has to be implemented within the numerical code. High evaporation rates could lead to numerical instabilities depending on the numerical algorithms used, therefore it is necessary to provide a stable implementation.

3.2.1 The interface temperature condition

Most of the evaporation models employed to simulate boiling flows assume thermodynamic equilibrium at the interface, with both the liquid and the vapor phases at the same temperature $T_l = T_v$, equal to the interface temperature T_{if} . By assuming thermodynamic equilibrium for each phase, liquid and vapor temperature correspond to the saturation temperature at the system ambient pressure p_∞ , it follows the interface temperature condition:

$$T_{if} = T_{sat}(p_\infty) \quad (3.15)$$

which imposes a continuous variation of the temperature field at the interface. Esmaeeli and Tryggvason [105] used the condition (3.15) to derive the following expres-

sion for the interphase mass flux \dot{m} from the energy jump condition (1.14):

$$\dot{m} = \frac{1}{h_{lv}} (\mathbf{q}_l - \mathbf{q}_v) \cdot \mathbf{n} = \frac{(\lambda_l + \lambda_v)}{h_{lv}} \nabla T \cdot \mathbf{n} \quad (3.16)$$

where λ is the thermal conductivity.

The Eq. (3.15) is an adequate assumption for many macroscale boiling problems, but in the microscale a significant deviation from thermodynamic equilibrium at the interface may exist. For instance, liquid and vapor pressures at the interface could not coincide when the laplacian jump in the pressure across the interface $\Delta p = \sigma \kappa$ is considerable. In this case, liquid and vapor temperatures computed referring to the respective saturation conditions are different and the (3.15) is not anymore valid. By considerations on small length scales, Tanasawa [109] argued that without an interface jump in temperature a net flux of molecules across the interface can not exist. Hardt and Wondra [7] showed that as a vapor-liquid interface approaches a heated wall, under a certain value of the distance the deviation of the interfacial temperature from the saturation condition can no longer be neglected. The mentioned reasons suggest to seek for a more general relationship than the condition (3.15) at the interface, when dealing with microscale boiling phenomena.

Schrage [106] assumed thermodynamic equilibrium within each phase but he supposed an interfacial jump in the temperature to exist, such that $T_{sat}(p_l) = T_l \neq T_v = T_{sat}(p_v)$. Schrage applied the kinetic theory of gases to express the net flux of molecules crossing the interface due to the phase change, as a function of the temperature and pressure jumps. When phase change occurs, a fraction σ of the molecules that from the bulk phase strike the interface crosses the interface and evaporates/condensates, while the fraction $1 - \sigma$ is reflected. The evaporation and condensation fractions σ_e and σ_c are often considered equal and referred to as *accommodation coefficient*. The net mass flux across the interface \dot{m} is given by the difference on the liquid-to-vapor and vapor-to-liquid mass fluxes and according to [95] takes the following expression:

$$\dot{m} = \frac{2\sigma}{2 - \sigma} \left(\frac{M}{2\pi R} \right)^{1/2} \left(\frac{p_v}{\sqrt{T_v}} - \frac{p_l}{\sqrt{T_l}} \right) \quad (3.17)$$

where M is the molecular weight and $R = 8.314 \text{ J}/(\text{mol}\cdot\text{K})$ is the universal gas constant, p_v and T_v are the vapor pressure and temperature at the interface, p_l and T_l

are the liquid pressure and temperature at the interface.

The accommodation coefficient σ is difficult to be measured experimentally and it is known only for a few liquids, with a large degree of uncertainty. As example, Marek and Straub [107] analyzed the published data for water and reported values in the range $[10^{-3}, 1]$. Wang *et al.* [108] showed that non polar-liquids have an experimentally determined accommodation coefficient of unity. In the simulations performed in this thesis, the accommodation coefficient was always set to one, this decision is justified in the validation Section 5.4.

Tanasawa [109] derived the Eq. (3.17) for vapor condensation on a liquid film. He referred to the vapor-liquid interface as the “liquid interface”, thus pressure and temperature of the liquid at the interface within the (3.17) are considered as interfacial temperature T_{if} and pressure p_{if} . The vapor pressure at the interface is assumed to be equal to the system ambient pressure p_∞ and the vapor temperature at the interface is set equal to the saturation temperature $T_v = T_{sat}(p_v) = T_{sat}(p_\infty)$. Tanasawa assumed that for small interface temperature jumps, such that $(T_v - T_{if}) \ll T_v$, the interphase mass flux depends linearly on the temperature jump:

$$\dot{m} = \frac{2\sigma}{2 - \sigma} \left(\frac{M}{2\pi R} \right)^{1/2} \frac{\rho_v h_{lv}}{T_v^{3/2}} (T_{if} - T_v) \quad (3.18)$$

where $T_v = T_{sat}(p_\infty)$. Thus, in the Tanasawa model, the interfacial mass flux is proportional to the interface superheating over the local vapor saturation condition. The Equation (3.18) leads to the following interface temperature condition:

$$T_{if} - T_{sat}(p_\infty) = \frac{\dot{m}}{\phi} \quad (3.19)$$

where ϕ is the so-called kinetic mobility and $1/\phi$ can be meant as the interfacial resistance to mass transfer.

Juric and Tryggvason derived in [20] an interface temperature condition more complete than the Eq. (3.19), by considering other terms in addition to the interfacial resistance to the heat transfer. They started from the interface jump on the Gibbs function and, by means of thermodynamical considerations, they obtained the

following interface temperature condition:

$$T_{if} - T_{sat} = \frac{T_{sat}}{h_{lv}} \left(\frac{1}{\rho_v} - \frac{1}{\rho_l} \right) (p_{if} - p_\infty) + \frac{c_{p,l} - c_{p,v}}{h_{lv}} (T_{if} - T_{sat})^2 + \frac{\sigma T_{sat} \kappa}{2h_{lv}} \left(\frac{1}{\rho_v} + \frac{1}{\rho_l} \right) - \frac{1}{2} \frac{T_{sat}}{h_{lv}} \left(\frac{1}{\rho_v} - \frac{1}{\rho_l} \right) [((\boldsymbol{\tau}_v + \boldsymbol{\tau}_l) \cdot \mathbf{n}) \cdot \mathbf{n}] + \frac{\dot{m}}{\phi} \quad (3.20)$$

where $T_{sat} = T_{sat}(p_\infty)$. The first and second terms at the RHS refer to the Gibbs function jump for a flat and static interface; the third term accounts for the effects of the curved interface; the fourth term is related to the shear stress at the interface and the fifth comes from the modeling of the irreversible production of entropy at the interface as a function of the kinetic mobility.

Note that if all the terms at the RHS are negligible, the condition (3.20) reduces to the (3.15), while if only the last term is not negligible it reduces to the (3.19).

The importance of each term within Eq. (3.20) depends on the case studied, in particular on the spatial scale. Juric and Tryggvason performed a scaling analysis and observed that the term related to the shear stress is negligible compared to the others.

We repeated their analysis by considering conditions representative of the cases simulated in this thesis: $q = 20 \text{ kW/m}^2$, $D = 0.5 \text{ mm}$, R113, R134a, R245fa and water as working fluids, $T_{sat} = 31 \text{ }^\circ\text{C}$ for the refrigerants and $T_{sat} = 100 \text{ }^\circ\text{C}$ for the water. The fifth term is estimated by considering $\dot{m} = 1$ and $\sigma = 1$ within ϕ . The results are reported in the Tab. 3.1 in terms of interfacial superheating occurring for each operating fluid tested, given by the (3.20), and in terms of the percentage contribution of each term of the (3.20) to the total interface superheating. For all

Fluid	p_∞ [bar]	$T_{if} - T_{sat}$ [$^\circ\text{C}$]	I [%]	II [%]	III [%]	V [%]
R113	0.56	0.1032	15.1	$2.2 \cdot 10^{-2}$	15.2	69.7
R134a	7.93	0.0106	6.1	$2.3 \cdot 10^{-3}$	6.5	87.4
R245fa	1.85	0.036	11.3	$8.2 \cdot 10^{-3}$	11.5	77.1
Water	1	0.2306	17.5	$2.2 \cdot 10^{-2}$	17.5	64.9

Table 3.1: Relative magnitude of the terms at the RHS of Eq. (3.20), as a percentage of the $T_{if} - T_{sat}$ computed by the (3.20) and reported in the third column. The magnitude of the fourth term is always negligible and it is not reported.

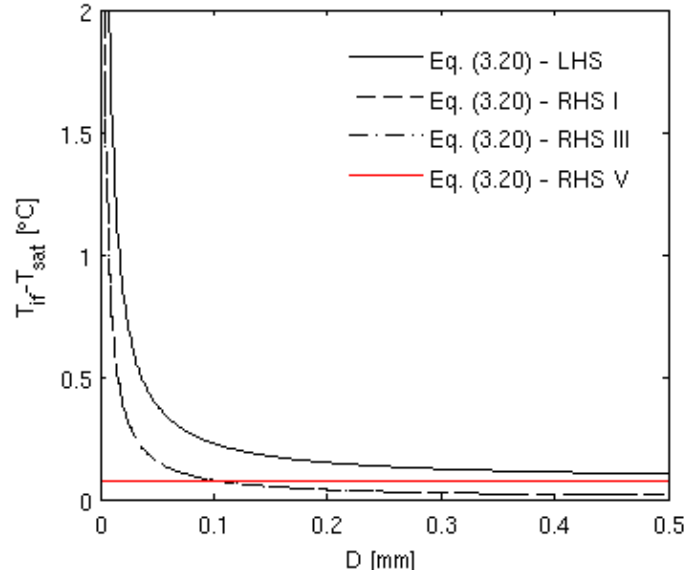


Figure 3.4: Contribution to the interfacial superheating given by the first, third and fifth terms of the Eq. (3.20), depending on the length scale. The second and fourth terms give a negligible contribution thus they are not reported. The fluid considered is R113 at $p_\infty = 0.56$ bar.

the fluids considered the interfacial resistance to mass transfer gives the dominant contribution to the interface superheating. The magnitude of the superheating is of the order of tenths of degree. However, the importance of the interfacial resistance depends on the chosen reference $\dot{m} = 1$, which is only an average estimation of its real value that, locally, can strongly exceed the unity.

The Figure 3.4 shows that the relative importance of the terms within the (3.20) changes considerably by decreasing the length scale below the 0.5 mm adopted in our simulations. For diameters below 0.1 mm the interface superheating becomes remarkable and other effects rather than the interfacial resistance, which remains constant, have to be considered. The second and fourth terms at the RHS of the (3.20) are always negligible and they are not shown in Figure 3.4.

The interfacial temperature condition implemented in this thesis neglects all the terms at the RHS of the Eq. (3.20) with the exception of the last, such that the

Tanasawa Eq. (3.18) is used to compute the interphase mass transfer. The validity of such assumption is proved in the validation Section 5.4.

3.2.2 The numerical model

A numerical method for the implementation of the mass and energy source terms related to the evaporation was proposed by Hardt and Wondra [7] and it is discussed in this Subsection.

According to the VOF formulation of the delta function (1.37), the evaporation mass source term S_ρ at the RHS of the mass conservation equation (1.15) can be expressed as:

$$S_\rho = \dot{m}|\nabla\alpha| \quad (3.21)$$

where $|\nabla\alpha|$ is expressed by the Eq. (3.2) and discretized through the Eqs. (3.3) and (3.4).

Note that the source term has to be expressed as mass per unit time and volume. Actually, by means of the VOF algorithm the mass conservation equation is replaced by the volume fraction conservation equation as discussed at the end of the Subsection 1.2.2. The volume fraction source term to be introduced at the RHS of Eq. (1.38) can be expressed as S_ρ/ρ .

By expressing the mass flux \dot{m} through the Tanasawa Eq. (3.18), the mass source term takes the following form:

$$S_\rho = \phi(T_{if} - T_{sat}(p_\infty))|\nabla\alpha| \quad (3.22)$$

The equality $p_v = p_\infty$ used to express the mass flux in Eq. (3.22), valid in Tanasawa analysis of liquid films within an infinitely extended vapor phase, can not be assumed a priori if vapor bubbles within liquid are considered. In this case, $p_v = p_\infty + \Delta p_{if}$ where p_∞ refers to liquid system ambient pressure and Δp_{if} is the laplacian pressure jump at the interface. However, the operating conditions simulated in this thesis involve small laplacian pressure jumps across the interface. As example, R113 vapor bubbles at $T_{sat} = 31$ °C, approaching the channel size of 0.5 mm (typical test conditions of our simulations), give a pressure jump across the interface of 132 Pa, which in turn generates a rise on the saturation temperature of the vapor of 0.06 K. Therefore, due to the negligible effect of the laplacian pressure jump on the saturation temperature of the flow, we assumed $p_v \simeq p_\infty$ and $T_v \simeq T_{sat}(p_\infty)$ as Tanasawa

did, and the expression (3.19) for the mass transfer is considered correct for our case as well.

The mass source term expressed in Eq. (3.22) is defined over the whole computational domain and it is non-zero only in a finite thickness region across the interface, where $|\nabla\alpha| \neq 0$. The local interface temperature T_{if} is given by the temperature field, the saturation temperature at the system ambient pressure is constant throughout the domain. The kinetic mobility ϕ is constant as well and it is computed as:

$$\phi = \frac{2\sigma}{2 - \sigma} \left(\frac{M}{2\pi R} \right)^{1/2} \frac{\rho_v h_{lv}}{T_{sat}^{3/2}(p_\infty)} \quad (3.23)$$

The mass source term could be implemented as expressed in (3.22). Hardt and Wondra [7] suggested that, since the evaporation takes place on the liquid side of the interface, the mass source term should reflect this phenomenon. Thus, S_ρ is first multiplied by the liquid volume fraction α_l , which is zero on the vapor side, and then multiplied by a normalization factor N to ensure the global actual evaporation rate, such that:

$$S_\rho = N \alpha_l \dot{m} |\nabla\alpha| \quad (3.24)$$

and the normalization factor is:

$$N = \frac{\int_\Omega |\nabla\alpha| d\Omega}{\int_\Omega \alpha_l |\nabla\alpha| d\Omega} \quad (3.25)$$

where Ω is the computational domain. The liquid volume fraction α_l is the updated volume fraction given by the solution of the volume fraction equation (1.38) if the liquid is the primary phase, otherwise α corresponds to the vapor volume fraction and $\alpha_l = 1 - \alpha$. The norm of the volume fraction gradient is independent of the reference phase chosen. The discrete version of the integral (3.25) is a sum over all the computational cells.

In principle, by referring to the RHS of the Eq. (3.24) as the original evaporation rate φ_0 , the mass source term could be implemented as $S_\rho = \varphi_0$ in the vapor side and $S_\rho = -\varphi_0$ in the liquid side. However, such a localized source term, concentrated just on interface cells, is proved to lead to numerical instabilities, due to very high evaporation rates concentrated in only a few cells.

Hardt and Wondra suggested to derive a smeared version φ of the original evaporation rate field φ_0 by solving, at each time step, a steady diffusion equation in which φ_0 represents the known term:

$$D\nabla^2\varphi = \varphi - \varphi_0 \quad (3.26)$$

together with the following Neumann condition at the domain boundary:

$$\mathbf{n} \cdot \nabla\varphi|_{\partial\Omega} = 0 \quad (3.27)$$

which ensures that the integrals over the whole domain of φ and φ_0 give the same result.

The diffusion constant D acts as a smoothing parameter to diffuse the evaporation rate at both sides of the interface. The larger is D , the smoother is φ thus preventing numerical instabilities. Nevertheless, Hardt and Wondra warned that for curved interfaces the larger is D , the more asymmetric is the smoothing of φ_0 at the interface sides, violating the local mass conservation. This error is proportional to the local curvature of the interface and it is zero where the interface is flat.

The smoothed scalar field φ , representing the evaporation rate, is thus used to express the mass source term, concentrating vapor creation on the vapor side and liquid disappearance in the liquid side, as follows:

$$S_\rho = N_v\alpha_v\varphi - N_l\alpha_l\varphi \quad (3.28)$$

The normalization factors N_v and N_l ensure that all the mass disappeared on the liquid side reappears on the vapor side and they are determined as follows:

$$N_v = \int_{\Omega} \varphi d\Omega / \int_{\Omega} \alpha_v \varphi d\Omega \quad (3.29)$$

$$N_l = \int_{\Omega} \varphi d\Omega / \int_{\Omega} \alpha_l \varphi d\Omega \quad (3.30)$$

The Figure 3.5 reports a snapshot of the fields of φ_0 , its smoothed version φ and the first and second terms at the RHS of the Eq. (3.28), across the interface of the evaporating bubble simulated as a benchmark for the evaporation model and

discussed in the Section 5.4. The initial source term φ_0 is concentrated only on superheated liquid side cells whose volume fraction gradient is non-zero (see Fig. 3.5(a)). Due to the chosen value of the diffusion constant, the smeared scalar field φ is non-zero in about 20 cells across the interface (see Fig. 3.5(b)). The vapor creation

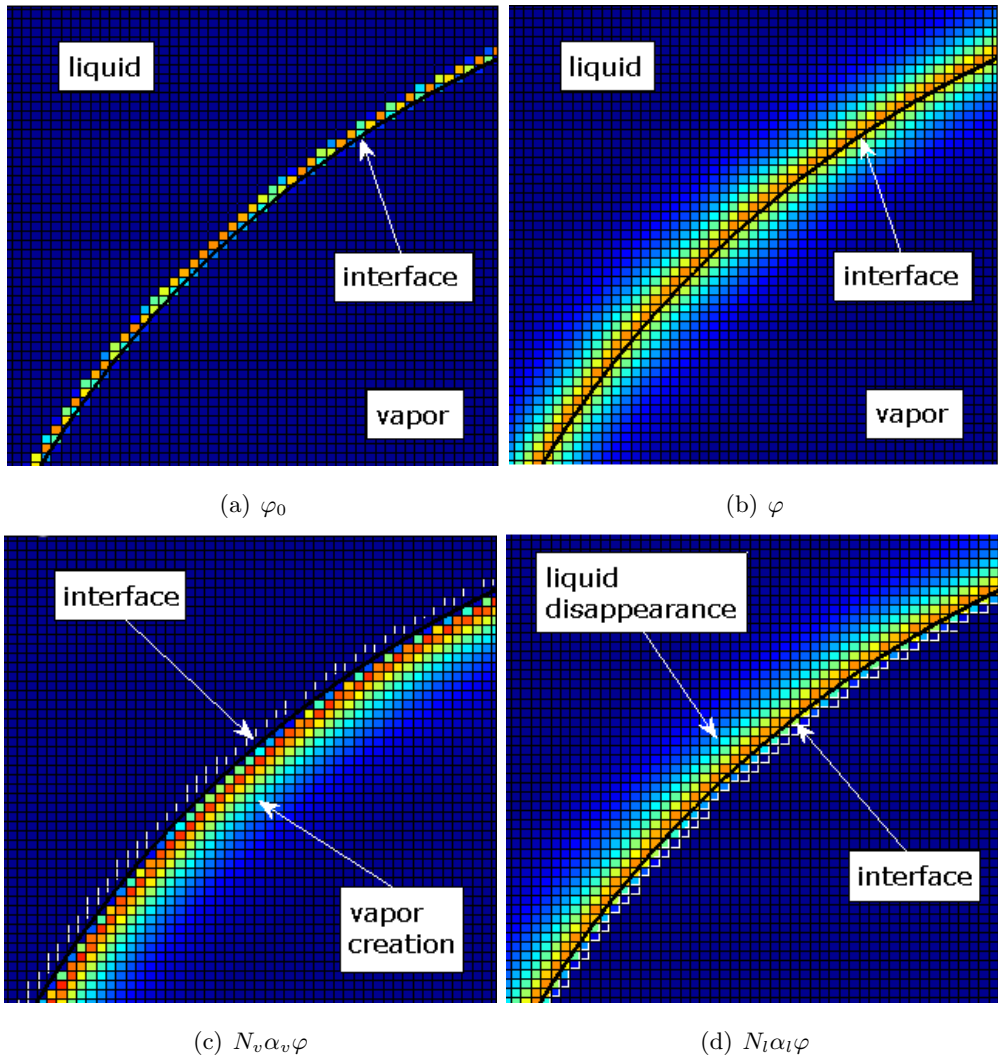


Figure 3.5: The subfigures are obtained through the simulation of a vapor bubble growing in superheated liquid, benchmark discussed in Section 5.4. (a) is the original evaporation rate field, (b) is the smeared version, (c) is vapor creation and (d) liquid disappearance.

is actually located in the vapor side (Fig. 3.5(c)) and the liquid disappearance in the liquid side (Fig. 3.5(d)).

The expression (3.28) represents the actual mass source term implemented in the numerical code.

The evaporation energy source term S_E at the RHS of the energy Eq. (1.17) can be expressed, by means of the (1.37), as:

$$S_E = -\dot{q}|\nabla\alpha| = -h_{lv}\dot{m}|\nabla\alpha| \quad (3.31)$$

where the interphase mass flux \dot{m} is computed by the (3.18) as done for the mass source term. However, in order to have energy sink only in the liquid side, where evaporation actually occurs, the energy source term (3.31) is modified as follows:

$$S_E = -h_{lv}\varphi_0 \quad (3.32)$$

which was proved to be numerically stable, without the need for smoothing.

Note that the energy source term has to be expressed as an energy per unit time and volume. The energy source term (3.32) is not yet complete, because it needs to account for the enthalpy related to the vapor created and the liquid disappeared, otherwise a non-physical local heating of the liquid and cooling of the vapor would happen. By calling $h_{ref,l}$ the specific enthalpy of the liquid and $h_{ref,v}$ the specific enthalpy of the vapor both at the reference temperature T_{ref} , the complete energy source term takes the following form:

$$S_E = -h_{lv}\varphi_0 + N_v\alpha_v\varphi[h_{ref,v} + c_{p,v}(T - T_{ref})] - N_l\alpha_l\varphi[h_{ref,l} + c_{p,l}(T - T_{ref})] \quad (3.33)$$

The expression (3.33) represents the actual energy source term implemented in the numerical code.

The complete evaporation model is constituted by the mass source term (3.28) and the energy source term (3.33). Hardt and Wondra demonstrated in [7] that such model leads to the correct evaporation rate through some numerical validation cases, for which analytical solution can be obtained. They performed test cases on Ansys Fluent and found good agreement with the analytical solutions.

Chapter 4

Ansys Fluent solver and the implementation of the UDF

Ansys Fluent is a numerical solver of the partial differential equations governing thermal-fluid-dynamics problems. The versions 6.3 and 12 were used to carry out the simulations for this thesis. The double precision version of the solver was employed to minimize the truncation errors.

Fluent itself contains a VOF-PLIC algorithm [38] for the simulation of multiphase flows. The only algorithm implemented for the interface curvature computation is based on the Youngs formulation discussed within the Section 3.1. Models for the computation of mass and energy exchange related to evaporation are not present.

Fluent allows the partial modification of the numerical code by means of the so-called *User-Defined Functions* (UDF), external functions that the user can write in C or C++ language and implement into the code. The UDF are a very powerful tool to modify the basic numerical code and to optimize it for the desired scope. Within this context, the physical and numerical models discussed in the previous Chapter have been implemented in the solver by means of UDF, to optimize the simulation of two-phase evaporating flows.

The objective of this Chapter is to give an overview of the Fluent solver, of the algorithms and the set-ups chosen to simulate the flows object of this thesis, and of the UDF implementation for the interfacial effects. Additional information about the solver can be found in the Fluent User's and UDF guides [110, 111].

This Chapter is organized as follows: first of all the equations set governing the multiphase flow is defined; then, the Fluent discretization procedure for the generic flow equation is outlined; subsequently, the numerical treatment of each flow equation is discussed separately, together with the specific algorithms and the boundary conditions; the implementation of the Height Function and evaporation algorithms by means of the UDF is explained in detail; finally, an overview of the Fluent solution procedure is given.

4.1 The flow equation set

The solution of the multiphase flow problem in an axisymmetrical domain requires the solution of a system of 6 coupled non-linear partial differential scalar equations: the continuity equation (1.21), the volume fraction equation (1.38), the momentum equation (1.16) in the axial and radial directions, the energy equation (1.17); the Eq. (3.26) to be solved to obtain the evaporation rate smoothed field, is intended as a conservation equation for the evaporation rate φ without transient and convective terms. In the following, the mentioned equations are reported by separating at the RHS the source terms discussed in the previous Chapter:

$$\nabla \cdot \mathbf{u} = 0 \quad (4.1)$$

$$\frac{\partial \alpha}{\partial t} + \frac{1}{\Omega} \int_S I(\mathbf{x}) \mathbf{u} \cdot \mathbf{n} dS = S_\alpha \quad (4.2)$$

$$\frac{\partial(\rho \mathbf{u})}{\partial t} + \nabla \cdot (\rho \mathbf{u} \mathbf{u}) + \nabla p - \nabla \cdot \mu \left[(\nabla \mathbf{u}) + (\nabla \mathbf{u})^T \right] - \rho \mathbf{g} = S_m \quad (4.3)$$

$$\frac{\partial(\rho c_p T)}{\partial t} + \nabla \cdot (\rho c_p \mathbf{u} T) - \nabla \cdot (\lambda \nabla T) = S_E \quad (4.4)$$

$$D \nabla^2 \varphi = S_\varphi \quad (4.5)$$

The viscous heating term in the energy equation has been neglected. Following the dimensional analysis proposed by Morini [112], we estimated the contribution of the viscous heating on the bulk temperature for a single phase flow under operating conditions typical for this thesis. We found such contribution to be of the order of 10^{-4} compared with the rise in temperature generated by the wall heat flux, therefore viscous heating was not included within Eq. (4.4).

The source terms of volume fraction S_α , momentum S_m , energy S_E and evaporation rate equation S_φ , developed in the previous chapters, are expressed as follows:

$$S_\alpha = \frac{N_v \alpha_v \varphi - N_l \alpha_l \varphi}{\rho} \quad (4.6)$$

$$S_m = \frac{\rho}{\langle \rho \rangle} \sigma \kappa \nabla \alpha \quad (4.7)$$

$$S_E = -h_{lv} \varphi_0 + N_v \alpha_v \varphi [h_{ref,v} + c_{p,v}(T - T_{ref})] - \\ - N_l \alpha_l \varphi [h_{ref,l} + c_{p,l}(T - T_{ref})] \quad (4.8)$$

$$S_\varphi = \varphi - \varphi_0 \quad (4.9)$$

where $\alpha_v \equiv \alpha$ and $\alpha_l = 1 - \alpha$ if the vapor phase is the reference one, *vice versa* if the liquid phase is the reference.

The system of the flow equations with appropriate boundary conditions is solved for the 6 independent unknowns α , p , u_x , u_y , T (or the energy E) and φ .

4.2 Fluent discretization procedure

Fluent employs a finite-volume formulation of the transport equations to transform the continuous non-linear partial differential equations in discrete linear algebraic equations, that can be solved numerically. The transport equation for a generic variable ϕ [110]:

$$\frac{\partial(\rho\phi)}{\partial t} + \nabla \cdot (\rho\phi\mathbf{u}) = \nabla \cdot (\Gamma\nabla\phi) + S_\phi \quad (4.10)$$

is integrated within a control volume of volume V and bounding area A :

$$\int_V \frac{\partial(\rho\phi)}{\partial t} dV + \int_A \rho\phi\mathbf{u} \cdot \mathbf{n} dA = \int_A \Gamma\nabla\phi \cdot \mathbf{n} dA + \int_V S_\phi dV \quad (4.11)$$

where the divergence theorem has been invoked to convert the volume integral of the divergence of a vectorial field into the surface integral of the scalar product between the vectorial field and the outgoing unit normal \mathbf{n} to the cell boundary. By assuming that the value of the integrand function at the center of the cell is equal to the average of the function within the cell, the volume integrals within the (4.11) can be approximated by multiplying the value of the integrand function at the cell center by the volume of the cell. As well, by assuming that the value of the integrand

function at the center of the cell face is equal to the average of the function on the cell face, the surface integrals within the (4.11) can be approximated with a midpoint rule by multiplying the value of the integrand function at each cell face center by the area A_f of the respective face. It follows:

$$\underbrace{\frac{\partial(\rho\phi)}{\partial t}V}_{\text{unsteady term}} + \underbrace{\sum_f^{N_f} \rho_f \phi_f \mathbf{u}_f \cdot \mathbf{n}_f A_f}_{\text{convective term}} = \underbrace{\sum_f^{N_f} \Gamma_f (\nabla\phi)_f \cdot \mathbf{n}_f A_f}_{\text{diffusive term}} + \underbrace{S_\phi V}_{\text{source term}} \quad (4.12)$$

where the subscript f identifies face centered values while the variables without the subscript f refer to cell centered variables. The sum is intended about the N_f cell faces of the control volume, as example with reference to the Fig. 4.1 the cell 0 has $N_f = 3$ and the cell 1 has $N_f = 4$.

Fluent employs a collocated technique with which the algebraic equations are solved for cell centered variables, thus interpolation schemes are required to express the face centered variables appearing in the (4.12) as function of the cell centered values. Furthermore, it is necessary to provide a scheme for the spatial discretization of the gradients. The unsteady term has to be somehow discretized with respect to the time.

These issues are discussed in the following subsections.

4.2.1 Temporal discretization

By grouping together as $F(\phi)$ all the terms appearing in the (4.12) but the unsteady term, the first order explicit and implicit time discretizations can be expressed as follows:

$$\text{explicit} \quad \frac{\phi^{n+1} - \phi^n}{\Delta t} = F(\phi^n) \quad (4.13)$$

$$\text{implicit} \quad \frac{\phi^{n+1} - \phi^n}{\Delta t} = F(\phi^{n+1}) \quad (4.14)$$

where Δt is the time step of the time discretization. The temporal update of the flow equations in both the implicit and explicit cases can be obtained by a time-marching procedure, since the equations are parabolic in the time variable.

The explicit time discretization is subject to a limit for what concerns the time step, to avoid numerical instabilities. The implicit formulation is unconditionally stable with respect to the time step, but requires an iterative procedure to solve

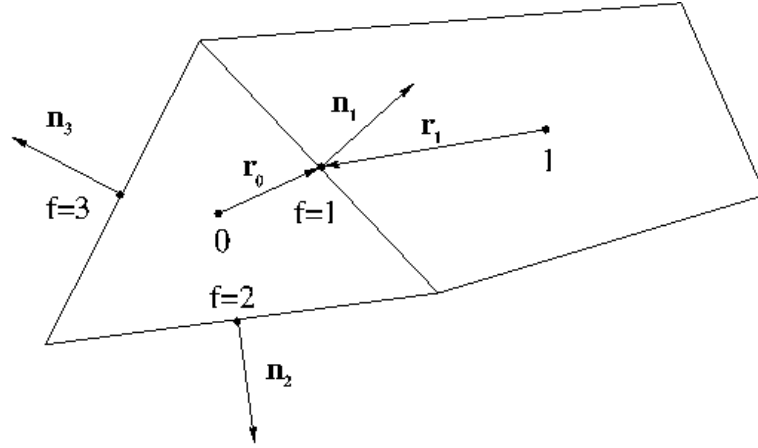


Figure 4.1: Example of a control volume used to discretize a generic transport equation. Figure adapted from [110].

the non-linear or coupled equations at each time step, until a converged solution is obtained.

The implicit time discretization is the only choice possible in Fluent for the momentum, energy and additional scalar equations when dealing with incompressible flows, a first order time discretization is chosen. Fixed or variable time steps are set depending on the test case being solved. The volume fraction equation is always solved with an explicit formulation which is discussed in the Section 4.3.

4.2.2 Spatial discretization

The choice of the spatial discretization technique provides the scheme for the interpolation of the cell centered variables on the cell face centers. Fluent offers several schemes to interpolate the face center variable ϕ_f appearing in the convective term of the (4.12). Here it is discussed only the chosen scheme, which is the more accurate available: the *Monotonic Upstream-centered Scheme for Conservation Laws* (MUSCL) developed by van Leer [113]. It is a blending of a central finite difference (CD) scheme and a second order upwind (SOU) scheme:

$$\phi_f = \theta\phi_{f,CD} + (1 - \theta)\phi_{f,SOU} \quad (4.15)$$

where θ is a blending coefficient. The face centered value given by the central difference scheme is:

$$\phi_{f,CD} = \frac{1}{2}(\phi_0 + \phi_1) + \frac{1}{2}[(\nabla\phi)_0 \cdot \mathbf{r}_0 + (\nabla\phi)_1 \cdot \mathbf{r}_1] \quad (4.16)$$

where the subscripts 0 and 1 refer to the cells that share the face f , $\nabla\phi$ is an appropriate discretization of the cell centered gradient (discussed in the next Subsection) and \mathbf{r} is the vector directed from the cell centroid to the face centroid, see Fig. 4.1. The face centered value given by the second order upstream scheme is:

$$\phi_{f,SOU} = \phi + \nabla\phi \cdot \mathbf{r} \quad (4.17)$$

where all the entities refer to the upstream cell.

The gradient evaluated at the cell face center $(\nabla\phi)_f$ appearing in the diffusive term of the (4.12) is always discretized with a central finite difference scheme:

$$(\nabla\phi)_f = \frac{1}{2}[(\nabla\phi)_0 + (\nabla\phi)_1] \quad (4.18)$$

4.2.3 Reconstruction of the cell centered gradients

Fluent uses the Green-Gauss theorem to compute the cell centered gradient of the scalar ϕ as face-area-weighted average of the cell face centered values:

$$\nabla\phi = \frac{1}{V} \sum_f^{N_f} \bar{\phi}_f \mathbf{n}_f A_f \quad (4.19)$$

Fluent computes the face value $\bar{\phi}_f$ according to the chosen scheme:

Green-Gauss cell based

The face value is taken from the arithmetic average of the values at the neighboring cell centers:

$$\bar{\phi}_f = \frac{\phi_0 + \phi_1}{2} \quad (4.20)$$

For quadrilateral meshes, it is equivalent to compute the cell center gradient using a 5 cells stencil.

Green-Gauss node based

The face value is taken from the arithmetic average of the nodal values on the face:

$$\bar{\phi}_f = \frac{1}{N_n} \sum_n^{N_n} \bar{\phi}_n \quad (4.21)$$

where N_n is the number of nodes of the face f . The nodal value $\bar{\phi}_n$ is constructed from the weighted average of the cell-centered values of the cells surrounding the node n :

$$\bar{\phi}_n = \frac{\sum_c^{N_c} w_c \phi_c}{\sum_c^{N_c} w_c} \quad (4.22)$$

where N_c is the number of cells surrounding the node n . ϕ_c are the cell centered values of the cells surrounding the node n . The weight coefficients w_c are a function of the distance of the cell centroid x_c from the node point x_n , derived as suggested by Rauch *et al.* [114].

For a quadrilateral mesh, the node based formulation corresponds to the computation of the cell center gradient using a 9 cells stencil. For quadrilateral meshes with constant grid spacings along the horizontal and vertical directions, the scheme is analogous to the Youngs discretization scheme of the volume fraction gradient expressed with the Eqs. (3.3) and (3.4).

In Fluent, the volume fraction gradient appearing in the surface tension term is reconstructed according to the gradient reconstruction scheme chosen. The choice of the Green-Gauss node based scheme, thus leading to the Youngs formulation, helps to enforce the balance among pressure and surface tension terms within the momentum equation, thus minimizing the magnitude of the spurious currents. To assess this issue, an inviscid static droplet simulation with unity density ratio was performed. The test case will be better illustrated in the Section 5.2, here it is only anticipated that the exact solution of the flow is a null velocity field, due to the absence of external forces. Thus, the magnitude of appearing numerical velocity gives an estimation of the error generated by the numerical algorithm used. A comparison between the node based formulation and the cell based one was carried out by adopting identical simulation set-ups with except of the gradient reconstruction scheme. In order to cancel the effect of the errors in the numerical computation of the interface curvature, an exact constant curvature was set within the Eq. (1.39). The

Gradient reconstruction	$ \mathbf{u}_{max} $ [m/s]
cell based	$5.8 \cdot 10^{-2}$
node based	$2.5 \cdot 10^{-16}$

Table 4.1: Comparison of the Green-Gauss cell based and node based schemes for the reconstruction of cell centered gradients. The magnitude of the maximum velocity in the domain after one time step is reported. The simulation set-up is discussed in the Section 5.2.

Table 4.1 reports the maximum magnitude of the velocity after one simulation time step ($\Delta t = 5 \cdot 10^{-7}$ s). The node based formulation gives a maximum velocity of the order of the machine accuracy, while the cell based one shows a magnitude several orders higher, thus proving the better consistency of the node based formulation.

4.2.4 The final algebraic equation

Through the discretization algorithms discussed in the previous subsections, the generic equation (4.12) contains the unknown value of ϕ at the center of the cell where the (4.12) is discretized, as well as the unknown values at the centers of the surrounding neighbor cells. The resulting equation can typically be non-linear, the linearization technique is part of the solution algorithm and the final linear algebraic equation for each domain cell takes the following form:

$$a\phi^{n+1} = \sum_{nb} a_{nb}\phi_{nb}^{n+1} + b \quad (4.23)$$

where the subscript nb refers to neighbor cells, a and a_{nb} are the linearized coefficients for ϕ and ϕ_{nb} , and b is the known term. For each flow equation, a linear system of N equations has to be solved, with N being the number of computational cells. The numerical solution of each flow equation thus consists in the solution of the linear system:

$$\mathbf{A}\phi^{n+1} = \mathbf{b} \quad (4.24)$$

with \mathbf{A} being a $[N \times N]$ sparse coefficient matrix, ϕ the $[N \times 1]$ unknown terms vector and \mathbf{b} the $[N \times 1]$ known terms vector. The order in which the equations are solved and the numerical methods used depend on the algorithms chosen to discretize the

specific terms appearing in each equation, such that each term is available when it is needed.

4.3 Discretization of the volume fraction equation: the PLIC and the split advection techniques

The volume fraction equation is discretized in time with a first order explicit scheme. The numerical stability of the explicit scheme poses a limitation on the time step used to solve the volume fraction equation, since the interface must travel less than one grid cell at each time interval. On the contrary, the time-implicit treatment of the other flow equations, allows an higher time step for their temporal discretization. Fluent allows the solution of the volume fraction equation with a finer time step with respect to the other equations, thus for each time iteration of the flow equations set, the volume fraction equation is updated more frequently.

The time step restriction for the volume fraction equation can be expressed by the Courant number Co . The Courant number is a dimensionless number that compares the simulation time step and the time it would take for the fluid to empty out the cell:

$$Co = \frac{\Delta t}{V / \sum_f^{N_f} \mathbf{u}_f \cdot \mathbf{n}_f A_f} \quad (4.25)$$

The numerical stability requires that $Co < 1$. Fluent uses the user input for the maximum Courant number to set the volume fraction equation time step as the minimum Δt obtained by looping the (4.25) on all the near-interface cells. The Fluent default value $Co=0.25$ is maintained in all the simulations performed in this thesis.

For those cells whose volume fraction gradient is zero, thus far from the interface, the convective term of the volume fraction Eq. (4.2) is replaced by $\nabla \cdot (\alpha \mathbf{u})$ and the consequent interpolation of face centered values is done through the MUSCL scheme. For those cells whose volume fraction gradient is non-zero, the volume fraction field is advected sequentially in the directions of the coordinates axis with a split technique. For the advection along each direction, a piecewise linear interface is reconstructed through the PLIC algorithm [38] described in the Section 3.1. Once the interface position within each interface cell is known, the volume fraction fluxes

across each near-interface cell face are reconstructed by geometrical relations, using an Eulerian technique.

To derive the split advection procedure, the marker function conservation equation (1.22) without source terms is rewritten:

$$\frac{\partial I}{\partial t} + \nabla \cdot (I\mathbf{u}) = I\nabla \cdot \mathbf{u} = 0 \quad (4.26)$$

Considering a two-dimensional geometry and expliciting the gradient and divergence operators:

$$\frac{\partial I}{\partial t} + \frac{\partial(Iu_x)}{\partial x} + \frac{\partial(Iu_y)}{\partial y} = I\left(\frac{\partial u_x}{\partial x} + \frac{\partial u_y}{\partial y}\right) \quad (4.27)$$

where u_x and u_y are respectively the horizontal and vertical components of the velocity vector. The unsteady term is discretized with the aforementioned first order explicit scheme, such that:

$$\frac{I^{n+1} - I^n}{\Delta t} + \frac{\partial(Iu_x)^n}{\partial x} + \frac{\partial(Iu_y)^n}{\partial y} = I^n\left(\frac{\partial u_x^n}{\partial x} + \frac{\partial u_y^n}{\partial y}\right) \quad (4.28)$$

Now, the unsteady term can be rewritten as follows:

$$\frac{I^{n+1} - I^n}{\Delta t} = \frac{I^{n+1} - I^* + I^* - I^n}{\Delta t} \quad (4.29)$$

where I^* refers to an intermediate marker function field. The (4.28) together with the (4.29) can be split into the following two equations:

$$\frac{I^* - I^n}{\Delta t} + \frac{\partial(Iu_x)^n}{\partial x} = I^n \frac{\partial u_x^n}{\partial x} \quad (4.30)$$

$$\frac{I^{n+1} - I^*}{\Delta t} + \frac{\partial(I^*u_y^n)}{\partial y} = I^* \frac{\partial u_y^n}{\partial y} \quad (4.31)$$

which represent the split advection along the x and y directions. I^* represents the volume fraction field updated after the advection along x . The procedure for a three-dimensional geometry is analogous.

In the following, the finite-volume discretization of the (4.30) is outlined. The integration of the (4.30) within a cell of volume V bounded by the area A leads to:

$$\int_V \frac{I^* - I^n}{\Delta t} dV + \int_A I^n \mathbf{u}_x^n \cdot \mathbf{n} dA = \int_V I^n \frac{\partial u_x^n}{\partial x} dV \quad (4.32)$$

where the horizontal velocity component in the second term at the LHS is considered as a vector and thus typed with a bold character. By using the definition of volume fraction (1.34) and considering an average value of $\partial u_x / \partial x$ within the cell, the integrals are discretized as follows:

$$\frac{\alpha^* - \alpha^n}{\Delta t} V + \sum_f^{N_f} I_f^n \mathbf{u}_{\mathbf{x}:f}^n \cdot \mathbf{n}_f A_f = \alpha^n \frac{\partial u_x^n}{\partial x} V \quad (4.33)$$

If the integration is made within the (i, j) cell of a two-dimensional uniform square grid with grid spacing h , the (4.33) takes the following form:

$$\frac{\alpha_{i,j}^* - \alpha_{i,j}^n}{\Delta t} h^2 + (I u_x h)_{i,j+1/2}^n - (I u_x h)_{i,j-1/2}^n = \alpha_{i,j}^n (u_{x:i,j+1/2} - u_{x:i,j-1/2})^n h \quad (4.34)$$

where the indexes $(i, j + 1/2)$ and $(i, j - 1/2)$ refer respectively to the right and the left face boundaries of the (i, j) cell, see Fig. 4.2(a). The derivative at the RHS of the (4.33) has been discretized with a central finite difference scheme.

Thanks to the explicit formulation of the volume fraction equation, the (4.34) involves only known variables, defined at the time-level n , while the only unknown term is the intermediate volume fraction $\alpha_{i,j}^*$:

$$\alpha_{i,j}^* = \frac{1}{h^2} \left\{ \alpha_{i,j}^n \left[h^2 + (u_x \Delta t \cdot h)_{i,j+1/2}^n - (u_x \Delta t \cdot h)_{i,j-1/2}^n \right] - (I u_x \Delta t \cdot h)_{i,j+1/2}^n + (I u_x \Delta t \cdot h)_{i,j-1/2}^n \right\} \quad (4.35)$$

which, by referring to the Fig. 4.2 (b) and (c), can be intended as the balance of three areas normalized by $1/h^2$:

$$\alpha_{i,j}^* = \frac{1}{h^2} \left(\alpha_{i,j}^n b + \Phi_{i,j-1/2}^n - \Phi_{i,j+1/2}^n \right) \quad (4.36)$$

where b/h^2 is a contraction/expansion coefficient for the (i, j) cell given by the flow field and the $\alpha_{i,j}^n b$ area is shown in Fig. 4.2(b) with pink color. The terms grouped as Φ are the volume fraction fluxes across the side faces of the (i, j) cell and they are evaluated geometrically by knowing the position of the PLIC reconstructed interface. Referring to the Fig. 4.2(c), the flux of volume fraction Φ across the $(i, j - 1/2)$ boundary (green color) is equal to the area of a trapezoid of height $u_{x:i,j-1/2}^n \Delta t$ bounded by the PLIC reconstructed interface in the cell $(i, j - 1)$, area computed through geometrical relationships. In a similar manner, the flux of volume fraction

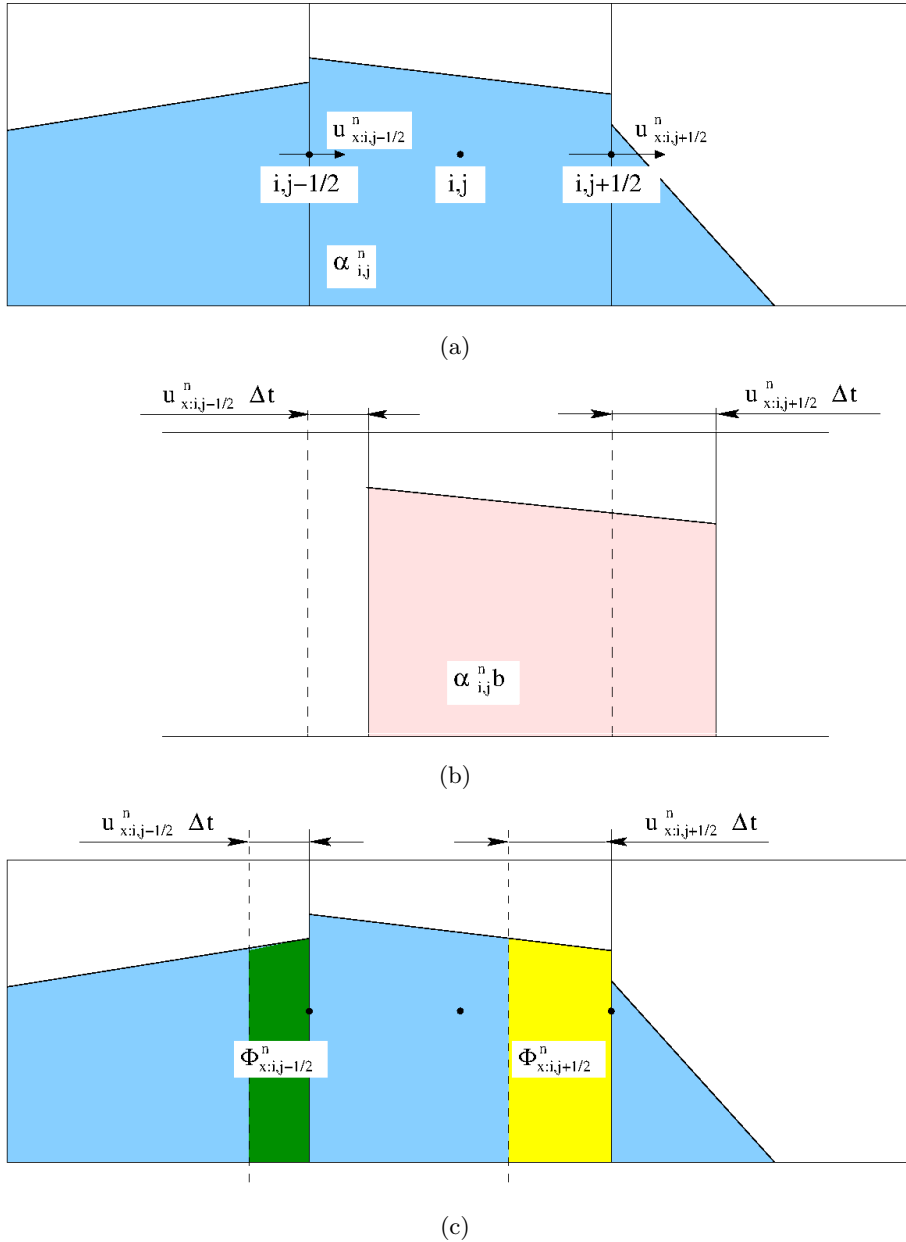


Figure 4.2: Sketch of the areas involved in the horizontal advection step of the volume fraction field for a square interfacial cell. (a) PLIC reconstructed interfaces, (b) contraction/expansion of the (i, j) cell, (c) geometrical reconstruction of the volume fraction fluxes across the vertical faces of the (i, j) cell.

Φ across the $(i, j + 1/2)$ boundary (yellow color) is reconstructed.

Once that the intermediate volume fraction field α^* is known throughout the domain, the PLIC algorithm updates the interface topology within each interfacial cell. Subsequently, the last advection, along the y direction, is performed to compute the new α^{n+1} field. Summarizing, the numerical solution of the volume fraction equation in two dimensions proceeds as follows:

1. PLIC reconstruction of the interface by the known α^n field;
2. For cells far from the interface ($\nabla\alpha^n = 0$), solution of the Eq. (4.2) with the methods described in Section 4.2;
3. For cells close to the interface ($\nabla\alpha^n \neq 0$), advection along the x direction by solving the Eq. (4.36) with the geometrical reconstruction of the fluxes through areas computation, thus deriving an intermediate α^* field;
4. New PLIC reconstruction of the interface by the known α^* field;
5. For cells close to the interface ($\nabla\alpha^n \neq 0$), advection along the y direction with the same procedure of step 3, thus deriving the final α^{n+1} field;

Since the solution of the volume fraction equation with the discussed method does not require the knowledge of terms at the time-level $n + 1$, it is the first equation solved in the Fluent solution algorithm. Subsequently, each fluid material property field can be updated at the new time-level by the Eq. (1.35).

Note that Fluent solves the following form of the volume fraction equation:

$$\frac{\partial(\rho_1\alpha)}{\partial t} + \nabla \cdot (\rho_1\alpha\mathbf{u}) = S_\alpha \quad (4.37)$$

where 1 refers to the primary phase, thus the volume fraction source term has to be provided as:

$$S_\alpha = N_v\alpha_v\varphi - N_l\alpha_l\varphi \quad (4.38)$$

differently from what expressed in the (4.6).

4.4 Pressure-velocity coupling: the PISO algorithm

In the flow equations set the pressure does not appear to be a primitive variable, as instead the density would be because of the continuity equation. For high Mach number flows, the density is treated as an independent variable and a density field is obtained by the solution of the continuity equation, while the pressure field is derived by an equation of state. For low Mach numbers the density-pressure linkage is weak or null in the limit of incompressible flows. In such a situation the pressure is treated as an independent variable and the continuity equation is replaced by a pressure equation, obtained by manipulating the continuity and momentum equations. In the Fluent software this solution approach is called *pressure-based*.

The solution procedure for the time-implicit momentum equations, which are non-linear and coupled one to each other, requires to resort to iterations. Furthermore, the pressure field is needed, such that the momentum and pressure equations form a system of 3 equations (in two dimensions) coupled and non-linear. With the segregated approach, the equations are decoupled in such a manner that they can be solved sequentially with an iterative procedure up to the convergence, when the final velocity field satisfies the momentum equations and the divergence-free condition.

The segregated algorithms available in Fluent are of the *predictor-corrector* class: an estimation of the velocity field is obtained by solving the momentum equations with a guess pressure field (predictor step); a pressure-correction equation is solved with the previously estimated velocity field, to obtain a pressure correction field; the estimated velocity field is corrected with the pressure correction field to derive a divergence-free velocity (correction step).

In the Fluent implemented SIMPLE (*Semi Implicit Method for Pressure-Linked Equations*) [115] and SIMPLEC (*SIMPLE Consistent*) [116] algorithms, the predictor-corrector operations are repeated iteratively up to the convergence of the pressure and the velocity fields. Differently, the original PISO algorithm (*Pressure Implicit Splitting of Operators*) [117] proposed by Issa involves a double corrector step, considered sufficient by the author to gain a converged field for pressure and velocity without resorting to iterations. However, since the momentum equation is not linear and discretized implicit in time, an iterative procedure for the solution is necessary.

Even if the cited algorithms were proposed for single-phase flows, they are effective also for multiphase flows. In order to choose the best pressure-velocity segregated

algorithm, the same inviscid static droplet simulation used to compare the gradient discretization algorithms (see Section 4.2) was performed. It was observed that all the pressure-velocity schemes lead to maximum velocity magnitudes of the same order $|\mathbf{u}_{\mathbf{max}}| \approx 10^{-16}$ m/s, however only the PISO algorithm reached convergence.

For this reason the PISO algorithm was used in all the simulations performed in this thesis. In the following, the PISO algorithm as originally proposed by Issa [117] is shown. First, the derivation of the pressure correction equation is discussed.

The author started with the following expressions of the continuity and momentum equations, for a generic flow with variable density similar in concept to the single fluid formulation of the two-phase flow:

$$\frac{\partial \rho}{\partial t} + \nabla \cdot (\rho \mathbf{u}) = 0 \quad (4.39)$$

$$\frac{\partial (\rho \mathbf{u})}{\partial t} = \nabla \cdot (\boldsymbol{\tau} - \rho \mathbf{u} \mathbf{u}) - \nabla p + \mathbf{f} \quad (4.40)$$

where \mathbf{f} identifies every external volume force, such as buoyancy or surface tension. The flow equations are discretized in time with an implicit first order formulation, such that:

$$\frac{\rho^{n+1} - \rho^n}{\Delta t} + \nabla \cdot (\rho \mathbf{u})^{n+1} = 0 \quad (4.41)$$

$$\frac{(\rho \mathbf{u})^{n+1} - (\rho \mathbf{u})^n}{\Delta t} = \nabla \cdot (\boldsymbol{\tau} - \rho \mathbf{u} \mathbf{u})^{n+1} - \nabla p^{n+1} + \mathbf{f}^{n+1} \quad (4.42)$$

By taking the divergence of the momentum equation and substituting the continuity equation, the following pressure-correction equation is derived:

$$\nabla^2 p^{n+1} = \nabla \cdot \nabla \cdot (\boldsymbol{\tau} - \rho \mathbf{u} \mathbf{u})^{n+1} + \nabla \cdot \mathbf{f}^{n+1} + \frac{1}{\Delta t} \nabla \cdot (\rho \mathbf{u})^n + \frac{\rho^{n+1} - \rho^n}{(\Delta t)^2} \quad (4.43)$$

The PISO algorithm proceeds as follows:

Predictor step

The pressure field prevailing at the time-level n is used in the solution of the implicit momentum equation (4.42) to yield the estimated velocity field \mathbf{u}^* :

$$\frac{1}{\Delta t} \rho^{n+1} \mathbf{u}^* = \frac{1}{\Delta t} (\rho \mathbf{u})^n + \nabla \cdot (\boldsymbol{\tau} - \rho^{n+1} \mathbf{u} \mathbf{u})^* - \nabla p^n + \mathbf{f}^* \quad (4.44)$$

where ρ^{n+1} is maintained since it is known from the updated volume fraction field. The two scalar momentum equations (in two dimensions) are coupled in the velocity components, thus an iterative solution is necessary.

First Corrector step

A new velocity field \mathbf{u}^{**} which satisfies the continuity equation at the level $**$ is sought:

$$\frac{\rho^{n+1} - \rho^n}{\Delta t} + \nabla \cdot (\rho^{n+1} \mathbf{u}^{**}) = 0 \quad (4.45)$$

The new velocity field is obtained as solution of the following explicit momentum equation:

$$\frac{\rho^{n+1} \mathbf{u}^{**} - (\rho \mathbf{u})^n}{\Delta t} = \nabla \cdot (\boldsymbol{\tau} - \rho^{n+1} \mathbf{u} \mathbf{u})^* - \nabla p^* + \mathbf{f}^* \quad (4.46)$$

in which the pressure field p^* is found as solution of the pressure equation obtained by taking the divergence of (4.46) and substituting the (4.45):

$$\nabla^2 p^* = \nabla \cdot \nabla \cdot (\boldsymbol{\tau} - \rho^{n+1} \mathbf{u} \mathbf{u})^* + \nabla \cdot \mathbf{f}^* + \frac{1}{\Delta t} \nabla \cdot (\rho \mathbf{u})^n + \frac{\rho^{n+1} - \rho^n}{(\Delta t)^2} \quad (4.47)$$

Second Corrector step

With the same procedure followed in the first correction step, the pressure correction equation leads to the new pressure field p^{**} :

$$\nabla^2 p^{**} = \nabla \cdot \nabla \cdot (\boldsymbol{\tau} - \rho^{n+1} \mathbf{u} \mathbf{u})^{**} + \nabla \cdot \mathbf{f}^{**} + \frac{1}{\Delta t} \nabla \cdot (\rho \mathbf{u})^n + \frac{\rho^{n+1} - \rho^n}{(\Delta t)^2} \quad (4.48)$$

and the new velocity field \mathbf{u}^{***} is thus obtained solving the momentum equation:

$$\frac{\rho^{n+1} \mathbf{u}^{***} - (\rho \mathbf{u})^n}{\Delta t} = \nabla \cdot (\boldsymbol{\tau} - \rho^{n+1} \mathbf{u} \mathbf{u})^{**} - \nabla p^{**} + \mathbf{f}^{**} \quad (4.49)$$

More corrector steps could be introduced as Fluent offers this possibility, but we observed that, as also proved in [117], two steps are sufficient, such that $\mathbf{u}^{n+1} \approx \mathbf{u}^{***}$ and $p^{n+1} \approx p^{**}$.

4.4.1 Interpolation of cell-centered pressures on cell faces

Fluent solves the momentum equation (4.3) by integration over a control volume of volume V and face area A , thus leading to:

$$\frac{\partial(\rho\mathbf{u})}{\partial t}V + \sum_f^{N_f}(\rho\mathbf{u}\mathbf{u} - \boldsymbol{\tau})_f \cdot \mathbf{n}_f A_f = \sum_f^{N_f} p_f \mathbf{n}_f A_f + S_m V \quad (4.50)$$

where S_m is an average of the source term within the cell. Equation (4.50) requires the values of the pressure at the cell face centroids. But, the use of a collocated technique to solve the pressure correction equation gives a field of pressure centered at the cell centroids.

Fluent offers a *body-force-weighted* scheme to interpolate the computed cell-centered pressures at the cell faces and a *Pressure Staggering Option* (PRESTO) algorithm that solves the pressure correction equation for a staggered control volume, thus leading to face-centered pressures without the need of interpolations. The second scheme is preferable for two-phase flows, where large body forces concentrated on a finite thickness interface exist. The interpolation errors caused by the body-force-weighted method prevent the correct balance among pressure gradient and surface tension force at the interface, thus generating spurious velocities.

In order to compare the performances of the PRESTO and body-force-weighted methods, the inviscid static droplet simulation was used again. As reported in the Table 4.2, the error given by the body-force-weighted formulation is several orders of magnitude higher than the PRESTO one.

Face-centered pressure formulation	$ \mathbf{u}_{max} $ [m/s]
body-force-weighted	$5 \cdot 10^{-2}$
PRESTO	$2.5 \cdot 10^{-16}$

Table 4.2: Comparison of the Fluent body-force-weighted and PRESTO formulations to compute face-centered pressures. The magnitude of the maximum velocity in the domain after one time step is reported.

4.5 The energy equation

Fluent solves the energy equation in the following form:

$$\frac{\partial(\rho E)}{\partial t} + \nabla \cdot [\mathbf{u}(\rho E + p)] = \nabla \cdot (\lambda \nabla T) + S_E \quad (4.51)$$

where E is a mass-average energy defined as:

$$E = \frac{\sum_q^{N_q} \alpha_q \rho_q h_q}{\sum_q^{N_q} \alpha_q \rho_q} \quad (4.52)$$

with N_q being the number of the phases and h the specific enthalpy. Thus, the energy equation is solved in the variable E , subsequently the temperature field is derived by the mass-average energy, where the specific enthalpy for each q -th phase is expressed as follows:

$$h_q = \int_{T_{q,ref}}^T c_{p,q} dT \quad (4.53)$$

with $T_{q,ref}$ being the reference temperature at which corresponds the zero value of the specific enthalpy for the q -th phase. Since Fluent sets automatically the enthalpy of each phase equal to zero at the temperature T_{ref} , the reference enthalpies within the energy source term (4.8) disappear:

$$S_E = -h_{lv} \varphi_0 + \varphi (N_v \alpha_v c_{p,v} - N_l \alpha_l c_{p,l})(T - T_{ref}) \quad (4.54)$$

4.6 The additional scalar equation for the evaporation rate

The numerical implementation of the evaporation model, discussed in Subsection 3.2.2, requires the solution of the transport equation (4.5) for the additional scalar field φ .

Fluent can solve additional transport equations for user-defined scalars, φ in this case. The form of the transport equation solved is the same as Eq. (4.10), as well as the numerical algorithms used for its discretization and solution. Unsteady and convective terms for the additional scalar equation can be neglected by the user, thus the following transport equation for φ is solved:

$$\nabla \cdot (\Gamma \nabla \varphi) + S_\varphi = 0 \quad (4.55)$$

In order for Eq. (4.55) to represent the (4.5), it is necessary to set a constant diffusion coefficient $\Gamma \equiv D$ and to implement the source term (4.9) with opposite sign:

$$S_\varphi = -\varphi + \varphi_0 \quad (4.56)$$

4.7 Boundary conditions

Fluent allows the user to set-up a boundary condition at each domain boundary. Through the Fluent internal algorithms, each boundary condition may act differently from one equation to another one. Thus, in this section the domain boundaries together with the applied boundary conditions are discussed separately.

The boundary condition for the scalar φ equation can be directly set by the user and it is set according to the (3.27).

Wall

Since this thesis deals with operating conditions whose Knudsen number is largely below 0.001, at each wall boundary a no-slip condition for the velocity is applied:

$$\mathbf{u}(\mathbf{x} = \mathbf{x}_w) = 0 \quad (4.57)$$

Such boundary condition is applied at the boundary faces of the next-to-boundary control volumes. The Fluent solver transfers this information to the centroids of the boundary cells by proper discretization of the momentum and pressure-correction equations.

For what concerns the energy equation, two different wall boundary conditions are applied:

$$\text{constant temperature} \quad T(\mathbf{x} = \mathbf{x}_w) = T_{wall} \quad (4.58)$$

$$\text{constant heat flux} \quad q(\mathbf{x} = \mathbf{x}_w) = q_{wall} = -\lambda \nabla T|_w \cdot \mathbf{n}_w \quad (4.59)$$

where the constant heat flux boundary condition is converted in a condition for the temperature field at the wall.

Inlet sections

At sections where a fluid inflow occurs, two different boundary conditions were set:

- *velocity inlet*, for which $\mathbf{u}(\mathbf{x} = \mathbf{x}_i) = u_{inlet}$ and $T(\mathbf{x} = \mathbf{x}_i) = T_{inlet}$.

This boundary condition imposes a fluid inflow, the pressure at the boundary is derived from the velocity condition input in the pressure-correction equation.

- *pressure inlet*, for which $p_T(\mathbf{x} = \mathbf{x}_i) = p_{T,inlet}$ and $T(\mathbf{x} = \mathbf{x}_i) = T_{inlet}$.

The subscript T refers to the total pressure, as the sum of static and dynamic pressure. The static pressure p_S and velocity at the boundary are adjusted to match the user input $p_{T,inlet}$, according to the Bernoulli equation:

$$p_T = p_S + \frac{1}{2}\rho|\mathbf{u}|^2 \quad (4.60)$$

Note that the pressure inlet condition does not force the fluid to enter the domain, thus the fluid velocity at the boundary as well as its direction, depends on the balance of the pressures among the inlet/outlet boundaries.

Outlet sections

At sections where a fluid outflow occurs, two different boundary conditions were set:

- *outflow*, for which no user input is necessary. The outflow boundary condition is equivalent to impose that the flow at the exit boundary only depends on the conditions upstream, such that the velocity and the pressure at the outflow boundary are obtained as part of the solution. In the algebraic equation (4.23) for a next-to-boundary cell, the outflow condition sets the coefficient a of the downstream neighbor cell to zero, such that the downstream cell does not influence the solution. Such condition can be interpreted as a null derivative in the direction normal to the outflow boundary: $\nabla\phi|_o \cdot \mathbf{n}_o = 0$.

The outflow boundary condition applies well where the above condition is a good assumption for the flow pattern, while it fails if inverted flow occurs at the exit.

- *pressure outlet*, for which $p_S(\mathbf{x} = \mathbf{x}_o) = p_{S,outlet}$.

Differently from the pressure inlet condition, it is the static pressure to be set by the user at the boundary, while Fluent computes the velocity at the boundary by proper discretization of the momentum and pressure-correction equations. Other variables, such as the temperature, are treated as for the outflow condition.

The pressure outlet condition works well also when inverted flow occurs and fluid enters from the boundary, but adequate backflow values for temperature and volume fraction have to be set by the user.

Symmetry axis

Fluent can solve the flow equations in an axisymmetrical domain but the symmetry axis has to be horizontal. The *axis* boundary condition imposes null derivatives along the direction normal to the axis: $\nabla\phi|_a \cdot \mathbf{n}_a = 0$.

The relative nature of the pressure

The pressure correction Eq. (4.43) only involves derivatives of the pressure, thus the computed pressure field is intended as relative.

For boundary conditions that do not involve the pressure, the absolute pressure field is obtained by shifting the computed field at the end of the calculation, such that the absolute pressure at a user input location matches a user input operating pressure value.

Where pressure boundary conditions are applied, it is preferable to set a magnitude relative to an operating pressure separately introduced by the user rather than an absolute value. Thus, the calculation procedure gives a relative pressure field and the absolute pressure is obtained by summing the user input operating pressure at the end of the calculation.

This management of the pressure as a relative pressure, with the operating pressure added at the end of the calculation, helps to avoid round-off errors, because the values of the absolute pressure are typically orders of magnitude higher than the pressure differences in the flow.

4.8 Implementation of the interfacial effects: User-Defined Functions

The models described in the Chapter 3 to evaluate the interfacial effects, leading to the flow equations source terms (4.38), (4.7), (4.54) and (4.56), have to be implemented in the numerical solver.

The numerical implementation has to be coherent with the physical models, optimized to avoid excessive slowing down of the computation, it needs to be numerically stable and, preferably, capable of parallel computing. The biggest effort in the work described with this thesis has been to achieve the cited tasks.

The aforementioned models have been implemented by means of the Fluent UDF. Among the several UDF available in Fluent, the following have been necessary in order to introduce and to set-up the models:

- *Define Adjust* function, executed at the beginning of each iteration, can be used to modify or to extract each variable defined in the flow problem, such that the user can compute additional quantities (integrals, calculation of minimums and maximums).
- *Define Source* function, executed at each iteration when the relative equation is being solved, can be used to define source terms in the form:

$$S_\phi = b + a\phi^{n+1} \quad (4.61)$$

where b contains the time-explicit part of the source term, not depending on ϕ^{n+1} , and a contains the time-implicit part. The user has to provide an expression for S_ϕ and for a . If a is set equal to zero Fluent will treat the source term as explicit and it will be inserted in the known terms vector \mathbf{b} in (4.24). If a non-zero expression for a is set, Fluent will insert the explicit part b in the known terms vector and the implicit term coefficient a in the coefficient matrix \mathbf{A} .

- *Define Init* function, executed before the beginning of the simulation, can be used to initialize the flow variables.
- *Define Execute at End* function, executed at the end of each time step, can be used to extract or modify each variable or to compute additional quantities. It is particularly useful to write text files where such quantities are saved, for the post-processing of the data.

Furthermore, a *User-Defined Scalar* equation has to be defined to solve the additional equation for φ and several *User-Defined Memories* are defined to store data useful for the post-processing, such as the source term fields.

4.8.1 Initialization of the volume fraction field

The initialization of the volume fraction field in all the simulations performed was done by using a Define Init function.

The initial shape of the interface can be introduced in the UDF by its analytical profile, and Fluent sets as 0 the volume fraction of the cells whose centroid is on one side of the interface, 1 if on the other side. Thus, the numerical interface at $t = 0$ has a stair-step aspect, but the Height Function algorithm works bad with such a volume fraction field.

For this reason, the exact initial field of the volume fraction is computed with an external software, by intersecting the analytical profile of the interface with the computational grid. The volume fraction of each interfacial cell is calculated as the area of the polygon bounded by the cell sides and the interface approximated with several points.

Subsequently, this accurate volume fraction field is exported as a text file and read by the Define Init function.

4.8.2 Implementation of the surface tension force

The Height Function algorithm reported in the Section 3.1.1 is introduced in the code by use of a Define Adjust function.

The curvature for each cell whose norm of the volume fraction gradient is non-zero is computed by extracting the volume fraction field.

Furthermore, Fluent internal values of the volume fraction gradients are adjusted, since errors were noticed in the calculation of the gradients next to domain boundaries.

The surface tension force within the momentum equation is introduced by use of a Define Source function. The surface tension force is discretized with a time implicit scheme, as the momentum equation, such that:

$$S_m = \frac{\sigma}{\langle \rho \rangle} (\rho \kappa \nabla \alpha)^{n+1} \quad (4.62)$$

where all the terms at the time level $n + 1$ are known since the volume fraction equation is the first one to be solved. The momentum source term does not depend on the velocity thus it is treated as explicit, with $a = 0$ in (4.61).

The HF algorithm requires up to 7×3 cells surrounding the cell for which the curvature is being calculated.

When an MPI protocol (Message Passing Interface) is used to execute parallel computation with Fluent, the whole domain is partitioned in subdomains. Each computing node has access only to the variables of its allocated subdomain, plus external next-to-boundary cells (one row). Thus, when computing the curvature of cells close to the partition boundaries, the HF algorithm requires the volume fraction of cells not available.

To overcome this limitation, Fluent versions of the C language *Send* and *Receive* commands are used to exchange data between each node and its neighbors. The objective of this thesis was to simulate axisymmetrical channels with high length-to-diameter ratios, thus in order to minimize the communication among the nodes the domain is partitioned in subdomains along the axial direction. By this method, each node communicates only with two neighbors, one upstream and one downstream of the channel. With such solution the scaling performance of the numerical code, as the number of parallel computing processors is raised, is very good.

4.8.3 Implementation of the evaporation model

A Define Adjust function computes the model proper constants N , N_v and N_l through integration all over the domain. For parallel simulations, each computing node performs an internal integration, the partial result is then sent to the host node which calculates the global sum and the values of the constants. Since the constants are defined as external variables, their values are available also for the Define Source functions used to introduce the source terms in the flow equations.

Volume fraction source term

Fluent requires the definition of two source terms, separately for the gas and liquid phase. Even if the convective term in the volume fraction equation is discretized in time with an explicit formulation, the source term is treated as implicit for the volume fraction but explicit for φ , to avoid coupling of the volume fraction with the φ equation (that Fluent does not handle):

$$S_{\alpha_v} = (N_v \varphi)^n \alpha_v^{n+1} \quad (4.63)$$

$$S_{\alpha_l} = (-N_l\varphi)^n \alpha_l^{n+1} \quad (4.64)$$

Treating the vapor as the primary phase, the coefficient $-N_l\varphi$ goes in the known terms vector and $\varphi(N_v + N_l)$ in the coefficient matrix.

Energy source term

The temperature is considered the primitive variable to express the source term. The energy equation is discretized in time with an implicit scheme and the same is done for the temperature in the energy source term. The volume fraction at the time level $n + 1$ is known. The φ term at the time level $n + 1$ is not known and the coupling is handled by the use of iterations. Thus, the energy source term takes the following form:

$$S_E = \left[N|\nabla\alpha|\alpha_l h_{lv}\phi T_{sat} - (N_v\alpha_v c_{p,v} - N_l\alpha_l c_{p,l})\varphi T_{ref} \right]^{n+1} + \left[(N_v\alpha_v c_{p,v} - N_l\alpha_l c_{p,l})\varphi - N|\nabla\alpha|\alpha_l h_{lv}\phi \right]^{n+1} T^{n+1} \quad (4.65)$$

with ϕ being here the kinetic mobility defined in Subsection 3.2.1. The term between the square brackets at the upper line of the equation above goes in the known terms vector while the one below goes in the coefficient matrix.

Evaporation rate equation source term

Similarly to the previous case:

$$S_\varphi = \left[N|\nabla\alpha|\alpha_l h_{lv}\phi(T - T_{sat}) \right]^{n+1} + (-1) \cdot \varphi^{n+1} \quad (4.66)$$

4.9 Fluent solution procedure

The solution of each flow equation requires the solution of the linear algebraic system (4.24). Fluent solves this linear system using a point implicit Gauss-Seidel linear equation solver in conjunction with an algebraic multigrid method, for which details it is referred to [110].

The solution of the set of non-linear and coupled equations requires an iterative procedure until convergence is achieved. The non-linear terms in the equation being

solved are linearized by using guess values, such that at the generic $i - th$ iteration:

$$\phi^{n+1,i} \cdot \phi^{n+1,i} \rightarrow \phi^{n+1,i} \cdot \phi_g^i \quad (4.67)$$

where $\phi^{n+1,i}$ is the dependent variable of the equation being solved and ϕ_g^i is a guess value for ϕ . As well, each variable independent of the equation, not known at the time level $n + 1$, is substituted by a guess value. At the first iteration $\phi_g^{i=1} \equiv \phi^n$, then at the beginning of each new iteration i the new guess is taken equal to the previous $\phi^{n+1,i-1}$ result obtained at the iteration $i - 1$, such that $\phi_g^i \equiv \phi^{n+1,i-1}$ (true only if the underrelaxation factor is 1, see the next paragraph).

The Fluent pressure-based segregated approach solves the flow equations set sequentially at each iteration, but also a non-iterative procedure with inner iterations is available. The order in which the equations are solved depends on the discretization schemes chosen for each equation, such that every term is known when it is needed.

The Figure 4.3 reports a diagram representing the Fluent solution procedure, on the basis of the algorithms that we have chosen for each equation. The volume fraction equation is explicit with time and it requires only variables at the time level n , thus it is the first one to be solved without the need of iterations. Once that the volume fraction field is updated, all the material properties can be updated with the (1.35).

Subsequently, the non-linear and time-implicit momentum equations coupled with the pressure correction equation are solved by means of the PISO algorithm. In the predictor step the momentum equations for each velocity component are solved sequentially, using guess values for the non-linear terms. Each corrector step involves the sequential solution of the pressure correction equation and the two momentum equations.

The new velocity field $\mathbf{u}^{n+1,i}$ is used to solve the time-implicit energy equation. The unknown φ^{n+1} required in the source term is substituted by the guess value φ_g^i .

Finally, the φ time-implicit equation is solved, with the not yet updated guess value T_g^i for the temperature appearing within the source term.

Now, if convergence is achieved the generic ϕ^{n+1} becomes the ϕ^n term for the new time step solution procedure, otherwise the guess values are updated and a new iteration restarts from the predictor step of the PISO algorithm.

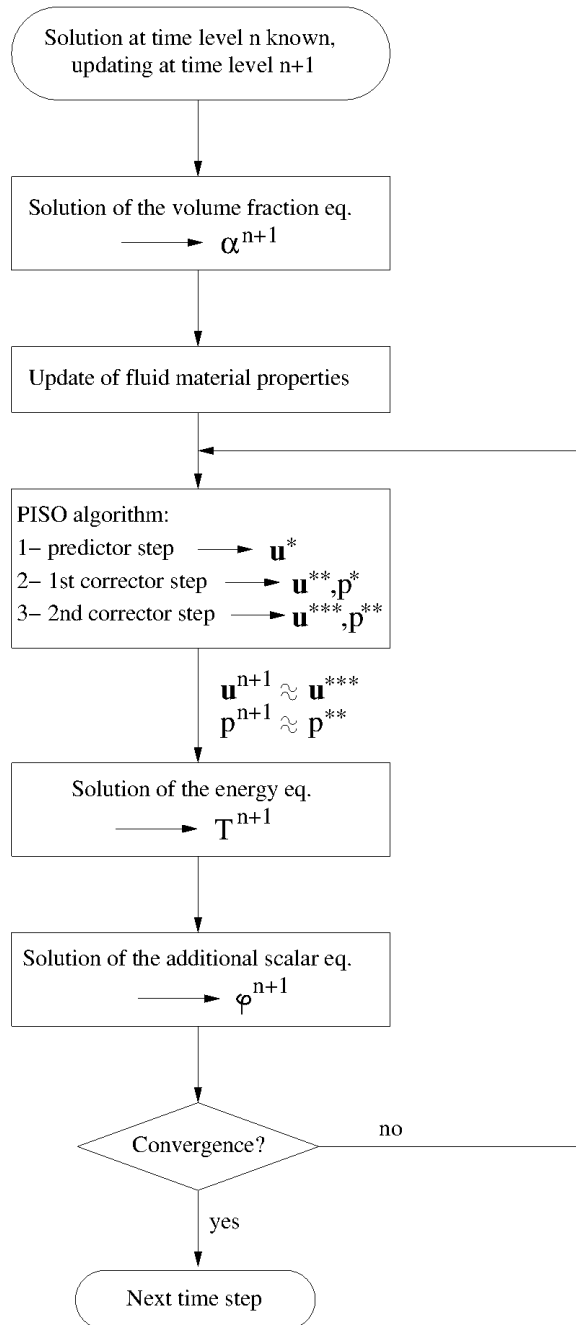


Figure 4.3: Fluent pressure-based segregated solution procedure for VOF-treated two-phase flows.

Underrelaxation

The use of underrelaxation factors helps to stabilize the iterative procedure for the solution of a non-linear equation, limiting the rate of changes of the variables estimated with guess values from iteration to iteration. The new guess value of the generic ϕ at the i -th iteration is computed as:

$$\phi_g^i = \phi_g^{i-1} + \gamma(\phi^{n+1,i-1} - \phi_g^{i-1}) \quad (4.68)$$

where γ , varying within the range $[0, 1]$, is the underrelaxation factor that limits the rate of change of the guess value. The previous statement that $\phi_g^i \equiv \phi^{n+1,i-1}$ is thus true only if $\gamma = 1$.

The optimal value of each underrelaxation factor depends on the discretization algorithm of the relative equation and on the problem being solved. Fluent defaults are kept in the simulations performed in this thesis.

Convergence criterion

A convergence criterion is necessary to define when the iterative procedure for the solution of the flow equations is converged, such that the solution procedure is applied to a new time level. The exact solution of the generic equation (4.23) for a generic computational cell c is the field ϕ that balances exactly the LHS and RHS terms, otherwise the residual error $R_c(\phi)$ is different from zero:

$$R_c(\phi) = \left| \sum_{nb} a_{nb}\phi_{nb} + b - a\phi \right|_c \quad (4.69)$$

As well, a residual vector $\mathbf{R}(\phi)$ can be defined to represent the error of the whole linear system solution, and its L_1 norm gives a practical index of the error:

$$L_1(\mathbf{R}(\phi)) = \sum_{c=1}^N \left| \sum_{nb} a_{nb}\phi_{nb} + b - a\phi \right|_c \quad (4.70)$$

where N is the number of the computational cells. A more practical index is the scaled residual error, defined as follows:

$$L_1^*(\mathbf{R}(\phi)) = \frac{\sum_{c=1}^N \left| \sum_{nb} a_{nb}\phi_{nb} + b - a\phi \right|_c}{\sum_{c=1}^N |a\phi|_c} \quad (4.71)$$

This scaled residual error is the convergence criterion used in Fluent. When each $L_1^*(\mathbf{R}(\phi))$ decreases below the threshold chosen for the relative variable, the solution is considered converged.

Instead, the convergence of the pressure correction equation is checked by monitoring whether continuity is achieved. The following continuity residual error norm is defined:

$$L_1(\mathbf{R}(\text{cont})) = \sum_{c=1}^N |\text{rate of mass creation}|_c \quad (4.72)$$

Convergence is obtained when the following scaled residual for the continuity decreases below the chosen threshold:

$$L_1^*(\mathbf{R}(\text{cont})) = \frac{L_1(\mathbf{R}(\text{cont}))}{\max(L_1(\mathbf{R}^{1-5}(\text{cont})))} \quad (4.73)$$

where the scaling factor at the denominator is the maximum continuity residual norm in the first five iterations.

In the simulations performed in this thesis, different values for the thresholds of the scaled residuals were chosen according to the case simulated. For the validation test cases discussed in the next Chapter, residuals within the range $[10^{-12}, 10^{-9}]$ were chosen. For the simulations shown in the Chapters 6 and 7, the range chosen was higher, $[10^{-6}, 10^{-3}]$ to speed-up the simulation time. The value 10^{-6} is a good compromise for accuracy and speed, however for the cases simulated with the highest threshold 10^{-3} it was preliminarily tested that the results were reliable and very close to those obtained with 10^{-6} .

4.10 Concluding remarks: flow solver set-up

We summarize the set-up chosen among Ansys Fluent several options. A VOF method is used to advect the interface and a time-explicit PLIC reconstruction of the volume fraction fluxes across the boundary faces of the interfacial cells is performed. The time step for the volume fraction equation is chosen by the solver according to the default maximum Courant number of 0.25. Momentum and energy equations are discretized in time with an implicit formulation. Fixed time steps

are chosen for the validation benchmarks described in Chapter 5 and the simulations presented in Chapter 6, variable time steps are set for the evaporating bubbles simulations discussed in Chapter 7. In the latter case, the time step for momentum and energy equations is computed by Fluent according to the user input of the maximum Courant number of 0.5 (not for volume fraction). We recommend the use of variable time steps in order to speed-up as possible the computations but preventing numerical instabilities, especially when the time scales vary considerably throughout the simulation. A third-order MUSCL scheme is used to discretize the convective terms within each equation. The Green-Gauss node-based scheme is used to reconstruct cell-centered gradients, since a test case assessed that the spurious currents generated by such algorithm are less than those given by other options. A PISO algorithm is chosen to deal with the velocity-pressure coupling, the other Fluent options led to the same accuracy but failed to converge. The PRESTO scheme is employed to compute pressures at the cell faces because a test case proved that other available options generate stronger unphysical vortices. The Height Function and evaporation models require the solution of one additional *User-Defined Scalar* equation for the evaporation rate. One *Define Adjust* function is used to compute the variables involved in the implemented models. Six *Define Source* functions are necessary to introduce the source terms within the flow equations. One *Define Init* function is used to initialize the flow variables. One *Define Execute at End* function writes selected variables on a text file at the end of each time step for the postprocessing with external softwares. Fifteen *User-Defined Memories* are enabled to store variables useful for the postprocessing internal to the Fluent software.

Chapter 5

Validation of the numerical framework

In this Chapter the validation benchmarks performed to test the Height Function and the evaporation models performances are discussed.

The first validation case is the geometrical reconstruction of a given interface profile and it involves the interface reconstruction algorithm alone. In the second test case the Height Function algorithm is used to compute the local interface curvature in the simulation of an inviscid static droplet, to test the implementation of the algorithm within the flow equations solver Fluent. The third test case compares the HF and Youngs performances on the simulation of gas bubbles rising in stagnant liquid due to buoyancy effects. The last test case is a validation benchmark for the whole framework, the HF and evaporation models compute the interfacial effects in the simulation of a vapor bubble growing in superheated liquid.

5.1 Reproduction of a circular interface

The capability of the Height Function and Youngs interface reconstruction algorithms to reproduce a known interface profile is tested in terms of norm vector and curvature error norms convergence rates.

Youngs local interface norm vector and curvature are computed by means of the Eqs. (3.1) and (3.5). HF interface topology is computed by means of the Eqs. (3.7) and (3.8) with heights evaluated through the procedure outlined in the Subsection

3.1.1 for a two-dimensional geometry.

A circular interface of radius $R = 5$ mm is placed inside a $L = 4R$ side square domain. Different uniform mesh sizes Δx are tested, in order to check the convergence rate of the methods. The coarsest mesh has 10×10 elements, with $R/\Delta x = 2.5$. This is the minimum resolution for the circular interface that the HF algorithm implemented is able to solve correctly. The most refined mesh has 600×600 elements, with $R/\Delta x = 150$. This is close to the maximum resolution of the interface obtained in the simulations discussed in the next Chapters.

The circle center is placed randomly around the domain center in the interval $([0, \Delta x], [0, \Delta x])$. For each mesh element size, 50 runs are performed to span the range of possible positions for the circle interface, then results are averaged. The parameters observed are L_2 and L_∞ error norms evaluated for both interface normal vector and curvature, defined as follows:

$$L_2(|\mathbf{n}|) = \sqrt{\frac{\sum_{i=1}^{N_i} |\mathbf{n}_i - \mathbf{n}_{ex}|^2}{N_i}} \quad (5.1)$$

$$L_\infty(|\mathbf{n}|) = \max(|\mathbf{n}_i - \mathbf{n}_{ex}|), \quad \text{for } i = 1, \dots, N_i \quad (5.2)$$

$$L_2(\kappa) = \frac{1}{\kappa_{ex}} \sqrt{\frac{\sum_{i=1}^{N_i} |\kappa_i - \kappa_{ex}|^2}{N_i}} \quad (5.3)$$

$$L_\infty(\kappa) = \frac{\max(|\kappa_i - \kappa_{ex}|)}{\kappa_{ex}}, \quad \text{for } i = 1, \dots, N_i \quad (5.4)$$

where \mathbf{n}_{ex} stands for the exact value of the i -th normal vector and \mathbf{n}_i for the computed value. The exact local interface unit norm vector is computed for each interface cell as the normalized vector connecting the center of the circular interface with the centroid of the cell. N_i is the total number of interface cells. $\kappa_{ex} = 1/R$ is the exact interface curvature, κ_i is the i -th interface cell calculated curvature.

The Figure 5.1 shows the convergence rate of the norm vector error norms. Youngs computed norm vector does not converge to the exact value as the mesh is refined, but the accuracy of the reconstruction remains constant. HF computed one converges with the first order with respect to the mesh element size. However, Youngs performs better for $R/\Delta x \leq 10$, when the interface is poorly solved by the mesh grid.

The Figure 5.2 shows the convergence rate of the curvature error norms. The

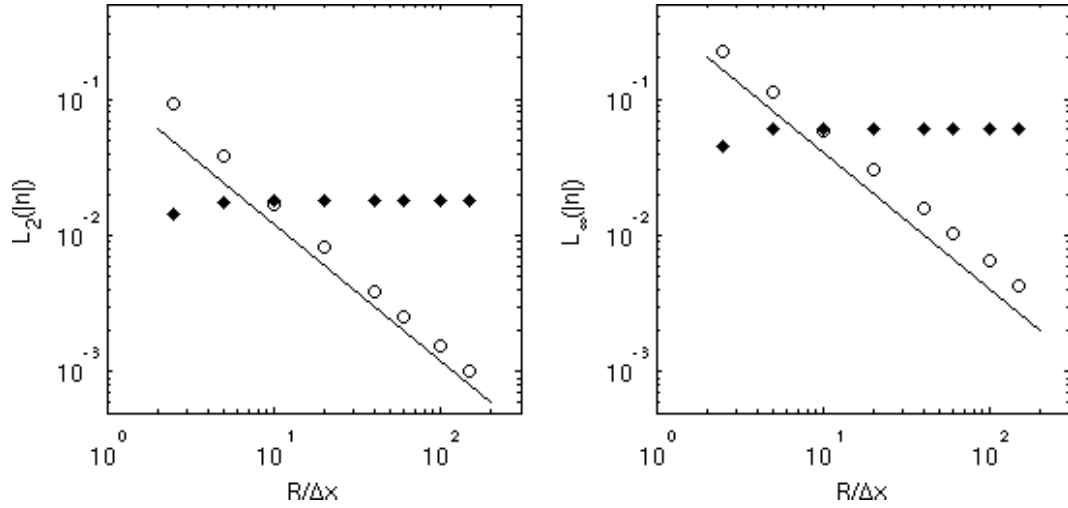


Figure 5.1: $L_2(|\mathbf{n}|)$ (left) and $L_\infty(|\mathbf{n}|)$ (right) error norms convergence rates. White circles are HF errors and black diamonds are Youngs ones. Solid line is first order convergence curve.

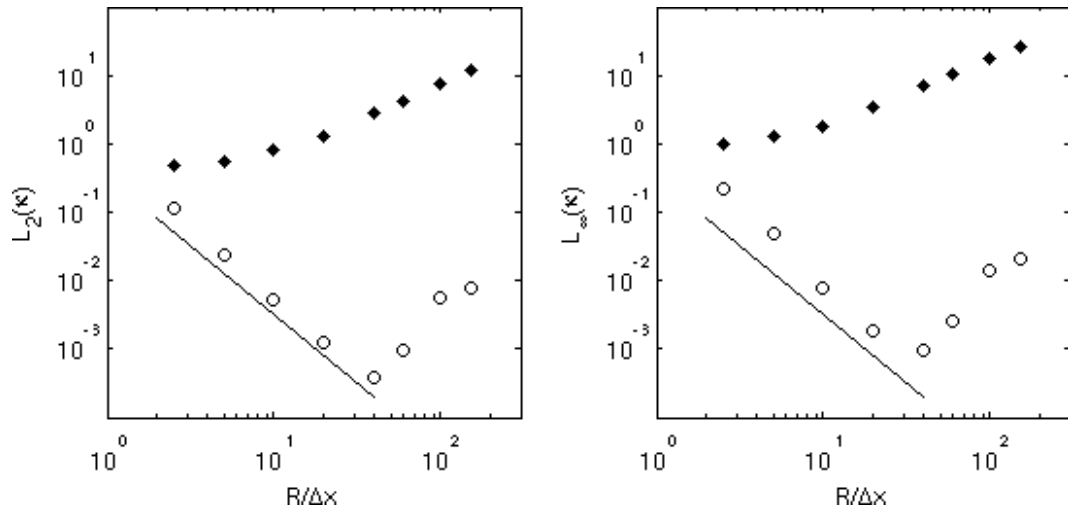


Figure 5.2: $L_2(\kappa)$ (left) and $L_\infty(\kappa)$ (right) error norms convergence rates. White circles are HF errors and black diamonds are Youngs ones. Solid line is second order convergence curve.

Youngs algorithm performs always worse than the HF one and the Youngs computed curvature diverges as the mesh is refined. The HF computed curvature converges

with the second order of the mesh element size for $R/\Delta x \leq 40$, in agreement with Cummins *et al.* [94] results. For resolutions higher than $R/\Delta x = 40$, the performances worsen and the published literature lacks of test cases with such a high resolution. The reason of the worsening is that the computation of the second order derivative of the heights, involved in the curvature expression (3.8), gets worse when the interface is less aligned with the background grid. For such high resolutions, the 7×3 stencil captures an interface nearly flat and a differencing scheme based on only three consecutive values of the height is not anymore adequate to estimate the curvature. However, note that even if the HF curvature at high resolutions does not converge, the maximum relative error at the highest mesh resolution is about 2%, fairly accurate for standard numerical simulations of multiphase flows.

5.2 Simulation of an inviscid static droplet

The Height Function and Youngs algorithms performances are assessed by means of the numerical simulation of an inviscid static droplet in equilibrium without gravity. The continuity and momentum equations for a two-dimensional geometry are solved with the numerical methods described in the previous Chapter.

The inviscid static droplet simulation is a typical benchmark to assess the performance of a multiphase CFD solver with surface tracking. The absence of gravitational and viscosity effects, as well as the absence of density gradients at the interface (both phases densities are set to unity), allow to test exclusively the accuracy of the implementation of the surface tension term within the Navier-Stokes equations and the solution algorithm.

The simplified momentum equation governing such flow is the Eq. (1.40). With the initial condition $\mathbf{u}(\mathbf{x}, t = 0)$ and wall domain boundaries, the exact solution of the (1.40) is a null velocity field at each $t > 0$, constant pressure within and outside the droplet and a pressure jump at the interface given by the Laplace law $\Delta p = \sigma \kappa$.

Thus, the magnitude of the arising velocity field in the numerical simulation as well as the error in the computed pressure field are the parameters observed to assess the performances of the numerical framework analyzed.

A circular droplet of radius $R = 5$ mm is centered on a $L = 4R$ side square do-

main. Different uniform mesh sizes Δx are tested, in order to check the convergence rate of the methods. The coarsest mesh has 20×20 elements, with $R/\Delta x = 5$. The most refined mesh has 160×160 elements, with $R/\Delta x = 40$. Surface tension and phase densities are set as unity. Viscous and gravity effects are neglected. A pressure outlet condition is set at all boundaries, with zero pressure. The simulation time step is $\Delta t = 5 \cdot 10^{-7}$ s.

The parameters observed are the non-dimensional velocity and interface pressure jump error norms defined as follows:

$$L_\infty(|\mathbf{u}^*|) = \frac{1}{U} \cdot \max(|\mathbf{u}_i|) \quad \text{for } i = 1, \dots, N \quad (5.5)$$

where N is the number of domain cells and U is a velocity scale defined as $U = (\sigma/2\rho R)^{1/2}$,

$$L_2(\Delta p^*) = \frac{1}{\Delta p_{ex}} \sqrt{\sum_{i=1}^m \frac{(\Delta p_i - \Delta p_{ex})^2}{m}} \quad (5.6)$$

where m is the number of interior droplet cells and $\Delta p_{ex} = \sigma/R$ is the exact value of the pressure jump across the interface.

The Figure 5.3 reports the velocity error norm convergence rate with respect to the mesh element size after 1 and 50 simulation time steps. Youngs velocity norm diverges with respect to the mesh element size, thus when using the Youngs algorithm to compute the interface topology a finer grid does not ensure more accurate results. The HF results show second order convergence for $R/\Delta x \leq 10$, then for higher resolutions the convergence order is within the range $[1, 2]$. A similar behavior was detected also by Francois *et al.* [48].

The Figure 5.4 shows the velocity field arising in the simulation when using the HF algorithm, after 1 and 400 time steps. The so-called spurious velocities appear as well-ordered vortices across the interface, presenting a fourfold symmetry. The same flow pattern was reported also by Mercinger and Zun [101] using alternatively PROST method [47] and a convolution technique [97] to compute curvatures, by Nichita [40] who employed a CLSVOF algorithm, by Popinet [49] and Francois *et al.* [48] using the HF method. Note also that the vortices after 400 time steps move the flow field in the opposite directions with respect to what is seen after 1 time step.

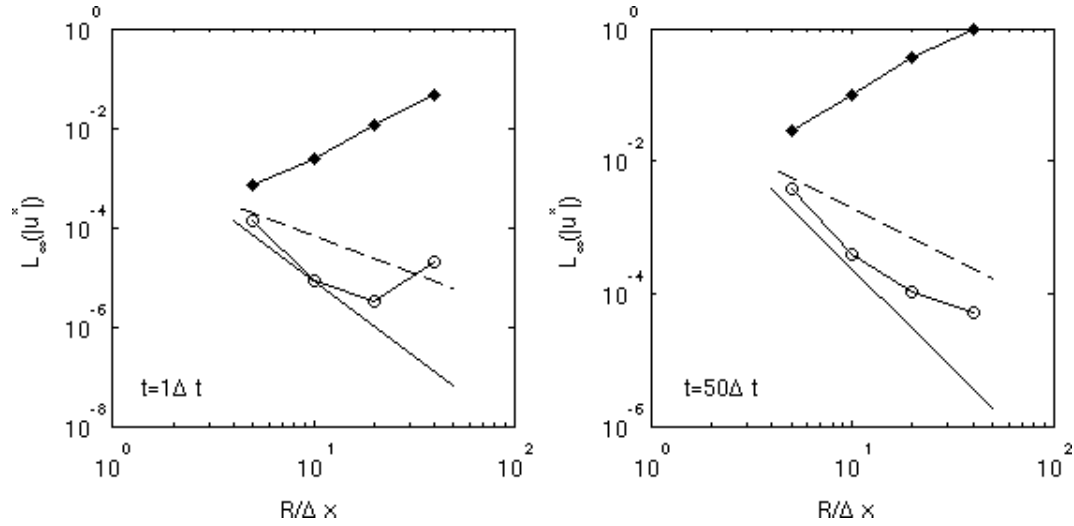


Figure 5.3: $L_\infty(|\mathbf{u}^*|)$ error norm after 1 (left) and 50 (right) time steps. White circles are HF errors and black diamonds are Youngs ones. The dash line is the first order convergence curve and the solid line is the second order curve.

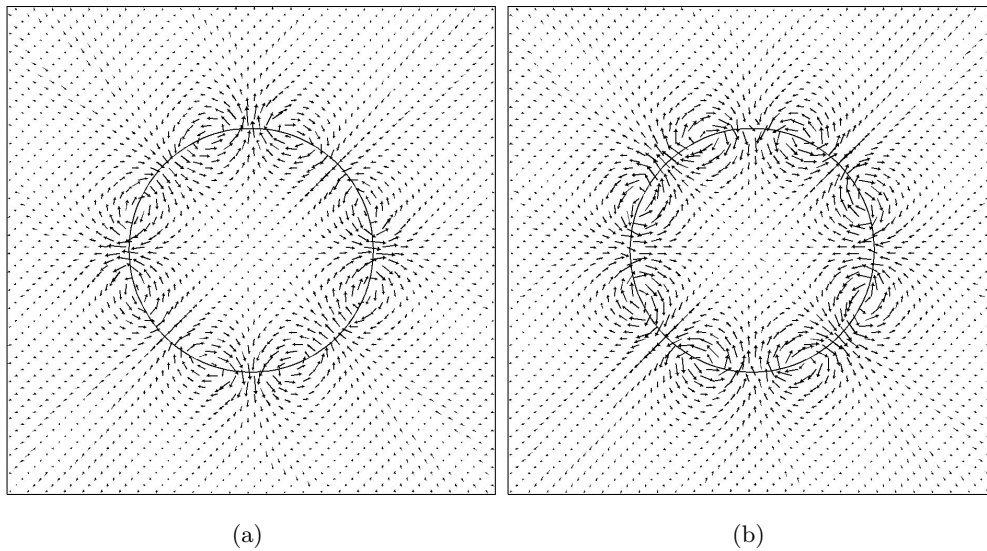


Figure 5.4: Velocity vectors after 1 (a) and 400 (b) simulation time steps, with the interface curvature computed by the HF method.

We found this behavior of the vortices to be curiously ordered for what is considered a “spurious” entity. Thus, we sought for a physical significance of such velocity field,

analyzing its numerical origin and its time-evolution. The results of this analysis are reported in the Appendix A.

The Figure 5.5 reports the pressure jump error norm convergence rate with respect to the mesh element size after 1 and 50 simulation time steps. No differences are evident for what concerns the convergence rate after 1 and 50 simulation time steps. The results obtained with the Youngs algorithm show a first order converging pressure norm for $R/\Delta x \leq 10$, then for higher mesh resolutions the pressure field diverges. The pressure field obtained by using the HF algorithm shows a convergence order within the range [1, 2].

The pressure field is observed also from a local point of view, as pressure profile across the droplet through an horizontal line located at $y^* = y/L = 0.5$, and through a diagonal line. The Figure 5.6 reports the profiles after 1 time step for the mesh resolution $R/\Delta x = 10$. The pressure profile relative to the HF algorithm has a sharp rise through the finite thickness interface and it is flat inside and outside the droplet, as it would be expected. By observing the Figs. 5.6(b) and 5.6(d), the pressure profile related to the HF method does not seem to be affected by the different interface

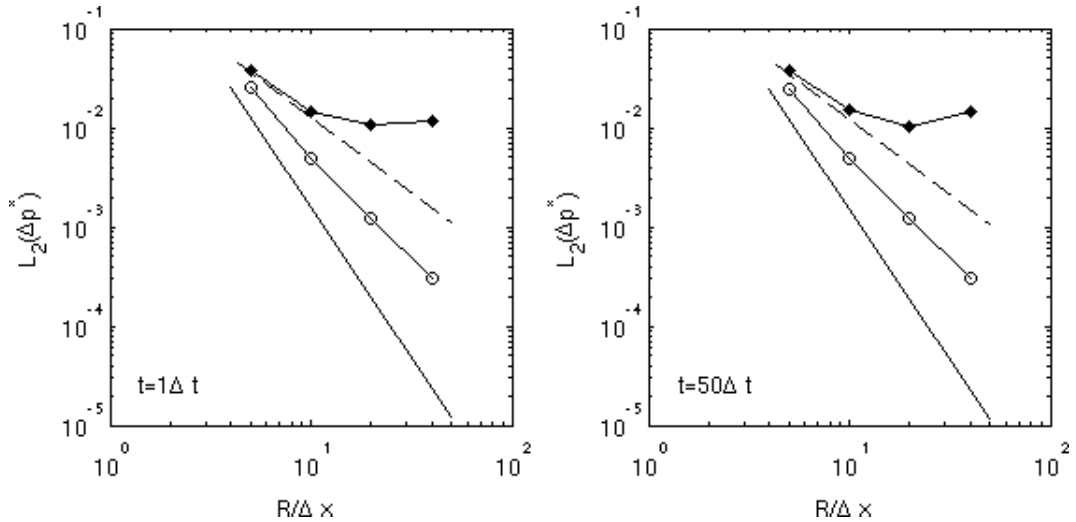


Figure 5.5: $L_2(\Delta p^*)$ error norm after 1 (left) and 50 (right) time steps. White circles are HF errors and black diamonds are Youngs ones. The dash line is the first order convergence curve and the solid line is the second order curve.

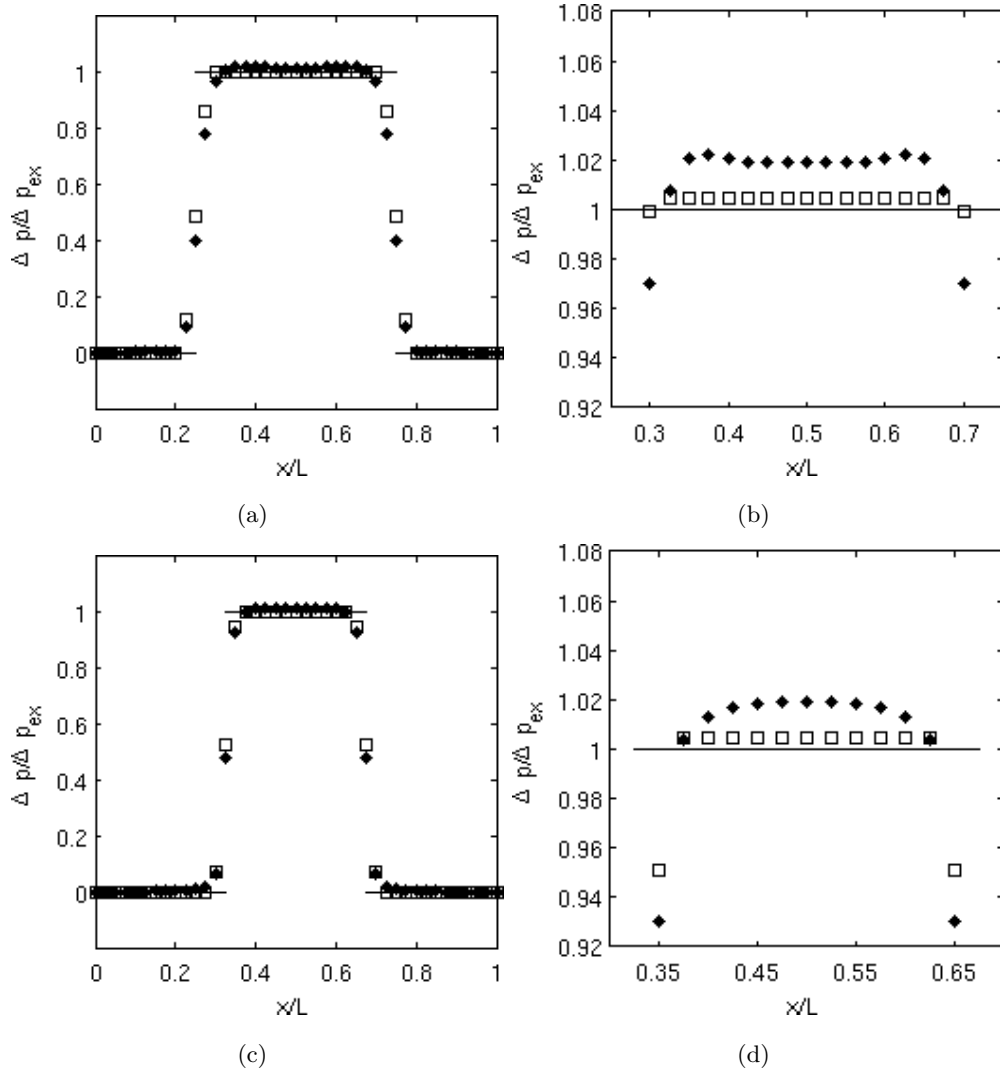


Figure 5.6: Non-dimensional pressure jump profile across the droplet for $R/\Delta x = 10$ after one simulation time step. Profiles are captured along an horizontal line $y^* = y/L = 0.5$ (a,b) and along the diagonal (c,d). White squares represent the HF and black diamonds the Youngs profiles. The solid line is the pressure jump exact profile.

orientation with respect to the background mesh.

The pressure field related to the Youngs algorithm shows a less sharp profile, with a pressure gradient non-zero not only on interface cells but also in neighbor cells. Moreover, the interface orientation has an appreciable influence. When the

interface is aligned to the background mesh (see Fig. 5.6(b)) the pressure profile within the droplet has a concave shape. Along the diagonal line (Fig. 5.6(d)) the pressure profile shows a convex shape.

5.3 Simulation of an isothermal bubble rising in stagnant liquid

In this Section the Height Function and Youngs algorithms are compared by simulations of a gas bubble rising in stagnant liquid due to buoyancy forces, for several different operating conditions. A circular gas bubble is patched at the bottom of a rectangular domain and the combination of inertial, gravitational, viscous and surface tension forces determines the terminal shape and velocity of the bubble.

The non-dimensional groups governing the flow are the Eötvös and Morton numbers defined in the Subsection 2.1.1, while the terminal velocity of the bubble U_b can be expressed by means of the Reynolds number $Re = \rho U_b D / \mu$ where D is the bubble initial diameter.

Two different series of simulations were conducted and are discussed separately in the following subsections: two-dimensional simulations with inviscid fluids and very high surface tension; axisymmetrical simulations of air bubbles rising in a viscous water/sugar solution.

5.3.1 Two-dimensional inviscid rising bubble

The inviscid rise of a gas bubble within stagnant liquid in a two-dimensional reference frame was simulated. Two fictitious fluids with very high surface tension were chosen in order to have surface tension dominance over inertia and buoyancy on the flow, such that the accuracy in the curvature computation becomes fundamental.

A $D = 2/3$ diameter bubble is placed on a $[-1, 1] \times [-1, 3]$ rectangular domain at $(0, 0)$. Two resolutions were tested for the flow domain mesh in order to observe the convergence rate of Youngs and HF methods: a coarser 40×80 and a finer 80×160 grid. Gas and liquid density is respectively 1.226 and 1000, surface tension is 728, gravity acceleration is set to -9.81 along the vertical axis, thus giving the Bond number defined in Eq. (2.5) $Bo = 5.989$. The simulation time step is $5 \cdot 10^{-4}$. Boundary conditions are symmetry for the box sides, pressure inlet for the bottom

and pressure outlet for the top.

These test conditions were analyzed by Francois *et al.* [48] with viscosity and later by Popinet [49], who neglected viscosity.

The Figure 5.7(a) reports the bubble shapes as half volume fraction contour for the coarse grid at different time instants. The HF and the Youngs methods lead to similar bubble top profiles and differences are evident on bubble rear at $t = 0.35$ and $t = 0.5$, when the Youngs computed curvature gives a bubble rear more indented. Francois *et al.* reported very similar bubble shapes when curvature was computed through the HF algorithm, see Figure 20(a) in [48].

The Figure 5.7(b) reports the bubble shapes for the fine grid. The differences among the HF-based simulations and Youngs one are evident at $t = 0.5$, when the

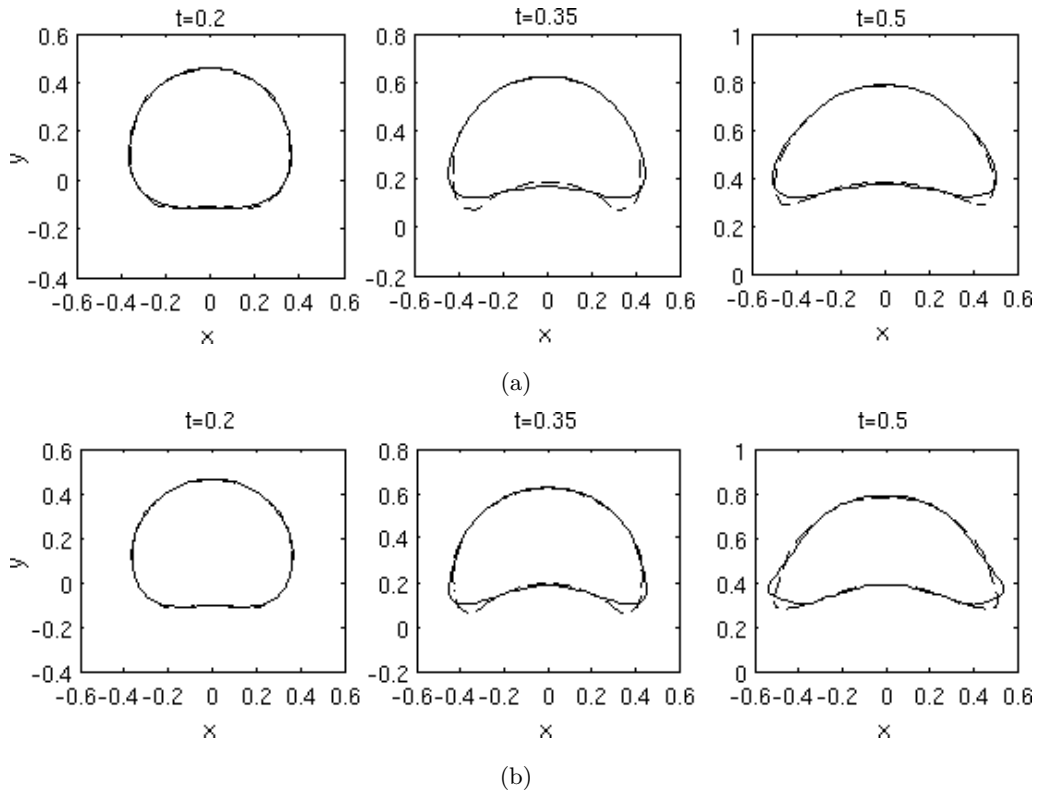


Figure 5.7: Bubble shapes as half volume fraction contours obtained for the coarse mesh in (a) and for the fine mesh in (b). Solid lines represent HF algorithm shapes and dash lines are Youngs ones.

Youngs computed side trailing edges are more closed toward the axis of the channel than HF computed ones. Such profile deviates slightly from Francois *et al.* shape shown in Figure 21 in [48], but it is closer to Popinet one obtained with a very fine 256×512 computational grid reported in Figure 18 in [49].

5.3.2 Axisymmetrical bubble rising in viscous liquid

The rise of an air bubble within a stagnant water/sugar solution in an axisymmetrical reference frame was simulated. Different terminal shapes and velocities of the bubble were obtained by changing the fluid properties in order to compare with Bhaga and Weber [118] experimental results.

Bhaga and Weber performed several test cases with air bubbles rising in a quiet water-sugar solution. Acting on sugar concentration, they could vary the liquid density and viscosity to span a wide range of Eötvös and Morton numbers, obtaining different bubble shapes and terminal velocities, expressed as bubble Reynolds number. Surface tension variations were negligible in their experiments.

Numerical and experimental results are compared for four different cases characterized by the same Eötvös number. The variation of the Morton number was possible in the simulations by changing only the liquid viscosity. It was proved that setting density ρ_l/ρ_g and viscosity μ_l/μ_g ratios as in the experiments leads to numerical errors. Since similitude with experiments is guaranteed by the Eötvös and Morton numbers which involve only the liquid properties, the gas properties are set in order to fix the aforementioned ratios to $\rho_l/\rho_g = 1000$ and $\mu_l/\mu_g = 100$.

Bhaga and Weber tested that wakes behind the bubbles are closed and symmetric until $Re < 110$. Since the simulations are performed on a 2D axisymmetrical domain, the cases chosen satisfy this condition.

A bubble of diameter $D = 3$ cm is centered at $(0, 2D)$ of a $[0, 4D] \times [0, 12D]$ axisymmetric rectangular domain, with $x = 0$ being the revolution axis. The domain size is set in order to avoid boundary influence, following Hua *et al.* sensitivity analysis [119]. Hua *et al.* showed also that a mesh resolution of $D/\Delta x \geq 20$ ensures grid independence, thus a 80×240 grid is chosen. Pressure inlet and outlet are set respectively on bottom and top boundaries. A free-slip condition is imposed on the domain sides. The time step for momentum and energy equations is 10^{-4} s.

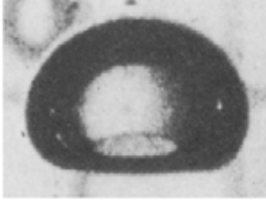
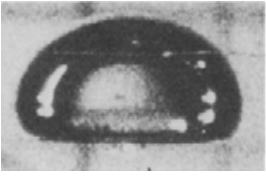
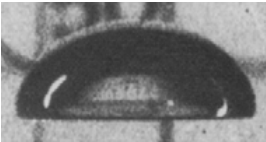
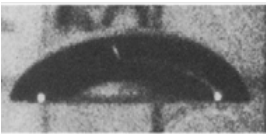
Test case	Test conditions	Experiments [118]	Simulations
I	$E_o = 116$ $Mo = 848$	 $Re = 2.47$	 $Re_{HF} = 2.37 (4\%)$ $Re_Y = 2.37 (4\%)$
II	$E_o = 116$ $Mo = 41.1$	 $Re = 7.16$	 $Re_{HF} = 7 (2.2\%)$ $Re_Y = 6.94 (3.1\%)$
III	$E_o = 116$ $Mo = 1.31$	 $Re = 20.4$	 $Re_{HF} = 19.66 (3.7\%)$ $Re_Y = 19.55 (4.2\%)$
IV	$E_o = 116$ $Mo = 0.103$	 $Re = 42.2$	 $Re_{HF} = 37.8 (10.4\%)$ $Re_Y = 39 (7.6\%)$

Table 5.1: Comparison of experimental and numerical gas bubbles terminal shape and Reynolds number. Solid lines are HF shapes, dash lines are Youngs shapes.

All the simulations are run until a steady state condition for the rising bubble is achieved, for both Height Function and Youngs algorithms. Then, the bubble terminal velocity is computed and the Reynolds number is evaluated for each case. The bubble velocity is the velocity of its center of gravity, evaluated at each time instant as dy_G/dt , where y_G is the axial position of the center of gravity computed as:

$$y_G = \frac{\sum_{c=1}^N y_c \alpha_c V_c}{\sum_{c=1}^N \alpha_c V_c} \quad (5.7)$$

where N is the number of computational cells, y_c the position of the c -th cell centroid, α the gas volume fraction and V the volume of the cell.

The Table 5.1 shows the comparison of experimental and numerical results. Experimental and numerical terminal shapes, together with the terminal Reynolds numbers for the four test conditions simulated are reported. The errors on the numerical Reynolds numbers between parenthesis are computed as $\text{err} = |\text{Re} - \text{Re}_{\text{num}}| / \text{Re}$.

The reflection of the light on the surface of the bubble in the experiments does not allow to see clearly the bubble indentation on the pictures, however the bubble external shapes for all the cases simulated are in good agreement with the experiments, independently of the interface reconstruction algorithm employed. The numerical simulations capture successfully the increase of the bubble velocity and the flattening of the bubble as the Morton number decreases.

For the test cases I, II and III, HF and Youngs methods show similar performances, with errors in the Reynolds number below 5 %. The HF method performs slightly better than Youngs one. Bubble shapes are very similar for both the methods.

The case IV is characterized by the highest bubble terminal velocity, hence by the highest difference in the gas-liquid phases velocity. The Figures 5.8(a) and 5.8(b) show the velocity field around the bubble respectively for cases I and IV.

In the case I the bubble terminal velocity is 0.065 m/s and the flow field in the wake near to the bubble rear moves liquid toward the bubble with a velocity of about 0.07 m/s. In the case IV the bubble terminal velocity is 0.107 m/s while the liquid is pushed on the bubble rear with a velocity of 0.14 m/s.

The difference among the liquid velocity in the wake and the bubble velocity in

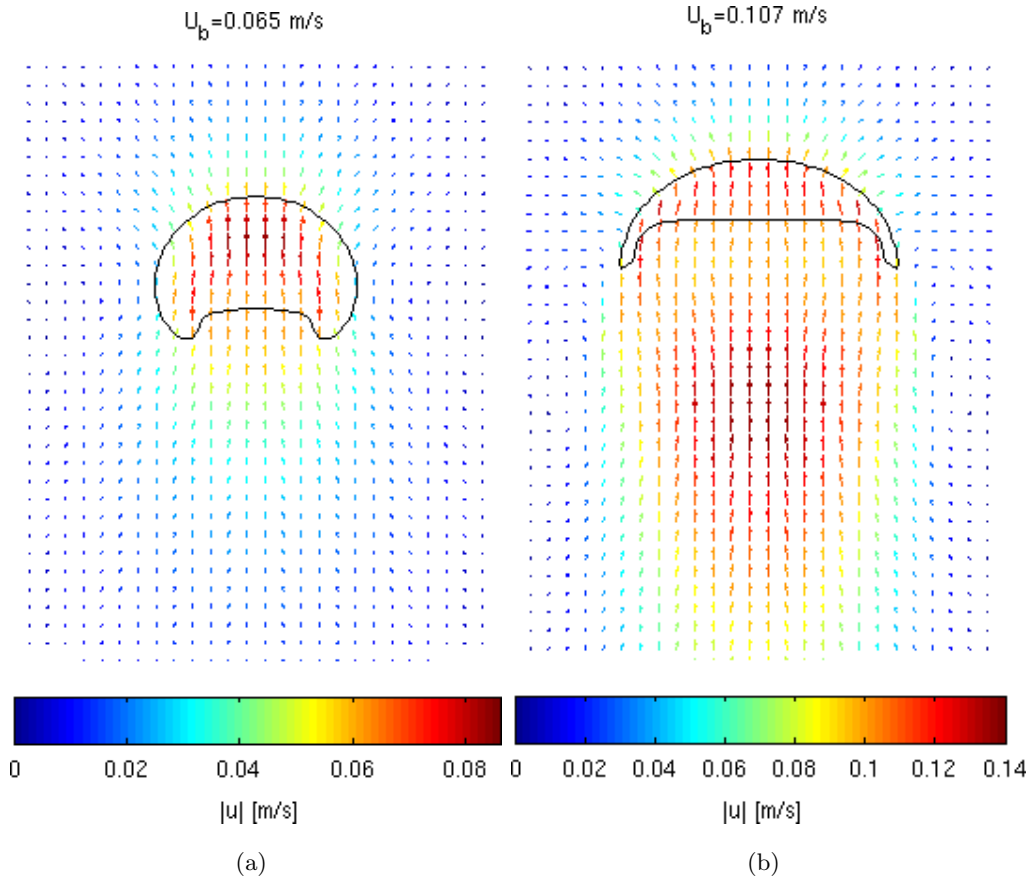


Figure 5.8: Velocity vectors colored by the velocity magnitude for cases I (a) and IV (b). The bubble terminal velocity U_b of each test case is reported on the top of each figure.

the case IV is much higher than that of the case I. Therefore, the bubble becomes more flattened because of the higher liquid push on the bubble rear and the change of the bubble concavity where the side trailing edge matches the indented edge becomes more abrupt.

In the case IV such region of the interface is poorly solved by the grid and the HF algorithm computes a wrong local geometry, leading to errors in the calculation of the capillary effects. This wrong forces computation leads to the detachment of little parts of gas at the bubble side trailing edges in the simulations, such that the smaller bubble main body moves with a lower velocity with respect to the experiments.

We repeated the test case IV with a twice refined 160×480 computational grid. The results obtained with the Height Function method are closer to the experiments than those obtained with the coarser mesh. On the contrary, the Youngs method gets worse with the finer mesh. This behavior is in agreement with what reported in the Section 5.1, also when simulating rising bubbles the refinement of the computational grid does not ensure better results when computing the interface curvature with the Youngs algorithm.

5.4 Simulation of a vapor bubble growing in superheated liquid

The Height Function interface reconstruction algorithm and the evaporation model were implemented in order to simulate the growth of a spherical vapor bubble in an infinitely extended superheated liquid. According to the Plesset and Zwick analysis [120], bubble growth process can be temporally split in two stages. A first stage, called inertia-controlled growth, which starts at bubble formation. At this stage, growth is governed by momentum interaction between bubble and surrounding liquid. At the beginning of this stage, temperature and pressure inside the bubble are at their maximum value. Temperature is equal to superheated liquid temperature, pressure is at saturation pressure for that temperature. Later, an asymptotic stage is reached, called heat-transfer-controlled growth. Temperature and pressure inside the bubble are at their lowest value, with pressure equal to the liquid pressure increased by pressure jump at the interface, and temperature is equal to the saturation temperature for that pressure. At this stage, characterized by a growth rate lower than the first stage, growth is limited by heat transport to the interface. This asymptotic stage is the object of our study. Scriven [121] has derived an analytical solution for this stage, neglecting viscous and surface tension effects and considering the interface at saturation temperature. He obtained an analytical bubble radius R as a function of time t :

$$R(t) = 2\beta\sqrt{\gamma t} \tag{5.8}$$

where β is a growth constant which details can be found in [121] and γ is liquid thermal diffusivity. This solution is used to validate numerical results.

5.4.1 Discrete domain and initial conditions

The growth of a spherical bubble of initial radius $R_0 = 0.1$ mm is simulated. The domain is axisymmetric and two-dimensional. The flow domain is rectangular, with size $8R_0 \times 4R_0$. The bubble is centered in the middle of symmetry axis, as reported in Fig. 5.9. A uniform mesh size is chosen, with $1\mu\text{m}$ element size. Such a fine grid is necessary in order to solve the thin thermal boundary layer surrounding the bubble interface. As boundary conditions, a pressure outlet is set at all boundaries except for the axis. Gravity effects are neglected. The initial bubble size is large enough to neglect vapor saturation temperature rising due to pressure jump across the interface, then saturation temperature is equal for both phases. The velocity field is zero. Initial temperature is saturation temperature for the bubble, while the liquid is superheated at a temperature $T_\infty = T_{sat} + 5^\circ\text{C}$.

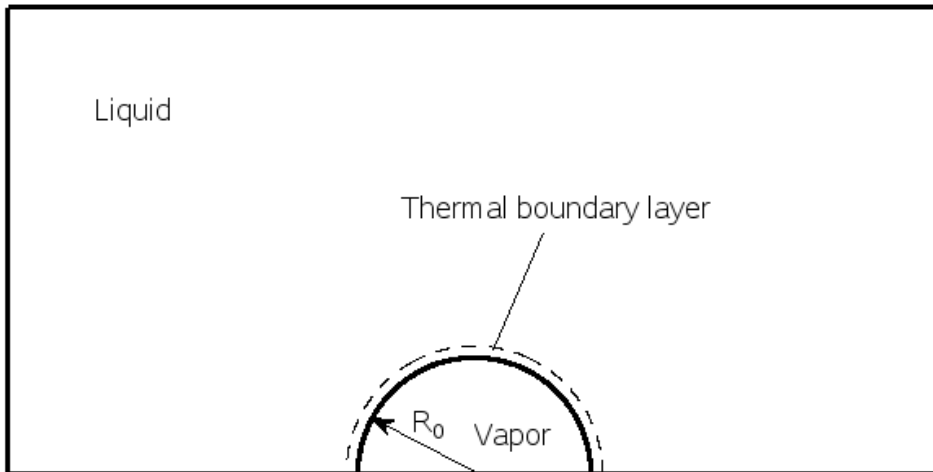


Figure 5.9: Initial condition for axisymmetric bubble growth simulation. The bubble is placed at the center of axis boundary. The bubble is at saturation temperature while the liquid is superheated. A thin thermal boundary layer surrounds the bubble on the liquid side.

5.4.2 Initial thermal boundary layer placement

A thin thermal boundary layer is placed around the interface on the liquid side. Since the simulation starts at $t = t_0$, when $R(t_0) = R_0$, a thermal boundary layer has been developing around the bubble since the beginning of heat-transfer-controlled growth stage. The temperature field around the bubble at $t = t_0$ can be extrapolated from the Scriven solution [121] as a function of spatial coordinate r and time. The thickness of initial thermal layer δ_T is defined as:

$$\delta_T = r(T = T_{sat} + 0.99(T_\infty - T_{sat})) - R_0 \quad (5.9)$$

Figure 5.10 reports an example of initial thermal layer profile in a dimensionless radial coordinate, as given by the Scriven solution. This profile is fitted through a parabolic curve in order to have an easier implementation. Coefficients of the parabola are obtained imposing the following boundary conditions:

$$\begin{aligned} T(r = R_0) &= T_{sat} \\ T(r = R_0 + \delta_T) &= T_\infty \\ \frac{\partial T}{\partial r}(r = R_0 + \delta_T) &= 0 \end{aligned}$$

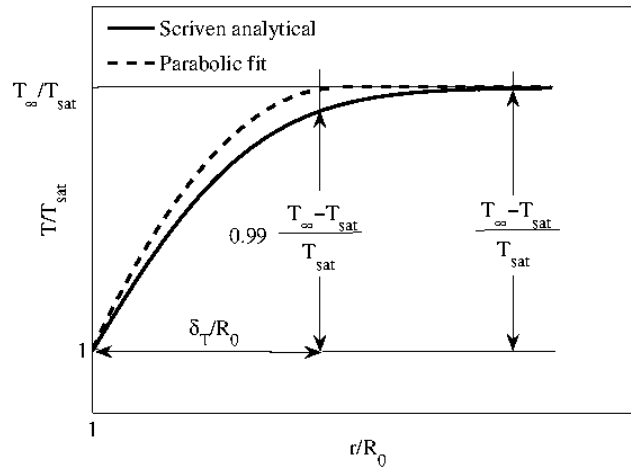


Figure 5.10: Initial dimensionless temperature profile at the bubble interface on the liquid side.

Great attention has to be paid to initial thermal boundary layer position. Analytical initialization suggests thermal layer to begin at $r = R_0$. This is true in those cells for which interface lays upon the background grid. Nevertheless, in those cells which interface is less aligned with the grid (close to $\pi/4$ and $3/4\pi$), cells centroids are located at $r > R_0$. Then, in those cells, thermal layer intersects the bubble interface, leading to a faster initial growth rate than analytical. To avoid this effect, the thermal boundary layer is initialized with a bit of misplacement, about 1-2 cells, outside the bubble interface.

5.4.3 Working fluids properties

Three different fluids were tested. Water at atmospheric pressure and HFE-7100 at 0.52 bar, both with $\beta = 15.1$ and $\delta_T = 7 \mu\text{m}$ and R134a at 0.84 bar, with $\beta = 9.34$ and $\delta_T = 11 \mu\text{m}$. The choice of each system pressure was done in order to have similar growth constants for the fluids. All vapor and liquid properties for the fluids are considered constant at the saturation temperature. They are summarized in Table 5.2. For what concerns the accommodation coefficient, Hardt and Wondra [7] performed some benchmarks to validate the evaporation model and obtained a good agreement with the analytical solutions with an accommodation coefficient set to 1. We repeated some of the Hardt and Wondra benchmarks and found the same

Property	Water		HFE-7100		R134a	
	Liquid	Vapor	Liquid	Vapor	Liquid	Vapor
ρ [kg/m ³]	958	0.597	1425	5.15	1388	4.43
c_p [kJ/kg·K]	4.22	2.03	1.43	0.9	1.27	0.72
λ [mW/m·K]	679	25	61.8	10.3	106	9
μ [$\mu\text{Pa}\cdot\text{s}$]	277	12.55	356	11.13	401	9.64
h_{lv} [kJ/kg]	2257		117.8		219.5	
σ [mN/m]	59		13.6		16	
ϕ [kg/m ² sK]	6.94		15.03		22	

Table 5.2: Properties of the working fluids. ϕ is the kinetic mobility, computed through Eq. (3.23). Saturation temperatures are 100 °C for water, 41 °C for HFE-7100 and -30 °C for R134a.

results, then the accommodation coefficient was always set as unity in the simulations performed.

5.4.4 Setting of diffusion parameter

The evaporation model computes the local evaporation rate at the interface and derives a smoothed rate by solving the diffusion equation (3.26). The diffusion parameter D does not influence only the numerical stability of the computation, but it is also responsible of the correct bubble growth rate with time. As a matter of fact, a too small value would not diffuse adequately evaporation rate φ_0 , leading to instabilities, but on the other hand a too large value could lead to violation of global mass conservation. The latter happens when diffusing the evaporation rate across a curved interface, because the integral over the domain of diffused φ evaporation rate is not the same on both sides of the interface, then the rate of liquid disappearing does not coincide with the rate of vapor created. Hardt and Wondra proved in [7] that this error scales with \sqrt{D}/R .

To explore the sensitivity of the diffusion constant, we solved the Eq. (3.26) in

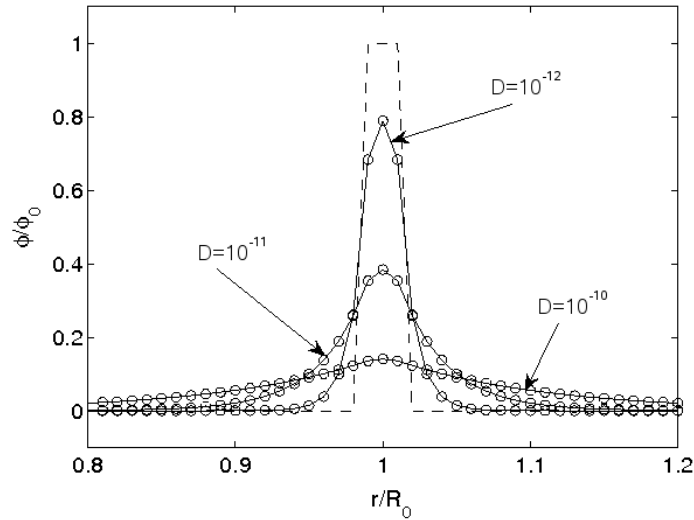


Figure 5.11: Smoothing of the original evaporation rate φ_0 (dash line) into φ (solid lines), for different values of the diffusion constant D . The white circles are the cell centroids positions.

a cylindrical reference frame invariant along the axial and angular coordinates, such that $\varphi = \varphi(r)$. A local evaporation rate $\varphi_0 = 1$ was concentrated on three computational cells located at $r = R_0$. The Figure 5.11 shows the profile of $\varphi(r)$ in a window including $r = R_0$ for different values of the diffusion constant. Diffusion constant $D = 10^{-12} \text{ m}^2$ lowers the peak of φ of about 20% and diffuses the evaporation rate over 6-7 cells per side. The choice $D = 10^{-11} \text{ m}^2$ is more conservative and it is the value set in the simulations for all the fluids. It lowers the peak to 40% of its unsmoothed value and diffuses evaporation rate over about 15 cells per side. The relative error in mass conservation is around 10^{-8} . Diffusion constants for HFE-7100 and R134a could be lower than the water one, since their growth rate is rather less. However, due to the small relative error in mass conservation, the same value was set.

5.4.5 Results

The bubble grows due to the evaporation of the liquid phase in interface cells, with evaporation rate locally proportional to interface cell superheating. At each time

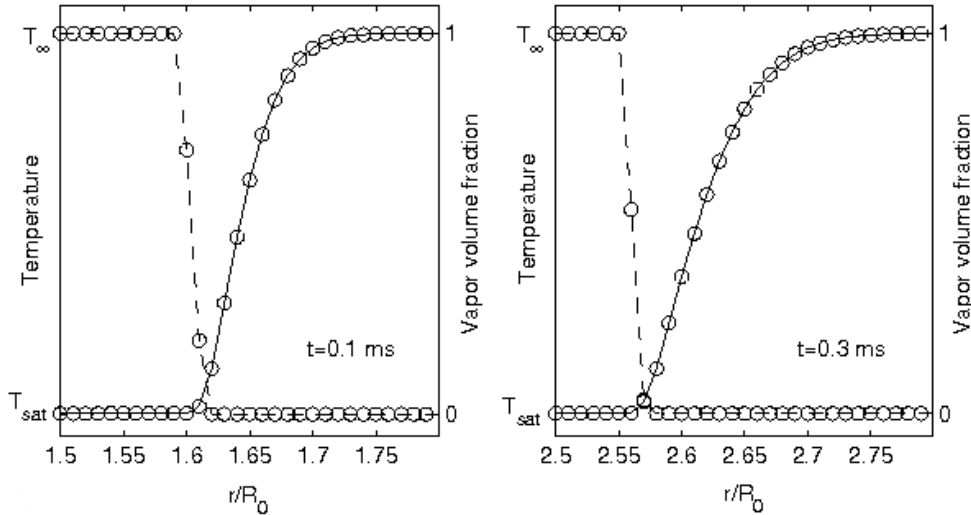


Figure 5.12: Temperature and vapor volume fraction profiles across the interface at different time instants for water. The solid line is temperature profile and the dash one is the volume fraction profile. White circles are cell centroids positions.

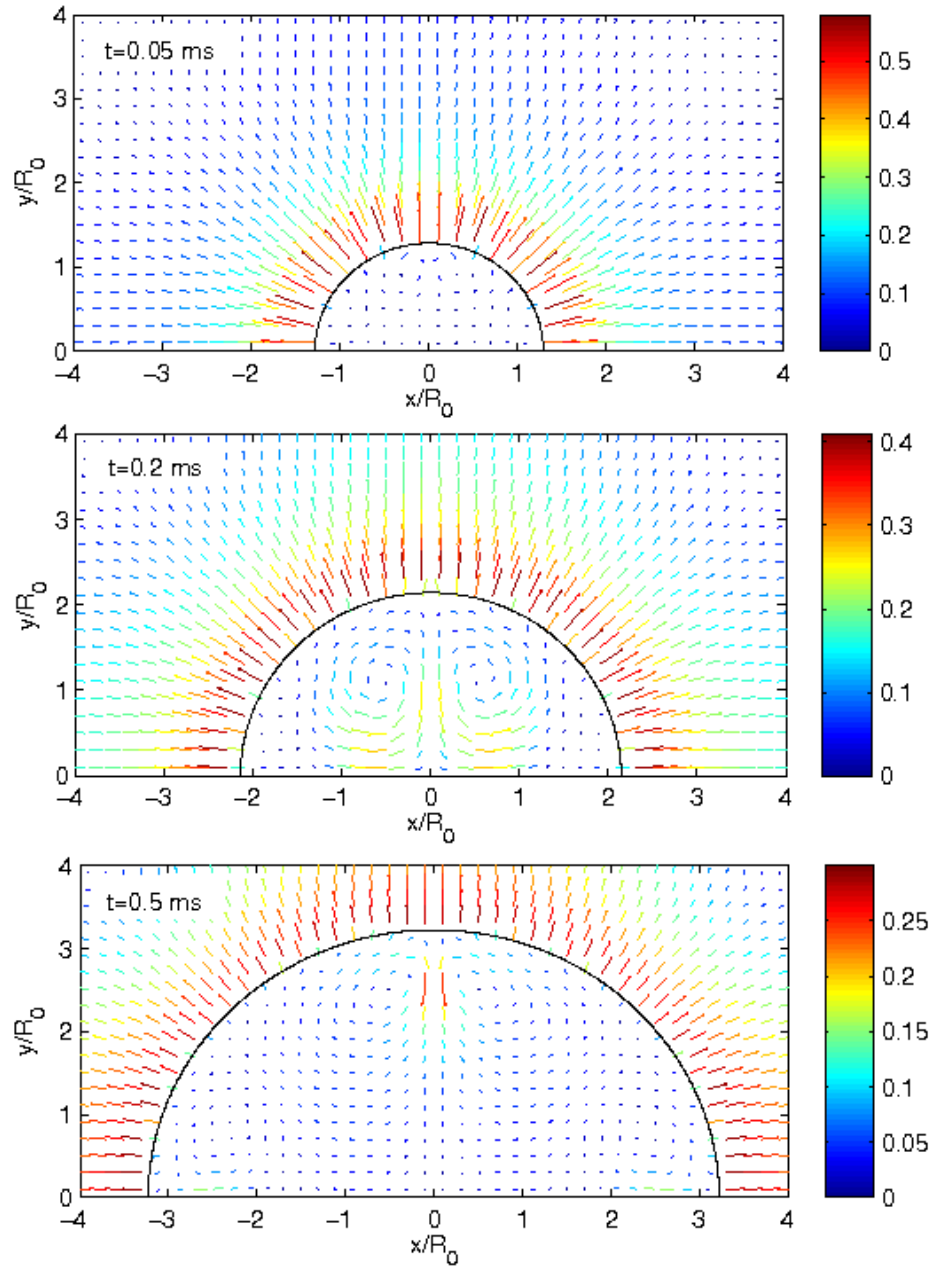


Figure 5.13: Velocity vectors and bubble interface positions for water bubble simulation at various time instants. Vectors are colored by velocity magnitude reported on the right in m/s units and interface positions are computed as half volume fraction contours.

step, the evaporation model takes away the latent heat from the interfacial cells where evaporation occurs, thus cooling down the cells to a temperature close to the saturation temperature. Then, the thermal layer moves with bubble growth, staying always in contact with the interface, as shown in the Fig. 5.12 for water at different time instants.

During the whole simulation, the bubble shape remains spherical. At the initial stage of this work, this was proved not to happen using Youngs method for evaluating interface curvature. Moreover, growth was too fast due to the high convective heat transfer led by spurious velocities. Instead, the spherical shape is kept during growth by the Height Function. The Fig. 5.13 shows water bubble interface and velocity vectors at different growth stages. Velocity vectors around the interface always point to the radial direction with uniform magnitude, as a consequence the growth proceeds radially and uniform with respect to the angular direction. The magnitude of the interface velocity vectors decreases with time as $1/R$, since bubble growth rate is proportional to liquid vapor interface ($\propto R^2$), but inversely proportional to volume ($\propto R^3$).

Figure 5.14 shows the bubble radius evolution obtained through the HF method, compared to analytical solutions, for all the fluids. Numerical data show very good

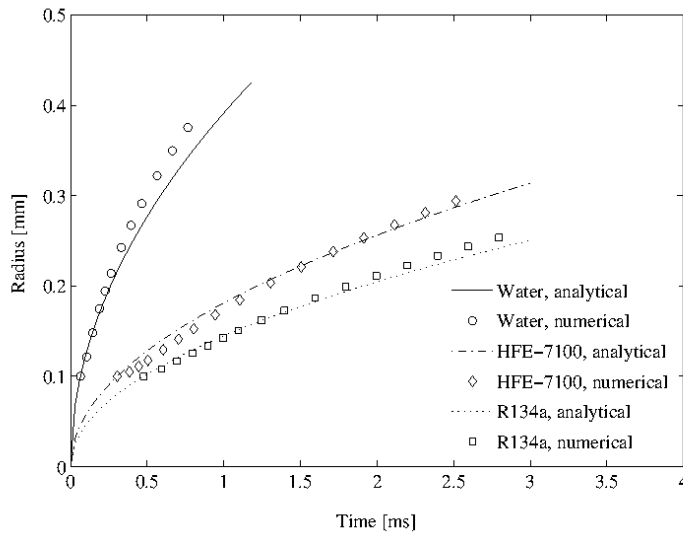


Figure 5.14: Vapor bubble radius over time for analytical and numerical solutions.

agreement with analytical results, thus validating our choice of an accommodation coefficient set as unity. Note that the analytical solution of the problem was obtained by setting the interface at saturation conditions, while the evaporation model in the numerical solver is based on interfacial superheating. Since the interfacial resistance to mass transfer is very low for all the fluids tested, the interfacial temperature stays always very close to the saturation condition (actually little above of about 0.1 K), hence analytical and numerical solutions can match.

For each fluid, the bubble numerical growth rate follows a \sqrt{t} proportional law, as it should be from Eq. (5.8). This does not happen during the initial growth phase, in a more evident way for HFE-7100 and R134a. The reason is that at the beginning of the simulations, the initially misplaced thermal boundary layer arranges to fit the interface position. This settlement phase is reflected on numerical growth rates lower than analytical ones at the beginning of the simulations. As detected by Kunkelmann and Stephan [122], the liquid thermal conductivity is the parameter that rules the length of this thermal layer settlement phase. The higher the liquid thermal conductivity is, the faster is thermal layer arrangement. For this reason, numerical bubble growth rate deviation from the analytical curve is more evident for refrigerant fluids and is highest for HFE-7100, which has the lowest thermal conductivity.

5.5 Concluding remarks: set-up of the evaporation model

There are two variables involved in the evaporation model which the user may need to tune when performing simulations. The first is the accommodation coefficient, which is a property of the fluid simulated and of the operating conditions as well and it can range from 0 to 1. Difficulties in its experimental measurement prevent the definition of a unique value for each fluid, however evidence suggests it to be very close to one for common fluids. Comparisons of numerical with analytical solutions confirm this hypothesis. As well, we obtained good agreement of numerical simulations with analytical solutions by setting an accommodation coefficient equal to one. For this reason, in the simulations discussed in the remainder of this thesis we always set a unity coefficient.

The second parameter to fix when setting-up the evaporation model is the diffu-

sion constant which governs the rate of smoothing of the evaporation rate, see Eq. (3.26). Note that it is a mathematical parameter which influences solely the local evaporation rate, but not the global integral of the evaporation rate, therefore the value chosen for D does not affect the global rate of vapor creation. However, this is true provided that excessive smoothing across curved interfaces is avoided, because the mathematical procedure can violate local mass conservation. Therefore, we suggest to set a value of the diffusion constant adequately small to smear the original evaporation rate only over few computational cells to avoid instabilities, however checking whether mass is preserved.

Chapter 6

Results on elongated bubbles motion in adiabatic condition

This Chapter deals with the further validation of the numerical framework by means of test cases more meaningful from the physical point of view than the analytical benchmarks discussed in the previous Chapter.

We study the rising of Taylor bubbles within vertical channels through stagnant liquid, due to buoyancy forces. Then, we analyze the flow of elongated bubbles within horizontal channels as consequence of a liquid inflow, neglecting gravitational effects. Both of the configurations are adiabatic, thus without phase change. The latter configuration is the starting point for the simulation of evaporating bubbles, which will be considered in the next Chapter.

In this Chapter, the results of the simulations of vertical rising and horizontal flowing bubbles are discussed separately and compared with experimental results and analytical models.

6.1 Taylor bubbles rising in vertical circular channels

It is referred to the Section 2.1 for the discussion of the regarding experimental and numerical literature which has been the background for the simulations that are going to be presented.

The target of this study is to analyze the set-up, the performances and the limits of the numerical framework on the axisymmetrical modeling of Taylor bubbles rising

within stagnant liquid due to buoyancy. The study is reported with the following outline: detailed analysis of the simulation sensitivity to initial conditions and numerical parameters; validation of the liquid flow field surrounding the bubble by comparison with the PIV results of Bugg and Saad [56]; simulation of nine test cases under various operating conditions in order to test the numerical method.

6.1.1 Simulation sensitivity analysis

We perform a sensitivity analysis of the numerical simulation to physical and numerical parameters and to bubble initial conditions. The case simulated has values of $Eo = 100$ and $Mo = 0.01$. The effect of the variation of the parameters is observed in the transient and terminal velocity of the bubble, computed as reported in the Eq. (5.7).

We initialize a gas bubble as a cylinder with spherical rounded ends, placed at the bottom (top) of the domain for fixed (moving) reference frame simulations. The boundary conditions are all no-slip for the fixed reference frame. For the moving reference frame simulations, we impose a fixed velocity at the side wall and the same velocity as liquid inflow at the top of the domain, an outflow condition at the bottom. As initial condition, velocity is zero throughout the domain for the fixed reference frame and equal to the velocity of the liquid inflow in the moving frame case. Figure 6.1 reports a sketch of bubble initial configuration for the fixed reference frame.

The following parameters are the objects of the analysis: reference frame, fixed or moving; domain length L ; initial film thickness δ ; initial bubble length L_b ; domain computational grid given as $D/\Delta x$, with $D = 10$ mm being the channel diameter and Δx the mesh size; simulation time step given as $\Delta t/(\Delta x/U_b)$, where $\Delta x/U_b$ is

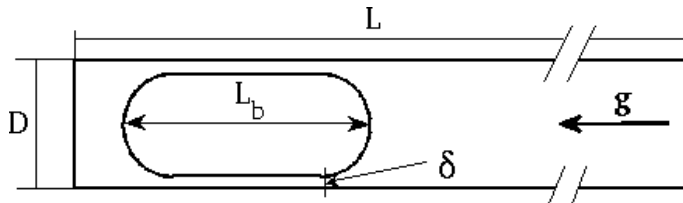


Figure 6.1: Bubble initial configuration.

a time scale representing the time it would take for the bubble to travel one grid spacing at the terminal velocity U_b estimated through the White and Beardmore flow pattern map reported in Fig. 2.1.

The first simulation of the sensitivity analysis was run fixing each parameter involved to a chosen starting value. Then, we performed several test cases varying one at a time each parameter object of the analysis within a chosen range of values.

We chose the starting value for each parameter according to Bugg *et al.* [61] set-up, but we considered also the set-up for the axisymmetrical simulations of Taha and Cui [64], Ndinisa *et al.* [62] and Hayashi *et al.* [66], summarized in the Table 6.1. The Table 6.1 reports also the values tested in the present work and, marked by an asterisk, the starting value chosen for each parameter.

Only Taha and Cui tested a moving reference frame and they reported a faster attainment of the steady state condition for the bubble rise. We started with a fixed reference frame.

We kept constant the domain length to $8D$ according to Bugg *et al.*. This length is sufficient for the bubble to reach a steady rising in a fixed frame, as well as to capture the whole flow disturbance caused by the bubble in a moving frame.

Taha and Cui set the initial film thickness according to a guess value calculated using a mass balance and an estimated terminal velocity. We chose the starting value $0.1D$ according to Hayashi *et al.* and Ndinisa *et al.* and we tested different initial thickness keeping constant the bubble volume.

We initialized the bubble as a cylinder with spherical rounded ends as well as

Parameter	[61]	[64]	[62]	[66]	Present work
ref. frame	fixed	moving	fixed	fixed	fixed*,moving
L	$8D$	$11D$	$8D$	$9D$	$8D$
δ/D	–	variable	$\simeq 0.13$	0.1	0.05,0.1*,0.15
L_b/D	2	$\simeq 2$	$\simeq 2.5$	$\simeq 2.3$	2*,3
$D/\Delta x$	50	104	76	64	30,40,60*
$\Delta t/(\Delta x/U_b)$	–	–	–	–	1/10*,1/50

Table 6.1: Numerical parameters and initial conditions for the considered literature and the present work. Values with asterisks are the starting settings.

Bugg *et al.* and Hayashi *et al.*. Ndinisa *et al.* chose a cylindrical shape and Taha and Cui a slug shape.

The bubble initial length is around $2D$ for all the studies considered, we tested also a $3D$ length keeping the starting value of the film thickness.

All the considered studies employed uniform computational grids. Rather than discuss on the mesh element size, it would be more reasonable to consider the minimum terminal film thickness to element size ratio for each published work. Such information is available only for Bugg *et al.* work in which the minimum film thickness is discretized by two cells and for Ndinisa *et al.* work which performed a single simulation with 9 cells within the terminal film. We started with $D/\Delta x = 60$ then we only coarsened the mesh, since excellent agreement was obtained already with the starting one.

We do not report the simulation time step of the considered studies since it depends on the numerical methods adopted.

We did not test the effect of different density and viscosity ratios. We set density ratio to 1000 and viscosity ratio to 50, as for water-air flow.

Figure 6.2 reports the bubble Froude number evolution with time for all the simulation runs. The White and Beardmore map [1] suggests for this configuration a terminal Froude number of 0.295. All the cases simulated lead to the same terminal value of $Fr = 0.293$, thus very close to experiments.

Differences are noticeable only in the transient behavior, depending on the reference frame and on the initial conditions for the bubble. The moving reference frame allows the bubble to reach the steady state 10% faster, thus decreasing the computational time of the simulation, as reported also by Taha and Cui [64]. We observed that the initialization of the velocity field with the value of the liquid inflow is fundamental to shorten the computational time in the moving reference frame case. A thinner film slows down the rising, since the velocity of the falling liquid in the film is limited by the viscous boundary layer, while a thicker film leads to a faster transient phase. The longer bubble has the slowest transient stage, since it takes more time for the bubble to adjust its shape according to the forces acting on it. Thus, it can be concluded that the initial conditions for the bubble shape influence only the transient rise.

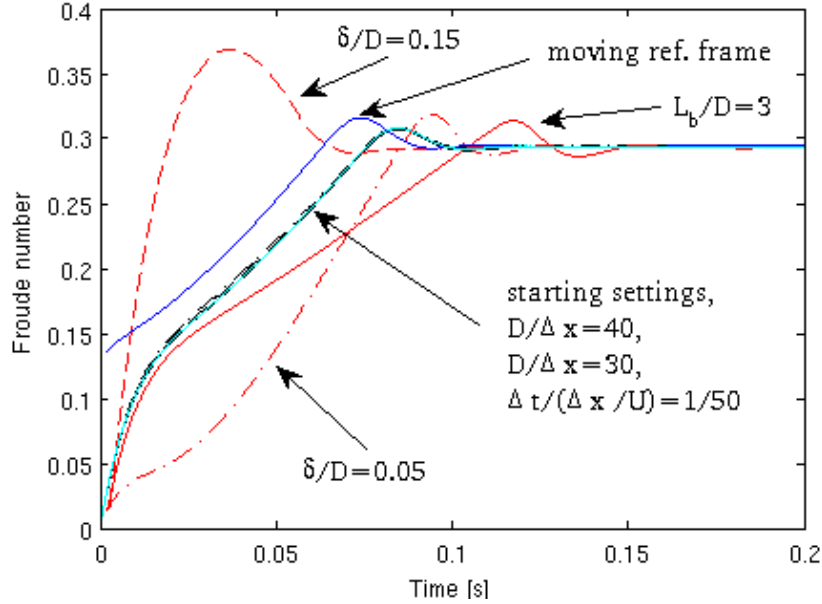


Figure 6.2: Bubble Froude number for $Eo=100$ and $Mo=0.01$ from the beginning of the simulations to the steady state.

All the computational grids tested give the same results, hence the liquid film is well-solved by all the grids. The coarsest mesh considered has $\delta/\Delta x = 3$, thus it can be concluded that 3 computational cells are enough to discretize the liquid film.

The starting time step value is sufficiently smaller than the defined time scale $\Delta x/U_b$ such that the bubble interface travels much less than one grid spacing in one simulation time step. This ensures a stable time-marching of the numerical solution and a smaller time step does not improve the results.

6.1.2 Comparison with PIV analysis

Bugg and Saad [56] made PIV measurements around an air Taylor bubble rising in stagnant olive oil. The configuration adopted yielded $Eo=100$ and $Mo=0.01$ and the terminal velocity of the bubble expressed by means of the Froude number led to $Fr=0.303$. The detected liquid velocity field showed an axisymmetrical flow field. Setting the parameters as marked by the asterisks in Tab. 6.1, we simulated the same conditions of the PIV experiment and in the following we compare the numer-

ical liquid flow around the bubble, at steady state, with the experimental data.

Figure 6.3 reports the liquid flow field across the bubble for the numerical simulation. The rising bubble accelerates the liquid ahead of it and this fluid is pushed sideways to allow the bubble to rise. The liquid is then pulled downward by the gravitational field and it accelerates within the film region, up to a constant velocity profile where the wall shear stress balances the weight of the film. Below the bubble, the liquid from the falling film moves toward the centerline of the axis. The weak effect of the viscosity causes recirculation to occur in the wake, the fluid changes direction moving upward along the channel axis thus pushing the bubble rear. As a consequence, the bubble rear shows an indented profile.

Figures 6.4 and 6.5 show the liquid velocity components, axial u_z^* and radial u_r^* , made non-dimensional by the bubble terminal velocity U_b . The radial and axial coordinates are expressed through dimensionless quantities computed respectively as $r^* = r/R$ and $z^* = z/D$, locating the reference $z = 0$ at the bubble nose. See the Fig. 6.3 as reference for the coordinates system and for the location of the visualization planes of the velocity profiles discussed in the following.

In both the experimental and numerical cases the axial velocity of the liquid at the bubble tip equals the bubble velocity while the radial component is negligible, as required by the symmetry condition. The Figure 6.4(a) shows that the axial velocity of the liquid along the axis decreases below $0.05U_b$ already at $D/3$ ahead of the bubble.

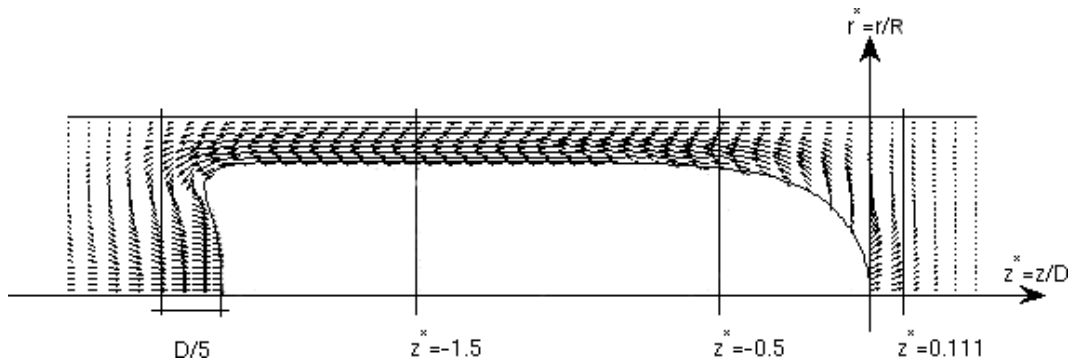


Figure 6.3: Liquid flow field around the bubble. Gas phase velocity vectors are not reported for the sake of clarity.

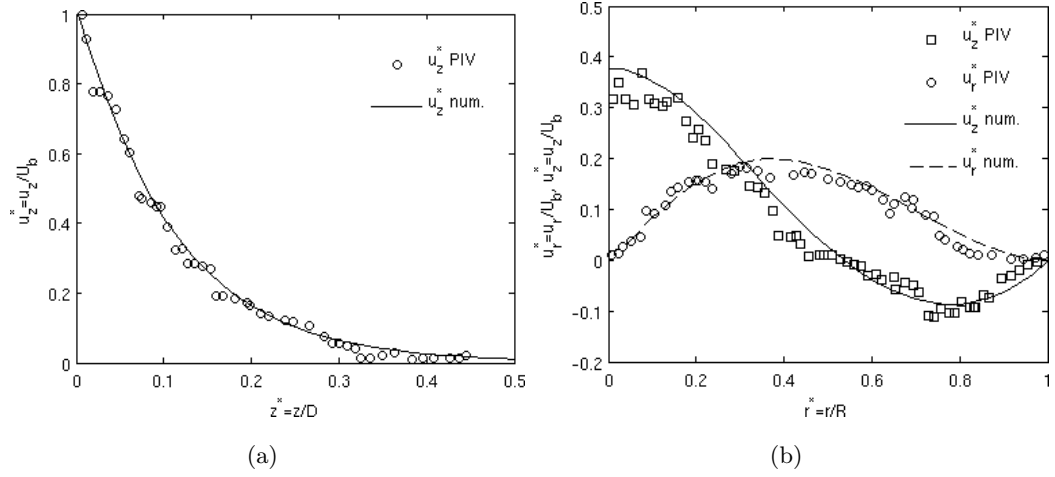


Figure 6.4: (a) Axial non-dimensional velocity along the axis above the bubble nose. (b) Axial and radial non-dimensional velocities at $z^* = 0.111$ (above the bubble).

Figure 6.4(b) shows the velocity components above the bubble, very close to the tip. The axial velocity is positive at the center of the channel, due to the liquid pushed by the bubble, then the gravity pulls down the liquid at the sides of the channel. The radial component is zero at the center of the channel and reaches a maximum close to mid-way between the center and the side.

Figure 6.5(a) shows the velocity components in the liquid film at $z^* = -0.5$, where liquid is still accelerating. The velocity still has a weak radial component due to the pushing effect of the interface, the axial component reaches a maximum close to the interface. Moving lower ($z^* = -1.5$), the liquid within the film has accelerated up to a velocity for which the wall shear stress is able to support the weight of the liquid. The radial velocity is zero while the axial one has a maximum localized at the interface, as shown by Fig. 6.5(a). The film is considered fully developed. The equilibrium film thickness in the simulation is $\delta/D = 0.122$, close to the experimental one of $\delta/D = 0.128$.

Figure 6.5(b) shows the velocity components at $D/5$ below the bubble, in the wake. The liquid from the falling film moves from the side to the center of the channel, as shown in Fig. 6.3, refilling the wake. This is the reason of the strong negative radial component of the velocity. The axial component shows a change in the direction from the side to the center, where liquid moves with the same velocity

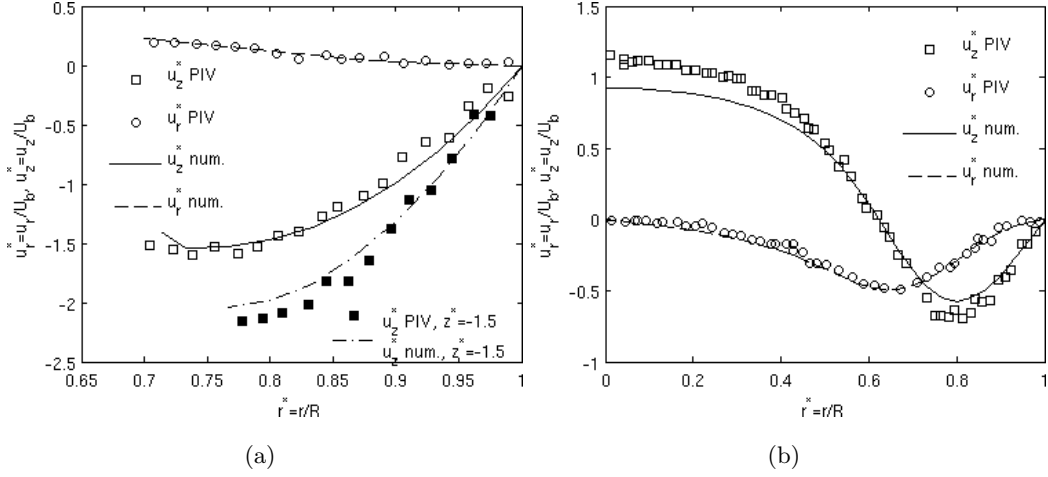


Figure 6.5: (a) Axial and radial non-dimensional velocities at $z^* = -0.5$ (across bubble nose) and $z^* = -1.5$ (across the bubble where the film is constant). (b) Axial and radial non-dimensional velocities at $D/5$ below the bubble.

of the bubble. The numerical axial component at the channel center underpredicts the experimental value by about 15%. The reasons are twofold: there is a slight difference in the bubble bottom shape from the simulation to the experiment, in which the bubble profile was sketched by hand from the PIV image; furthermore, the flow in the wake changes very rapidly along z , therefore even small errors in the location of the distance $D/5$ lead to high differences in the velocity.

However, we can conclude stating an excellent agreement of the numerical flow field was found in comparison with the experimental one.

6.1.3 Numerical simulations of Taylor bubbles: results

We simulated Taylor flows for nine different couples of Eo and Mo numbers, combining $Eo = 10, 40, 100$ with $Mo = 10^{-8}, 10^{-2}, 10$. The couples chosen span widely all the regions of the White and Beardmore [1] flow pattern map shown in the Fig. 2.1. Our objective is to test the range of reliability of the axisymmetrical model to simulate Taylor bubbles.

The numerical and the physical parameters of the simulations, as the initialized bubble, are set as reported in the Tab. 6.1. Figure 6.6 summarizes terminal bubbles shapes, velocity and liquid film thickness. The terminal velocities are compared with

White and Beardmore map [1] and film thicknesses with the Brown [52] theoretical expression reported in Eq. (2.1), but also the Han and Shikazono correlation [3] reported in Eq. (2.14) is taken into account.

Cases 1 and 2 share the feature to have an inverse viscosity number N_f greater than 500, respectively 3162 and 1590, then according to Campos and Guede de Carvalho [54] the flow is not axisymmetric. The axisymmetrical simulation is not capable of capturing the physics of the flow and the errors cause the detachment of some parts of gas from the main bubble. The rise does not reach a steady state, but the velocity of the bubble oscillates around a value very close to experiments.

Case 3 satisfies the condition on the inverse viscosity number. The combined effect of a low Morton number (low viscosity) and a relatively small Eötvös number (high surface tension) tends to flatten the center of the bubble bottom but to round the bottom sides. It is not possible to define a unique value for the film thickness, since it is not constant along the bubble. Campos and Guede de Carvalho [54] obtained theoretically the expression (2.3) for the minimum length of the bubble $L_{b,min}$ to reach a constant film thickness.

In this case $L_{b,min} = 2.3D$ while bubble length is $L_b = 1.7D$. The condition expressed in Eq. (2.3) is not satisfied, for this reason the film thickness does not become stable, but an average can still be defined. The value reported in Fig. 6.6 refers to the minimum film thickness across the bubble, located at its bottom. It underpredicts the theoretical one. The averaged film thickness in the central portion of the bubble is $\delta/D = 0.067$, which is in better agreement with theory. It is remarkable that, even with a not completely developed film, the Froude number is very well predicted, with a negligible error. This is consistent with White and Beardmore observation that the terminal velocity of cylindrical bubbles is independent of the length of the bubble.

Cases 4 and 5 both satisfy the minimum bubble length condition such that a stable condition for the film is reached, therefore the bubbles show a cylindrical shape below the nose. The Morton number is still low enough to lead to a flattened bubble bottom, but the higher surface tension of case 5 with respect case 4 justifies the change in concavity. Numerical film thicknesses and Froude number agree in excellent way with theory and experiments. Han and Shikazono correlation for the film thickness [3] leads respectively to $\delta/D = 0.115$ for case 4 and $\delta/D = 0.1$ for case

5, in reasonable agreement with numerical results.

Case 6 shows a constant film thickness below the bubble top. With respect to case 5, the lower Eötvös number leads to the rounding and enlargement of the bubble bottom. Thus, even if condition (2.3) is largely satisfied, the flat liquid film is disturbed by the bottom of the bubble. The numerical film thickness reported in Fig. 6.6 refers to the minimum value, but the thickness observed in the stable region is $\delta/D = 0.103$, very closer (3% error) to Brown theory. For this case Han and Shikazono correlation predicts a very thinner film, around $\delta/D = 0.038$. Froude number is well predicted, the relatively high deviation with experiments (10%) is due to the difficulty to extrapolate such a low value on White and Beardmore map.

Cases 7 and 8 are characterized by the highest Morton number and the very high viscosity tends to round the bottom of the bubble. The high ratio of viscous forces over surface tension effects produces the longest bubbles of the simulated series. The long and stable films have thicknesses which accord very well with Brown theoretical values. Also Han and Shikazono correlation gives good results, leading respectively to $\delta/D = 0.148$ and $\delta/D = 0.12$.

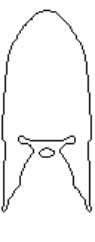
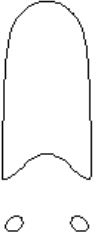
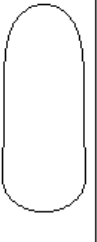
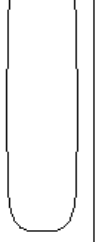
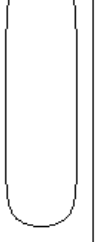
Case	1	2	3	4	5	6	7	8	9
Mo	10^{-8}	10^{-8}	10^{-8}	10^{-2}	10^{-2}	10^{-2}	10	10	10
Eo	100	40	10	100	40	10	100	40	10
									
Fr [1]	0.34	0.32	0.175	0.295	0.22	0.03	0.145	0.065	0.005
Fr_{num} (err)	0.35(2.9)	0.325(1.6)	0.175(0)	0.293(0.7)	0.225(2.3)	0.033(10)	0.139(4.1)	0.062(4.8)	0.006(20)
δ/D [2]	0.042	0.051	0.059	0.123	0.134	0.1	0.161	0.155	0.098
δ/D_{num}(err)	0.058(38)	0.067(31)	0.042(29)	0.122(0.8)	0.135(0.7)	0.09(10)	0.158(1.8)	0.153(1.3)	0.09(8.2)

Figure 6.6: Terminal shape of the Taylor bubbles for the numerical simulations. Terminal velocity is compared with White and Beardmore map [1], film thickness with Eq. (2.1) by Brown [52]. Relative errors are computed as $\frac{|\text{exp-num}|}{\text{exp}} \times 100$.

Case 9, as previous cases 3 and 6, shows a rounded bottom bigger than the top of the bubble, an effect related to the dominance of surface tension effects. It is remarkable that all the cases showing this behavior have the same $Eo=10$, indicating high capillary to gravitational effects. The numerical minimum film thickness underpredicts the theoretical value, while the thickness in the stable region is $\delta/D = 0.103$, closer to theory. Han and Shikazono correlation predicts a lower film thickness $\delta/D = 0.039$, resulting not reliable for this case. The reason for the 20% error in the Froude number prediction is the same as for case 6.

The Figure 6.7 summarizes the results of the nine physical configurations simulated. The axisymmetrical CFD modeling of rising Taylor bubbles is reliable only for $N_f < 500$ in agreement with Campos and Guede de Carvalho [54] experimental

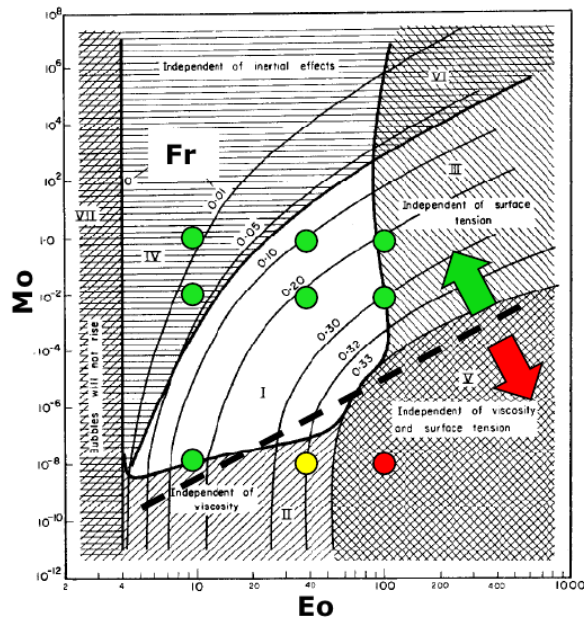


Figure 6.7: Rising Taylor bubbles simulation runs placed within the White and Beardmore [1] flow pattern map. Green circles identify successful simulations, the red circle identifies a failed simulation and the yellow one an intermediate result. The dash black line locates Campos and Guede de Carvalho [54] threshold for axisymmetric Taylor flow.

evidence. For $N_f > 500$ the numerical simulations terminates with the break-up of the bubble.

When the flow is axisymmetric the numerical framework gives excellent results, bubbles terminal velocities agree very well with White and Beardmore [1] map and the shapes are consistent with the effects of the dominant forces. The film thickness in the numerical simulations is in good agreement with Brown theory [52], but at low Eötvös numbers the surface tension tends to enlarge the bubble bottom and the Brown equation overpredicts the liquid thickness in that region. The Han and Shikazono correlation [3] for the liquid film thickness, obtained by fitting data on horizontal flows, is not reliable to predict the thickness for vertical Taylor flows.

6.2 Elongated bubbles flowing in horizontal circular channels

It is referred to the Section 2.2 for the discussion of the regarding experimental and numerical literature which has been the background for the simulations that are going to be presented.

The objective of this study is to test the performance of the numerical framework in simulating the flow of elongated bubbles within horizontal channels drifted by a liquid inflow. We simulated some test cases and the numerical results on pressure drops, film thickness and bubble velocity are compared with experimental correlations. The pressure drops across the bubble are compared with Kreutzer *et al.* correlation [72] reported in Eq. (2.13), the film thickness with Han and Shikazono correlation [3] shown in Eq. (2.14) and the terminal bubble velocity with the expression (2.19) where the Eq. (2.14) is used to calculate the film thickness.

The pressure and velocity field for a chosen test condition is particularly analyzed to detect the differences with respect to the single phase flow, in order to figure out the reasons of the enhanced momentum and energy transport provided by the slug flow.

The flow domain is modeled as a two-dimensional axisymmetrical channel with diameter $D = 1$ mm and length $L = 8D$. The bubble is initialized as a cylinder with spherical rounded ends for the cases at low surface tension and as a slug for

the cases at higher surface tension. The bubble initial length is always $3D$ and the bubble volume is 1.77 mm^3 for the slug shape and 1.65 mm^3 on the other case. The gravity vector is set to zero. The liquid flow into the channel is modeled as a fully developed laminar velocity profile set as boundary condition at the channel inlet and outlet. Each simulation is run until a steady state condition for the bubble velocity is reached. The bubble velocity is computed at each time instant as reported in Eq. (5.7).

Two series of simulations were executed by varying the surface tension and the density of two fictitious fluids, to obtain the chosen Capillary and Reynolds numbers. The viscosity is always set to $0.001 \text{ Pa}\cdot\text{s}$ and the mean velocity of the liquid inflow to $U_l = 0.25 \text{ m/s}$. The liquid to gas density ratio is set to 1000 and the viscosity ratio to 50. The surface tension of the first series is set to 0.01 N/m and four operating conditions were tested by setting the liquid density to 62.5, 250, 1250 and 2500 kg/m^3 . With such conditions the Capillary number is $\text{Ca} = 0.025$ and $\text{Re} = 15.625, 62.5, 312.5, 625$ with both the numbers computed through the liquid mean velocity as reference. The computational grid is a uniform $D/\Delta x = 100$ mesh in order to have at least 5 cells discretizing the predicted liquid film thickness, according to Gupta *et al.* [83] recommendation. The second series has surface tension $\sigma = 0.02 \text{ N/m}$ such that $\text{Ca} = 0.0125$. The densities tested, then the Reynolds numbers, are the same of the first series. The computational domain is refined to $D/\Delta x = 200$ to capture adequately the liquid film dynamics.

The Figure 6.8 shows the bubble terminal shapes for the numerical simulations. For each simulations series the increase of the Reynolds number tends to sharpen the bubble nose, to flatten the rear and to thicken the liquid film as effect of the inertia, as already observed by Aussillous and Quéré [71] and Kreutzer *et al.* [72].

At low Reynolds numbers the liquid film is flat but, as Reynolds is increased, the bubble rear enlarges thus squeezing locally the film. At the highest Reynolds number simulated, the bubble rear in Figs. 6.8(g) and (h) shows some waves whose wavelength seems to be a function of the surface tension. In such a situation the liquid film does not reach a constant thickness because from the bubble nose toward the rear it becomes thinner and then wavy.

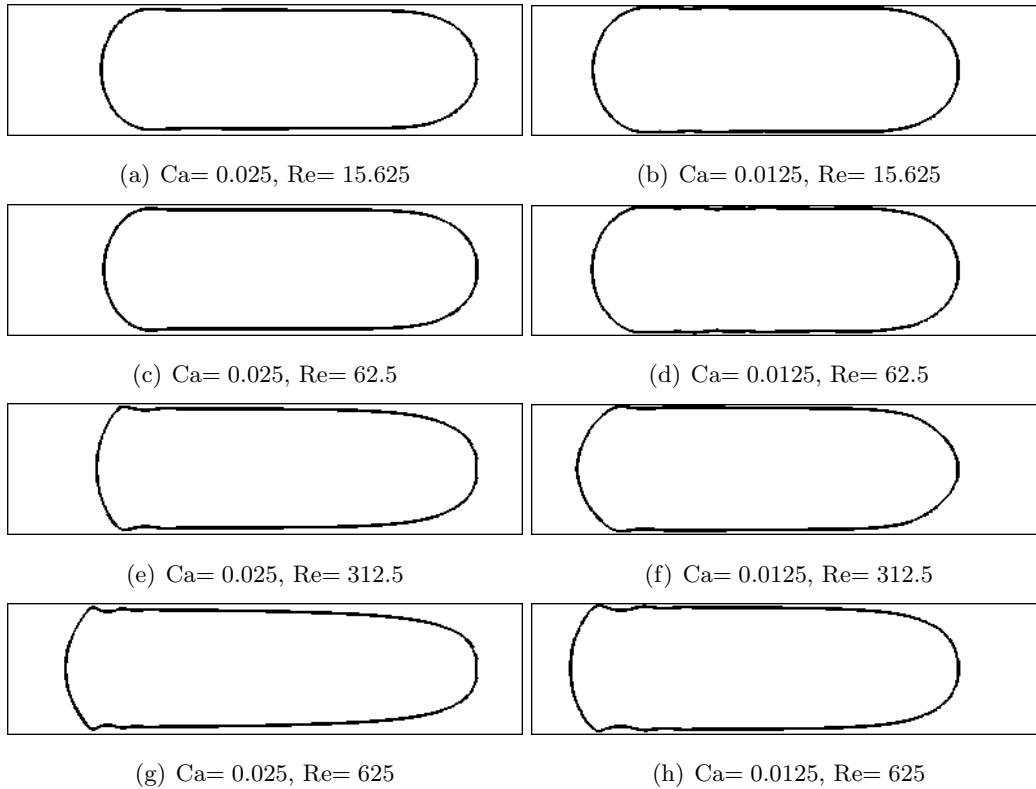


Figure 6.8: Bubble terminal shapes for different test conditions.

By comparing the shapes obtained with $Ca = 0.0125$ with those relative to $Ca = 0.025$, the thinning of the liquid film is evident, as effect of the higher surface tension that tends to round off and thus shorten the bubble.

The Figures 6.9(a) and (b) report the static pressure profiles along the channel axis separately for each simulations series. The zero pressure reference is located at the channel end. The front of the bubble is always more curved than the rear such that the laplacian jump in pressure across the interface generates a higher pressure jump in the front of the bubble than in the rear. The inertia tends to increase the difference among the front and rear curvatures such that the pressure jump across the bubble grows as the Reynolds number is increased. Since the laplacian pressure jump is proportional to the surface tension value, the cases with $Ca = 0.0125$ are characterized by a higher pressure within the bubble.

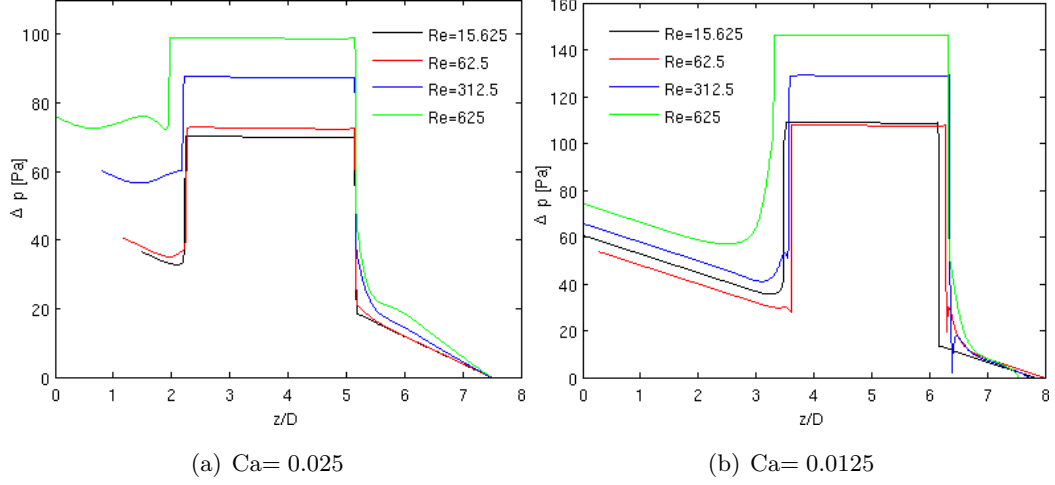


Figure 6.9: Static pressure profiles along the channel axis.

The Table 6.2 summarizes the numerical results on pressure drops, liquid film thickness and bubble terminal velocity compared with the considered correlations. Kreutzer *et al.* correlation (2.13) computes the pressure drops across the bubble. The values reported in the table refer to the pressure drop on the entire channel, which can be predicted by adding an additional term to Eq. (2.13) to account for the pressure drop in the liquid slug:

$$\Delta p = 1.08 \left(\frac{\sigma}{D} \right) (3Ca)^{2/3} Re^{1/3} + \frac{64}{Re} \left(\frac{1}{2} \rho U_s^2 \right) \frac{L_s}{D} \quad (6.1)$$

where L_s is the length of the liquid slug and U_s is the flow superficial velocity required to compute the Capillary and Reynolds numbers. For each simulation run, the flow superficial velocity is obtained by summing the mean liquid velocity and an estimation of the gas superficial velocity. This estimation is computed by considering the simulated channel as part of a longer channel, where the bubbles flow with velocity U_b and frequency $U_b/(8D)$. An estimation of the gas volumetric flow rate is built by multiplying the bubble volume V_b by the transit frequency thus leading to the following expression for the gas superficial velocity:

$$U_{sg} = \frac{V_b \cdot U_b / (8D)}{\pi R^2} \quad (6.2)$$

The simulations reproduce well the rise of the pressure drops as effect of the increase

Ca		0.025			
Re		15.625	62.5	312.5	625
U_s [m/s]		0.331	0.331	0.330	0.333
Δp [Pa]	Eq. (6.1)	60	65	69	73
	num (err)	52 (13.3)	54 (16.9)	71 (2.9)	80 (9.6)
δ/D	Eq. (2.14)	0.0494	0.0493	0.052	0.0573
	num (err)	0.05 (1.2)	0.047 (4.7)	0.05 (3.8)	0.06 (4.7)
U_b [m/s]	Eq. (2.19)	0.308	0.308	0.311	0.319
	num (err)	0.308 (0)	0.305 (1)	0.305 (1.9)	0.315 (1.3)
Ca		0.0125			
Re		15.625	62.5	312.5	625
U_s [m/s]		0.328	0.328	0.330	0.332
Δp [Pa]	Eq. (6.1)	62	67	74	80
	num (err)	57 (8.1)	58 (13.4)	61 (17.6)	82 (2.5)
δ/D	Eq. (2.14)	0.0326	0.0327	0.0349	0.0377
	num (err)	0.0279 (14.4)	0.028 (14.4)	0.035 (0.3)	0.038 (0.8)
U_b [m/s]	Eq. (2.19)	0.286	0.286	0.289	0.292
	num (err)	0.279 (2.4)	0.278 (2.8)	0.285 (1.4)	0.291 (0.3)

Table 6.2: Comparison of numerical results with experimental correlations. The errors between parenthesis are computed as $\frac{|\text{exp-num}|}{\text{exp}} \times 100$.

of the Reynolds number for both the series, the maximum error with Kreutzer *et al.* correlation is of 17.6% and the average error is $8 \div 10\%$. The dimensionless groups involved in the Eq. (2.14) for the liquid film thickness are computed through the bubble terminal velocity measured in each simulation, as suggested by the authors of the correlation. It is not possible to identify a unique value of the film thickness for each simulation run. At low Reynolds the value reported in the Table refers to the thickness on the central region of the film, where it is almost constant. At high Reynolds a constant thickness region does not exist and the value reported in the Table refers to the location where the smooth profile of the bubble matches the wavy profile at the rear, then such value has to be intended as an average.

The thickening effect of the inertia on the liquid film is well captured by the

simulations as well as the thinning effect of the capillary forces, such that the film thickness increases as Ca and Re grow. The accordance with Han and Shikazono correlation is very good and the errors are within the 5% with the exception of the cases with $Ca=0.0125$ and $Re=15.625, 62.5$ whose errors are about 14%. However, the values of the film thickness reported on the Table are average values of the actual thickness in the simulations, which oscillates within $[0.022, 0.032]$ for $Re=15.625$ and $[0.02, 0.038]$ for $Re=62.5$.

The Eq. (2.19) estimates the terminal velocity of the bubble in excellent agreement with the numerical simulations for all the simulation runs, with errors included within 3%. The rise of Ca and Re thickens the liquid film and the bubble shape adjusts to a better hydrodynamic profile, reducing the liquid drag effect thus moving faster. The Armand and Treschev [75] correlation (2.18) overpredicts the bubble velocity by a 25%, but replacing the flow superficial velocity with the mean velocity of the liquid inflow the error would be within 5%.

Analysis of the flow field for $Ca=0.0125$ and $Re=625$

Among the operating conditions simulated, the one characterized by $Ca=0.0125$ and $Re=625$ is the closest to the test conditions of the simulations with phase change that are going to be discussed in the next Chapter, for this reason it is particularly studied in this Subsection.

The Figures 6.10(a) and (b) report the pressure and velocity field across the bubble at the steady state. The pattern of the velocity vectors allows to identify the disturbance on the flow field generated by the bubble transit, which extends less than one diameter behind and ahead of the bubble. The liquid film appears to be almost stagnant, with very small vectors in the central region.

The density of the gas is low enough to make the effect of the inertia negligible within the bubble, as well as the viscous stress. As a consequence, the pressure is uniform throughout the gas phase and its value of about 150 Pa corresponds to the average of the laplacian jump in pressure across the entire bubble interface. The pressure in the central region of the liquid film, where it is almost cylindrical, can be estimated as $p_{bubble} - \sigma/R \approx 110$ Pa because the interface curvature in the (r, z) plane is nearly zero and the second curvature is approximately $1/R$. The wavy profile of the interface at the rear of the bubble is characterized by a curvature that

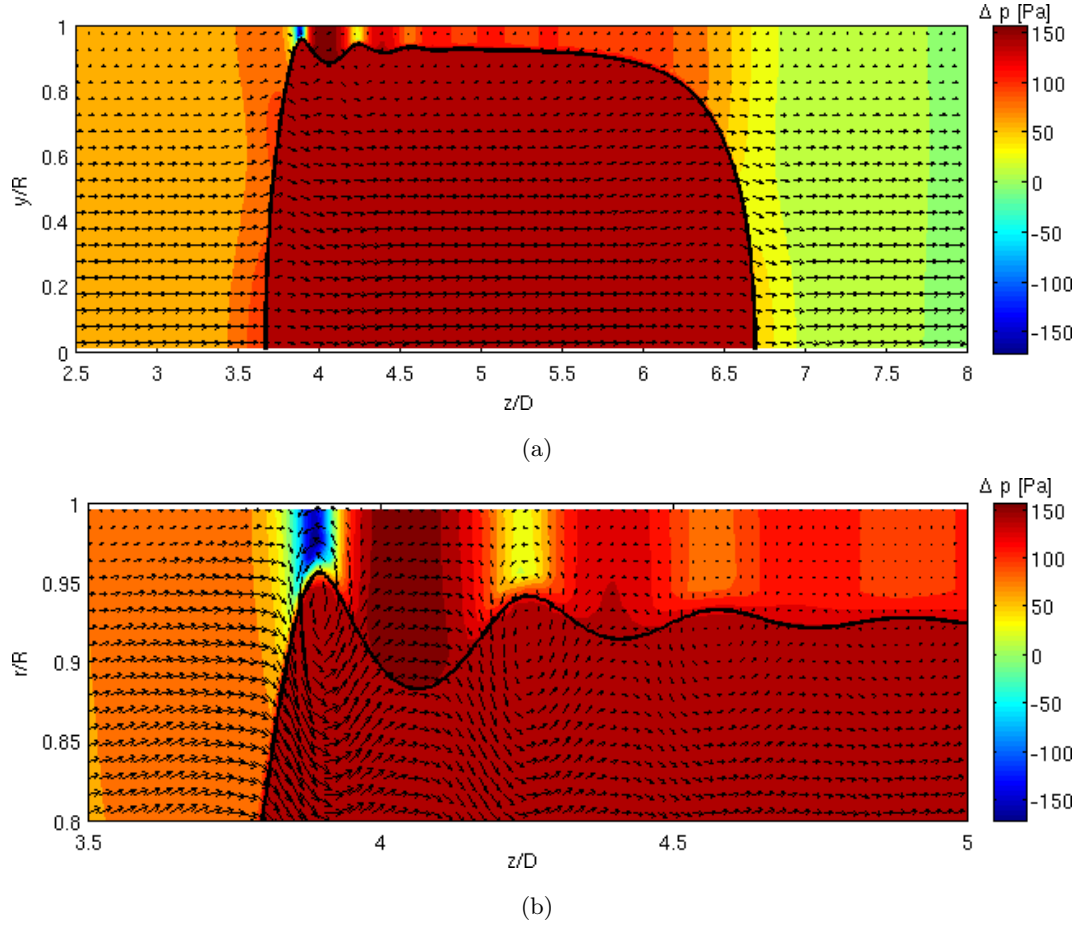


Figure 6.10: Pressure field and velocity vectors across the bubble for $Ca = 0.0125$ and $Re = 625$. (b) is a zoom of the rear bubble region. The figures are not in scale.

changes its sign in the (r, z) plane, generating regions within the film with over- and undershoots of the pressure with respect to the gas phase. These pressure fluctuations force a local recirculation of liquid which may enhance locally the transport of momentum and energy in the proximity of the channel wall.

In order to quantify the effect of the bubble passage in the liquid flow field we reported in the Figures 6.11(a) and (b) the radial profiles of the axial velocity separately in the wake and the film regions, at different axial locations z/D . The position of the bubble rear interface on the channel axis is $z/D \approx 3.7$. The velocity is made

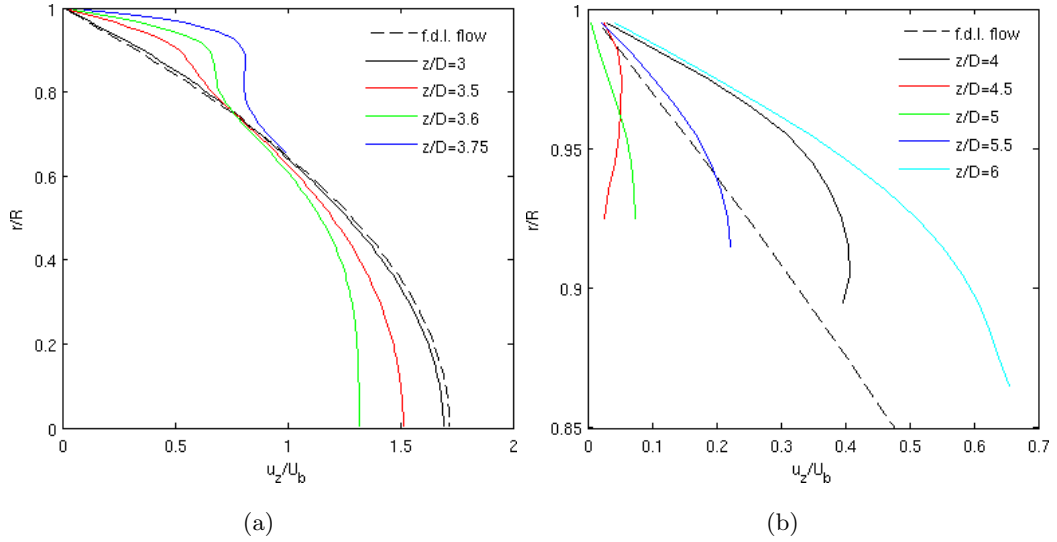


Figure 6.11: Profiles of the dimensionless axial velocity of the liquid along the radial direction at various axial locations in the wake (a) and in the liquid film (b) for $Ca = 0.0125$ and $Re = 625$. F.d.l. stands for fully developed laminar flow. The bubble velocity is $U_b = 0.291$ m/s.

nondimensional by use of the bubble velocity $U_b = 0.291$ m/s. The figures depict also the velocity profile of a fully developed laminar flow given by the Poiseuille law $u(r) = 2U_l(1 - (r/R)^2)$.

At $z/D = 3$, less than one diameter behind the bubble, the axial velocity profile matches the fully developed profile, then the bubble disturbance on the liquid flow becomes negligible behind this location. Moving toward the bubble rear the liquid velocity profile modifies, the value on the channel axis decreases from the maximum value of the Poiseuille profile to the bubble velocity. Since the continuity condition imposes a constant liquid volumetric flow rate behind the bubble, if the liquid velocity on the channel axis decreases it is necessary that moving radially toward the wall the velocity increases with respect to a fully developed profile, as proved by the axial profiles at $z/D = 3.5, 3.6$ shown in Fig. 6.11(a). The higher liquid velocity in the proximity of the channel wall guarantees a better energy exchange among the wall and the liquid if heat exchange exists, but the higher axial velocity gradient increases the wall shear stress thus leading also to higher pressure drop. The axial location $z/D = 3.75$ is partially within the bubble and the liquid axial velocity pro-

file is strongly influenced by the presence of the first recirculation pattern.

The axial velocity profiles in the liquid film region reported in the Fig. 6.11(b) depend on the local recirculation pattern. At $z/D = 4$ a strong clockwise rotating vortex exists (see Fig. 6.10(b)) thus generating a high radial gradient of the axial velocity. At $z/D = 4.5, 5$, the bubble profile is nearly flat such that recirculation within the film is negligible and the liquid velocity is almost zero. Moving downstream toward the bubble nose the film thickens, the bubble interface becomes more oblique and the liquid accelerates in the streamwise direction as demonstrated by the velocity profiles at $z/D = 5.5, 6$.

The Figure 6.12 shows the streamlines of the defect flow field $\mathbf{u} - U_b$ in the wake and the film region. Behind the bubble along the centerline of the channel the liquid velocity exceeds the bubble one as previously discussed, while moving radially toward the wall at above $r/R \approx 0.6 \div 0.7$ the liquid moves slower than the bubble. Thus, the liquid in the wake region undergoes a recirculating motion in a reference frame moving with the bubble and the liquid from the center of the channel is drifted toward the wall. Here, it comes in contact with a liquid layer leaving the film region which tends to adhere to the channel wall. Such adherent film may constitute a ther-

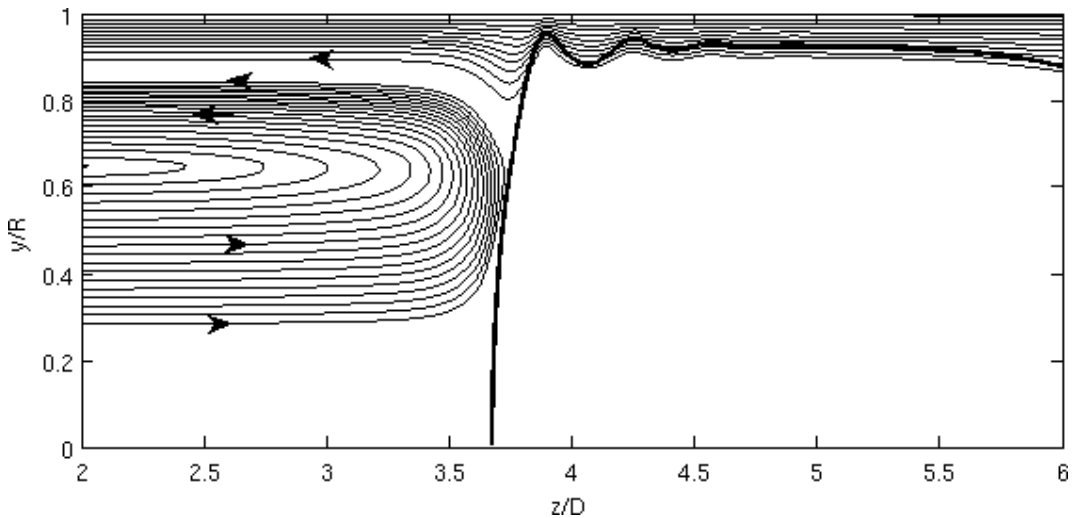


Figure 6.12: Streamlines of the defect flow field $\mathbf{u} - U_b$ in the wake and the film region for $Ca = 0.0125$ and $Re = 625$.

mal inertia for the energy transfer among the bulk liquid and the channel wall, He *et al.* [88] accounted for its effect in the development of a phenomenological model for the heat transfer.

By summarizing the results discussed, the slug flow may enhance momentum and energy transport compared to the single phase flow due to the following effects:

- at high Reynolds numbers, the undulations at the rear of the bubble interface induce small recirculation patterns close to the wall;
- the bubble perturbs the liquid flow field in the wake by increasing the liquid velocity in proximity of the channel wall;
- a recirculation pattern in the bubble wake, whose length scale is of the order of the channel radius, moves liquid from the centerline of the channel to the wall.

6.3 Concluding remarks: limits of the computations

The capability of the numerical framework to simulate elongated bubbles flowing within horizontal circular microchannels has limitations which are intrinsic on the mathematical and numerical models used. The chosen orders of magnitude of liquid-gas density and viscosity ratios, respectively 10^3 and 10^2 , are the maximum values of interfacial jumps in properties that the PISO algorithm, together with the selected options for the solver, is able to manage giving numerically stable computations. The axisymmetrical formulation of horizontal flows adopted is a good approximation as long as capillary forces overwhelm gravitational effects, otherwise a comparison with experimental results obtained for horizontal microscale flows is not feasible. This condition poses a limitation on the surface tension coefficient, which has to be high enough to give a Confinement number over unity. On the other hand, the liquid film thickness decreases as the surface tension is raised, hence when using uniform mesh grids the computational cost of the simulation increases to adequately solve the flow within the film. As well the velocity of the liquid inlet, thus the Reynolds number, has effect on the liquid film thickness. An increase of the Reynolds number leads to thicker liquid films, at least for typical flow configurations with $Ca < 0.01$, but it has

to be also kept below 2000 to avoid turbulent flows. In conclusion, the mesh element size which ensures reliable results and quick computations depends on the operating conditions simulated. However, the computational cost of simulations whose domain is discretized with uniform elements limits the minimum film thickness achievable.

Chapter 7

Results on elongated bubbles motion with evaporation

This Chapter presents the results of various simulations of elongated bubbles flows with phase change. Firstly, the optimal set-up of the numerical and physical parameters involved in the simulation of an evaporating flow is discussed. A grid convergence analysis is performed to obtain the minimum number of computational cells necessary to accurately discretize the temperature and velocity gradients occurring within the liquid film region. The effect of two different sets of boundary conditions at the channel inlet and outlet sections on the bubble dynamics is investigated.

Then, the features of the local temperature and flow fields induced by the evaporating bubble are described, in order to figure out the mechanisms that enhance the wall heat transfer when a slug flow occurs.

Actual experiments on two-phase flows in microchannels involve multiple bubbles in sequence. The results of a simulation run with two bubbles allow to understand the mutual influence among consecutive bubbles and the effect on the wall heat transfer. By assuming that the flow of two bubbles in sequence is a good approximation of an actual flow dealing with the periodical transit of bubble-liquid slug pairs, the heat transfer performance is compared with models and correlations available in the related scientific literature.

7.1 Grid convergence analysis

When a thermal load is applied at the wall of a channel initially filled with saturated liquid, a thermal developing region is generated.

When the interface of a vapor bubble flowing within the heated channel gets in contact with the superheated thermal boundary layer, the evaporation starts. For elongated bubbles such contact likely occurs in the liquid film region, where the thickness of the thermal layer approaches the height of the film.

The evaporation model described in the Section 3.2 cools down locally the liquid temperature to maintain the bubble interface close to the saturation temperature. Therefore, the liquid temperature within the film drops sharply from the highest value at the channel wall to the lowest value at the bubble interface. For this reason, in the film region high temperature gradients take place and the computational grid needs to be fine enough in order to solve the gradients properly. The accurate discretization becomes fundamental in conjunction with the evaporation model, which computes the rate of evaporation proportional to the local interface superheating.

Gupta *et al.* [83] criterion, which suggests that a minimum of 5 cells should discretize the liquid film, is valid in the case of adiabatic or diabatic flows without phase change, but it can not be assumed a priori in the present case.

The objective of this Section is to find out the minimum number of computational cells necessary to discretize the liquid film in order to model properly the temperature gradients, thus leading to correct evaporating bubble dynamics and wall heat transfer.

The flow of an elongated bubble within a heated channel is simulated with four different computational grids. The flow domain is modeled as a two-dimensional axisymmetrical channel with diameter $D = 0.5$ mm and length $L = 20D$. The channel is split in an adiabatic region of length $8D$ followed by an heated region of length $12D$. The bubble is initialized as a cylinder with spherical rounded ends and it is placed at the upstream of the adiabatic region of the channel. The initial bubble length is $L_b = 3D$.

The operating fluid is R113 at the pressure $p = 1.097$ bar and saturation temperature $T_{sat} = 50$ °C, the vapor and liquid material properties are reported in the Table 7.1. The bubble is pushed by a liquid inflow of mass flux $G = 600$ kg/m²s.

Property	Liquid	Vapor
ρ [kg/m ³]	1502	8
c_p [kJ/kg·K]	0.943	0.695
λ [mW/m·K]	63.2	9.62
μ [μ Pa·s]	477	10.4
h_{lv} [kJ/kg]	143.54	
σ [mN/m]	14.4	

Table 7.1: Properties of R113 liquid and vapor at saturation conditions for $T_{sat} = 50^\circ\text{C}$. Pressure is $p = 1.097$ bar.

A flat velocity profile with $U_l = G/\rho_l = 0.4$ m/s is set at the inlet section while at the outlet section an outflow condition is imposed. The temperature of the liquid inflow is equal to the saturation temperature. A constant heat flux of $q = 9$ kW/m² is applied at the heated wall.

The initial velocity and temperature fields are obtained by a preliminary single phase steady state simulation at the same flow conditions. The Figure 7.1 reports a sketch of the simulation conditions with the initial temperature field, the Figures 7.2(a) and (b) show the initial wall temperature profile and heat transfer coefficient computed as:

$$h(z, t = 0) = \frac{q}{T_w(z) - T_{sat}} \quad (7.1)$$

where z is the axial coordinate and T_w the wall temperature.

By considering the inflow velocity as reference, Han and Shikazono correlation [3] predicts a liquid film thickness of $\delta/D = 0.035$. Four computational grids are employed, ranging the predicted film thickness to mesh element ratio from 3.5 to 14, such that the grids are characterized by the channel diameter to mesh element size ratios $D/\Delta x = 100, 200, 300, 400$. For each computational grid the simulation is run until the nose of the bubble reaches the end of the channel.

The grid convergence analysis is performed by examining the differences on the numerical bubble dynamics and wall heat transfer obtained with the computational

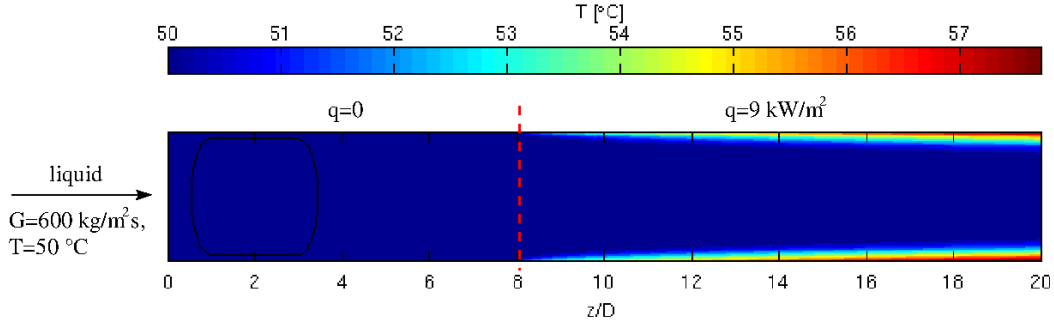


Figure 7.1: Initial temperature field. The bubble interface is represented by the black line profile at the upstream of the channel. The figure is stretched vertically to enlarge the thermal boundary layer at the heated wall.

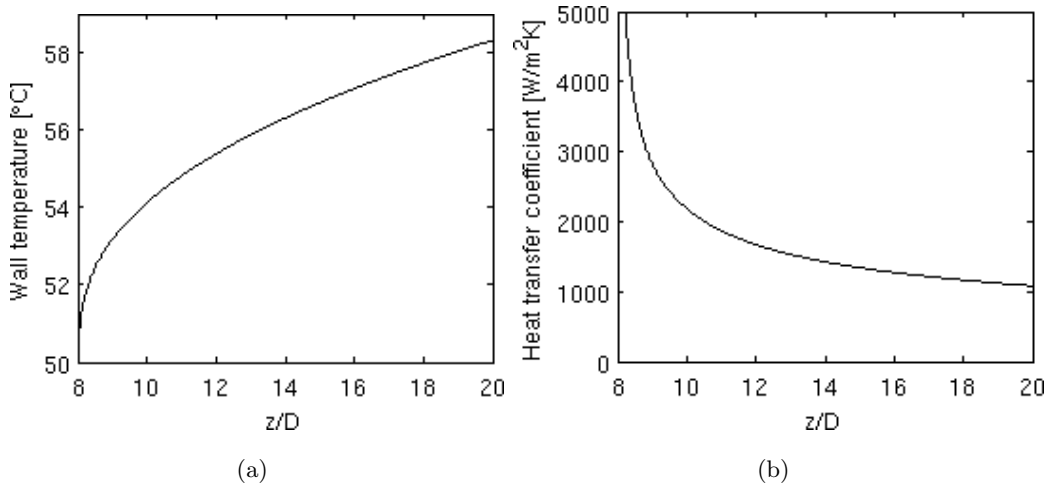


Figure 7.2: Initial wall temperature and heat transfer coefficient along the heated region.

grids employed. The bubble dynamics is reconstructed by computing at each time instant the bubble nose velocity as dz_N/dt and the bubble growth rate as dV_b/dt , where z_N is the bubble nose position and V_b the volume of the vapor bubble.

The Figure 7.3 reports the bubble nose velocity as a function of the time. There is a short stage that lasts less than one millisecond in which the bubble shape modifies from the initialized shape to attain a steady motion. After this settlement period the

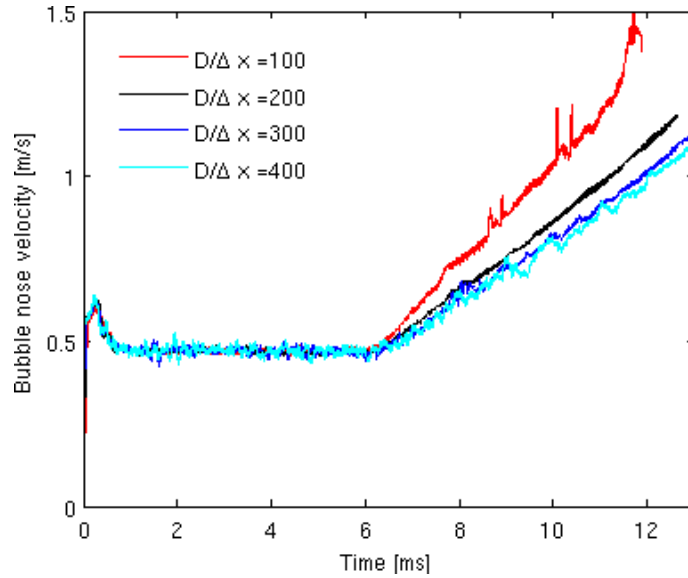
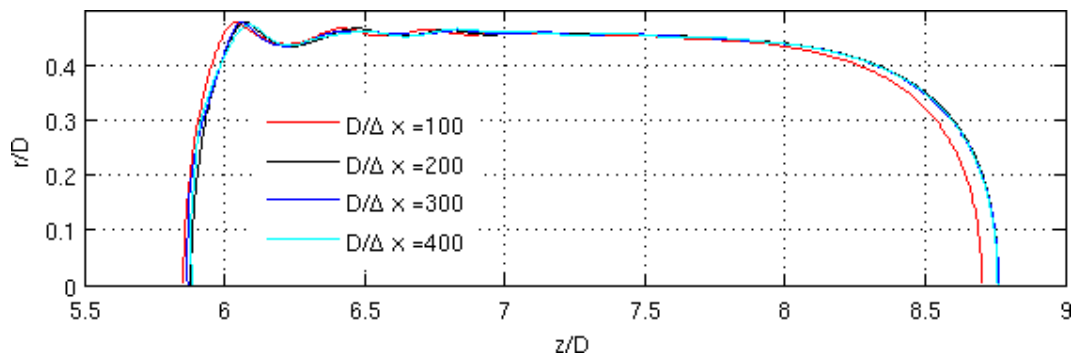


Figure 7.3: Velocity of the bubble nose.

bubble flows steadily up to the heated region with a constant velocity of $U_b = 0.47$ m/s which is the same for all the computational grids employed.

The Figure 7.4 shows the bubble profiles obtained with the various mesh grids at $t = 5.5$ ms, just before evaporation begins. The bubble nose is already within the heated region because $z_N/D > 8$, but the evaporation has not started yet because the interface has still to get in contact with the superheated liquid within the developing thermal layer at the wall. All the bubble profiles overlap as a sign that

Figure 7.4: Bubble profiles at $t = 5.5$ ms.

also the coarsest mesh is adequate to capture the adiabatic flow and $\delta/D \approx 0.045$, close to the predicted value. Han and Shikazono correlation predicts a value of 0.039 when using the terminal bubble velocity to compute the dimensionless numbers.

We observed unexpected oscillations of the bubble rear when running the finest grid simulation case. We found out the reason to be the numerical error in the computation of the local interface curvature with the Height Function algorithm when the interface is less aligned with the grid, causing a wrong computation of the surface tension force. The Figure 5.2 of Section 5.1 proves that the computed curvature of a R radius circle does not converge with the mesh refinement when $R/\Delta x > 40$ and the maximum relative error rises from 10^{-3} to over 10^{-2} when $R/\Delta x = 150$. In the present elongated bubble simulation the bubble rear is rather flat, with an estimated $R/\Delta x > 1000$ when discretizing the domain with the finest $D/\Delta x = 400$ grid (here R is an estimation of the bubble rear radius of curvature). Therefore, we believe that the worsening of the performances of the HF algorithm for such high radius of curvature to mesh element size ratios gives rise to the observed effects.

The Figure 7.3 suggests evaporation to start at around $t = 6$ ms, when the bubble nose begins to accelerate. The beginning of the evaporation phenomenon is clearly detected by the plot of the bubble volume growth rate in Fig. 7.5. Henceforth

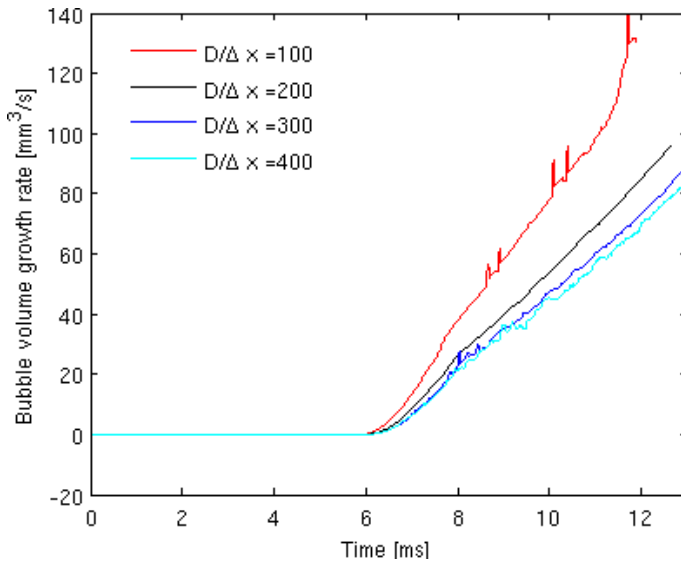


Figure 7.5: Bubble volume growth rate.

the different performances of the computational grids become evident. The computed evaporation rate decreases as the mesh is refined converging to similar profiles for the grids with $D/\Delta x = 300$ and 400 . Instead, an inadequate mesh element size within the liquid film leads to a faster growth of the bubble, as a consequence of the inaccuracy on the discretization of the local temperature gradients. The Figure 7.6 shows some snapshots of the bubble evolution at various time instants for all the grids. The location of the bubble rear z_R is the same for all the computational grids at each time instant considered, this is not surprising because it is a simple function of the elapsed time $z_R(t) = z_R(t = 0) + U_I t$. The bubble nose for $D/\Delta x = 100$ moves faster as effect of the wrong higher evaporation rate and for $D/\Delta x = 200$ the

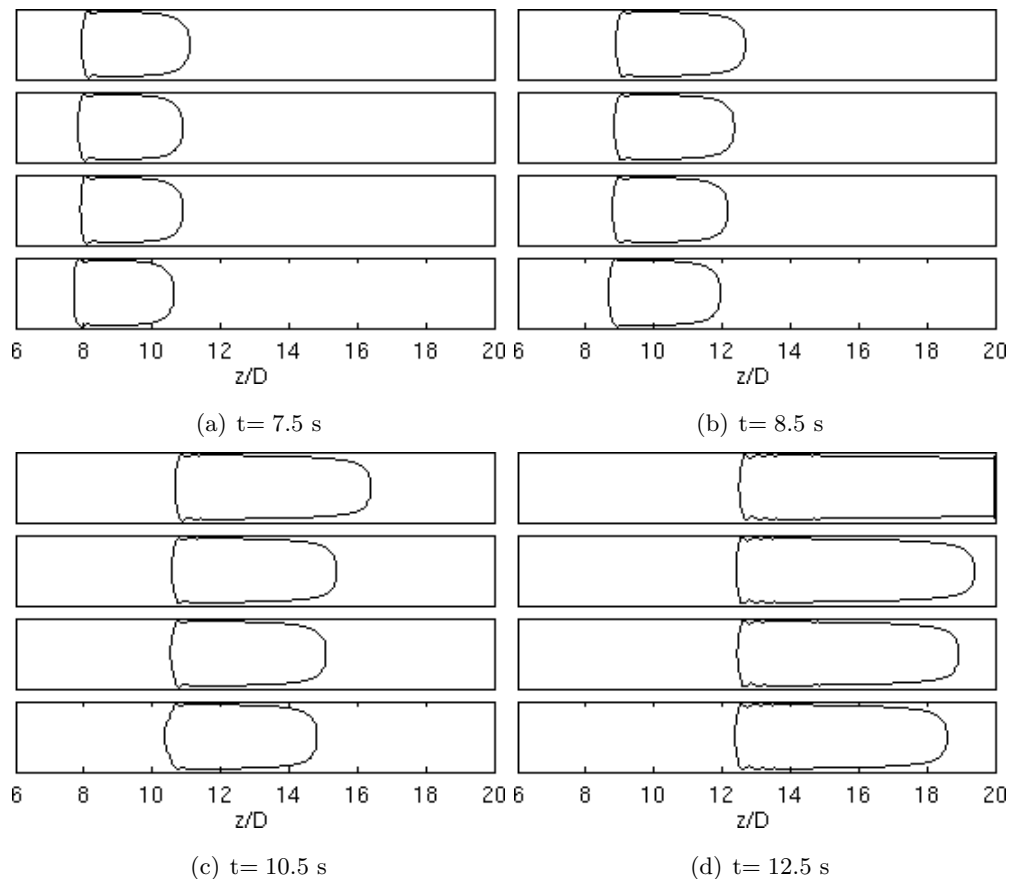


Figure 7.6: Bubble evolution at various time instants. For each time instant, the plots are sorted from the coarsest grid on the top, to the finest grid on the bottom.

dynamics appears to be already well represented.

The Figures 7.7 and 7.8 show the heat transfer coefficient at chosen time instants. The heat transfer coefficient is computed considering the saturation temperature as reference, as reported in Eq. (7.1). The effect of the bubble transit on the wall heat transfer begins to be evident in the film region in the proximity of the bubble rear, while it becomes negligible toward the nose. The enhancement of the heat transfer increases moving upstream to the channel and it is maximum in the wake region behind the bubble.

The higher evaporation rate of the simulation with the grid $D/\Delta x = 100$ gives also a false higher heat transfer coefficient, because the higher latent heat sunk cools down wrongly the channel wall. The peaks on the heat transfer coefficient observed for $D/\Delta x = 100$ are related to the numerical errors in the temperature gradient discretization.

As the mesh grid is refined, the heat transfer coefficient converges and for $D/\Delta x = 300$ and 400 the profiles are similar. The simulation with $D/\Delta x = 400$ shows spatial oscillations in the heat transfer coefficient. We believe this to be an effect of the discussed numerical errors in the curvature computation, which force unphysical vortices enhancing the wall heat transfer. However, in absence of the numerical errors the heat transfer coefficient for $D/\Delta x = 400$ would be very similar to the one obtained with the $D/\Delta x = 300$ grid. The grid with $D/\Delta x = 300$ has a minimum film thickness to mesh element size ratio $\delta_{min}/\Delta x \approx 7$. Therefore, the grid convergence analysis suggests that the minimum number of cells necessary to solve the thermal boundary layer within the liquid film is 7. Note that 7 cells was also the minimum size of the initial thermal boundary layer in the vapor bubble growth simulation discussed in the Section 5.4.

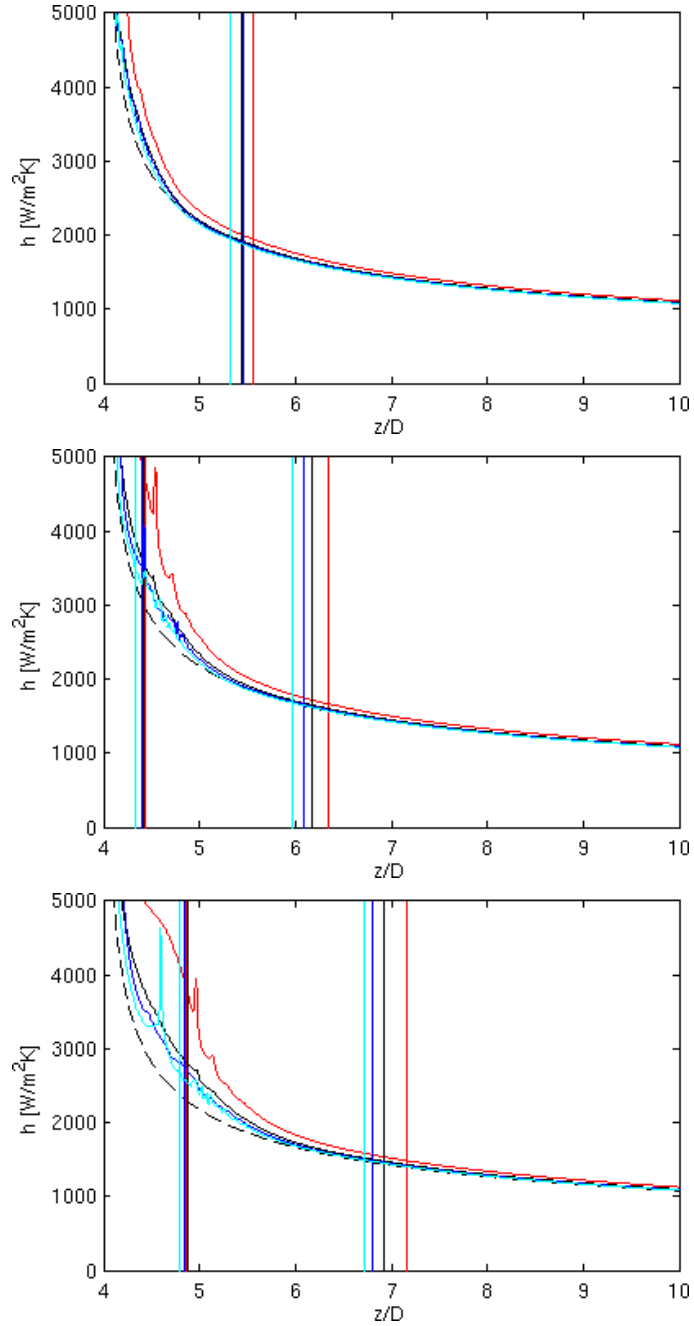


Figure 7.7: Heat transfer coefficient and positions of the bubble nose and rear (vertical lines) at $t = 7.5, 8.5, 9.5$ ms. Red lines: $D/\Delta x = 100$; black lines: $D/\Delta x = 200$; blue lines: $D/\Delta x = 300$, cyan lines: $D/\Delta x = 400$. Dash line: single phase.

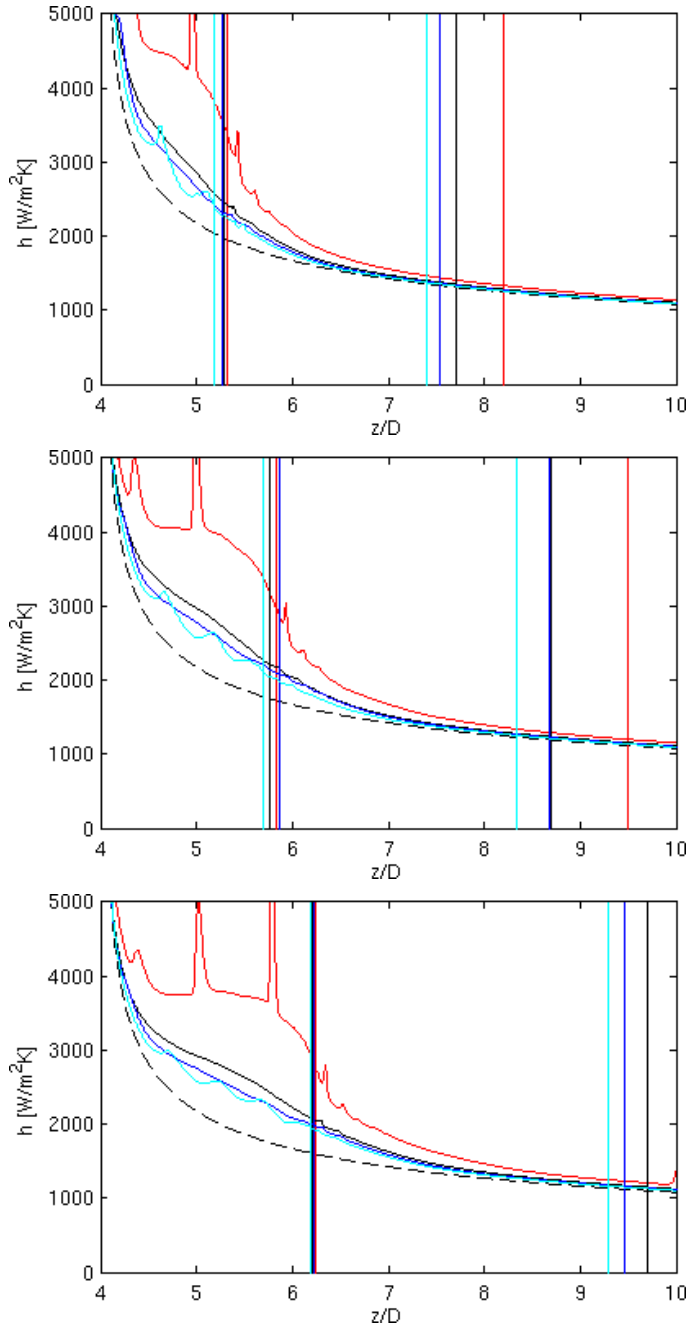


Figure 7.8: Heat transfer coefficient and positions of the bubble nose and rear (vertical lines) at $t = 10.5, 11.5, 12.5$ ms. Red lines: $D/\Delta x = 100$; black lines: $D/\Delta x = 200$; blue lines: $D/\Delta x = 300$, cyan lines: $D/\Delta x = 400$. Dash line: single phase.

7.2 Flow boundary conditions

For the grid convergence analysis, the simulations were conducted by imposing velocity inlet / outflow boundary conditions for the momentum equations at the channel's inlet and outlet. The different boundary conditions pressure inlet / pressure outlet can be imposed as well. In the remainder of this Section it will be referred to the velocity / outflow boundary condition as V, to the pressure inlet /outlet as P.

The choice of the velocity inlet boundary condition forces the liquid flow rate set to enter the channel regardless of the flow dynamics downstream, while due to the outflow boundary condition pressure and velocity at the outlet section depend only on the flow upstream.

On the contrary, the boundary condition on the pressure makes the flow rate at the inlet / outlet sections to depend on the phenomenon occurring within the domain, thus inverted flows are possible.

In absence of evaporation both the couple of boundary conditions lead to the same bubble and flow dynamics, while remarkable differences arise with the appearance of the phase change.

In order to study the dynamics involved, the same simulation set-up is run twice by varying the boundary conditions. The operating conditions for the simulations are the same of the grid convergence analysis, the computational grid used is the $D/\Delta x = 300$ one. The pressure gauge set between the terminal sections is the value leading to the same bubble steady velocity of the V boundary condition case before the bubble enters in the heated region.

The Figure 7.9 shows the bubble evolution for both the boundary conditions at regular time intervals. The bubble moved with the P condition shows a delay that appears to increase as time elapses after the beginning of the evaporation. The reason is closely related to the boundary condition. The bubble accelerates the fluid in front of it thus increasing the pressure drop. In order to maintain constant the pressure difference among the inlet and outlet sections, the inlet flow rate decreases thus slowing down the bubble with respect to the V case.

The Figure 7.10(a) shows the bubble volume growth rate, which is similar for both cases. The Figure 7.10(b) reports the velocity of the bubble rear. The oscillations observed in the adiabatic region are related to the settlement of the rear of the bubble as a consequence of the initialization and they are dumped by the

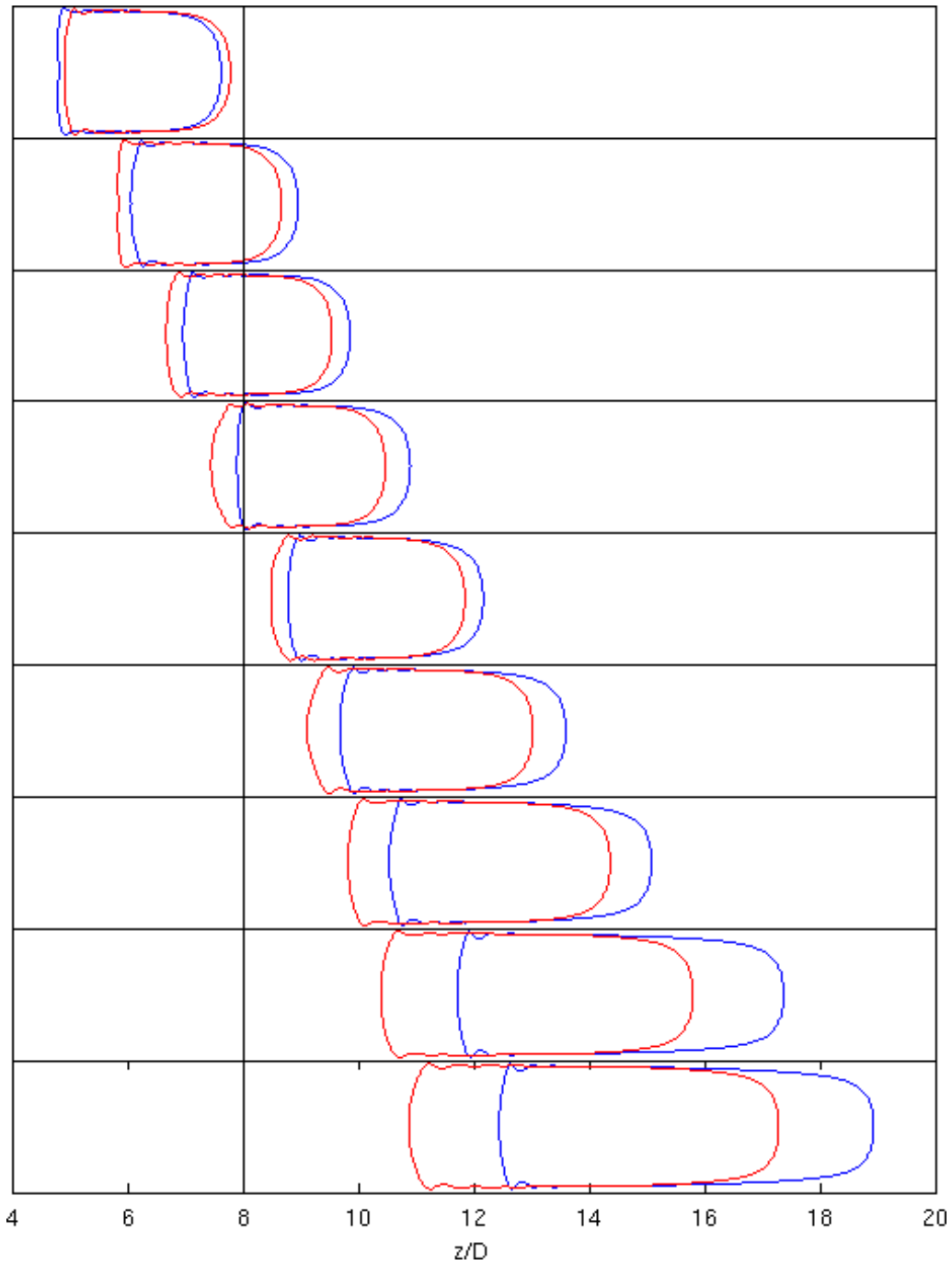


Figure 7.9: Bubble evolution during evaporation, from $t = 4.5$ ms to 12.5 ms at time intervals of 1 ms. Blue: V condition; red: P condition.

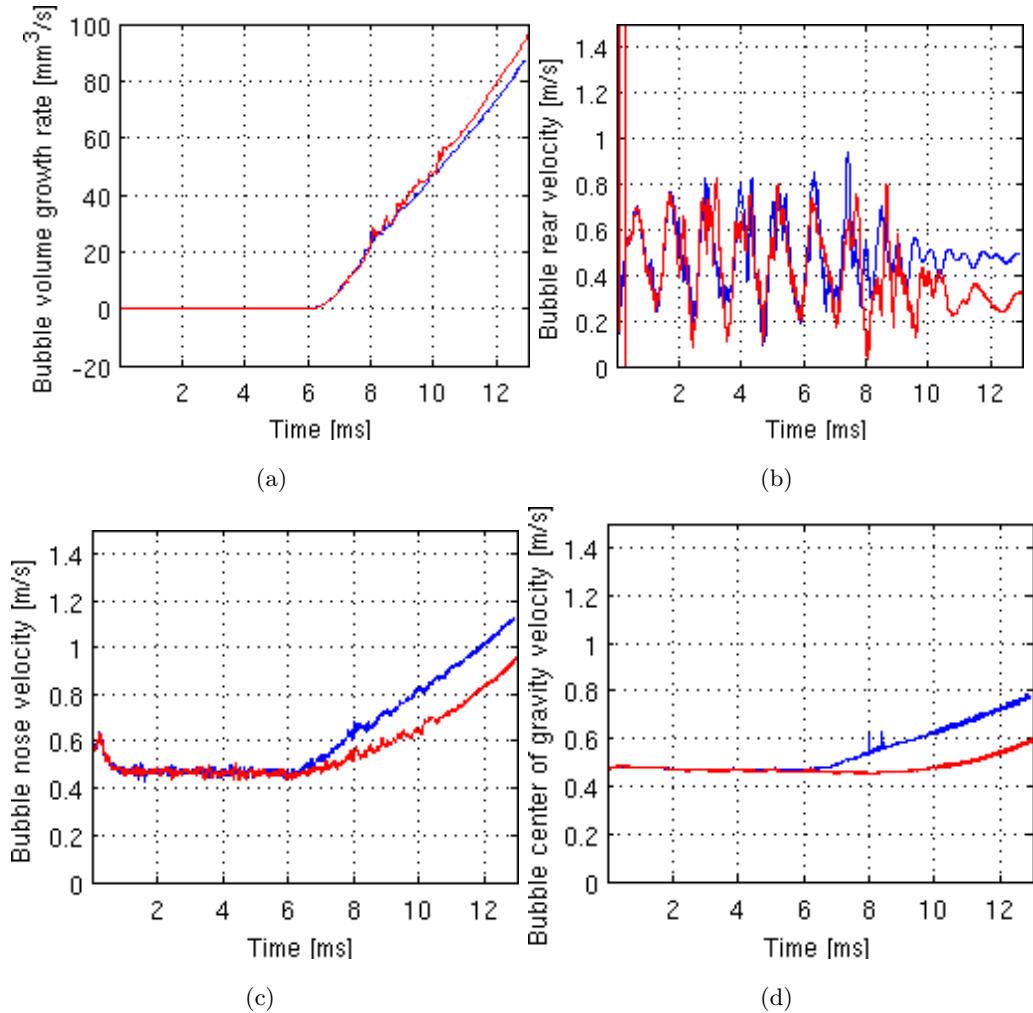


Figure 7.10: (a) Bubble volume growth rate, (b) rear velocity, (c) nose velocity and (d) center of gravity velocity. Blue: V condition; red: P condition.

evaporation. After the beginning of the evaporation, the rear of the bubble for the V condition continues to move at a velocity stabilizing at $U_b = 0.47$ m/s, while the velocity of the bubble pushed by the P condition decreases as effect of the reduction in the inlet flow rate. The velocity of the nose of the bubble is reported in the Fig. 7.10(c). As the evaporation starts, the nose of the bubble pushed by the fixed inflow accelerates uniformly (actually the law of the motion is exponential as will be shown in Subsection 7.3.1). The velocity of the nose for the P condition case increases more gradually because of the reduced inlet flow rate.

In the following, the differences on the bubble profiles induced by the evaporation, when different boundary conditions are applied, are discussed.

We observed the evaporation to take place at the interface between the bubble and the liquid film, where superheated liquid exists. Such film evaporation mechanism was suggested to rule the heat transfer in the elongated bubble regime by Thome and co-workers [5] as well. However, the local film evaporation when employing the V condition is not reflected in a decrease of the thickness. The Figure 7.11(a) reports the profiles of the bubble at $t = 12.5$ ms for V and P cases, the two profiles are shifted such that the axial position of the nose is the same. The figure reports also the steady thickness of the liquid film during the adiabatic stage, measured at the valley of the third wave from the left side at the rear of the bubble. The film evaporation is expected to get the film thinner, but the figure shows it to remain almost equal to the adiabatic value. This is a direct consequence of the outflow condition. According to Han and Shikazono [3] and previous studies as well, a thinner film is the consequence of a decreased Capillary number, as though the capillarity is overcoming the viscous effects. But the velocity of the bubble is not decreased, rather is increasing due to the evaporation, so Ca is actually increasing. Therefore as the film gets thinner because of the evaporation, the hydrodynamic forces (proportional to Ca) tend to recover the thickness to a value depending on Ca , thus to a thickness equal or higher than the one before. The outflow boundary condition does not set any restriction on the bubble nose motion, as a consequence the bubble is free to rearrange its shape by varying the film thickness in accord with the acting forces, while the vapor created gets the bubble longer rather than larger.

The situation is different when the P condition is applied, because the velocity of the nose is limited by the boundary condition set. Therefore, the bubble is not free to arrange its shape and a slight decrease in the film thickness with respect to the adiabatic value is noticeable in Figure 7.11(a) as a consequence of the film evaporation.

However, it is important to remark that the configuration simulated is only a model of the real physics involving multiple bubbles flowing in sequence. In the real dynamics of the evaporation, the acceleration of the nose of each bubble is limited also by the presence of another bubble downstream to the channel, not considered here.

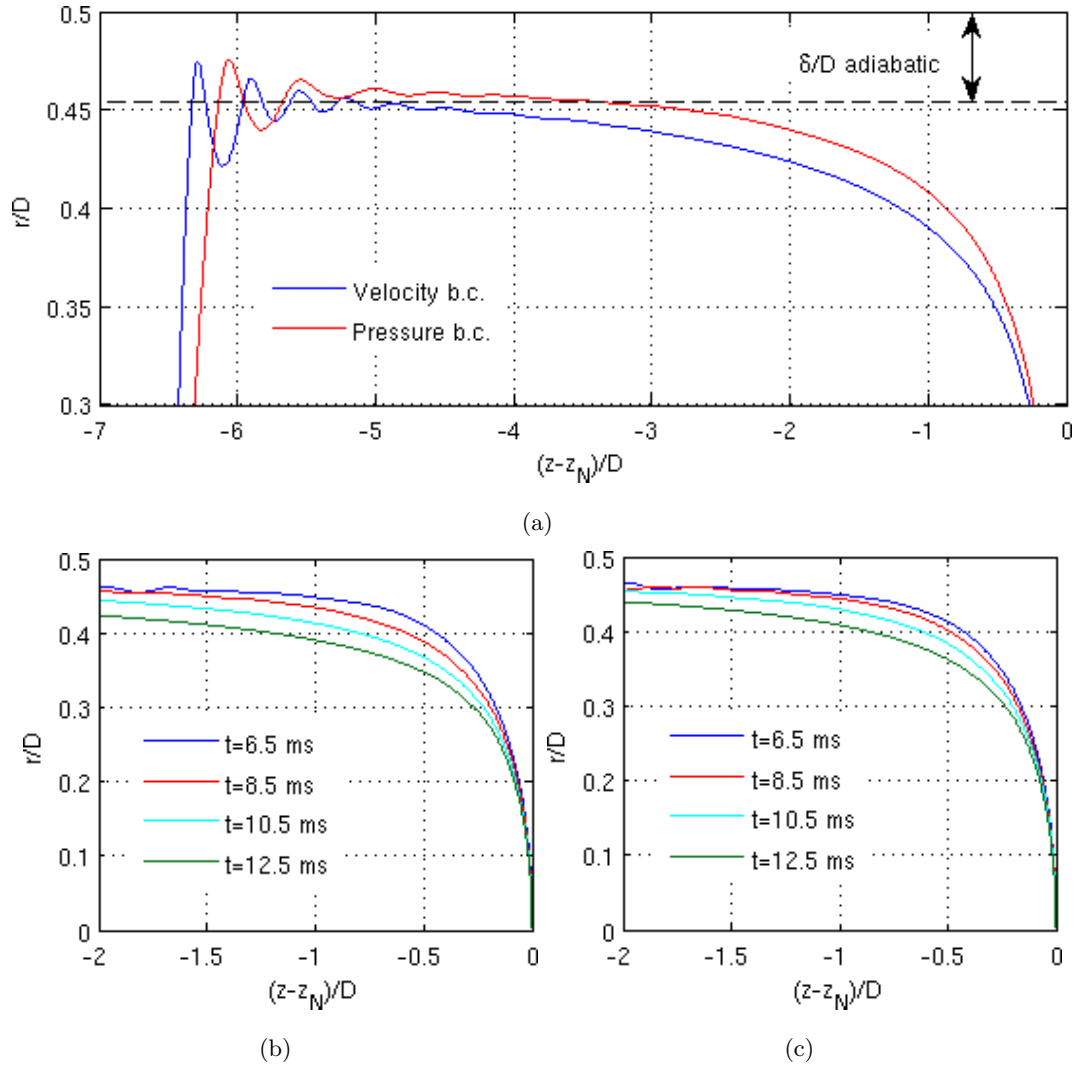


Figure 7.11: (a) Bubble profile at $t = 12.5$ ms. Profile of the bubble nose at various time instants obtained with the V condition (b) and the P condition (c). Within each figure the profiles are shifted in order to match the nose positions.

Figures 7.11(b) and 7.11(c) report the shape of the nose of the bubble at various time instants after that evaporation has begun. In both V and P cases, as the velocity of the bubble increases the nose becomes sharper and its curvature increases because of the inertia effects, in accord with Aussillous and Qu  r   [71] and Han and Shikazono [3] scaling analysis of the forces acting on the bubble.

The P boundary condition does not guarantee the flow of the bubble downstream to the channel, but it depends on the pressure drop generated by the evaporation. The high acceleration of the fluid in front of the bubble causes the velocity profile to deviate from the fully developed parabolic profile and the pressure drop increases due to the formation of a hydrodynamic entrance region.

The pressure drop in the liquid slug behind the bubble and across the bubble can be neglected with respect to the pressure drop in the accelerated liquid ahead of the bubble. Thus, the pressure drop across the entire channel can be estimated proportional to the liquid mass flow rate at the channel exit, given by the continuity condition:

$$\Delta p \propto \dot{m}_o = \dot{m}_i + \dot{m} \left(\frac{\rho_l - \rho_v}{\rho_v} \right) \quad (7.2)$$

where \dot{m}_i and \dot{m}_o are the liquid mass flow rates at the channel inlet and outlet and \dot{m} is the vapor mass flow rate generated by the evaporation. If the heat flux is used only to evaporate the liquid and the latent heat is absorbed only from the heat load at the wall, the Eq. (7.2) becomes:

$$\dot{m}_o = \dot{m}_i + \frac{q\pi DL_h}{h_{lv}} \left(\frac{\rho_l - \rho_v}{\rho_v} \right) \quad (7.3)$$

where L_h is the heated length of the channel. The terms at the RHS are of comparable magnitude in the present case. Thus, the pressure drop induced by the evaporation is sensible of the heat flux applied and it increases as the heat flux is increased.

In the discussed test case P the heat flux is $q = 9 \text{ kW/m}^2$ and the pressure drop generated by the evaporation still allows the bubble to move downstream. We repeated the simulation with both the V and P conditions, raising the heat flux to $q = 20 \text{ kW/m}^2$ to investigate the effect of the heat flux. The channel length is increased to $L = 30D$, with ten heated diameters more than the previous case. The evolution of the bubble is shown in Fig. 7.12. As the whole bubble is entered in the heated region, the evaporation is very strong and the liquid highly accelerated, such that the pressure drop generated causes backflow at the inlet in the P case. As reported in the Figure 7.13(a), the velocity of the bubble rear quickly decreases and becomes negative. The shape of the rear of the bubble becomes similar to the nose,

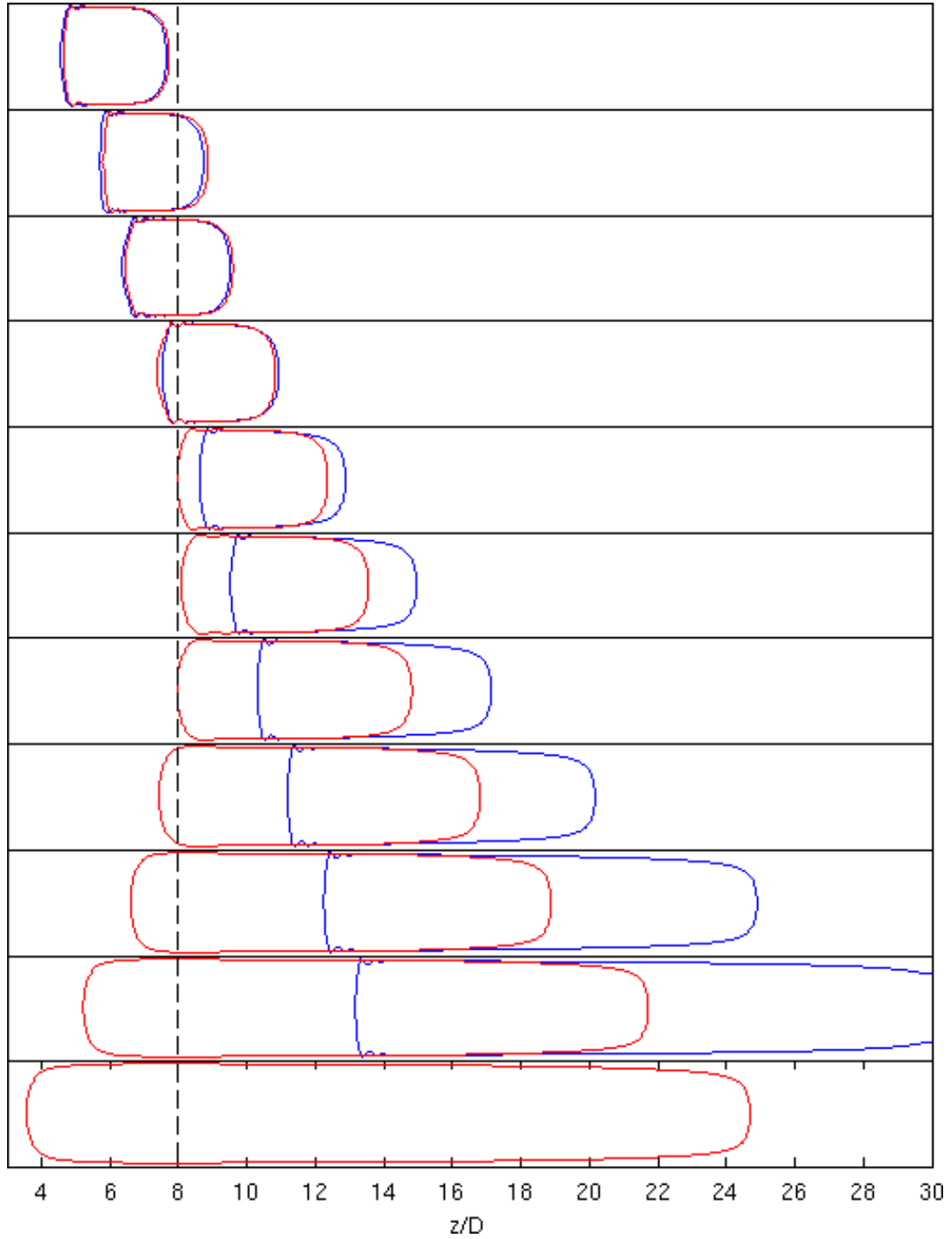


Figure 7.12: Bubble evolution during evaporation, from $t = 4.5$ ms to 14.5 ms at time intervals of 1 ms, $q = 20$ kW/m². Blue: V condition; red: P condition.

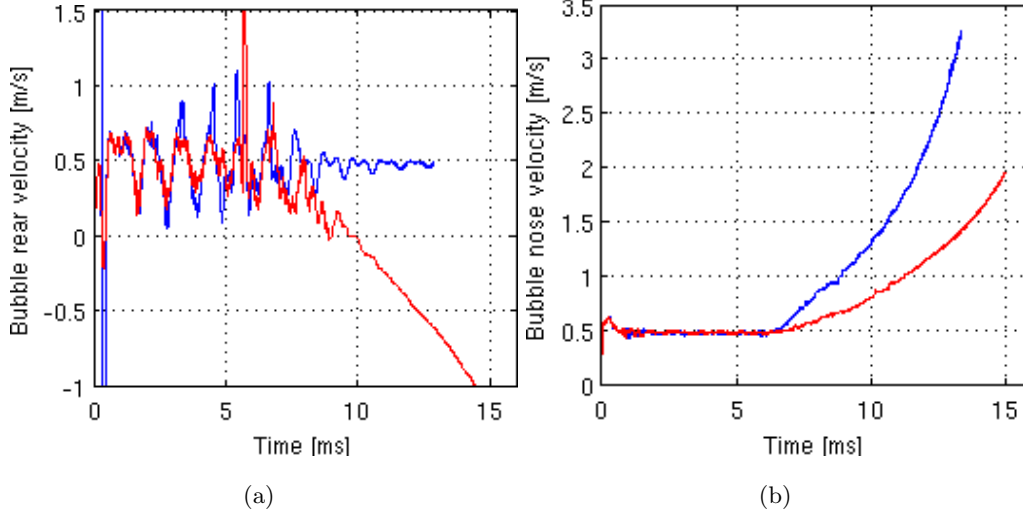


Figure 7.13: Velocity of the bubble (a) rear and (b) nose for $q = 20 \text{ kW/m}^2$. Blue: V condition; red: P condition.

but with a less curved profile because the velocity is lower. The nose of the bubble continues to move downstream with gradually growing velocity.

In this Section the different bubble dynamics led by velocity and pressure boundary conditions were presented. The best boundary conditions to be set at the channel's inlet and outlet depend only on the objective of the simulation. As instance, reversed flows may arise in parallel microchannels with a common manifold and their numerical modeling through a single channel simulation would require the use of pressure boundary conditions with time-varying pressure. The objective of the following sections is to study the wall heat transfer induced by an evaporating bubble. In order to compare with experiments, a constant mass flux throughout the simulation is favourable, therefore a velocity boundary condition is more appropriate.

7.3 Analysis of the flow and temperature field induced by an evaporating bubble

In this Section the test case run with the $D/\Delta x = 300$ computational mesh, whose operating conditions are described in Section 7.1, is particularly analyzed. The ob-

jective is to relate the flow and temperature field to the dynamics of the evaporating bubble and to explain the consequent trend of the heat transfer performances.

The flow is captured at the time instant $t = 12.5$ ms. At this time instant the velocity of the nose of the bubble is $U_{b,N} = 1.07$ m/s, the center of gravity moves at $U_b = 0.76$ m/s. The axial location of the bubble nose at the center of the channel is $z_N/D = 18.91$, the location of the rear is $z_R/D = 12.43$. In the following, when it is referred to the single phase case, or flow without the bubble, it is considered the steady flow obtained with a preliminary simulation with only liquid.

The contours and isolines of the velocity field are depicted in the Fig. 7.14. The figure shows also the liquid bulk axial and radial velocities plotted as a function of the axial coordinate. Both average velocities are calculated at each axial location z as:

$$u_{mean}(z) = \frac{2}{R^2 - (R - \delta(z))^2} \int_{R-\delta(z)}^R u(r, z) r dr \quad (7.4)$$

The Figures 7.15 and 7.16 show the contours and isolines of the temperature field respectively in the wake of the bubble and in the region occupied by the bubble. A black dash line represents the thickness of the thermal boundary layer δ_T for the single phase case computed as:

$$\delta_T(z) = R - r(T = T_{sat} + 0.01(T_w(z) - T_{sat})) \quad (7.5)$$

Each figure reports also the wall temperature T_w and the heat transfer coefficient obtained in presence of the bubble (subscript *tp*: two-phase) and without the bubble (*sp*: single phase). Both the heat transfer coefficients are computed as reported in Eq. (7.1) by considering the saturation temperature as reference (subscript *sat*).

In addition to the saturation based heat transfer coefficient, a bulk heat transfer coefficient is defined (subscript *b*). It is based on the bulk temperature T_b as reference instead of the saturation one, computed as:

$$T_b(z) = \frac{\int_0^R \rho c_p T |u_z| r dr}{\int_0^R \rho c_p |u_z| r dr} \quad (7.6)$$

with u_z being the axial velocity. This coefficient is introduced in order to compare the results with the published data for heat transfer without phase change in the

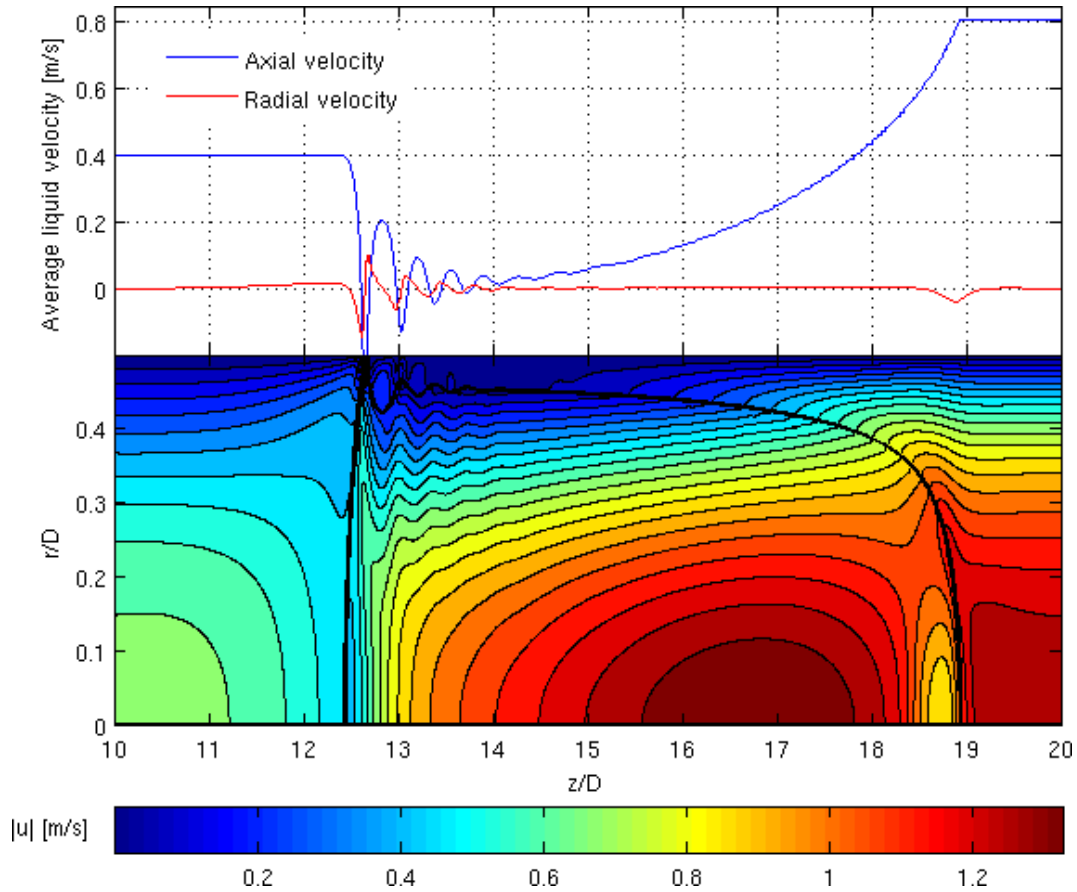


Figure 7.14: Average liquid axial and radial velocity (above) defined in Eq. (7.4) and contours of the velocity field (below).

elongated bubble regime.

The Figure 7.17 reports two curves identifying the relative difference between each two-phase heat transfer coefficient defined and the single phase one.

The analysis of the flow field begins from the wake region. The effect of the bubble transit is evident in the wall and liquid temperature fields reported in Fig. 7.15 from the entrance in the heated region located at $z/D = 8$, to the rear of the bubble. The bubble passage squeezes the thermal boundary layer on the channel wall and the film evaporation cools down locally the superheated liquid to the saturation condition. The axial velocity profiles reported in the Figs. 7.18(a) and 7.18(b) show that

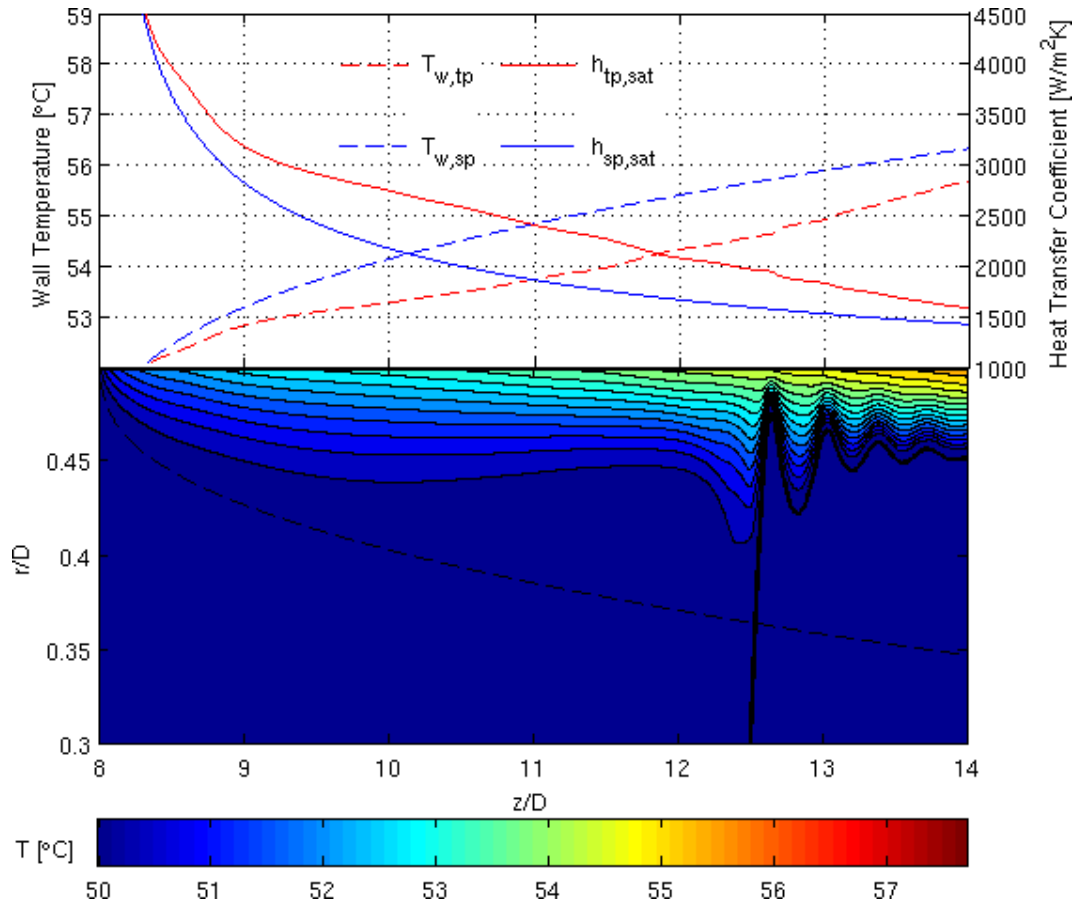


Figure 7.15: Wall temperature and heat transfer coefficient (above) in the wake. The subscripts w stands for wall, sp and tp respectively for single phase and two-phase, sat for saturation temperature as reference. Below, the contours and isolines of temperature are reported. The black dash line represents the width of the thermal boundary layer for the single phase case.

the bubble disturbance on the liquid flow field is negligible until a location placed between $z/D = 10$ and $z/D = 11$. The isolines of the velocity field in Fig. 7.14 are horizontal until approximately $z/D = 10.5$, thus suggesting that disturbance arises only downstream such location.

Therefore, in the region within $z/D = [8, 10.5]$ the thermal boundary layer is developing with the time toward the steady situation holding before of the bubble transit and the local heat transfer performances are enhanced by such transient heat

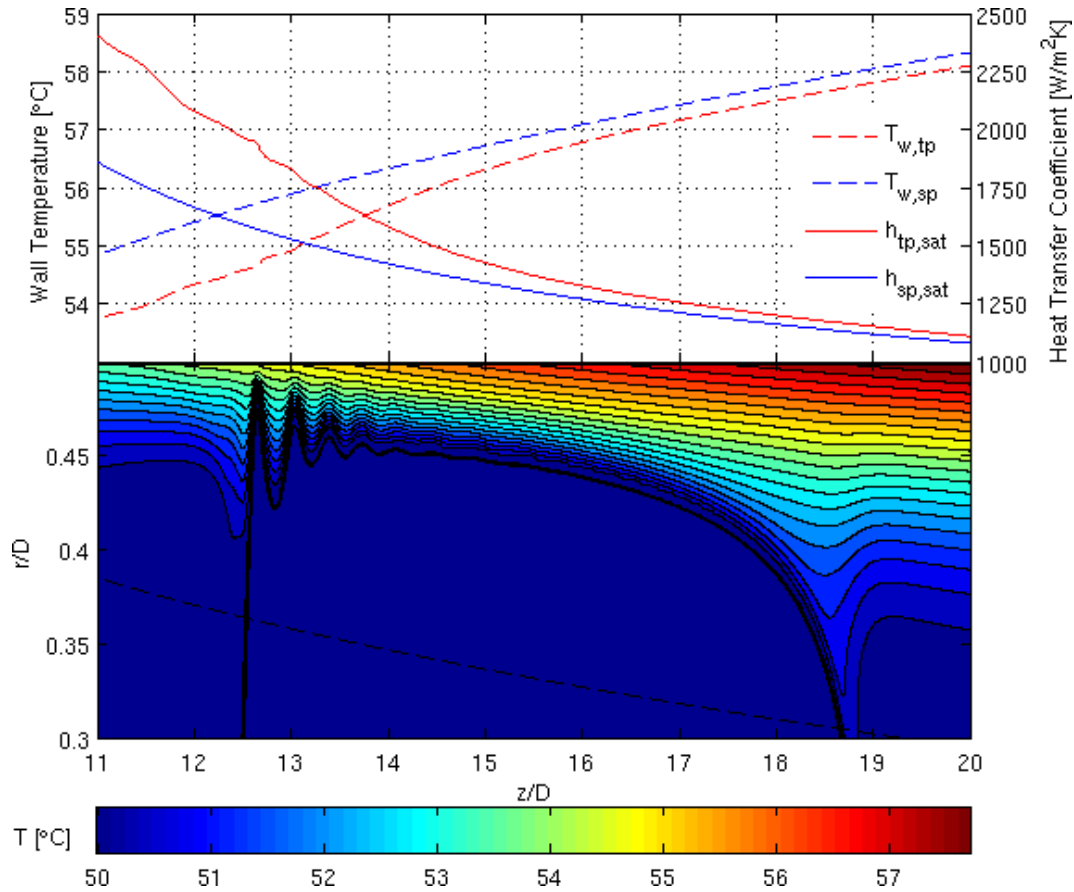


Figure 7.16: Wall temperature and heat transfer coefficient (above) in the region occupied by the bubble. The subscripts w stands for wall, sp and tp respectively for single phase and two-phase, sat for saturation temperature as reference. Below, the contours and isolines of temperature are reported. The black dash line represents the width of the thermal boundary layer for the single phase case.

convection mechanism. As a consequence, the heat transfer coefficient shows a substantial increase with respect to the single phase profile, see Fig. 7.15.

At $z/D > 10.5$ the bubble disturbance on the liquid flow behind it becomes remarkable. The axial velocity profile deviates from the parabolic shape as shown in Fig. 7.18(b) because the rear of bubble is moving at the velocity $U_{b,R} = 0.47$ m/s, while the liquid velocity at the centerline of the channel is around $2U_l = 0.8$ m/s. The

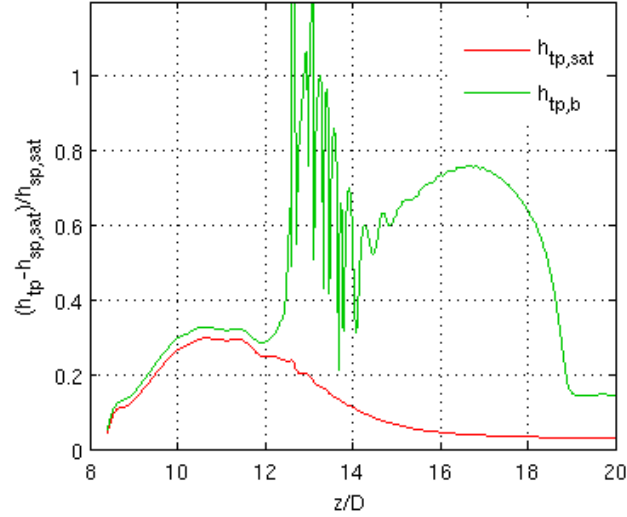


Figure 7.17: Local enhancement on the heat transfer induced by the two-phase flow.

axial velocity profile becomes more flat when sections closer to the bubble rear are considered, as discussed in the Section 6.2. Nearby the bubble rear, at $z/D = 12.4$, the Fig. 7.18(c) shows that the axial velocity at the axis of the channel matches the bubble rear velocity of 0.47 m/s. Due to the continuity condition, the liquid velocity in the region near the wall increases, thus preventing the thermal boundary layer from developing similarly to a hydrodynamically developing flow. Such effect is evident in the Fig. 7.15. The thermal layer profile evolves in the axial direction increasing the thickness until $z/D \approx 10.5$, then for $z/D > 10.5$ such increase stops. Actually, the thickness decreases slightly because a positive radial component of the velocity field exists. The combined effect of transient heat convection and flat velocity profile behind the bubble drops locally the wall temperature by more than 1 °C, see the temperature profiles in Figs. 7.18(a) and 7.18(b). This region shows in Fig. 7.17 the maximum enhancement on the heat transfer performance. The saturation based heat transfer coefficient is constantly more than 25 % higher than the single phase value within $z/D = [10.5, 12]$, with a peak of 30 %.

Moving toward the rear of the bubble, the isolines of the velocity field at $r/D > 0.35$ converge on the channel wall, at the location $z/D = 12.65$ of the first crest

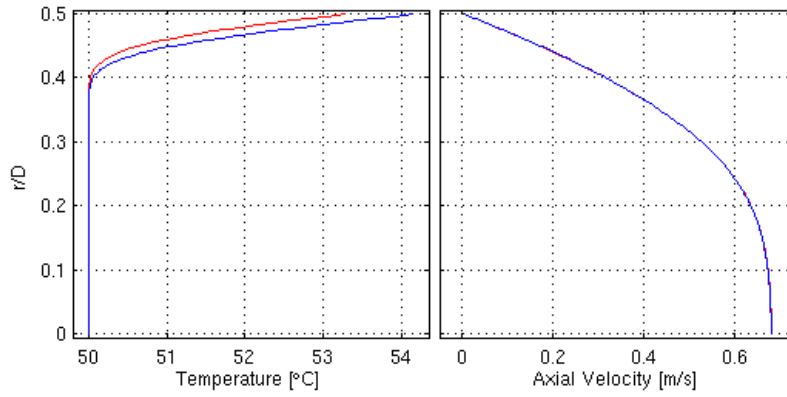
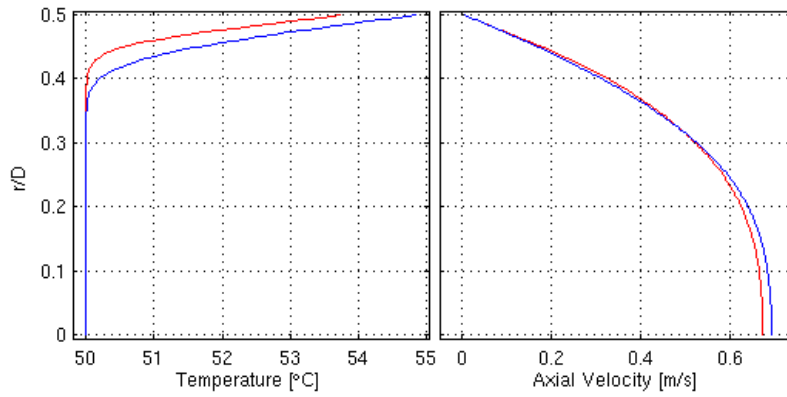
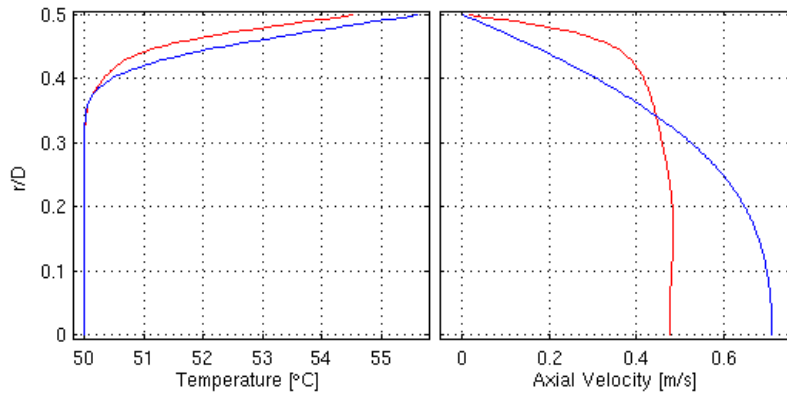
(a) $z/D = 10$ (b) $z/D = 11$ (c) $z/D = 12.4$

Figure 7.18: Left: temperature profile, right: axial velocity profile. Red: two-phase, blue: single phase.

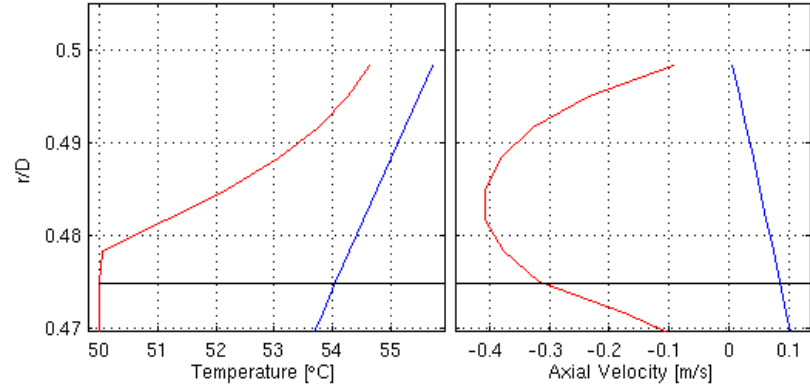
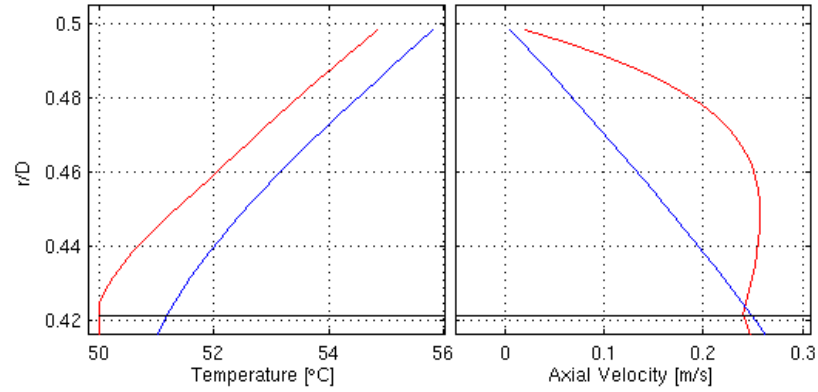
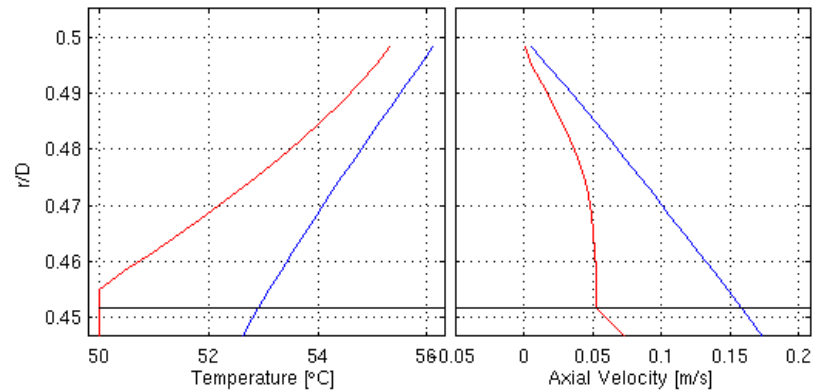
(a) $z/D = 12.65$ (b) $z/D = 12.83$ (c) $z/D = 13.5$

Figure 7.19: Left: temperature profile, right: axial velocity profile. Red: two-phase, blue: single phase. Black horizontal line: radial location of the interface.

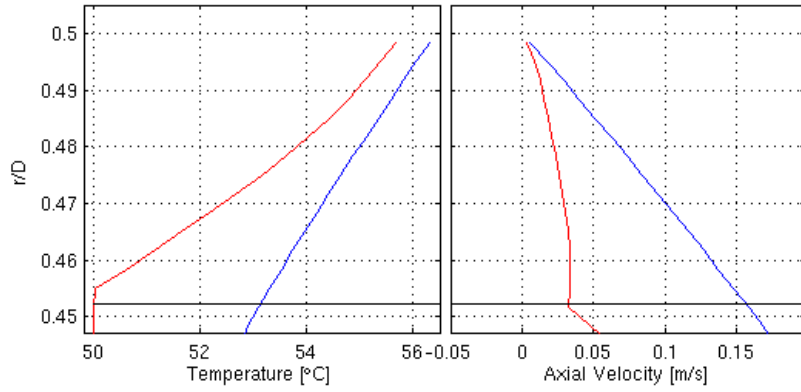
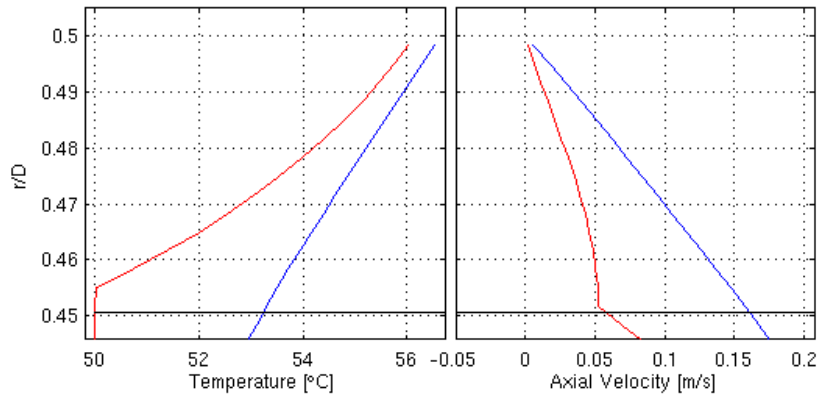
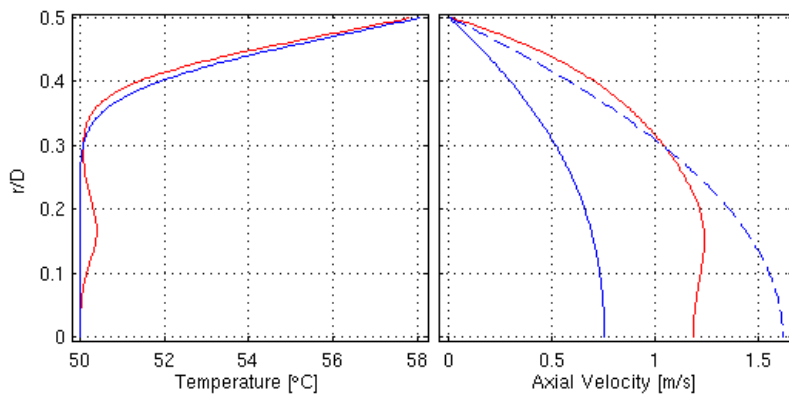
(a) $z/D = 14$ (b) $z/D = 14.5$ (c) $z/D = 19$

Figure 7.20: Left: temperature profile, right: axial velocity profile. Red: two-phase, blue: single phase. Black horizontal line: radial location of the interface. Blue dashed line: fully developed laminar flow with the same flow rate of the liquid at that location.

of the interfacial wave in the film region. The wavy profile at the rear of the bubble generates liquid recirculation as shown by the velocity vector field in Fig. 7.21. Upon each crest anticlockwise vortices exist and the local axial velocity is negative, as depicted by the profile at $z/D = 12.65$ reported in Fig. 7.19(a). Upon each valley clockwise vortices can be observed. The Fig. 7.19(b) reports a positive axial velocity profile at the location of the first valley $z/D = 12.83$. The anticlockwise vortex in proximity of the first crest drifts downward the liquid on the left, as can be seen by the velocity vectors in Fig. 7.21. Such flow pattern transports energy toward the center of the channel, thus thickening locally the thermal boundary layer behind the bubble within $z/D = [12, 12.4]$. Such effect is visible in the Fig. 7.15, magnified by the vertical stretching of the figure.

In the liquid film region at the rear of the bubble, within $z/D = [12.5, 15]$, the velocity contours of Fig. 7.14 shows an almost null velocity of the liquid phase. Actually, the undulations of the interface profile generate a series of counter-rotating vortices whose axial average velocity is small but not null and oscillates around the zero value. The average axial velocity shows local minimums at each crest of the wave and maximums at each valley and it changes the sign in between. Proceeding downstream to the channel, the amplitude of the interfacial wave decreases, as well as the oscillations on the average axial velocity profile.

In this region, the bulk temperature based local heat transfer coefficient shows the maximum values with peaks over two times the single phase coefficient, see Fig. 7.17. The curve representing the bulk heat transfer coefficient is highly irregular, because it is strongly influenced by the dynamics of the flow field within the film. In order to investigate such behavior, the Figure 7.21 reports the temperature contours plot together with the velocity vectors, the bulk heat transfer coefficient and the average axial velocity. The $h_{tp,b}$ values drop at each axial location where the vortices change the roll direction, thus where the average axial velocity is zero. Such behavior was detected also by Gupta *et al.* [83] for flow without phase change. On the contrary, the heat transfer shows peaks at each crest and valley of the interface, where the magnitude of the axial velocity is maximum.

The wall temperature is weakly influenced by the dynamics of the vortices, thus by the axial variations of the average axial velocity. Therefore, the saturation based

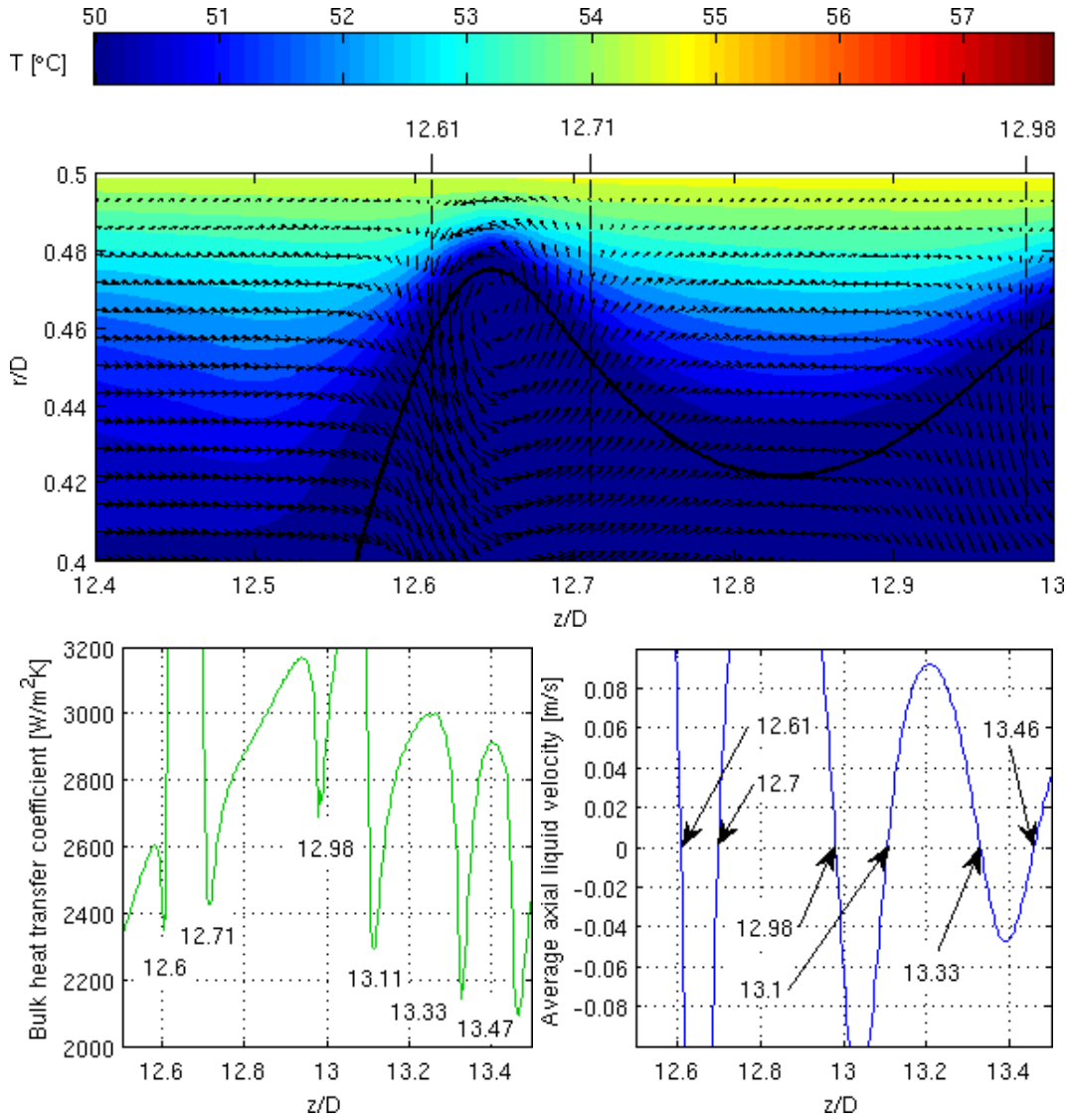


Figure 7.21: Fluid flow, temperature field and heat transfer in the wavy region of the film. The data boxes within the figures report the axial locations at which the vortices change the roll direction. The boxes in the figure on the left identify the local minimums on the bulk heat transfer coefficient and on the right the zeros of the average axial velocity.

heat transfer coefficient decreases smoothly toward the bubble nose, giving within $z/D = [12.5, 14]$ a mean improvement of 20% with respect to the single phase case.

The three zones model proposed by Thome *et al.* [5] assumes that for $D/\delta > 100$ the liquid film is sufficiently thin to become stagnant, thus allowing the estimation of the heat transfer coefficient by one-dimensional heat conduction. The liquid film is considered flat and the thickness decreasing linearly from the bubble nose to the rear. The maximum and minimum thicknesses are derived through correlations based on the flow conditions. In order to test specifically the assumption of pure heat conduction within the film, a one-dimensional heat conduction based heat transfer coefficient h_{cond} is computed by considering heat transfer across the actual profile of the liquid film:

$$h_{cond}(z) = \frac{\lambda_l}{R \ln\left(\frac{R}{R-\delta(z)}\right)} \quad (7.7)$$

The Figure 7.22 shows a good agreement of the bulk with the heat conduction based heat transfer coefficient in the region under analysis, in which the liquid velocity is small. The heat conduction based heat transfer coefficient captures well the magnitude of the peaks on the heat transfer located at the first four crests of the wavy bubble profile. The comparison of the average bulk heat transfer coefficient with the heat conduction based one within $z/D = [12.6, 14]$ is very positive, with the former

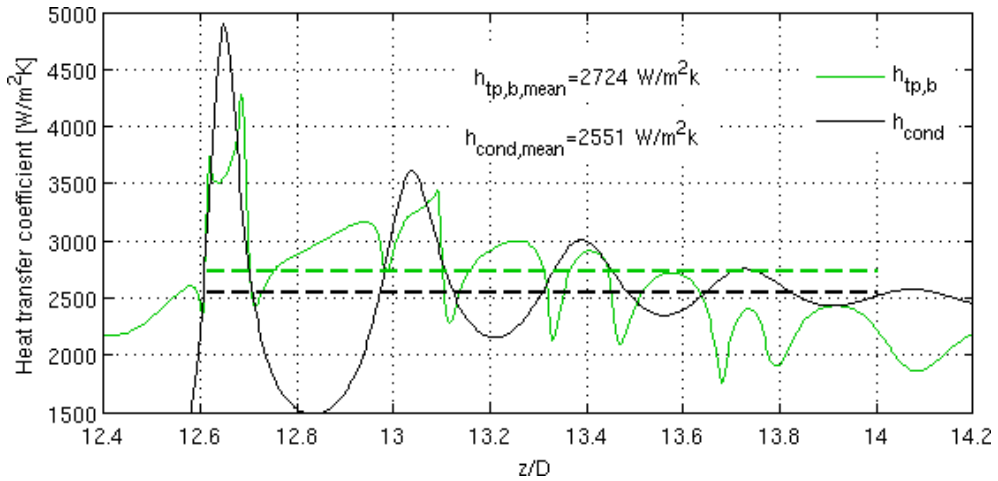


Figure 7.22: Comparison of the local bulk heat transfer coefficient with the heat conduction based heat transfer coefficient defined in Eq. (7.7). The dashed lines represent the average values within $z/D = [12.6, 14]$, where the velocity of the liquid within the film is small.

exceeding the latter by only the 6.8%.

However, the average value of the heat conduction based heat transfer coefficient is 40 % higher than the saturation based coefficient in the same axial interval. Thus, the pure heat conduction across the film can not be assumed as the dominant mechanism for heat transfer in such situation. This is not surprising because the local film is much more thicker ($D/\delta \approx 20$) than the values assumed by Thome and coworkers, therefore an axial convective transport of energy still exists.

From $z/D = 14$ toward the bubble nose, the film thickness increases smoothly without waves. The liquid included between the bubble and the channel wall is accelerated as effect of the evaporation. The enhancement on the heat transfer led by the bubble decreases moving downstream to the channel and at $z/D = 17$ the difference among the two-phase and the single phase heat transfer coefficient has reached an horizontal asymptote. The remaining gap between single and two-phase coefficients for $z/D > 17$ is ascribed to different hydrodynamic conditions for the flows. Since the liquid is accelerated by the evaporation, the flow in the liquid region around the nose and ahead of the bubble is less developed than a single phase flow at the same axial location, therefore the wall heat transfer is higher.

Because of the high acceleration given by the evaporation to the liquid ahead of the bubble nose, the local axial velocity profile depicted in Fig. 7.20(c) is rather different with respect to a fully developed laminar profile. The figure reports as reference the Poiseuille parabolic profile of a flow with the same liquid mass flow rate of the simulated case at $z/D = 19$. The velocity profile of the accelerated liquid is flat at the channel axis and shows a higher derivative at the wall than the theoretical profile, thus raising the pressure drop in the remaining part of the channel.

Global heat transfer coefficients are obtained by averaging the local values over the entire heated length of the channel. The enhancement of the heat transfer relative to the single phase flow is of 47 % when considering the bulk temperature and 12.4 % if referring to the saturation conditions. Both the values are small with respect to the expected performance of a two-phase flow, however the flow simulated deviates significantly from actual experimental test conditions. In experiments the heated length is much longer, such that thermally developed conditions are guaranteed.

Multiple bubbles flow in sequence, thus affecting the time development of the thermal boundary layer leading to better heat exchange performances. The heat transfer coefficient is measured several diameters downstream to the entrance in the heated region.

The numerical literature about CFD simulations without phase change reports enhancements of the bulk heat transfer coefficient, for the elongated bubble regime, from two to six times the fully developed single phase laminar case, at least 25% higher than the value obtained in the present study. The reason of such deviation is again connected to the multiple bubbles simulated in the cited literature. Moreover, the mentioned studies simulate flows without phase change such that the temperature of the gas phase increases considerably due to the high thermal diffusivity of the gas. As a consequence, the local bulk temperature shows high peaks in presence of the bubble and the wall-bulk temperature difference decreases thus increasing the heat transfer coefficient.

7.3.1 Comparison of the bubble nose position with a theoretical model

Consolini and Thome describe in [8] a phenomenological model to predict the boiling heat transfer in the coalescing bubble regime. Within the model the time law for the position of the bubble nose is derived and it is reported in the Eq. (2.21). The objective of this Subsection is to compare the position of the bubble nose in the simulation with the mentioned theoretical relationship.

Firstly, two assumptions of the model not valid in the simulation are described. The phases are in thermodynamic equilibrium, while in the numerical simulation superheated is allowed. The heat flux is used only to evaporate the liquid, while in the simulation the heat flux can warm up the liquid.

The version (2.21) of the theoretical nose position is valid if the bubble nucleates at the time $t = 0$ at the entrance of the heated section located at $z = 0$. In the simulation the bubble enters the heated section located at $z_0 = 4$ mm at the time instant $t_0 = 4.7$ ms, thus such initial conditions have to be introduced within the Eq. (2.21). Furthermore, the model as $t \rightarrow 0$ gives a bubble nose initial velocity equal to the velocity of the liquid inflow $U_{b,N} = U_l = G/\rho_l$. In the simulation the velocity of the bubble, before that evaporation begins, exceeds the velocity of the liquid

inflow, as expressed with the theoretical relationship (2.19). The adiabatic velocity of the bubble is $U_b = 1.175U_l$, thus the G/ρ_l term within the (2.21) is multiplied by 1.175. The final version of the time law for the prediction of the bubble nose position becomes:

$$z_N(t) = z_0 + 1.175 \frac{G}{\rho_l} \frac{\rho_v h_{lv} D}{4q} \left[\exp\left(\frac{4q}{\rho_v h_{lv} D}(t - t_0)\right) - 1 \right] \quad (7.8)$$

The Figure 7.23(a) shows the comparison of Eq. (7.8) with the simulation data. There is a good agreement between model and simulation. The model overestimates slightly the bubble velocity at a first stage, then in the simulation the bubble nose accelerates more than the value predicted. The same trend is observed on the bubble volume V_b depicted in Fig. 7.23(b), whose theoretical expression is derived from the model:

$$V_b(t) = V_{b,0} + \frac{\pi D^2}{4} \frac{\rho_l}{\rho_l - \rho_v} \left[z(t) - z_0 + 1.175 \frac{G}{\rho_l} (t - t_0) \right] \quad (7.9)$$

The origin of the initial overestimation of nose position and bubble volume is due to the delay in the beginning of the evaporation in the simulation. Even if the bubble nose crosses the entrance in the heated region at $t_0 = 4.7$ ms, the evaporation starts at around $t = 6$ ms, when the interface gets in contact with the superheated liquid

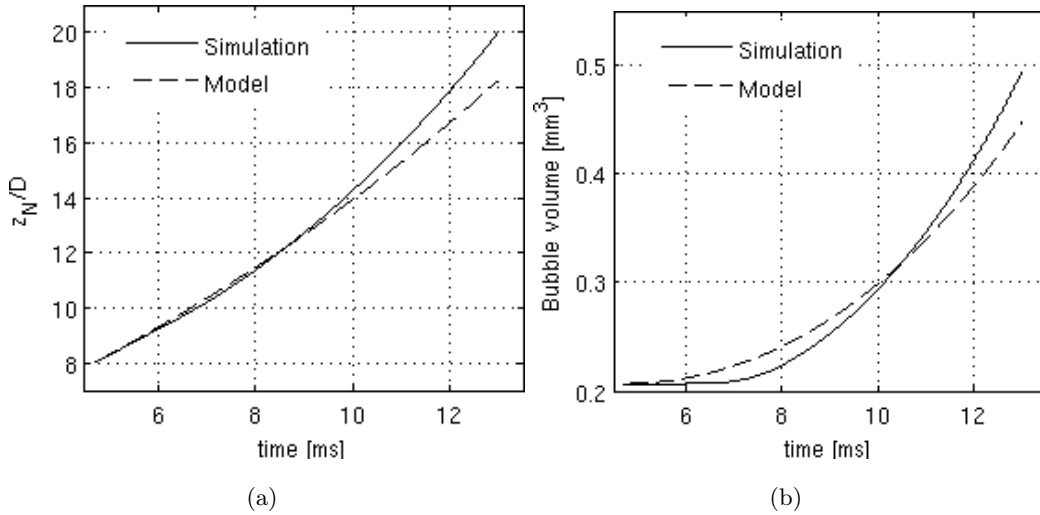


Figure 7.23: Comparison of (a) bubble nose position and (b) bubble volume between numerical results and theoretical model.

in the thermal boundary layer.

As the time elapses, the bubble growth rate in the simulation exceeds the theoretical prediction and the deviation increases with the time. The reason is the model assumption of a constant wall heat flux used only to evaporate the liquid. In the simulation, the heat power absorbed by the evaporation varies with the time. Such heat power is obtained from the sensible heat of the superheated liquid and it can exceed or be smaller than the wall heat flux. In order to obtain an estimation of the time-varying heat flux q_e absorbed by the bubble evaporation, the power absorbed to generate vapor is divided by the heated surface actually traveled by the bubble at the time instant t :

$$q_e = \frac{(dV_b/dt)\rho_v h_{lv}}{\pi D(z_N(t) - z_0)} \quad (7.10)$$

The Figure 7.24 shows that $q_e < q$ until $t < 8$ ms, which is the time instant at which the entire bubble enters within the heated region. For greater t , the vapor generation absorbs an increasing amount of heat flux given by the whole wall heat flux plus part of the liquid sensible heat. This is possible since the liquid has stored energy before

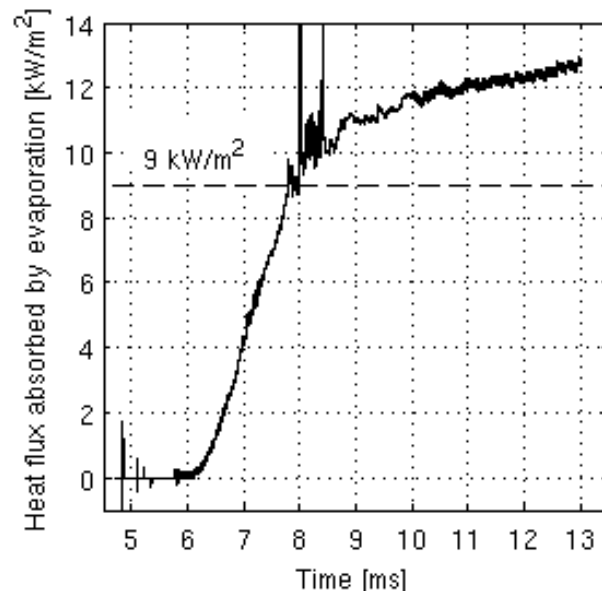


Figure 7.24: Heat flux absorbed by the bubble evaporation, computed through Eq. (7.10).

of the bubble transit. The consequence is that as $t > 8$ ms the difference between the numerical and the theoretical bubble growth rate increases, thus raising the deviation between theoretical and numerical results as observed in Figs. 7.23(a) and (b).

7.4 Dynamics and heat transfer induced by multiple bubbles

The previous Section treated the results of the simulation of a single evaporating bubble. It was demonstrated that the bubble dynamics induces disturbance on the flow field in the wake behind it, thus affecting the development of the thermal boundary layer at the wall. As a consequence, a trailing bubble would experience different flow and thermal conditions, leading to different bubble dynamics and wall heat transfer.

Actual operating conditions in boiling heat transfer experiments involves the presence of multiple bubbles flowing in series and each bubble influences the dynamics of the trailing bubble, in a way depending on the length of the liquid slugs trapped in between.

In order to simulate an elongated bubble flow comparable with actual experiments, the evaporating flow of two consecutive bubbles is simulated.

7.4.1 Simulation conditions

Two vapor bubbles are patched at the upstream of a microchannel, at the beginning of an adiabatic region. The adiabatic region is followed by a diabatic region heated with a constant heat flux. The length of the heated region is increased with respect to the test case presented in Section 7.3, in order to evaluate the heat transfer performances sufficiently downstream to the thermal entrance section. A further adiabatic portion of the channel follows the heated part to allow both the bubbles to get out of the heated region without being influenced by the channel outlet section.

The refrigerant R113 is disappearing from the experimental research on boiling flows because of its high environmental impacts, thus the simulation of such fluid has little importance for the scientific community. We decided to simulate R245fa because the material properties in terms of saturation pressure, surface tension and vapor density, are similar to R113 at the same saturation temperature.

The operating conditions simulated are set accordingly to Consolini and Thome [123] experiments on microchannel boiling heat transfer. The chosen diameter of the channel is $D = 0.5$ mm, leading to a Confinement number $Co \approx 2$ which is largely within the condition $Co > 1$ suggested by Ong and Thome [69] for an axisymmetric flow. The mass flux is $G = 550$ kg/m²s set by a velocity inlet boundary condition, leading to a predicted film thickness well solved by the $D/\Delta x = 300$ computational mesh and to a Reynolds number ensuring laminar flow. The saturation temperature is $T_{sat} = 31$ °C accordingly to [123]. The saturation properties of R245fa at 31 °C are listed in the Table 7.2.

The heat flux set in the simulation is $q = 5$ kW/m², which is lower than the values adopted in the experimental campaign of [123]. Such a low value is set in order to limit the bubble growth in the simulation. The bubble length at the exit of the heated region is proportional to the wall heat flux. The last adiabatic part of the simulated channel needs to be long enough to store both the bubbles. Thus, higher heat flux means longer channel, therefore higher computational cost of the simulation. The value of the heat flux set in the simulation limits the length of each bubble, predicted through Consolini and Thome model [8], to 7 – 8 diameters.

The length of the adiabatic region upstream to the channel is $16D$ and it is considered enough for the bubbles to reach a steady adiabatic flow. The heated length is $22D$. The length of the thermal entrance with the flow conditions simulated is around $210D$ for a laminar single phase flow. However, recent publications [6, 79] showed that the thermal entrance length for slug flows is much shorter than for a

Property	Liquid	Vapor
ρ [kg/m ³]	1322	10.5
c_p [kJ/kg·K]	1.352	0.926
λ [mW/m·K]	88.2	14.4
μ [μ Pa·s]	376	10.5
h_{lv} [kJ/kg]	187.29	
σ [mN/m]	13.28	

Table 7.2: Properties of R245fa liquid and vapor at saturation conditions for $T_{sat} = 31$ °C. Pressure is $p = 1.85$ bar.

continuous flow and several CFD studies [87, 85, 89] were conducted with around $20D$ heated. The length of the last adiabatic part of the channel is 34 diameters.

The boundary condition at the channel inlet section is a fixed constant velocity of the liquid inflow, computed as $U_l = G/\rho_l = 0.416$ m/s. The liquid enters the channel as a saturated liquid. At the channel outlet an outflow condition is set. The bubbles are initialized as slugs of $3D$ of length, with the vapor at the saturation temperature. The distance between them is $6D$. The initial condition for the velocity and temperature fields is obtained through a preliminary single phase steady state simulation run with the same flow conditions.

7.4.2 Bubbles dynamics

Within the adiabatic portion of the channel both the bubbles reach a steady flow condition. The velocity of the bubbles is $U_b = 0.485$ m/s and the thickness of the film before the wavy region is $\delta/D = 0.04$. The velocity is in perfect accord with Eq. (2.19) which predicts $U_b = 0.486$ m/s with the actual film thickness. The film thickness is in good accord with Han and Shikazono correlation [3] which predicts $\delta/D = 0.0373$ with Reynolds and Capillary numbers evaluated through the actual bubble velocity.

The Figure 7.25 shows the bubbles evolution within the heated region, which is included within $z/D = [16, 38]$. It is immediately evident that the trailing bubble grows less than the one ahead, while transiting into the heated region.

The Figures 7.26(a) and (b) report respectively the position and the velocity of the nose and the rear of the bubbles as a function of the time. The first bubble enters the heated region at $t = 4$ ms and starts to evaporate at around $t = 5$ ms, when the nose begins to accelerate. Until the trailing bubble has not begun to grow, the dynamics of the first bubble during the evaporation proceeds as though the bubble flows alone in the channel. The nose accelerates while the rear moves at a constant velocity equal to the adiabatic velocity of the bubble. At $t = 14$ ms the trailing bubble starts to evaporate. The acceleration of the nose is lower than that of the leading bubble. The transit of the bubble ahead has cooled down the superheated liquid near the wall and the thermal boundary layer has not had enough time to rearrange to the steady situation. Therefore, the trailing bubble crosses a region cooler than before the leading bubble passed and the growth rate is lower. The rear

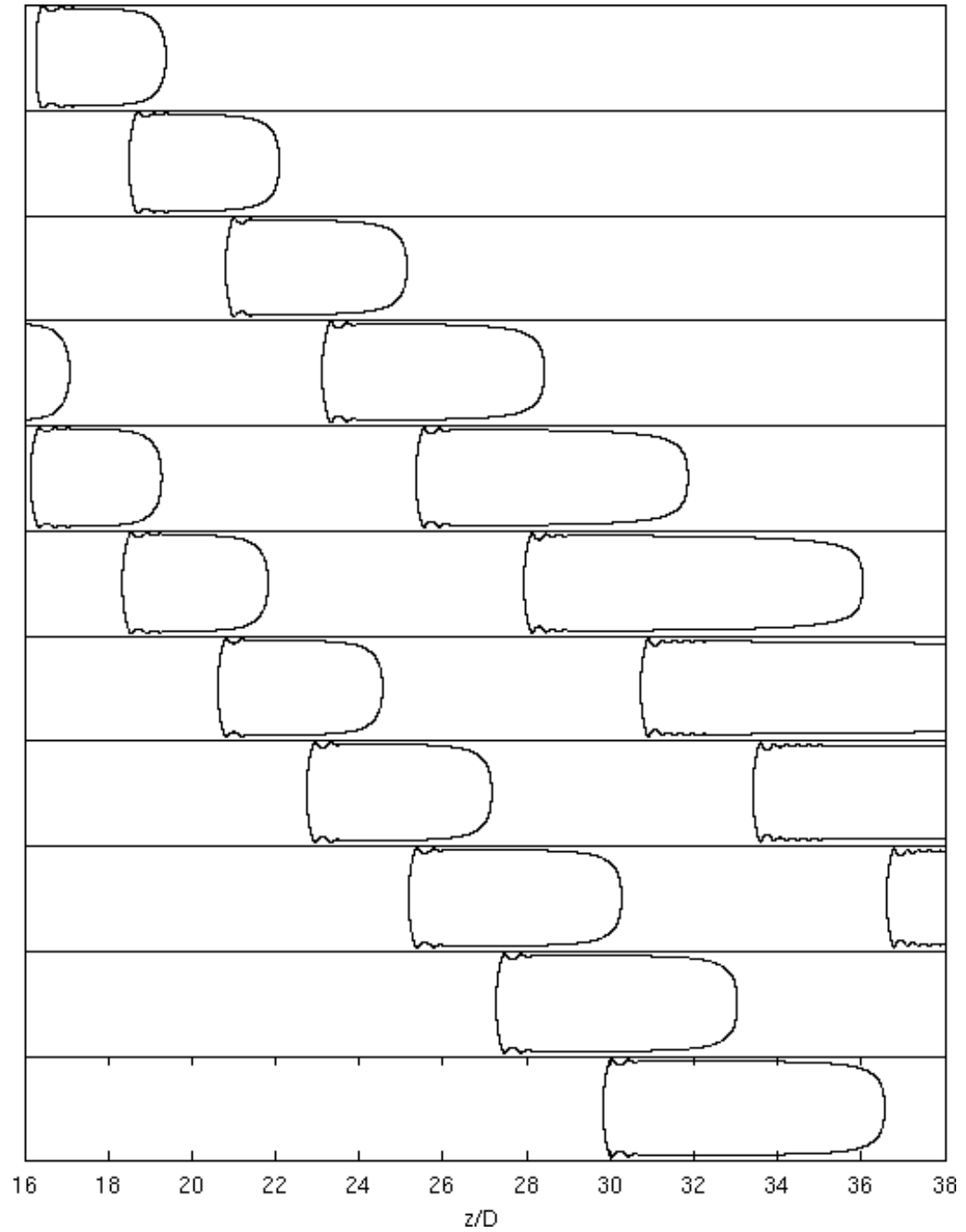


Figure 7.25: Evolution of two bubbles flowing in sequence during evaporation, from $t = 7$ ms to 30 ms at time intervals of 2.3 ms.

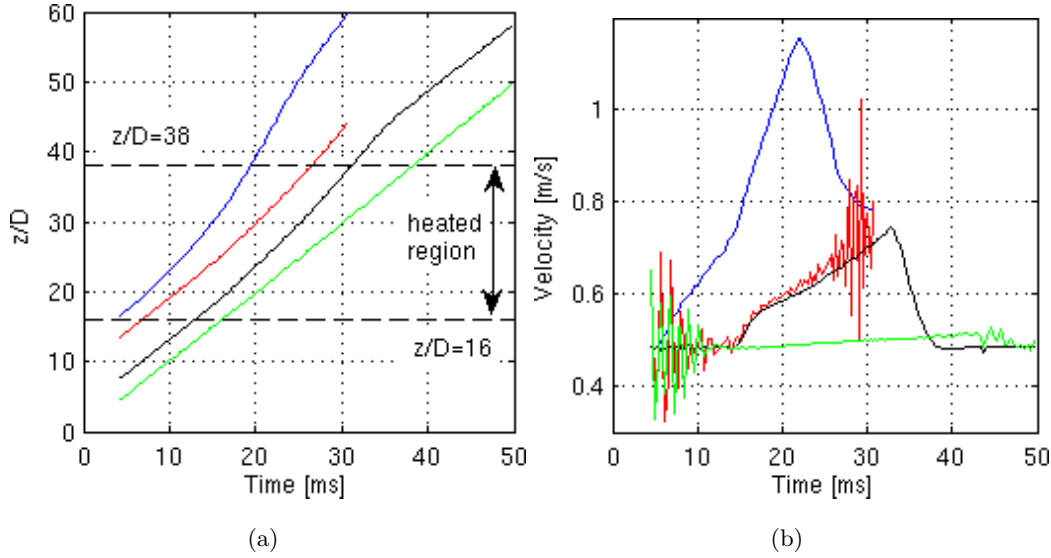


Figure 7.26: Bubbles position (a) and velocity (b). Blue and red: nose and rear of the bubble ahead, black and green: nose and rear of the trailing bubble.

of the leading bubble accelerates as well because of the liquid pushed by the evaporation of the trailing bubble. The velocity of the rear of the bubble ahead arranges at a value which exceeds slightly the velocity of the nose of the bubble behind, thus increasing the length of the liquid slug trapped.

At $t = 19$ ms the nose of the leading bubble exits of the heated region, but it continues to accelerate until $t = 22$ ms because of the superheated liquid transported by the flow within the adiabatic zone. The Figure 7.27 reports the profile of the leading bubble at $t = 19$ ms. The bubble has reached the length of $9D$ and the film thickness is increased to $\delta/D = 0.05$ because of the increased bubble velocity. As the nose of the leading bubble decelerates, while the bubble crosses the terminal section of the heated region, the rear restarts to oscillate as before evaporation began. When the bubble ahead leaves entirely the heated region the length is increased to $15D$.

The nose of the trailing bubble reaches the end of the heated section at $t = 31$ ms, the profile of the bubble at this time instant is reported in Fig. 7.27. The length of the bubble is $7D$ and the liquid film thickness is increased to $\delta/D = 0.045$. When also the trailing bubble gets out completely of the heated region the terminal length

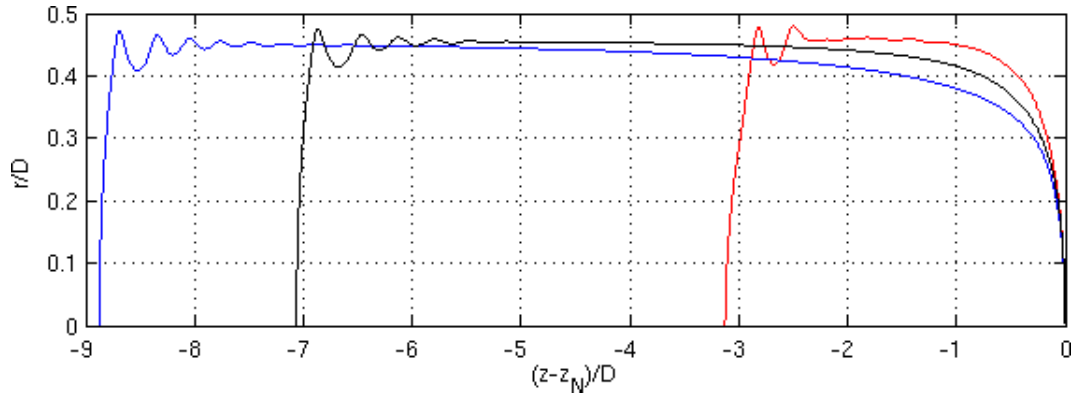


Figure 7.27: Profiles of the bubbles. Red: adiabatic; blue: bubble ahead at $t = 19$ ms, when the nose exits of the heated region; black: bubble behind at $t = 31$ ms, when the nose exits of the heated region. The profiles are shifted in order to match the nose positions.

is $9D$. The length of the liquid slug trapped between the bubbles is increased from the initial value of $6D$ to $7D$.

In conclusion, the leading bubble has the effect to cool down the liquid when evaporating within the heated region. As a consequence, the trailing bubble flows across a zone which has not had the time to restore the steady temperature field and the growth rate is less. Such effect is proved by the different length of the bubbles at the end of the growth stage. The leading bubble is grown to $15D$, the trailing one to $9D$.

At a given axial location the successive transit of multiple bubbles equally distanced would generate a time-periodic flow and temperature field. The number of bubble-liquid slug cycles necessary to attain such steady situation is unknown because in the present case only two bubbles are simulated. In the next heat transfer analysis it is assumed that the steady-periodic condition is achieved for the cycle which the second bubble is part of.

7.4.3 Heat transfer performance

The heat transfer performance obtained with the two-phase flow simulated is analyzed by means of the heat transfer coefficient, computed with the saturation tem-

perature as reference, see Eq. (7.1). The subscript *sat* is dropped in the following. The heat transfer coefficient h_{tp} as a function of the time, at four axial locations, is shown in the Fig. 7.28. The axial coordinate z_h is measured with respect to the location of the entrance in the heated region ($z_h = 0$). Each subfigure reports a black horizontal dash line identifying the value of the heat transfer coefficient in the preliminary single phase simulation at the given location. Time-averaged heat transfer coefficients are computed separately for the leading and the trailing bubble cycles at each axial location as:

$$\bar{h}_{tp}(z) = \int_{t(z=z_N+Ls/2)}^{t(z=z_R-Ls/2)} h_{tp}(z, t) dt \quad (7.11)$$

where $t(z = z_N + Ls/2)$ is the time instant at which the axial location of the bubble nose plus half length of the trapped liquid slug crosses the section which the heat transfer is being averaged at. Half length of the liquid trapped is considered as well behind the bubble rear. Thus, each bubble cycle includes the bubble plus the length of the trapped liquid slug, half ahead of the bubble and half behind. The averaged heat transfer coefficients are reported as horizontal dash blue lines in Fig. 7.28. Each line extends within the time-window considered to compute the average value, the limits of the window are identified as vertical red lines.

The first axial location which the heat transfer is reported at in Fig. 7.28 is $z_h/D = 4$. The heat transfer coefficient for the preliminary single phase simulation is $2234 \text{ W/m}^2\text{K}$, about three times the value for thermally developed laminar flow with constant heat flux $4.36 \cdot (\lambda_l/D) = 769 \text{ W/m}^2\text{K}$. The two-phase heat transfer coefficient begins to rise when about half bubble has crossed the location considered, similarly to the case discussed in the Section 7.3. As well, a peak in the heat transfer coefficient is reached in the wake behind each bubble rear. The peak at the rear of the leading bubble (first cycle) is $3331 \text{ W/m}^2\text{K}$ and it is 49% higher than the single phase value at that axial location. The average value of the heat transfer coefficient for the first bubble cycle is $2626 \text{ W/m}^2\text{K}$ which is 18% more than the single phase value. After the peak reached when the rear of the leading bubble is passing, the heat transfer coefficient drops as the thermal boundary layer at the wall is being restored while the liquid slug transits. The local minimum on the heat transfer coefficient is the 85% of the peak value. The drop in the heat transfer performance is limited by the transit of the trailing bubble, which raises h_{tp} to values higher than

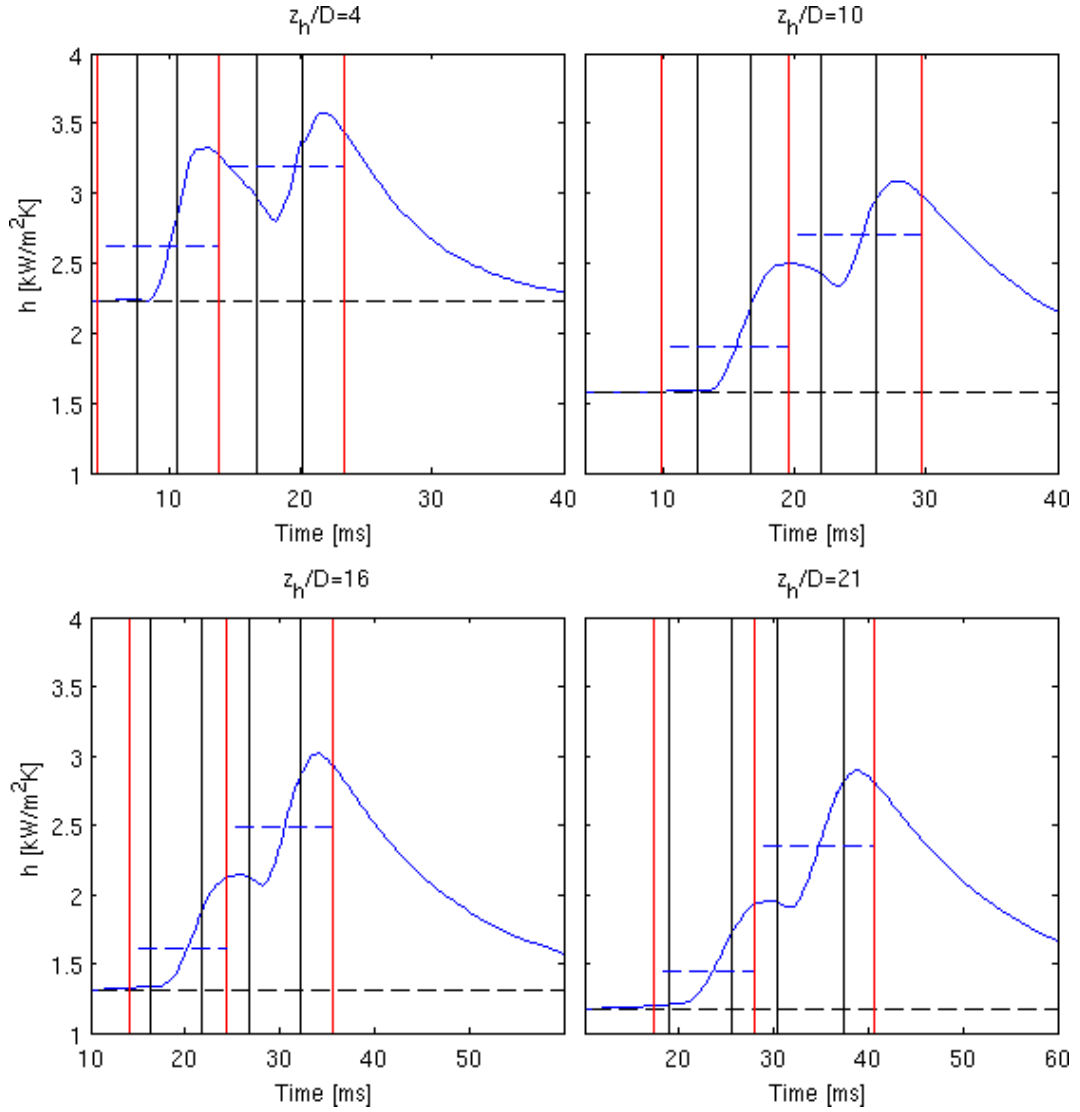


Figure 7.28: Heat transfer coefficient at various axial locations. The axial location is reported by referring to the entrance in the heated region. The black vertical lines locate the transit of the bubbles nose and rear, the red lines locate the limits of the time intervals which the coefficients are averaged within. The horizontal black dash lines identify the value of the heat transfer coefficient in the single phase case.

those measured for the first cycle. The peak related to the second bubble cycle is $h_{tp} = 3571$ W/m²K (60%) while the average is $\bar{h}_{tp} = 3195$ W/m²K (43%). The

reason of the higher values is that the trailing bubble comes across a region whose thermal layer has not restored to the steady situation, therefore the effects of two consecutive transits overlap partially. Note that, as a consequence of the transit of both the bubbles, at $z_h/D = 4$ the thermal layer takes about 30 ms to restore completely, over twice the time taken for both the bubbles to pass.

Moving on downstream axial locations, peaks and average values of the heat transfer coefficient reduce, as shown in Fig. 7.29(a) which plots the average values of h_{tp} . The two-phase flow profiles for both the bubble cycles decrease similarly to the Graetz solution for single phase flow, as detected also by Walsh *et al.* [6]. The Table 7.3 lists the heat transfer coefficients at the sections whose time-varying coefficients are plotted in Fig. 7.28.

The axial location $z_h/D = 21$ is the most downstream location analyzed and it is next to the exit of the heated region (22 diameters long). The absolute efficiency has decreased with respect to the locations upstream, but the enhancement with respect to the single phase flow has grown. The average heat transfer coefficient for the first cycle has increased up to 24% over the single phase value, from 18% at $z_h/D = 4$. For the second cycle the growth is much more sensible, from 43% at $z_h/D = 4$ to 100%. The reasons to explain such an improvement on the second cycle, as downstream locations are considered, are various. Firstly, the time lag between the transit of the rear of the leading bubble and the nose of the trailing bubble reduces because of the acceleration of the evaporating bubbles. The time left for the thermal layer to develop to the steady configuration is less, such that

z_h/D	h_{sp}	$\bar{h}_{tp,1}$	$\max(h_{tp,1})$	$\bar{h}_{tp,2}$	$\max(h_{tp,2})$
4	2234	2626 (18)	3331 (49)	3195 (43)	3571 (60)
10	1571	1907 (21)	2496 (59)	2697 (72)	3090 (97)
16	1305	1604 (23)	2138 (64)	2486 (90)	3014 (131)
21	1171	1447 (24)	1950 (67)	2343 (100)	2891 (147)

Table 7.3: Heat transfer coefficients in W/m²K units at the axial locations considered in the plots of Fig. 7.28. The value between parenthesis is the relative enhancement with respect to the single phase value reported in the second column and it is computed as $\frac{h_{tp}-h_{sp}}{h_{sp}} \times 100$.

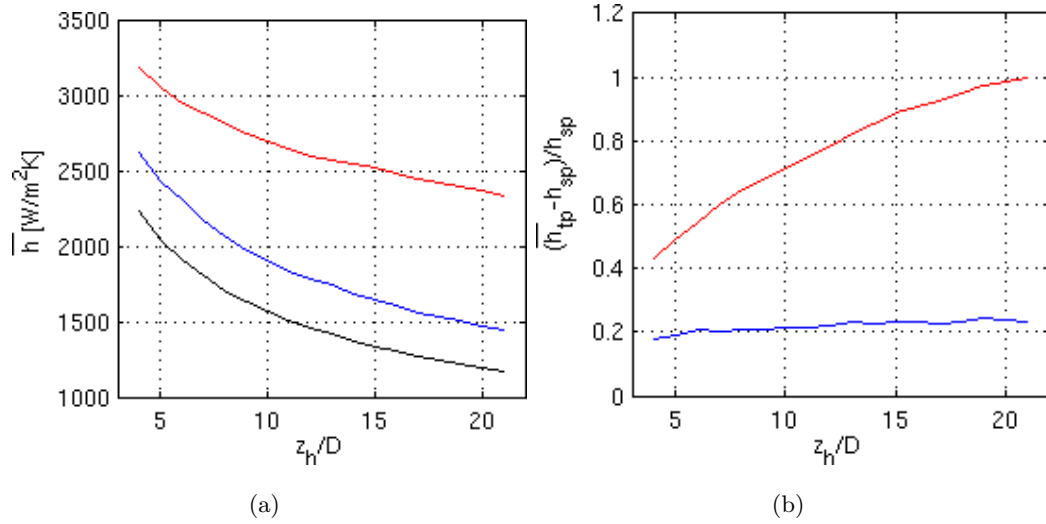


Figure 7.29: (a) Time-averaged heat transfer coefficient along the axial coordinate, (b) enhancement on the heat transfer coefficient with respect to the local single phase value. Black: single phase case, blue: leading bubble cycle, red: trailing bubble cycle.

the drop in the heat transfer coefficient is almost disappeared at $z_h/D = 21$, see Fig. 7.28. Secondly, the liquid within the trapped slug is getting faster because it is being pushed by the nose of the accelerating trailing bubble, thus the local Peclet number increases. The Peclet number is related to the heat transfer performance in a thermal entrance region, correlations for hydrodynamically developed flow takes typically the following aspect:

$$\text{Nu}_x = \frac{C}{(x^*)^\alpha} = C \left(\frac{\text{Pe} \cdot D}{x} \right)^\alpha \quad (7.12)$$

where C and α are constants relative to the particular correlation considered. The axial location x can be meant here as the distance from the rear of the leading bubble, where the thermal layer restarts to develop. Therefore, at the same distance from the rear of the bubble, a higher Peclet number means a higher Nusselt number, thus better heat transfer performance. In addition, the velocity profile within the trapped liquid slug is far from the hydrodynamic developed condition. The profile is more flat as shown in Fig. 7.20(c), the velocity at the wall is higher thus slowing down the reforming of the thermal boundary layer.

The Figure 7.29(b) shows that the enhancement on the heat transfer led by the

first bubble cycle is almost flat at around 20% more than the single phase value. Differently, the trailing cycle raises strongly the cooling efficiency compared to the single phase flow as downstream sections are observed. The Figure 7.29(b) suggests that for a distance from the thermal entrance region greater than $21D$, the heat transfer coefficient tends to be over twice the single phase flow one.

Comparison with correlations for slug flow without phase change

The average value of the heat transfer coefficient at the last $z_h/D = 21$ heated section is compared with correlations obtained for elongated bubbles flow without phase change, introduced in the Section 2.2. Such correlations express the time-averaged Nusselt number for a bubble-liquid slug cycle, by considering a steady-periodic flow. It is assumed that the heat transfer at $z_h/D = 21$ has already reached the periodic condition for the trailing bubble cycle. It means that a third bubble equally distanced from the bubble ahead of it, would give the same profile $h_{tp}(t)$ while passing at the chosen axial location. The correlations considered were obtained by fitting the Nusselt number data calculated through reference to the bulk temperature, therefore they might overestimate a coefficient based on the saturation temperature. On the other hand, such correlations refer to thermally developed two-phase flow, while the axial location considered is still within the thermal entrance region as the profile of \bar{h}_{tp} at $z_h/D = 21$ is not yet asymptotic. Therefore, the simulation value is slightly above the fully developed value that would hold more downstream of the thermal entrance section. For this reason the two-phase Nusselt number relative to the single phase flow value at $z_h/D = 21$ is observed in addition to the absolute value.

The average two-phase Nusselt number for the trailing bubble cycle in the simulation and the relative enhancement on the heat transfer performance are:

$$\overline{\text{Nu}}_{tp} = \frac{\bar{h}_{tp}D}{\lambda_l} = 13.29, \quad \frac{\overline{\text{Nu}}_{tp}}{\text{Nu}_{sp}} = 2 \quad (7.13)$$

where $\text{Nu}_{sp} = 6.64$.

Lakehal *et al.* [85] developed a correlation for elongated bubbles flow based on the results of numerical simulations. The correlation is reported in Eq. (2.25), but the asymptotic value for constant heat flux 4.36 replaces the value for constant temperature 3.67. To compute the bubble Reynolds number, we used both the adiabatic bubble velocity $U_b = 0.485$ m/s and the mean velocity $U_b = 0.58$ m/s

while crossing the location $z_h/D = 21$.

Walsh *et al.* [6] proposed a correlation for slug flow based on experimental results. The correlation that they proposed is reported in Eq. (2.23). The term $1 - \epsilon$, used to reduce the data, accounts for the percentage contact area of the liquid slug, since the gas slug does not contribute to the wall cooling. However in the present case, in which phase change occurs, the region occupied by the bubble gives a great contribute to the heat transfer due to the presence of the liquid film, thus the term $1 - \epsilon$ is dropped.

Gupta *et al.* [87] only modified a multiplying coefficient within Walsh *et al.* correlation according to the results of numerical simulations. See Eq. (2.26) for reference.

The values predicted by the cited correlations are reported in the Table 7.4. The correlations of Walsh *et al.* and Gupta *et al.* give results in accord with Lakehal *et al.* prediction, thus the drop of the term $1 - \epsilon$ is a valid approximation. The Nusselt number obtained through the simulation is in very good accord with the correlations. It is placed within the range [12.2, 15.67] given by the experimental models and the relative error is within 15% for all the predictions considered. As well, the two-phase to single phase flow Nusselt number ratio is well within the range [1.8, 2.6] obtained through the correlations. The maximum relative error is 23% for the comparison with Lakehal *et al.* prediction with $U_b = 0.58$ m/s, while it is within 15% in the other cases.

	$\overline{\text{Nu}}_{tp}$	$\frac{\overline{\text{Nu}}_{tp}}{\overline{\text{Nu}}_{sp}}$
Simulation	13.29	2
Lakehal <i>et al.</i> [85]	14.16 – 15.67	2.25 – 2.6
Walsh <i>et al.</i> [6]	14.57	2.34
Gupta <i>et al.</i> [87]	12.2	1.8

Table 7.4: Comparison of the heat transfer performance obtained with the simulation with the values predicted by correlations. The single phase Nusselt number used as reference is 6.64 for the simulation and 4.36 for all the correlations.

Comparison with a heat transfer model for evaporation

The time evolution of the heat transfer coefficient $h_{tp}(t)$ at the axial location $z_h/D = 21$ is compared with a heat transfer model for evaporation based on the actual flow configuration. The principle is similar to the three zones model of Thome *et al.* [5], which is not applicable entirely to the simulated conditions.

The three zones model computes time-averaged heat transfer coefficients for liquid slug, film and dryout zones by integration of $h(t)$ over the time intervals estimated for each zone. The length of each zone is derived through models and correlations involving the operating conditions of the flow, correlations validated by a large experimental database. Introducing the general coefficients for the model reported in [78], the fluid properties, the wall heat flux and the saturation pressure lead to a bubble-liquid slug pair transit period of 6.5 s, generated by the bubble formation process. The mass flow rate imposed at the channel inlet section leads to a vapor quality of the order of 10^{-5} to obtain bubbles of length comparable with the simulation. The model with such parameters predicts the formation of bubbles $8D$ long, separated by liquid slugs more than $5000D$ long, dryout does not occur. Differently, in the simulation the bubble formation process is not accounted for and the length of the trapped liquid slug is set arbitrarily to $6D$ at the beginning of the simulation. As a consequence, the average heat transfer coefficient given by the three zones model is insensitive of the liquid film zone around the bubble, whose length is $1/1000$ of the liquid slug one, and it is influenced only by single phase heat convection within the slug. In the simulation liquid and bubble zones have similar length and contribute equally to the average heat transfer.

In addition, the modified version of the Moriyama and Inoue [124] correlation for the film thickness used in the model predicts a value of $\delta/D \approx 1/250$, ten times higher than the simulation result. As a consequence, the assumption of heat conduction gives an average heat transfer coefficient of $40000 \text{ W/m}^2\text{K}$ within the film zone, more than one order of magnitude higher than the simulation one. However, the correlation for the film thickness involves variables estimated through considerations on the flow induced by the evaporation process occurring upstream of the axial location considered. Thus, the reason of the high deviation is again the different flow configuration.

According to the configuration simulated, the following sequence of patterns crosses the axial location under analysis: liquid slug ahead of the leading bubble, leading bubble, trapped liquid slug, trailing bubble, liquid slug behind the trailing bubble. During the transit of each pattern, the heat transfer coefficient as a function of the time can be estimated through the same models employed in the three zones model:

- liquid slug ahead of the leading bubble: by neglecting the acceleration of the liquid due to the evaporation, the heat transfer is constant and depends only on the axial location.

$$\Rightarrow h(z_h, t) = h(z_h) = h_{sp}(z_h) \quad (7.14)$$

- leading and trailing bubbles: it is assumed heat conduction across the film, whose geometry is modeled as an annulus.

$$\Rightarrow h(z_h, t) = \frac{\lambda_l}{R \ln\left(\frac{R}{R - \delta(z_h, t)}\right)} \quad (7.15)$$

where the actual film thickness measured in the simulation is introduced as $\delta(z_h, t)$.

- trapped liquid slug and liquid slug behind the trailing bubble: the flow is assumed to be hydrodynamically and thermally developing, the London and Shah correlation given by the VDI [125] for laminar developing flow is used.

$$\Rightarrow h(z_h, t) = \left(\frac{\lambda_l}{D}\right) 0.455 \text{Pr}^{1/3} \left(\frac{\text{Re } D}{z_R(z_h, t) - z_h}\right)^{1/2} \quad (7.16)$$

where the Reynolds number is computed with the inflow liquid velocity as a reference. The thermal boundary layer is assumed to reform from the rear of the bubble, whose location $z_R(z_h, t)$ can be intended as thermal entrance, thus the distance of z_h from the the thermal entrance $z_R(z_h, t) - z_h$ is introduced in the correlation.

The liquid film thickness decreases from the value R at the nose of the bubble to the minimum value next to the rear. Thus, the assumption of heat conduction gives increasing values of the heat transfer coefficient from the value zero at the nose of the bubble. To allow a smooth transition from the liquid slug to the bubble zone,

the heat transfer coefficient is computed through Eq. (7.16) while the Eq. (7.15) gives a smaller value, even if the bubble is passing.

The Figure 7.30 plots the heat transfer coefficient for the simulation compared with the result of the described model. The heat conduction assumption overestimates the heat transfer performance on both the film regions. In particular at the rear of the leading bubble the estimation is almost twice the value measured in the simulation. This is not surprising because in the Section 7.3 it was already shown that the saturation based heat transfer coefficient was quite smaller than the heat conduction based one. Therefore, the heat conduction assumption is not verified even in this case, but consider that the liquid film is rather thick.

The heat transfer coefficient computed by the correlation for developing flow reaches high peaks next to the rear of each bubble, where z_R is very close to z_h . At

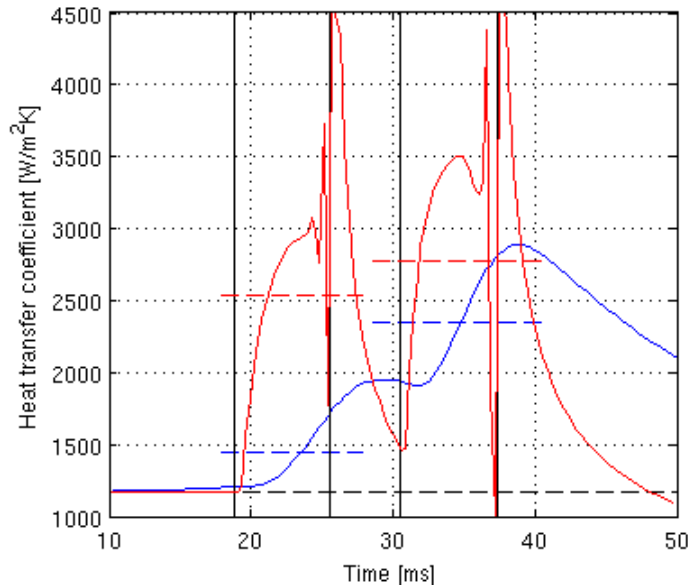


Figure 7.30: Comparison of the simulation heat transfer coefficient (blue) at $z_h/D = 21$ with the model (red). The blue and red dash horizontal lines identify the average values for each cycle, the black dash horizontal line the single phase coefficient, the black solid vertical lines the time instants of the transit of each nose and rear of the bubbles.

the rear of the bubble the model overestimates the result of the simulation, afterwards it drops sharply as the liquid slug transits. For the reason previously discussed, in the simulation the heat transfer in the wake of the bubble remains high. The dynamics of the flow behind the bubble is very different from a developing flow, thus it is not surprising that the correlation is not able to predict the actual heat transfer performance. Furthermore the initial condition, from which the thermal layer develops, depends on the thermal and fluid dynamics occurred during the transit of the bubble.

The good agreement between the average coefficients for the trailing bubble cycle (relative deviation of 20 %) is due mainly to the balance of local overestimation in the liquid film and local underestimation in the bubble wake.

In general, the model does not predict the local heat transfer coefficient in a satisfactory way. The correlations adopted are not able to capture the peculiar dynamics of the flow in the film and in the wake region, which determines the local trend of the heat transfer coefficient.

However, the model has to be meant as a starting point. A thorough study of the flow field in the film and the liquid slug regions can lead to more detailed analytical or phenomenological descriptions of the flow. The route toward a reliable prediction of the heat transfer passes across the accurate modeling of the flow in the mentioned regions.

Conclusions

The project of this three years doctoral course was to improve a CFD solver in order to model the evaporation of bubbles in the slug flow regime in microchannels. The objective was to analyze the thermal and fluid dynamics of the flow, thus providing a better understanding of the mechanisms leading to an enhanced wall heat transfer with respect to single phase flow.

The numerical framework employed is based on the commercial CFD software Ansys Fluent, improved with self-implemented models to accurately account for the interfacial effects that dominate the flow. An Height Function method allows the accurate computation of the local interface curvature, leading to a correct evaluation of the surface tension force. An evaporation model computes the rates of mass and energy exchange at the phases interface on the basis of the local interface superheating, accounting for the kinetic mobility of liquid and vapor molecules that generates an interfacial resistance to mass transfer.

Typical benchmarks for the validation of multiphase aimed numerical schemes assessed the reliability of the numerical framework, providing the following conclusions.

- The Height Function reconstructs a circular interface with errors in the curvature computation that scale with the second order with respect to the mesh element size when $D/\Delta x < 80$. The Fluent default Youngs algorithm gives errors that worsen as the mesh is refined. When $D/\Delta x > 80$ the interface reconstruction worsen for the HF as well, but the accuracy remains more than three orders of magnitude better than Youngs one.
- Errors in the curvature computation generate unphysical vortices across the interface thus preventing the numerical results on the flow field from being

reliable nearby the interface. If the HF method is employed the magnitude of such spurious velocities scales with a convergence order in the range $[1, 2]$ as the mesh is refined, on the contrary Youngs generated vortices get faster.

- The Green-Gauss node based reconstruction of the face centered gradients allows better balance of pressure gradient and surface tension terms at the interface, minimizing pressure overshoots and undershoots in proximity of the interface and the magnitude of the unphysical flows.
- The simulation of the heat-transfer-controlled stage of a vapor bubble growing in superheated liquid showed that excellent agreement between numerical and analytical bubble growth rates is obtained when the accommodation coefficient is set as unity.
- The magnitude of the spurious vortices arising when employing the Youngs method to compute the interface curvature leads to a wrong faster growth rate due to the unphysical convective flows and prevents the bubble from maintaining the spherical shape. The growth rate obtained with the HF method accords very well with the analytical solution.

The validated numerical framework was employed to perform preliminary simulations of adiabatic flows. An axisymmetrical formulation of the flow equations is adopted in order to fulfill grid resolution requirements but keeping low computational time. The comparison of the simulations results with experimental findings and published correlations was very satisfactory and the reliability of the improved CFD tool to model actual flow configurations was assessed.

In particular, the numerical code is able to capture the concurrent effects of capillary, viscous and inertial forces on the liquid film thickness and pressure drop related to elongated bubbles drifted by a liquid flow rate within a horizontal circular microchannel. Such flow configuration corresponds to the adiabatic version of the flow which this thesis deals with, therefore the good results obtained provide an optimal starting point to ensure a reliable modeling of bubble and flow dynamics as energy equation and evaporation model are turned on.

The evaporating flow was obtained by simulating bubbles flowing within a circular horizontal channel, heated by a constant heat flux. The flow conditions were chosen in order to guarantee a laminar flow ($Re_l < 2000$) and negligible gravitational effects

($Co > 1$ [69]), the latter allowing an axisymmetrical formulation of the flow problem. The liquid flowing into the channel is at saturated conditions, as well as liquid and vapor phases at the beginning of the simulation, except the thermal boundary layer. A superheated developing thermal boundary layer is placed at the heated wall, as result of a preliminary steady state single phase simulation.

The analysis of the thermal and hydrodynamics features of the flow and the wall heat transfer led to the conclusions that follow.

- Velocity boundary condition at the channel inlet forces the bubble to move downstream but the thinning of the liquid film as effect of the evaporation is not captured. Differently, when a fixed pressure difference is imposed among the terminal sections of the channel, the bubble slows down as evaporation starts, thus decreasing the film thickness. The bubble may decelerate generating a backflow, even though the nose continues to travel downstream to the channel.
- The heat transfer performance is improved by the two-phase flow with respect to the single phase case throughout the heated length of the channel. The maximum enhancement is measured in the wake of the bubble, with the two-phase flow heat transfer coefficient exceeding the single phase one by more than 20 % along 3 diameters behind the bubble. There are two main reasons for such an improvement. Firstly, the bubble transit has squeezed the thermal boundary layer against the wall and the local film evaporation has cooled down the superheated liquid. The thermal layer then develops to reach the steady situation that was holding before the bubble passage, in the meantime the transient heat convection is more efficient. Secondly, the bubble modifies the velocity profile of the liquid behind it from parabolic to flat. The liquid velocity in the proximity of the channel wall is temporarily increased, therefore the development of the thermal layer to the steady situation is delayed.
- The measured liquid film thickness gives $D/\delta \approx 20$. For such thickness the film can not be assumed stagnant and the assumption of pure heat conduction across the film leads to overestimation of the heat transfer coefficient.
- When multiple bubbles evaporate in sequence, the bubble ahead cools down the thermal layer such that the bubble behind grows less. The time-averaged heat transfer coefficient at given axial locations is higher for the trailing bubble

cycle, due to the effect of the transit of two consecutive bubbles on the local thermal layer development. After a heated length of $21D$, the leading bubble cycle measures an average heat transfer coefficient of 20% higher than the single phase one, while the trailing cycle doubles the single phase value. The transient heat convection mechanism in the wake of the bubble has a strong influence on the average heat transfer performance of the bubble cycle. Hence, models aimed to predict the heat transfer performance of a slug flow should solve properly the transient heat convection problem holding in such region.

- The average Nusselt number measured for the trailing bubble cycle accords well with the prediction given by three correlations proposed for slug flow without phase change, the errors are included within 15%. The chosen length of the trapped liquid slug does not reflect actual flow boiling conditions, thus the comparison of the heat transfer performance with flow boiling experimental results or prediction models is not feasible.

Further improvements

The set-up of the simulations of evaporating bubbles could be modified to model actual experimental conditions on flow boiling and the numerical framework could be improved to decrease the computational time. By the following modifications, the heat transfer coefficients measured far downstream the entrance in the heated region are expected to reproduce experimental results closely, thus providing an efficient prediction tool.

- Instead of patching vapor bubbles at the beginning of the simulation, both vapor and liquid phases can be introduced within the channel as coflow streams at the inlet section. In this way, bubbles and liquid slugs length reflects the flow conditions. The existence of univocal vapor and liquid flow rates make possible the definition of a void fraction and a vapor quality, which are parameters fundamental to characterize a two-phase flow.
- The heated length can be increased, in order to obtain thermally developed flow conditions as in experiments.

- The computational grid should be refined at the wall, where the most important phenomena occur, while coarsened at the center of the channel. Such arrangement could reduce considerably the computational cost of the simulations, thus allowing the modeling of flows with much thinner liquid films. Nevertheless the Height Function method should be modified to work with non-uniform grids or replaced by more flexible interface reconstruction algorithms.

Appendix A

Numerically induced capillary waves in the simulation of multiphase flows

Francois *et al.* [48] showed that employing a balanced-force algorithm for the pressure-velocity coupling and providing the exact curvature, the parasitic currents across a static droplet in equilibrium without gravity are of the round-off error order. Thus, the non-zero velocity field appearing when computing the local curvature through an interface reconstruction algorithm (an Height Function algorithm was employed), was interpreted by these authors as the consequence of an insufficiently accurate curvature estimation. Recently, Popinet [49] showed that running longer in time the same static droplet simulation and reconstructing the interface with an Height Function algorithm, it is possible to recover the exact balance between pressure and surface force terms. At the end of a transient stage, the velocity fields magnitude decreases to the round-off error. This is in contrast with the concept of “parasitic” entity, which should hold independently of time. Moreover, Popinet observed that the time period of the velocity field oscillations detected also by Francois *et al.* was compatible with the evolution of a physical capillary wave, induced by the numerical errors in the droplet profile initialization. Thus, he suggested a physical consistence for those velocity fields.

We have performed several numerical simulations of a two-dimensional inviscid static droplet in equilibrium without gravity, for a wide range of numerical and

physical parameters. Our aim is to confirm Popinet interpretation proving that the space and time evolution of the droplet interface agrees with the results of a stability analysis of the droplet, subject to initial small amplitude perturbations.

A.1 Stability analysis of a static droplet

The stability analysis of a static droplet in equilibrium without gravity is performed, for small amplitude initial perturbations. Viscous effects are not taken into account. The droplet is modeled in two dimensions, thus it can be considered as a cylinder and perturbations are invariant along the z axis. Using a polar coordinates reference frame (r, θ) centered at the droplet center, continuity and momentum equations have the following form:

$$\frac{1}{r} \left[\frac{\partial(r u_r)}{\partial r} \right] + \frac{1}{r} \frac{\partial u_\theta}{\partial \theta} = 0 \quad (\text{A.1})$$

$$\rho_l \left[\frac{\partial u_r}{\partial t} + u_r \frac{\partial u_r}{\partial r} + \frac{u_\theta}{r} \frac{\partial u_r}{\partial \theta} - \frac{u_\theta^2}{r} \right] = -\frac{\partial p}{\partial r} \quad (\text{A.2})$$

$$\rho_l \left[\frac{\partial u_\theta}{\partial t} + u_r \frac{\partial u_\theta}{\partial r} + \frac{u_\theta}{r} \frac{\partial u_\theta}{\partial \theta} + \frac{u_\theta u_r}{r} \right] = -\frac{1}{r} \frac{\partial p}{\partial \theta} \quad (\text{A.3})$$

where $u_r(r, \theta, t)$ and $u_\theta(r, \theta, t)$ are the radial and the angular velocity components and $p(r, \theta, t)$ is the pressure. Equations from (A.1) to (A.3) can be rewritten substituting each variable with the sum of a steady plus a perturbed quantity, as example $u_r = \bar{u}_r + u'_r$. Neglecting the products of perturbed quantities and reminding that the steady velocities are zero and the steady pressure is constant inside the droplet, the equations simplify in the form:

$$\frac{1}{r} \left[\frac{\partial(r u'_r)}{\partial r} \right] + \frac{1}{r} \frac{\partial u'_\theta}{\partial \theta} = 0 \quad (\text{A.4})$$

$$\rho_l \frac{\partial u'_r}{\partial t} = -\frac{\partial p'}{\partial r} \quad (\text{A.5})$$

$$\rho_l \frac{\partial u'_\theta}{\partial t} = -\frac{1}{r} \frac{\partial p'}{\partial \theta} \quad (\text{A.6})$$

Applying the operators $\frac{1}{r} \frac{\partial[r(\cdot)]}{\partial r}$ and $\frac{1}{r} \frac{\partial}{\partial \theta}$ to the Eqs. (A.5) and (A.6) and summing the results, the following Laplace equation yields for the pressure:

$$\frac{1}{r} \frac{\partial}{\partial r} \left[r \frac{\partial p'}{\partial r} \right] + \frac{1}{r^2} \frac{\partial^2 p'}{\partial \theta^2} = 0 \quad (\text{A.7})$$

Initial interface perturbation is supposed to be in the form:

$$R(\theta, t = 0) = R_0 + \delta_0 e^{im\theta} \quad (\text{A.8})$$

where R_0 and δ_0 are the initial droplet radius and the perturbation amplitude, m is the mode of oscillation. By adding a $\delta_{0,j} e^{im_j\theta}$ term to Eq. (A.8) for each j -th additional mode, the presence of more than one mode of oscillation is accounted for. Pressure and velocities evolution can be expressed as products of single variable functions:

$$p'(r, \theta, t) = \hat{p}(r)A(t)e^{im\theta} \quad (\text{A.9})$$

$$u'_r(r, \theta, t) = \hat{u}_r(r)A(t)e^{im\theta} \quad (\text{A.10})$$

$$u'_\theta(r, \theta, t) = \hat{u}_\theta(r)A(t)e^{im\theta} \quad (\text{A.11})$$

Substituting the Eq. (A.9) in (A.7), the following ordinary differential equation yields for the pressure:

$$r^2 \frac{d^2 \hat{p}}{dr^2} + r \frac{d\hat{p}}{dr} - m^2 \hat{p} = 0 \quad (\text{A.12})$$

The solution of Eq. (A.12) can be expressed as a linear combination of two solutions:

$$\hat{p}(r) = c_1 r^m + c_2 r^{-m} \quad (\text{A.13})$$

but the second term is singular at $r = 0$, then $c_2 = 0$. Substituting Eqs. (A.9), (A.10) and (A.13) in (A.5), the following relation can be found:

$$\frac{dA/dt}{A} = -\frac{mc_1 r^{m-1}}{\rho_l \hat{u}_r} = \beta \quad (\text{A.14})$$

Since the left and the center sides of the equation are independent one of the other, in order for the equation to be true they both have to be equal to a constant that will be called β . Solving left hand with right hand side equation, the function of time $A(t)$ is found:

$$A(t) = a_0 e^{\beta t} \quad (\text{A.15})$$

It is evident that β is related to the stability of the time perturbation. The interface evolution with time is postulated to be in the form:

$$R(\theta, t) = R_0 + \delta_0 e^{im\theta} B(t) \quad (\text{A.16})$$

where $B(t = 0) = 1$. The expression for $B(t)$ can be found imposing that the time derivative of the interface has to equalize the radial velocity at the interface: $dR/dt = u'_r(r = R_0, \theta, t)$. It follows:

$$B(t) = \frac{\hat{u}_r(R_0)a_0}{\delta_0\beta} e^{\beta t} \quad (\text{A.17})$$

and the constant a_0 is obtained imposing initial condition on $B(t)$, then $a_0 = \beta\delta_0/\hat{u}_r(R_0)$. Interface evolution with time takes the following form:

$$R(\theta, t) = R_0 + \delta_0 e^{im\theta} e^{\beta t} \quad (\text{A.18})$$

The time-constant β is a complex number. Its imaginary part identifies non-damped oscillations, a positive real part leads to growing oscillations and a negative one to damped oscillations. To find the value of the constant β , the pressure jump at the interface is imposed through the Laplace law:

$$(p - p_e)_{r=R_0} = \sigma\kappa(\theta, t) \quad (\text{A.19})$$

where p_e is the pressure outside the droplet. $\kappa(\theta, t)$ is the local interface curvature, which in polar coordinates is evaluated as follows:

$$\kappa = \frac{R^2 + 2R_\theta^2 - RR_{\theta\theta}}{(R^2 + R_\theta^2)^{3/2}} = \frac{1 - \delta/R_0}{R_0} + \frac{m^2\delta}{R_0^2} \quad (\text{A.20})$$

with $\delta(\theta, t)$ being the local perturbation amplitude $\delta = \delta_0 e^{im\theta} e^{\beta t}$. The subscript θ indicates the order of derivation with respect to the angular coordinate. Using the fact that $(\bar{p} - \bar{p}_e)_{r=R_0} = \sigma/R_0$, Eq. (A.19) leads to the following expression:

$$\beta^2 = -\frac{\sigma}{\rho_l R_0^3} m(m^2 - 1) \quad (\text{A.21})$$

For $m > 1$, Eq. (A.21) has always two pure imaginary solutions, then the perturbations do not grow with time, but they have an oscillatory behavior. Wave pulsation is $\omega = \text{Im}(\beta)$, and it is related to the time period of the perturbation as $\omega = 2\pi/T$. Thus, the perturbation time period can be expressed as:

$$T = \sqrt{\frac{4\pi^2 \rho_l R_0^3}{\sigma m(m^2 - 1)}} \quad (\text{A.22})$$

This expression underlines that a bigger and more dense droplet evolves more slowly than a smaller and lighter one. The surface tension can be meant as the elastic constant of the droplet surface, thus a higher surface tension leads to oscillations with higher frequency.

A.2 Numerical origin of the capillary wave in the static droplet simulations

The capillary wave evolution in the equilibrium static droplet simulations takes its origin from the droplet initialization. A circular droplet of radius R_{ex} is initialized by the volume fraction mapping over a discrete uniform meshed domain. The volume fraction values are 1 for inside droplet cells and 0 outside. For cells cut by the interface, the volume fraction is computed as the area included within the discrete interface and the cell sides. Thus, the droplet has initially an exact shape.

However, the Height Function computed curvature is not uniform along the droplet interface. Due to the numerical errors, the HF computed curvature is more accurate where the interface is aligned with the grid ($\theta = (k\pi)/2$, $k \in \mathbb{Z}$) and less accurate where worst aligned ($\theta = (1 + 2k)\pi/4$). The Fig. A.1 shows the initial local radius of the droplet $R(\theta, t = 0)$, as a black dash-dot line with asterisks. The asterisks indicates the droplet local radius evaluated as the inverse of the HF computed curvature, at the angular coordinates θ of the discrete locations of the interface cells centroids. The profile is clearly periodic with period $\Theta = \pi/2$. The Figure A.1 reports also the theoretical initial droplet profile, as a black solid line, given by the

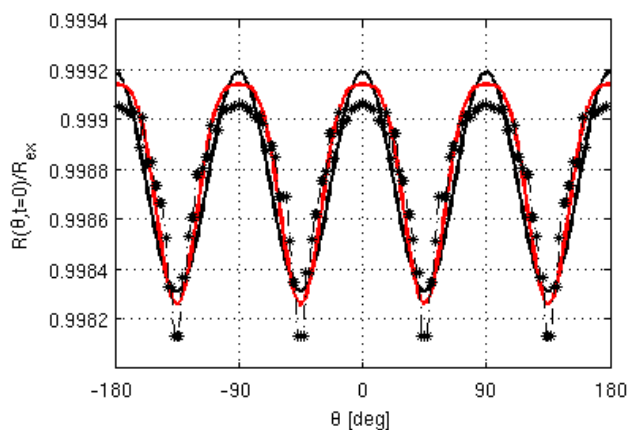


Figure A.1: Initial non-dimensional droplet radius distribution. The asterisks represent the numerical profile, lines are the analytical profiles given by Eq. (A.8): the black solid line is $m = 4$ wave and the red one is the sum of a two modes of oscillations wave with $m = 4, 8$.

real part of Eq. (A.8), with R_0 and δ_0 extrapolated from numerical data. R_0 and δ_0 depend only on the mesh element size, the droplet size and its position with respect to the background grid. Mode of oscillation is $m = 2\pi/\Theta = 4$. The red solid line in the figure is the initial theoretical profile given by a wave with two modes of oscillation, its meaning will be introduced in Section A.3.2.

Since Eq. (A.8) represents the initial interface perturbation, it is clear that the initial HF non-uniform computation of the droplet curvature is the spark for the capillary phenomenon in the simulations. As the simulation starts, surface tension algorithm gets a perturbed interface and acts to uniform the droplet numerical curvature. As a consequence, the droplet evolves oscillating and recovering exact numerical balance.

In order to prove that the numerical droplet evolves as a capillary wave, we have to show that it obeys to the relations developed in Section A.1. The numerical interface position is expected to follow the evolution given by Eq. (A.18) and the time period of the oscillations has to agree with Eq. (A.22).

A.3 Numerical simulations of the static droplet

With the aim of comparing the numerical with the theoretical results based on the stability analysis, 19 two-dimensional inviscid static droplet simulations were performed. The reference case was a droplet of radius R_{ex} placed inside a $L = 4R_{ex}$ side square domain. This droplet was centered at $(x_C = L/2 + \Delta x/2, y_C = L/2 + \Delta x/2)$, with Δx being the cell size. The domain was meshed with a uniform 80×80 grid. The surface tension and both phases' densities were set as unity. Viscous and gravity effects were neglected. The free-slip boundary condition was applied at all boundaries. The simulation time step Δt for the reference case had a value of $0.1\Delta t_{CFL}$, with Δt_{CFL} being the Courant-Friedrichs-Lewy condition. Starting from this reference case, 18 simulations were performed changing one at a time the parameters listed in Table A.1. The term ρ_e stands for the density of the external fluid.

Parameter	Range
R_{ex}	$L/16 - L/4$
h	$R_{ex}/20 - R_{ex}/5$
σ	$10^{-4} - 10^4$
$\rho_l = \rho_e$	$10^{-3} - 10^3$
ρ_l/ρ_e	$10^{-3} - 10^3$
(x_C, y_C)	$(L/2 + \Delta x/2, L/2 + \Delta x/2) - (L/2, L/2)$
$\Delta t/\Delta t_{CFL}$	$10^{-1} - 10^{-2}$

Table A.1: Summary of the parameters varied in the numerical simulations.

A.3.1 Oscillation time period

In order to identify the numerical oscillation time period T_{num} , we considered the following numerical non-dimensional velocity norm:

$$L_2(|\mathbf{u}^*|) = \frac{1}{U} \sqrt{\sum_{i=1}^n \frac{|\mathbf{u}_i|^2}{n}} \quad (\text{A.23})$$

with n being the number of interface cells and \mathbf{u}_i being the i -th cell-centered velocity. Thus, this velocity norm can be meant as the average velocity of the interface. $U = [\sigma/(\rho_l + \rho_e)R_{ex}]^{1/2}$ is the velocity scale chosen as reference. Figure A.2 reports the velocity norm for the reference case, with respect to dimensionless time. $T_\sigma = [4(\rho_l + \rho_e)R_{ex}^3/\sigma]^{1/2}$ is the time scale associated to U . The velocity norm defined oscillates with time with the same period T of the capillary wave. The numerical time period of the oscillation was identified as the time-interval between the beginning of the simulation and the second local minimum of the velocity norm. It can be seen that $T_{num} \approx 0.4T_\sigma$ as reported by Popinet [49].

Theoretical time period T of the oscillations was computed by Eq. (A.22), setting $m = 4$ and replacing ρ_l with $\rho_l + \rho_e$ to include the presence of an external fluid, as suggested by Fyfe *et al.* [126]. The numerical and analytical time periods of the oscillations are reported in Table A.2 for all the test cases. The agreement is good for the cases 1-9, with a constant error around 5%. For the cases 10-13, characterized by a density ratio not unitary, the velocity error norm evolution was not as smooth as the one reported in Fig. A.2, however it was still possible to identify

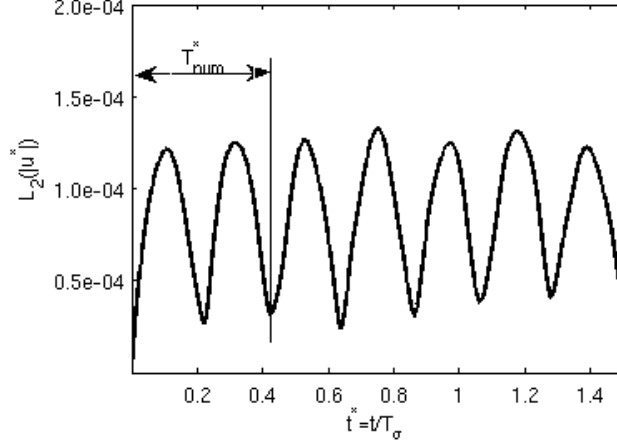


Figure A.2: Numerical dimensionless velocity norm defined in Eq. (A.23) with respect to the non-dimensional time, for the reference case. Velocity and time are made non-dimensional using respectively U and T_σ as reference scales.

a time period. Results are satisfactory with except for the case 13, which shows an error about 10% due to numerical errors generated by the high density ratio. Cases 14-17 share the feature to have a $R_{ex}/\Delta x$ ratio lower than the reference case, leading to less accuracy in the computation of the interface effects. Shifting the droplet at the center of the domain (case 18) has the effects of placing the interface tangent to the grid where they are aligned, as a consequence the error becomes half than the original. The case 19 shows that a finer time step does not change the accuracy of the numerical computation.

A.3.2 Droplet profile evolution

The numerical droplet profile evolution with time $R(\theta, t)$ is compared to the theoretical profile. Figure A.3 reports the numerical and two analytical profiles, at different time instants. The analytical profile plotted with the black solid line refers to the real part of Eq. (A.18) with $m = 4$ and R_0, δ_0 set in order to fit the numerical profile at the instant $t = 0$. The analytical profile matches well the numerical data at the time instants $t = T/2$ and $t = T$. However, it fails to predict numerical waves at $t = T/4$ and $t = 3/4T$, because at these time instants the time component of Eq. (A.18) is zero. But the numerical wave is not null at $t = T/4$ and $t = 3/4T$, there-

Case	Modified parameter	T [s]	T_{num} [s] (err.)
1	-	$4.06 \cdot 10^{-4}$	$4.26 \cdot 10^{-4}$ (5%)
2	$\sigma = 10^2$	$4.06 \cdot 10^{-5}$	$4.26 \cdot 10^{-5}$ (5%)
3	$\sigma = 10^4$	$4.06 \cdot 10^{-6}$	$4.26 \cdot 10^{-6}$ (5%)
4	$\sigma = 10^{-2}$	$4.06 \cdot 10^{-3}$	$4.26 \cdot 10^{-3}$ (5%)
5	$\sigma = 10^{-4}$	$4.06 \cdot 10^{-2}$	$4.26 \cdot 10^{-2}$ (5%)
6	$\rho_l = \rho_e = 10^2$	$4.06 \cdot 10^{-3}$	$4.26 \cdot 10^{-3}$ (5%)
7	$\rho_l = \rho_e = 10^3$	$1.284 \cdot 10^{-2}$	$1.347 \cdot 10^{-2}$ (5%)
8	$\rho_l = \rho_e = 10^{-2}$	$4.06 \cdot 10^{-5}$	$4.26 \cdot 10^{-5}$ (5%)
9	$\rho_l = \rho_e = 10^{-3}$	$1.284 \cdot 10^{-5}$	$1.355 \cdot 10^{-5}$ (5.5%)
10	$\rho_l/\rho_e = 10^2$	$2.882 \cdot 10^{-4}$	$2.98 \cdot 10^{-4}$ (3.4%)
11	$\rho_l/\rho_e = 10^3$	$2.869 \cdot 10^{-4}$	$2.955 \cdot 10^{-4}$ (3%)
12	$\rho_l/\rho_e = 10^{-2}$	$2.888 \cdot 10^{-3}$	$2.706 \cdot 10^{-3}$ (6.3%)
13	$\rho_l/\rho_e = 10^{-3}$	$9.074 \cdot 10^{-3}$	$8.08 \cdot 10^{-3}$ (10.1%)
14	$R_{ex} = L/8$	$1.434 \cdot 10^{-4}$	$1.625 \cdot 10^{-4}$ (13.3%)
15	$R_{ex} = L/16$	$5.07 \cdot 10^{-5}$	$6.4 \cdot 10^{-5}$ (26.2%)
16	$h = R_{ex}/10$	$4.06 \cdot 10^{-4}$	$4.605 \cdot 10^{-4}$ (13.4%)
17	$h = R_{ex}/5$	$4.06 \cdot 10^{-4}$	$5.12 \cdot 10^{-4}$ (26.1%)
18	$(x_C, y_C) = (L/2, L/2)$	$4.06 \cdot 10^{-4}$	$4.16 \cdot 10^{-4}$ (2.5%)
19	$\Delta t/\Delta t_{CFL} = 10^{-2}$	$4.06 \cdot 10^{-4}$	$4.26 \cdot 10^{-4}$ (5%)

Table A.2: Comparison of analytical and numerical periods of the oscillations. The error between the brackets is computed as $|T - T_{num}|/T$.

fore the capillary wave has at least a second mode of oscillation. This second mode has a spatial frequency double with respect to the main mode, thus a wave number of $m = 8$. The amplitude is several times less and it is shifted by $\pi/8$ with respect to the main mode. This higher frequency mode of oscillation is able to capture the flattening of the $t = 0$ droplet numerical profile where the interface is best aligned with the background grid and the sharpening when worst aligned, as can be seen coming back to Fig. A.1. Adding this second mode of oscillation to Eq. (A.18) and adjusting R_0 , the resulting theoretical profile, which is shown as a red solid line in Fig. A.3, matches better the numerical interface profile at $t = T/4$ and $t = 3/4 T$.

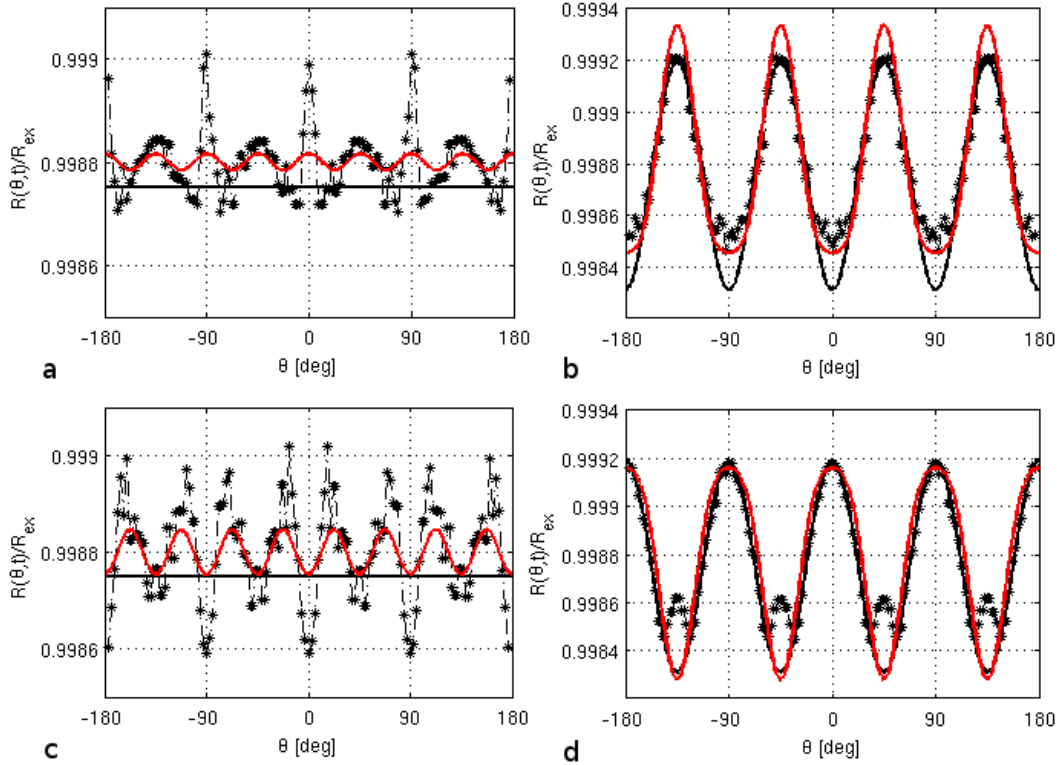


Figure A.3: Non-dimensional droplet radius evolution at $t = T/4$ (a), $t = T/2$ (b), $t = 3/4T$ (c) and $t = T$ (d), for case 1. The dash-dot line with the asterisks is the numerical profile, the black solid line is the analytical profile given by Eq. (A.18) with $m = 4$, the red line is the theoretical profile with both $m = 4, 8$ modes of oscillation.

A.3.3 Velocity fields

We observed that the flow field across the droplet shows the oscillatory behavior of the capillary wave. Counter-current velocity vortices appear at the interface and they decay rapidly far from it, see Fig. 5.4. We compared the numerical velocity norm defined in Eq. (A.23) with the time-derivative of the theoretical interface profile given by Eq. (A.18). Both of the velocities showed the same periodical behavior, but the theoretical one overpredicted the numerical norm. The choice of a more representative index for the numerical velocity is still an open issue.

Bibliography

- [1] E. T. White and R. H. Beardmore. The velocity of rise of single cylindrical air bubbles through liquids contained in vertical tubes. *Chemical Engineering Science*, 17:351–361, 1962.
- [2] R. Revellin, V. Dupont, T. Ursenbacher, J. R. Thome, and I. Zun. Characterization of diabatic two-phase flows in microchannels: Flow parameter results for R-134a in a 0.5 mm channel. *Int. J. of Multiphase Flow*, 32:755–774, 2006.
- [3] Y. Han and N. Shikazono. Measurement of the liquid film thickness in micro-tube slug flow. *Int. J. of Heat and Mass Transfer*, 30:842–853, 2009.
- [4] K. A. Triplett, S. M. Ghiaasiaan, S. I. Abdel-Khalik, and D. L. Sadowski. Gas-liquid two-phase flow in microchannels Part I: two-phase flow patterns. *Int. J. of Multiphase Flow*, 25:377–394, 1999.
- [5] J. R. Thome, V. Dupont, and A. M. Jabobi. Heat transfer model for evaporation in microchannels. Part I: presentation of the model. *Int. J. of Heat and Mass Transfer*, 47:3375–3385, 2004.
- [6] P. A. Walsh, E. J. Walsh, and Y. S. Muzychka. Heat transfer model for gas-liquid slug flows under constant heat flux. *Int. J. of Heat and Mass Transfer*, 53:3193–3201, 2010.
- [7] S. Hardt and F. Wondra. Evaporation model for interfacial flows based on a continuum-field representation of the source terms. *J. of Computational Physics*, 227:5871–5895, 2008.

- [8] L. Consolini and J. R. Thome. A heat transfer model for evaporation of coalescing bubbles in microchannel flow. *Int. J. of Heat and Fluid Flow*, 31:115–125, 2010.
- [9] J. B. Marcinichen, J. R. Thome, and B. Michel. Cooling of microprocessors with micro-evaporation: A novel two-phase cooling cycle. *Int. J. of Refrigeration*, 33:1264–1276, 2010.
- [10] B. Agostini, M. Fabbri, J. E. Park, L. Wojtan, J. R. Thome, and B. Michel. State of the art of high heat flux cooling technologies. *Heat Transfer Engineering*, 28:258–281, 2007.
- [11] *Ansys Fluent*. <http://www.ansys.com>.
- [12] M. Z. Podowski and R. M. Podowski. Mechanistic multidimensional modeling of forced convection boiling heat transfer. *Science and Technology of Nuclear Installations*, 2008.
- [13] M. Ishii. *Thermo-fluid Dynamic Theory of Two-Phase Flow*. Eyrolles, Paris, 1975.
- [14] W. E. Ranz and J. R. Marshall. Evaporation from drops. Part I. *Chemical Engineering Progress*, 48:141–146, 1952.
- [15] N. Kurul and M. Z. Podowski. On the modeling of multidimensional effects in boiling channels. In *Proceedings of the 27th National Heat Transfer Conference*, Minneapolis, MN, USA, 1991.
- [16] J. Y. Tu and G. H. Yeoh. On numerical modelling of low-pressure subcooled boiling flows. *Int. J. of Heat and Mass Transfer*, 45:1197–1209, 2002.
- [17] B. Končar, I. Kljenak, and B. Mavko. Modelling of local two-phase flow parameters in upward subcooled flow boiling at low pressure. *Int. J. of Heat and Mass Transfer*, 47:1299–1513, 2004.
- [18] E. Chen, Y. Li, and X. Cheng. CFD simulation of upward subcooled boiling flow of refrigerant-113 using the two-fluid model. *Applied Thermal Engineering*, 29:2508–2517, 2009.

- [19] G. Tryggvason, R. Scardovelli, and S. Zaleski. *Direct numerical simulations of gas-liquid multiphase flows*. Cambridge University Press, Cambridge, 2011.
- [20] D. Juric and G. Tryggvason. Computations of boiling flows. *Int. J. of Multiphase Flow*, 24:387–410, 1998.
- [21] G. Ryskin and L. G. Leal. Numerical solution of free-boundary problems in fluid mechanics. Part 1. the finite-difference technique. *J. of Fluid Mechanics*, 148:1–17, 1984.
- [22] C. W. Hirt, A. A. Amsden, and J. L. Cook. An arbitrary Lagrangian-Eulerian computing method for all flow speeds. *J. of Computational Physics*, 135:203–216, 1997.
- [23] J. Li, M. Hesse, J. Ziegler, and A. W. Woods. An arbitrary Lagrangian-Eulerian method for moving-boundary problems and its application to jumping over water. *J. of Computational Physics*, 208:289–314, 2005.
- [24] S. Ganesan and L. Tobiska. Computation of flows with interfaces using arbitrary Lagrangian Eulerian method. In *European Conference on Computational Fluid Dynamics ECCOMAS 2006*, TU Delft, The Netherlands, 2006.
- [25] F. Harlow and J. E. Welch. Numerical calculation of time-dependent viscous incompressible flow of fluid with a free surface. *Physics of Fluids*, 8:2182–2189, 1965.
- [26] J. E. Welch, F. H. Harlow, J. P. Shannon, and B. J. Daly. The MAC method. Technical Report LA-3425, Los Alamos National Laboratory, 1965.
- [27] S. McKee, M. F. Tomé, V. G. Ferreira, J. A. Cuminato, A. Castelo, F. S. Sousa, and N. Mangiavacchi. Review: the MAC method. *Computers and Fluids*, 37:907–930, 2008.
- [28] D. Lakehal, M. Meier, and M. Fulgosi. Interface tracking towards the direct simulation of heat and mass transfer in multiphase flows. *Int. J. of Heat and Fluid Flow*, 23:242–257, 2002.

- [29] G. Tryggvason, B. Bunner, A. Esmaeeli, D. Juric, N. Al-Rawahi, W. Tauber, J. Han, S. Nas, and Y.-J. Jan. A front-tracking method for the computations of multiphase flow. *J. of Computational Physics*, 169:708–759, 2001.
- [30] S. O. Unverdi and G. Tryggvason. A front-tracking method for viscous, incompressible, multi-fluid flows. *J. of Computational Physics*, 100:25–37, 1992.
- [31] C. S. Peskin and D. M. McQueen. A general method for the computer simulation of biological systems interacting with fluids. In *SEB Symposium on Biological Fluid Dynamics*, Leeds, England, 1994.
- [32] M. Sussman, P. Smereka, and S. Osher. A level set approach for computing solutions to incompressible two-phase flow. *J. of Computational Physics*, 114:146–159, 1994.
- [33] J.-S. Jiang and D. Peng. Weighted ENO schemes for Hamilton-Jacobi equations. *J. of Scientific Computing*, 21:2126–2143, 2000.
- [34] M. Sussman, E. Fatemi, P. Smereka, and S. Osher. An improved level set method for incompressible two-phase flows. *Computers and Fluids*, 27:663–680, 1998.
- [35] C. W. Hirt and B. D. Nichols. Volume of fluid (VOF) method for the dynamics of free boundaries. *J. of Computational Physics*, 39:201–225, 1981.
- [36] M. Malik, E. Sheung-Chi Fan, and M. Bussmann. Adaptive VOF with curvature-based refinement. *Int. J. for Numerical Methods in Fluids*, 55:693–712, 2007.
- [37] W. F. Noh and P. Woodward. The SLIC (Simple Line Interface Calculation) method. Technical Report UCRL-52111, Lawrence Livermore Laboratory, 1976.
- [38] D. L. Youngs. Time-dependent multi-material flow with large fluid distortion. In K. W. Morton and M. J. Baines, editors, *Numerical Methods for Fluid Dynamics*, pages 273–285. Academic Press, 1982.

- [39] M. Sussman and E. G. Puckett. A coupled level set and volume-of-fluid method for computing 3D and axisymmetric incompressible two-phase flows. *J. of Computational Physics*, 162:301–337, 2000.
- [40] B. Nichita. *An improved CFD tool to simulate adiabatic and diabatic two-phase flows*. PhD thesis, Ecole Polytechnique Fédérale de Lausanne (EPFL), Lausanne, Switzerland, 2010.
- [41] E. Aulisa, S. Manservigi, and R. Scardovelli. A mixed markers and volume-of-fluid method for the reconstruction and advection of interfaces in two-phase and free-boundary flows. *J. of Computational Physics*, 188:611–639, 2003.
- [42] D. Enright, R. Fedkiw, J. Ferziger, and I. Mitchell. A hybrid particle level set method for improved interface capturing. *J. of Computational Physics*, 183:83–116, 2002.
- [43] J. U. Brackbill, D. B. Kothe, and C. Zemach. A continuum method for modeling surface tension. *J. of Computational Physics*, 100:335–354, 1992.
- [44] B. Lafaurie, C. Nardone, R. Scardovelli, S. Zaleski, and G. Zanetti. Modelling merging and fragmentation in multiphase flows with SURFER. *J. of Computational Physics*, 113:134–147, 1994.
- [45] X.-D. Liu, R. P. Fedkiw, and M. Kang. A boundary condition capturing method for Poisson’s equation on irregular domains. *J. of Computational Physics*, 160:151–178, 2000.
- [46] D. J. E. Harvie, M. R. Davidson, and M. Rudman. An analysis of parasitic current generation in Volume Of Fluid simulations. *Applied Mathematical Modelling*, 30:1056–1066, 2006.
- [47] Y. Renardy and M. Renardy. PROST: a Parabolic Reconstruction of Surface Tension for the volume-of-fluid method. *J. of Computational Physics*, 183:400–421, 2002.
- [48] M. M. Francois, S. J. Cummins, E. D. Dendy, D. B. Kothe, J. M. Sicilian, and M. J. Williams. A balanced-force algorithm for continuous and sharp interfacial surface tension models within a volume tracking framework. *J. of Computational Physics*, 213:141–173, 2006.

- [49] S. Popinet. An accurate adaptive solver for surface-tension-driven interfacial flows. *J. of Computational Physics*, 228:5838–5866, 2009.
- [50] D. T. Dumitrescu. Strömung an einer luftblase im senkrechten rohr. *Zeitschrift für Angewandte Mathematik und Mechanik*, 23:139–149, 1943.
- [51] F. P. Bretherton. The motion of large bubbles in tubes. *J. of Fluid Mechanics*, 10:166–188, 1961.
- [52] R. A. S. Brown. The mechanism of large bubbles intubes. I. bubbles velocities in stagnant liquids. *Canadian Journal of Chemical Engineering*, 43:217–223, 1965.
- [53] D. J. Nicklin, J. O. Wilkes, and J. F. Davidson. Two-phase flow in vertical tubes. *Transactions of the Institution of Chemical Engineers*, 40:61–68, 1962.
- [54] J. B. L. M. Campos and J. R. F. Guedes de Carvalho. An experimental study of the wake of gas slugs rising in liquids. *J. of Fluid Mechanics*, 196:27–37, 1988.
- [55] J. B. L. M. Campos and J. R. F. Guedes de Carvalho. An experimental study of the wake of gas slugs rising in liquids. *J. of Fluid Mechanics*, 196:27–37, 1988.
- [56] J. D. Bugg and G. A. Saad. The velocity field around a Taylor bubble rising in a stagnant viscous fluid: numerical and experimental results. *Int. J. of Multiphase Flow*, 28:791–803, 2002.
- [57] S. Nogueira, M. L. Riethmuler, and J. B. L. M. Campos ans A. M. F. R. Pinto. Flow in the nose region and annular film around a Taylor bubble rising through vertical columns of stagnant and flowing newtonian liquids. *Chemical Engineering Science*, 61:845–857, 2006.
- [58] Z.-S. Mao and A. E. Duckler. The motion of Taylor bubbles in vertical tubes I. a numerical simulation for the shape and rise velocity of Taylor bubbles in stagnant and flowing liquids. *J. of Computational Physics*, 91:132–160, 1990.

- [59] A. Tomiyama, I. Zun, A. Sou, and T. Sakaguchi. Numerical analysis of bubble motion with the VOF method. *Nuclear Engineering and Design*, 141:69–82, 1993.
- [60] M. Kawaji, J. M. DeJesus, and G. Tudsoe. Investigation of flow structures in vertical slug flow. *Nuclear Engineering and Design*, 175:37–48, 1997.
- [61] J. D. Bugg, K. Mack, and K. S. Rezkallah. A numerical model of Taylor bubbles rising through stagnant liquids in vertical tubes. *Int. J. of Multiphase Flow*, 24:271–281, 1998.
- [62] N. V. Ndinisa, D. E. Wiley, and D. F. Fletcher. Computational fluid dynamics simulations of Taylor bubbles in tubular membranes model validation and application to laminar flow systems. *Chemical Engineering Research and Design*, 83:40–49, 2005.
- [63] *Ansys CFX*. <http://www.ansys.com>.
- [64] T. Taha and Z. F. Cui. CFD modelling of slug flow in vertical tubes. *Chemical Engineering Science*, 61:676–687, 2006.
- [65] Y. Chen, R. Kulenovic, and R. Mertz. Numerical study of the formation of Taylor bubbles in capillary tubes. *Int. J. of Thermal Science*, 48:234–242, 2009.
- [66] K. Kayashi, R. Kurimoto, and A. Tomiyama. Terminal velocity of a Taylor drop in a vertical pipe. *Int. J. of Multiphase Flow*, 37:241–251, 2011.
- [67] F. Fairbrother and A. E. Stubbs. The bubble-tube method of measurement. *J. of Chemical Society*, 1:527–529, 1935.
- [68] P. A. Kew and K. Cornwell. Correlations for prediction of flow boiling heat transfer in small-diameters channels. *Applied Thermal Engineering*, 17:705–715, 1997.
- [69] C. L. Ong and J. R. Thome. Macro-to-microchannel transition in two-phase flow: Part 1 - two-phase flow patterns and film thickness measurements. *Experimental Thermal and Fluid Science*, 35:37–47, 2011.

- [70] G. I. Taylor. Deposition of a viscous fluid on the wall of a tube. *J. of Fluid Mechanics*, 10:161–165, 1960.
- [71] P. Aussillous and D. Quéré. Quick deposition of a fluid on the wall of a tube. *Physics of Fluids*, 12:2367–2371, 2000.
- [72] M. T. Kreutzer, F. Kapteijn, J. A. Moulijn, C. R. Kleijn, and J. J. Heiszwolf. Inertial and interfacial effects on pressure drop of Taylor flow in capillaries. *A.I.Ch.E. Journal*, 51:2428–2440, 2005.
- [73] J. R. Thome. *Wolverine Engineering Data Book III*. Available free at <http://www.wlv.com/products/databook/db3/DataBookIII.pdf>, 2004.
- [74] R. Revellin and J. R. Thome. A new type of diabatic flow pattern map for boiling heat transfer in microchannels. *J. of Micromechanics and Microengineering*, 17:788–796, 2007.
- [75] A. A. Armand and G. G. Treschev. The resistance during the movement of a two-phase system in horizontal pipes. *Izvestiya Vsesoyuznogo Teploekhnicheskogo Instituta*, 1:16–23, 1946.
- [76] B. Agostini, R. Revellin, and J. R. Thome. Elongated bubbles in microchannels. Part I: Experimental study and modeling of elongated bubble velocity. *Int. J. of Multiphase flow*, 34:590–601, 2008.
- [77] A. M. Jacobi and J. R. Thome. Heat transfer model for evaporation of elongated bubble flows in microchannels. *J. of Heat Transfer*, 124:1131–1136, 2002.
- [78] V. Dupont, J. R. Thome, and A. M. Jabobi. Heat transfer model for evaporation in microchannels. Part II: comparison with the database. *Int. J. of Heat and Mass Transfer*, 47:3387–3401, 2004.
- [79] J. A. Howard, P. A. Walsh, and E. J. Walsh. Prandtl and capillary effects on heat transfer within laminar liquid-gas slug flows. *Int. J. of Heat and Mass Transfer*, 54:4752–4761, 2011.
- [80] R. Revellin and J. R. Thome. Adiabatic two-phase frictional pressure drops in microchannels. *Experimental Thermal and Fluid Science*, 31:673–685, 2007.

- [81] D. Qian and A. Lawal. Numerical study on gas and liquid slugs for Taylor flow in a T-junction microchannel. *Chemical Engineering Science*, 61:7609–7625, 2006.
- [82] V. Kumar, S. Vashisth, Y. Hoarau, and K. D. P. Nigam. Slug flow in curved microreactors: Hydrodynamic study. *Chemical Engineering Science*, 62:7494–7504, 2007.
- [83] R. Gupta, D. F. Fletcher, and B. S. Haynes. On the CFD modelling of Taylor flow in microchannels. *Chemical Engineering Science*, 64:2941–2950, 2009.
- [84] K. Fukagata, N. Kasagi, P. Ua-arayaporn, and T. Himeno. Numerical simulation of gas-liquid two-phase flow and convective heat transfer in a micro tube. *Int. J. of Heat and Fluid Flow*, 28:72–82, 2007.
- [85] D. Lakehal, G. Larrignon, and C. Narayanan. Computational heat transfer and two-phase flow topology in miniature tubes. *Microfluid Nanofluid*, 4:261–271, 2008.
- [86] *TransAT CMFD*. <http://www.ascomp.ch>.
- [87] R. Gupta, D. F. Fletcher, and B. S. Haynes. CFD modelling of flow and heat transfer in the Taylor flow regime. *Chemical Engineering Science*, 65:2094–2107, 2010.
- [88] Q. He, Y. Hasegawa, and N. Kasagi. Heat transfer modelling of gas-liquid slug flow without phase change in a micro tube. *Int. J. of Heat and Fluid Flow*, 31:126–136, 2010.
- [89] A. Mehdizadeh, S. A. Sherif, and W. E. Lear. Numerical simulation of thermofluid characteristics of two-phase slug flow in microchannels. *Int. J. of Heat and Mass Transfer*, 54:3457–3465, 2011.
- [90] A. Mukherjee and S. G. Kandlikar. Numerical simulation of growth of a vapor bubble during flow boiling of water in microchannel. *Microfluid Nanofluid*, 1:137–145, 2007.
- [91] A. Mukherjee. Contribution of thin-film evaporation during flow boiling inside microchannels. *Int. J. of Thermal Sciences*, 48:2025–2035, 2009.

- [92] A. Mukherjee, S. G. Kandlikar, and Z. J. Edel. Numerical study of bubble growth and wall heat transfer during flow boiling in a microchannel. *Int. J. of Heat and Mass Transfer*, 54:3702–3718, 2011.
- [93] Y. Suh, W. Lee, and G. Son. Bubble dynamics, flow, and heat transfer during flow boiling in parallel microchannels. *Numerical Heat Transfer, Part A*, 54:390–405, 2008.
- [94] S. J. Cummins, M. M. Francois, and D. B. Kothe. Estimating curvature from volume fractions. *Computers and Structures*, 83:425–434, 2005.
- [95] V. P. Carey. *Liquid-vapor phase change phenomena*. Taylor and Francis, 1992.
- [96] E. G. Puckett, A. S. Almgren, J. B. Bell, D. L. Marcus, and W. J. Rider. A high-order projection method for tracking fluid interfaces in variable density incompressible flows. *J. of Computational Physics*, 130:269–282, 1997.
- [97] M. W. Williams. *Numerical methods for tracking interfaces with surface tension in 3-D mold filling processes*. PhD thesis, University of California, Davis, 2000.
- [98] J. Helmsen, P. Colella, and E. G. Puckett. Non-convex profile evolution in two dimensions using volume of fluids. Technical Report LBNL-40693, Lawrence Berkeley National Laboratory, 1997.
- [99] J. Hernandez, J. Lopez, P. Gomez, C. Zanzi, and F. Faura. A new volume of fluid method in three dimensions-Part I: Multidimensional advection method with face-matched flux polyhedra. *Int. J. for Numerical Methods in Fluids*, 58:897–921, 2008.
- [100] R. Scardovelli and S. Zaleski. Analytical relations connecting linear interfaces and volume fractions in rectangular grids. *J. of Computational Physics*, 164:228–237, 2000.
- [101] J. Mencinger and I. Zun. On the finite volume discretization of discontinuous body force field on collocated grid: Application to VOF method. *J. of Computational Physics*, 221:524–538, 2007.

- [102] M. Francois and B. K. Swartz. Interface curvature via volume fractions, heights, and mean values on nonuniform rectangular grids. *J. of Computational Physics*, 229:527–540, 2010.
- [103] G. Bornia, A. Cervone, S. Manservigi, R. Scardovelli, and S. Zaleski. On the properties and limitations of the height function method in two-dimensional Cartesian geometry. *J. of Computational Physics*, 230:851–862, 2011.
- [104] J. Lopez, C. Zanzi, P. Gomez, R. Zamora, F. Faura, and J. Hernández. An improved height function technique for computing interface curvature from volume fractions. *Computer Methods in Applied Mechanics and Engineering*, 198:2555–2564, 2009.
- [105] A. Esmaeeli and G. Tryggvason. Computations of film boiling. Part I: numerical method. *Int. J. of Heat and Mass Transfer*, 47:5451–5461, 2004.
- [106] R. W. Schrage. *A theoretical study of interphase mass transfer*. Columbia University Press, New York, 1953.
- [107] R. Marek and J. Straub. Analysis of the evaporation coefficient and the condensation coefficient of water. *Int. J. of Heat and Mass Transfer*, 44:39–53, 2001.
- [108] H. Wang, S. V. Garimella, and J. Y. Murthy. Characteristics of evaporating thin film in a microchannel. *Int. J. of Heat and Mass Transfer*, 50:3933–3942, 2007.
- [109] I. Tanasawa. Advances in condensation heat transfer. In J. P. Hartnett and T. F. Irvine, editors, *Advances in Heat Transfer*. Academic Press, San Diego, 1991.
- [110] *Fluent 6.3 User's Guide*. Fluent Inc., Lebanon, NH, 2006.
- [111] *Fluent 6.3 UDF Manual*. Fluent Inc., Lebanon, NH, 2006.
- [112] G. L. Morini. Viscous heating in liquid flows in micro-channels. *Int. J. of Heat and Mass Transfer*, 48:3637–3647, 2005.

- [113] B. van Leer. Towards the ultimate conservative difference scheme. V. A second-order sequel to Godunov's method. *J. of Computational Physics*, 32:101–136, 1979.
- [114] R. D. Rauch, J. T. Batira, and N. T. Y. Yang. Spatial adaption procedures on unstructured meshes for accurate unsteady aerodynamic flow computations. Technical Report AIAA-91-1106, AIAA, 1991.
- [115] S. V. Patankar. *Numerical Heat Transfer and Fluid Flow*. Hemisphere Publishing, New York, 1980.
- [116] J. P. Vandoormaal and G. D. Raithby. Enhancements of the SIMPLE method for predicting incompressible fluid flows. *Numerical Heat Transfer*, 7:147–163, 1984.
- [117] R. I. Issa. Solution of the implicitly discretized fluid flow equations by operator-splitting. *J. of Computational Physics*, 62:40–65, 1985.
- [118] D. Bhaga and M. E. Weber. Bubbles in viscous liquid: shapes, wakes and velocities. *J. of Fluid Mechanics*, 105:61–85, 1981.
- [119] J. Hua, J. F. Stene, and P. Lin. Numerical simulation of 3D bubbles rising in viscous liquids using a front tracking method. *J. of Computational Physics*, 227:3358–3382, 2008.
- [120] M. S. Plesset and S. A. Zwick. The growth of vapor bubbles in superheated liquids. *J. of Applied Physics*, 25:493–500, 1954.
- [121] L. E. Scriven. On the dynamics of phase growth. *Chemical Engineering Science*, 10:1–13, 1959.
- [122] C. Kunkelmann and P. Stephan. CFD simulation of boiling flows using the Volume-of-Fluid method within OpenFOAM. *Numerical Heat Transfer, Part A*, 56:631–646, 2009.
- [123] L. Consolini and J. R. Thome. Micro-channel flow boiling heat transfer of R-134a, R-236fa, and R-245fa. *Microfluid Nanofluid*, 6:731–746, 2009.

- [124] K. Moriyama and A. Inoue. Thickness of the liquid film formed by a growing bubble in a narrow gap between two horizontal plates. *J. of Heat and Mass Transfer*, 118:132–139, 1996.
- [125] *VDI-Wärmeatlas*. Springer-Verlag, Berlin, Heidelberg, 1997.
- [126] D. E. Fyfe, E. S. Oran, and M. J. Fritts. Surface tension and viscosity with Lagrangian hydrodynamics on a triangular mesh. *J. of Computational Physics*, 76:349–384, 1988.

List of Scientific Publications

B. Pulvirenti, M. Magnini and D. Modenini. Rarefied air flow over a Mars descent vehicle in supersonic regime. *XXVII UIT Conference*, Reggio Emilia, Italy, 2009.

M. Magnini and B. Pulvirenti. Numerical study of vapor bubble growing in superheated liquid. *XXVIII UIT Conference*, Brescia, Italy, 2010.

M. Magnini and B. Pulvirenti. Height Function interface reconstruction algorithm for the simulation of boiling flows. *6th International Conference on Computational and Experimental Methods in Multiphase and Complex Flows*, Kos, Greece, 2011.

M. Magnini, J. R. Thome and B. Pulvirenti. Numerical study of Taylor bubbles rising in vertical circular channels. *XXIX UIT Conference*, Torino, Italy, 2011.

M. Magnini and B. Pulvirenti. Numerical induced capillary waves in the simulation of multiphase flows. *XXIX UIT Conference*, Torino, Italy, 2011.

Curriculum Vitae

PERSONAL DATA

Name	Mirco Magnini
Date of birth	31st August, 1982
Birthplace	Cattolica (RN), Italy
Nationality	Italian

EDUCATION

2011	Visiting Doctoral Student , Laboratory of Heat and Mass Transfer, Swiss Federal Institute of Technology Lausanne (EPFL), Switzerland.
2009-2011	Doctoral Student , Department of Energy, Nuclear and Environmental Control Engineering, University of Bologna, Italy.
2001-2007	Master of Science in Mechanic Engineering , University of Bologna, Italy.
1996-2001	High School Certificate , Liceo Scientifico G. Marconi, Pesaro, Italy.

WORKING EXPERIENCE

2012	Department of Energy, Nuclear and Environmental Control Engineering, University of Bologna, Italy Doctoral Research Assistant.
2011	University of Bologna, Italy Assistant Professor of the course <i>Termofluidodinamica Applicata</i> for the Junior degree in Mechanic Engineering, Polo di Forlì.
2009-2010	University of Bologna, Italy Assistant Professor of the course <i>Fisica Tecnica</i> for the Junior degree in Mechanic Engineering.
2009-2010	Consultant for the R&D department of the company G.D s.p.a., Bologna, Italy .
2008	Department of Energy, Nuclear and Environmental Control Engineering, University of Bologna, Italy Research Assistant.
2007	Radiant Bruciatori, Pesaro, Italy Laboratory Engineer.